Title
Micro/Nanorobotics: from Locomotion to Biomedical Applications

Author
Li, Jinxing

Publication Date
2017

UNIVERSITY OF CALIFORNIA, SAN DIEGO

Micro/Nanorobotics:
from Locomotion to Biomedical Applications

A dissertation submitted in partial satisfaction of the requirements for the degree

Doctor of Philosophy

in

Nano Engineering

by

Jinxing Li

Committee in charge:

Professor, Joseph Wang, Chair
Professor, Ying Shirley Meng
Professor, David Saintillan
Professor, Mike Tolley
Professor, Liangfang Zhang

2017

The Dissertation of Jinxing Li is approved, and it is acceptable in quality and form for publication on microfilm and electronically:

Chair

University of California, San Diego

2017

DEDICATION

To my mom and dad.

EPIGRAPH

“The mountains are calling and I must go.”

\- *John Muir*

“Having fun, this is the most important.”

\- *Joseph Wang*

TABLE OF CONTENTS

LIST OF FIGURES

ACKNOWLEDGEMENTS

First and foremost, I would like to thank my advisor professor Joseph Wang. We firstly met in August 2011 at Nanjing. Even though I was an electrical engineer by the time I applied for PhD study, the privilege to work with him cemented my decision to come to San Diego, which is best place to perform research on this planet. During the past 5 years, he had devoted incredible time and efforts to guide me, to support me, and to work with me towards the success of research projects. He had also given me significant freedom and trust to think outside the box and initiate "wild" multi-disciplinary projects. His full dedication and pursuit and to truly innovative ideas, excellent findings, and scientific rigors, has profoundly shaped my sentiments and my professionalism. His enthusiasm and persistence have inspired me and have allowed me to accomplish more than I ever would have expected as a graduate student.

I would like to thank Prof. Liangfang Zhang, who is my co-adviser and our key faculty collaborator. He played a crucial role in many of my final projects. His brilliant insights gave me a sense of the art of scientific research, and also opened my eyes to the intersection of medicine, bioengineering, and material science. I also highly appreciate the research contributions his lab had made, especially the great efforts from Pavimol Angsantikul, Soracha Kun Thamphiwatana, and Dr. Weiwei Gao, who contributed significant time on biomaterials and animal study.

Over the last five years, I have had the wonderful opportunity to work beside and learn from almost one hundred fellow members of the Wang Group. Wei Gao is one of my earliest colleagues in the lab. His help and advice have been invaluable, and I wish him a great success as a faculty member. Sirilak Sattayasamitsathit is an expert on electrochemistry and gave me the skill sets on this. Ewa Liu and Berta Estaban helped me a lot in finding solutions for many of the challenging projects and to push them moving forward. I also acknowledge the great friendship and collaboration with Tianlong Li, Fernando Soto, Renfeng Dong, Zhiguang Wu, Chuanrui Chen, Xiaolong Lu, Xiaocong Chang, Tailin Xu, Victor Gacia, Beatriz Jurado-Sanchez, Virendra V. Singh, Emil Karshalev, and Rajan Kumar. I also thank all of the undergraduate researchers, Isaac Rozen, Elodie Sandraz, Jason Zhao, Yuyan Liang, Kevin Kaufmann, Isaac Campos, Ryan Tam, and Yuri Fedorak who have worked with me with their smart efforts and I wish they all have promising careers ahead.

I would like to give my special thanks to my faculty collaborators Prof. Anna Balazs and Prof. David Saintillan, who also gave me significant support in my career development. I highly appreciate Prof. Yongfeng Mei, who was my adviser of master study, for giving me persistent and generous support throughout my academic career. I also thank Prof. Boubacar Kante, Prof. Zhaowei Liu, Prof. Shaochen Chen, Prof. Seth Cohen, Prof. Alexander Leshansky, and Prof. Ed Callaway for willingly contributing their time and resources to our shared projects. I acknowledge the creative and collaborative efforts from Oleg E. Shklyaev, Henry Park, Babak Bahari, Xiao Yu, Barath Ezhilan, Peichao Li, and Espoir Kyubwa, who are great scientists from their labs.

I offer special thanks to Prof. Ying Shirley Meng, Prof. Michael Tolley for serving on my defense committee, and giving me support and advices for my academic career. I would like to thank Dana Jimenez, and many of other fantastic nanoengineering staffs, to navigate the trivia of my graduate study. I also thank the Dan David foundation at Tel Aviv University in Israel, and the Siebel Scholar foundation for giving the recognition of my graduate research.

Finally, I would like to thank my family for the consistent support and countless sacrifices.

Chapter 1 is based, in part, on the material as it appears in Science Robotics, 2017, by Jinxing Li, Berta Esteban-Fernández de Ávila, Wei Gao, Liangfang Zhang, Joseph Wang. The dissertation author was the primary investigator and author of these papers.

Chapter 2.1, in full, is a reprint of the material as it appears in Nanoscale, 2014, by Jinxing Li, Sirilak Sattayasamitsathit, Renfeng Dong, Wei Gao, Ryan Tam, Xiaomiao Feng, Stephen Ai, Joseph Wang; Chapter 2.2, in full, is a reprint of the material as it appears in Nano Letters, 2015, by Jinxing Li, Tianlong Li, Tailin Xu, Melek Kiristi, Wenjuan Liu, Zhiguang Wu, Joseph Wang. The dissertation author was the primary investigator and author of these papers.

Chapter 3.1, in full, is a reprint of the material as it appears in Nature Communications, 2014, by Jinxing Li, Wei Gao, Renfeng Dong, Allen Pei, Sirilak Sattayasamitsathit, Joseph Wang. Chapter 3.2, in full, is a reprint of the material as it appears in Nano Letters, 2016, by Jinxing Li, Wenjuan Liu, Tianlong Li, Isaac Rozen, Jason Zhao, Babak Bahari, Boubacar Kante, Joseph Wang. Chapter 3.3, in full, is a reprint of the material as it appears in Nano Letters, 2015, by Jinxing Li, Oleg E Shklyaev, Tianlong Li, Wenjuan Liu, Henry Shum, Isaac Rozen, Anna C Balazs, Joseph Wang. The dissertation author was the primary investigator and author of these papers.

Chapter 4.1, in full, is a reprint of the material as it appears in ACS Nano, 2015, by Wei Gao, Renfeng Dong, Soracha Thamphiwatana, Jinxing Li, Weiwei Gao, Liangfang Zhang, Joseph Wang. Chapter 4.2, in full, is a reprint of the material as it appears in ACS Nano, 2016, by Jinxing Li, Soracha Thamphiwatana, Wenjuan Liu, Berta Esteban-Fernández de Ávila, Pavimol Angsantikul, Elodie Sandraz, Jianxing Wang, Tailin Xu, Fernando Soto, Valentin Ramez, Xiaolei Wang, Weiwei Gao, Liangfang Zhang, Joseph Wang. The dissertation author was the primary investigator and author of these papers.

Chapter 5 is based, in part, on the material as it appears in Science Robotics, 2017, by Jinxing Li, Berta Esteban-Fernández de Ávila, Wei Gao, Liangfang Zhang, Joseph Wang. The dissertation author was the primary investigator and author of these papers.

VITA

2008	Bachelor of Science, Huazhong University of Science and Technology
2012	Master of Science, Fudan University
2017	Doctor of Philosophy, University of California San Diego

PUBLICATIONS

1. J. Li, B. Estaban, W. Gao, L. Zhang, J. Wang. “Micro/nanorobots for Biomedicine: Delivery, Surgery, Sensing, and Detoxification”. *Science Robotics* 2017, 2, eaam6431.
2. J. Li, W. Liu, T. Li, I. Rozen, J. Zhao, B. Bahari, B. Kante, J. Wang. “Swimming Micro-Robot Optical Nanoscopy”, *Nano Lett.* 2016, 16, 6604–6609.
3. J. Li, S. Thamphiwatana, W. Liu, B. Estaban, P. Angsantikul, E. Sandraz, J. Wang, T. Xu, F. Soto, V. Ramez, X. Wang, W. Gao, L. Zhang, J. Wang. “Enteric Micromotor Can Selectively Position and Spontaneously Propel in the Gastrointestinal Tract”, *ACS Nano* 2016, 10, 9536–9542.
4. J. Li, I. Rozen, J. Wang. “Rocket Science on the Nanoscale”, *ACS Nano* 2016, 10, 5619–5634.
5. J. Li, O. Shklyaev, T. Li, W. Liu, H. Shum, I. Rozen, A. C. Balazs, J. Wang. “Self-Propelled Nanomotors Autonomously Seek and Repair Cracks”, *Nano Lett.* 2015, 15, 7077–7085.
6. J. Li, T. Li, T. Xu, M. Kiristi, W. Liu, Z. Wu, J. Wang. “Magneto-Acoustic Hybrid Nanomotor”, *Nano Lett.* 2015, 15, 4814–4821.
7. W. Gao, R. Dong, S. Thamphiwatana, J. Li, W. Gao, L. Zhang, J. Wang. “Artificial Micromotors in the Mouse’s Stomach: a Step toward *in vivo* Use of Synthetic Motors”, *ACS Nano* 2015, 9, 117–123.
8. J. Li, W. Gao, R. Dong, A. Pei, S Sattayasamitsathit, J. Wang. “Nanomotor Lithography”, *Nature Commun.* 2014, 5, 5026.
9. J. Li, S. Sattayasamitsathit, R. Dong, W. Gao, R. Tam, X. Feng, S. Ai, J. Wang. “Template Electrosynthesis of Tailored-Made Helical Nanoswimmers”, *Nanoscale* 2014, 6, 9415–9420.

FIELDS OF STUDY

Major Field: Nanoengineering, Bioengineering, and Chemical Engineering

Studies in Nanoengineering

Professor Joseph Wang

ABSTRACT OF THE DISSERTATION

Micro/Nanorobotics:
from Locomotion to Biomedical Applications

by

Jinxing Li

Doctor of Philosophy in Nano Engineering

University of California, San Diego, 2017

Professor Joseph Wang, Chair

Robotics has markedly extended the reach of human beings in sensing, manipulating, and transforming the world around us. One of the most inspiring challenges in science and technology is to extend our capacity with tiny robots towards operations at the micro/nanoscales, a dimension where we can directly interact with fundamental biological building blocks. This thesis is devoted to advancing micro/nanorobotics to extend human being's capacities in following three themes, with a special focus being given to biomedical applications. The first theme focuses on design and fabrication of bio-inspired un-tethered nanorobots with efficient locomotion, adaptive operation,

collective regulation, and eventually biological function towards operation in whole blood. The second theme explores the versatility of functional micro/nanorobots to perform diverse tasks including writing (nanolithography), reading (superresolution imaging), destroying (warfare agents), and repairing (surface cracks), all at the micro/nanoscale. The third theme employs self-propelling microrobot as an active delivery technique that autonomously and precisely transports the therapeutic agents inside live animal’s gastrointestinal tract, improving therapeutic efficacy for bacterial infection treatment. This technique opens the door for micro/nanorobots as an active delivery platform for medical treatment and is promising for a wide range of personalized diagnostic and therapeutic applications. Ultimately, micro/nanorobots has the potential to change the game of science, engineering, and medicine by extending our capacity at the micro/nanoscale. The novel applications presented in this thesis are just a few examples showing the power of micro/nanorobots, with countless more avenues waiting to be explored towards living and active matter, and eventually artificial intelligence and synthetic life at the micro/nanoscale.

Chapter 1 Introduction

1.1 Motivations, challenges, and solutions for nanolocomotion

A robot is a machine capable of carrying out a complex series of actions automatically. Nature's ability to create sophisticated and functionalized organisms has long been an inspiration for scientists to make ever-more capable machines. At the macroscopic scale, the agile motor behaviors of animals have inspired the rapid development of bio-robotics—the construction of biologically inspired or biomimetic robots [1]. Advanced robotic systems have dramatically extended the reach of human beings in sensing, interacting, manipulating and transforming the world around us [2]. In particular, the confluence of diverse technologies has enabled a revolution in medical applications of robotic technologies toward improving health care. Whereas industrial robots were developed primarily to automate routine and dangerous macroscale manufacturing tasks, medical robotic devices are designed for entirely different environments and operations relevant to the treatment and prevention of diseases. Therefore, unlike conventional "old" robots, which are built with large mechanical systems, medical robots require miniaturized parts and smart materials for complex and precise operations and mating with the human body. The rapid growth in medical robotics has been driven by a combination of technological advances in motors, control theory, materials, and medical imaging and increase in surgeon/patient acceptance [3,4]. For example, robotic surgical systems, such as the da Vinci system, allow translation of the surgeon's hand movements into smaller, precise movements of tiny instruments within the patient's body.

Despite widespread adoption of robotic systems for minimally invasive surgery, there are still major technical difficulties and challenges [5]. The mechanical parts of existing medical robotic devices are still relatively large and rigid to access and treat major previously inaccessible parts of the human body. Designing miniaturized and tetherless robots of a few micrometers or less would allow access throughout the whole human body, leading to new procedures down to the cellular level and offering localized diagnosis and treatment with greater precision and efficiency. Advancing the miniaturization of robotic systems at the micro- and nanoscales thus holds considerable promise for enhancing the treatment of a wide variety of diseases and disorders [6,7].

The concept of nanotechnology and tiny machines, which is initially introduced by visionary physicist Richard Feynman, has inspired scientists and engineers to manufacture devices and structures in micro/nanometer scale. The efficient locomotion capacity and functional complexity of biological motors, such as bacteria and spermatozoa, are a nanoengineer's dream. However, due to the size-dependent competition between inertial and viscous forces within a fluid, the physics governing the microscopic organisms (e.g. bacteria, spermatozoa) and macroscopic organisms (e.g. fish, humans) are quite different [8]. The Reynolds number, $Re = \rho U L/\mu$, (with ρ and μ are the density and dynamic viscosity of the fluid, and U and L characteristic speed and dimension) is a dimensionless parameter which measures the ratio of inertial forces to viscous forces in a fluid. Locomotion at large Reynolds numbers, swimming can be achieved by reciprocal motion (i.e. identical under a time-reversal symmetry), by imparting momentum into the fluid opposite the direction of locomotion. For swimming microorganisms, inertia plays a negligible role and viscous force dominates the motion. In such a low Reynolds number regime, a reciprocal motion leads to zero net propulsion. The natural microswimmer, *Escherichia coli* bacteria, a unicellular eukaryote that lives in the gut, is equipped with a set of helical flagellums which rotate to enable swimming [9]. For some eukaryotic spermatozoa, they swim by propagating a planar traveling wave along the flagellum [10]. Overall, microrganisms are able to circumvent the constraints of the scallop theorem by deforming their bodies or flagella in a wave-like fashion to break the time-reversibility requirement.

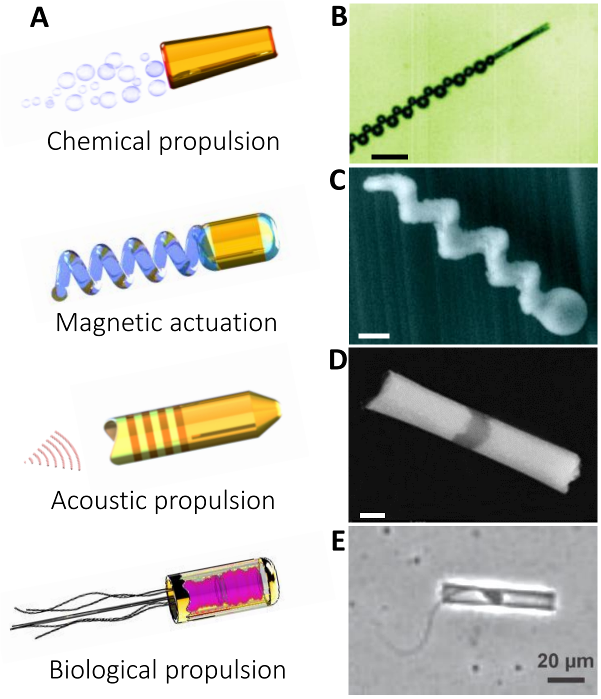

Figure 1.1 Actuation mechanisms of various types of micro/nanorobots. (A) Typical propulsion mechanisms of micro/nanoscale robots. (B) Chemically powered microrocket [11]. Scale bar: 50 µm. (C) Magnetically actuated helical nanoswimmer (31). Scale bar: 200 nm. (D) Acoustically propelled nanowire motor [32]. Scale bar: 200 nm. (E) Biologically propelled sperm hybrid microrobot [33].

To design a microscale or nanoscale robot that can propel in a purposeful way, one needs both a swimming strategy that works in these low Reynolds number environments as well as a strategy for steering and directing the motion to overcome Brownian motion. Following Feynman's vision, an explosion of different fabrication methods has become available for the preparation of nanostructures with controlled shape and size, providing a foundation for exciting advances in making micro/nanomachines. The advanced nanofabrication technique allows scientists to make nanostructures which could not only mechanically mimic natural swimmers but also be able to transform diverse other energy sources into mechanical motions. The resulted micro/nanorobots, which are motorized micro- and nanoscale devices, are able performing diverse tasks though designed mechanical movements.

Several types of micro/nanorobots based on distinct actuation principles (Fig. 1.1) have been developed in the past decade. Typically, these tiny machines rely on either chemically-powered motors that convert locally supplied fuels to force and movement or externally-powered motors that mostly utilize magnetic and ultrasound energies (and sometime optical, thermal, and electrical energies) to drive their motion [12–22]. The fundamental principles of these nanomachines, with rich underlying physics and chemistry, have been discussed in several comprehensive articles [6,12,23–25]. Chemically-powered motors can propel themselves through aqueous solution by using surface reactions for generating local gradients of concentration, electrical potential, and gas bubbles [17,23,24]. Magnetic swimmers successfully use magnetic actuation to reproduce the motions of natural swimming microorganisms with helical or flexible flagella [6]. The proposed propulsion mechanism of acoustic nanomotors suggests that they use asymmetric steady streaming to produce a finite propulsion speed along the axis of the symmetry of the device and perpendicular to the oscillation direction [25]. Optical, thermal, and electrical energies can also be harvested to drive the motion of micro/nanostructures with unique principles [26–29]. Synthetic micro/nanodevices can also be integrated with motile organisms to build biologically powered hybrid nanorobots [20,30]. These different propulsion principles have led to several micro/nanorobotic prototypes, including fuel-powered tubular microrockets [11], magnetically-actuated helical swimmers [31], ultrasound-powered nanowire motors [32], and sperm-powered biohybrid microrobot [33] (Fig. 1B-D).

1.2 Biomedical applications of micro/nanorobots

Tremendous efforts from the nanorobotic community have greatly improved the power, motion control, functionality versatility, and capabilities of the various micro/nanorobotic prototypes. The growing sophistication of these nano/microscale robots offers great potential for diverse biomedical applications. Many studies have demonstrated that these micro/nanorobots could navigate through complex biological media or narrow capillaries to perform localized diagnosis, remove biopsy samples, take images, and autonomously release their payloads at predetermined destinations. The energy used to actuate these untethered micro/nanorobots does not require any cables, tethers, or batteries. Many of the micro/nanorobots are made of biocompatible materials that can degrade and even disappear upon the completion of their mission. Significantly, the actuation and biomedical function of several micro/nanorobots in a live animal's body have been carefully characterized in recent studies. These preliminary in vivo micro/nanorobot operations have demonstrated their enhanced tissue penetration and payload retention capabilities. Such untethered micro/nanorobots represent an attractive alternative to invasive medical robots and passive drug carriers, and are expected to have a major impact on various aspects of medicine. The potential biomedical applications of micro/nanorobots, as demonstrated in recent proof-of-concept studies, are introduced in the following four categories: targeted delivery, precision surgery, sensing of biological targets, and detoxification. Representative examples of such biomedical applications are displayed in Fig. 1.2A-E [34–37].

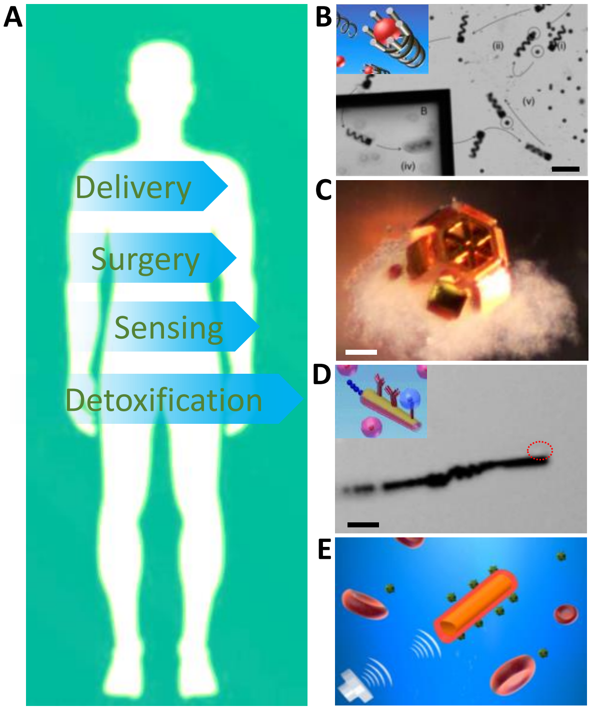

Figure 1.2 (A) Potential biomedical applications of nanorobots. (B) Magnetic helical microrobot for cargo delivery [34]. Scale bar: 50 μm. (C) Micro-grippers for high precision surgery [35]. Scale bar: 100 μm. (D) Antibody-immobilized microrobot for sensing and isolating cancer cells [36]. Scale bar: 30 μm. (E) Red blood cell (RBC) membrane-coated nanomotor for biodetoxification [37].

1.2.1 Micro/Nanorobots for Targeted Delivery

Existing drug delivery micro/nanocarriers rely on systemic circulation and lack the force and navigation required for localized delivery and tissue penetration beyond their passive mass transport limitation. To achieve precise delivery of therapeutic payloads to targeted disease sites, drug delivery vehicles are desired to possess some unique capabilities, including a propelling force, controlled navigation, cargo-towing and release, and tissue penetration. While these remain unmet challenges for current drug delivery systems, micro/nanorobots represent a new and attractive class of delivery vehicles that can meet these desirable features. The motor-like micro/nanorobots have the potential to rapidly transport and deliver therapeutic payloads directly to disease sites, thereby improving the therapeutic efficacy and reducing systemic side effects of highly toxic drugs.

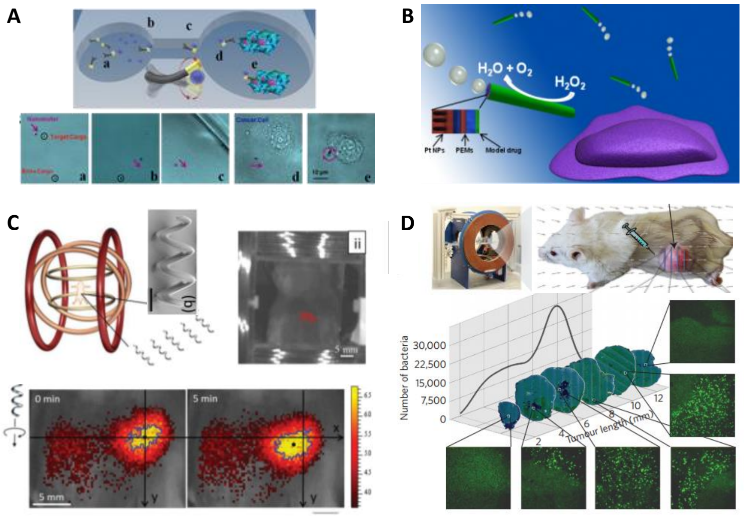

Figure 1.3 Representative examples of micro/nanorobot-based delivery. (A) Magnetic nanoswimmer for targeted delivery drug to cancer cell [38]. (B) Self-assembled polymer multilayer nanorockets for drug deliver and release [39]. (C) Controlled in vivo swimming of a swarm of bacteria-like microrobotic flagella [49]. (D) Magneto-aerotactic motor-like bacteria delivering drug-containing nanoliposomes to tumor hypoxic regions [50].

Numerous initial studies have been conducted to demonstrate the delivery function and performance of these micro/nanorobots in test-tubes and *in vitro* environments [40–44]. For example, Gao *et al.* demonstrated the magnetic micromotor vehicle for directed drug delivery by transporting drug-loaded magnetic polymeric particles to HeLa cells (Fig. 1.3A) [45], while Wu *et al.* reported the preparation of a multilayer tubular polymeric nanomotor encapsulating the anticancer drug doxorubicin *via* a porous-membrane template-assisted layer-by-layer (Fig. 1.3B) (LbL) assembly [46]. While the majority of these studies have been performed *in vitro*, initial *in vivo* studies are already undergoing and have demonstrated encouraging results [47–51]. Servant *et al.* reported the *in vivo* imaging and actuation of a swarm of helical microswimmers under rotating magnetic fields in deep tissue (Fig. 1.3C) [49]. Specifically, the magnetically controlled motion of the microswimmers in the peritoneal cavity of an anesthetized mouse was tracked in real time using fluorescence imaging. These results indicate the possibility of using such magnetic motors for optimal delivery of drugs to a targeted site guided by external magnetic field. Moreover, Felfoul *et al*. demonstrated the use of magneto-aerotactic bacteria, *Magnetococcus marinus* strain MC-1, to transport drug-loaded nanoliposomes into hypoxic regions of tumors (Fig. 1.3D) [50]. These results suggest that harnessing swarms of microorganisms exhibiting magneto-aerotactic behavior can significantly improve the delivery efficiency of drug nanocarriers to tumor hypoxic regions.

Among the various micro/nanorobotic platforms, synthetic motors that are powered by biological fluids such as gastric acid and water are of interest for *in vivo* applications. In addition to efficient propulsion, these motors can carry a large amount of different cargos, release payloads in a responsive autonomous manner, and eventually degrade themselves to nontoxic byproducts. The recent advances of using artificial micromotor for actively drug delivery *in vivo* and enhanced therapeutic efficacy, which is one of the main focuses of this thesis, will be discussed in Chapter 4. Considering the tremendous progress made recently in the development of micro/nanorobots and their uses toward *in vivo* delivery, these micro/nanorobots are expected to become powerful active-transport vehicles that may enable a variety of therapeutic applications, which are otherwise difficult to achieve through the exiting passive delivery systems.

1.2.2 Precision Surgery

Robotic systems have been introduced for reducing the difficulties associated with complex surgical procedures, and for extending the capabilities of human surgeons. Such robot-assisted surgery is a rapidly evolving field that allows doctors to perform a variety of minimally-invasive procedures with high precision, flexibility and control [52,53]. Unlike their large robotic counterparts, tiny robots can potentially navigate throughout human body and operate in many hard-to-reach tissue locations, and hence target many specific health problems.

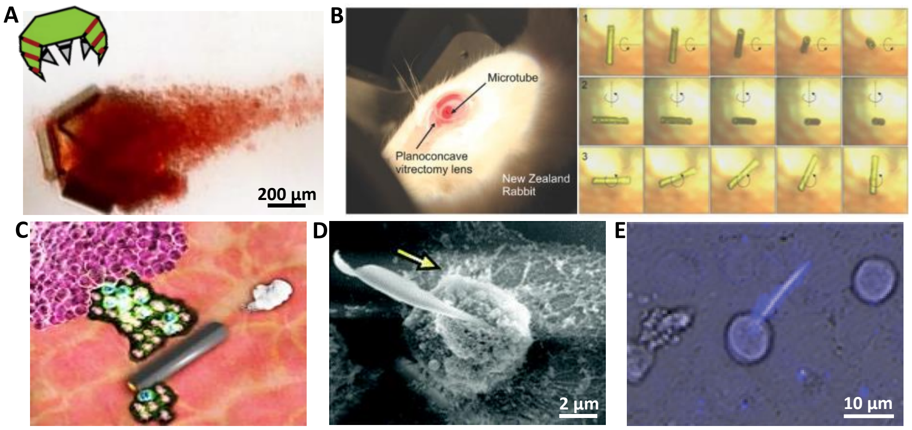

Figure 1.4 Representative examples of micro/nanorobot-enabled precision surgery. (A) Tetherless thermobiochemically-actuated microgrippers capturing live fibroblast cells [35]. (B) Electroforming of implantable tubular magnetic microrobots for wireless eye surgery [54]. (C) Acoustic droplet vaporization and propulsion of perfluorocarbon-loaded microbullets for tissue ablation [55]. (D) Self-propelled nano-driller operating on a single cell [56]. (E) Medibots: dual-action biogenic microdaggers for single-cell surgery [57].

Recent advances in micro/nanorobots have shown considerable promise for addressing these limitations and for using these tiny devices for precision surgery [6,58]. Untethered micro/nanorobotic tools, ranging from nanodrillers to micro-grippers and microbullets (Fig. 1.4A-E), offer unique capabilities for minimally invasive surgery. With dimensions compatible with those of the small biological entities that they need to treat, micro/nanorobots offer major advantages for high precision minimally-invasive surgery. Powered by diverse energy sources, the moving micro/nanorobots with nanoscale surgical components are able to directly penetrate or retrieve cellular tissues for precision surgery. Unlike their large robotic counterparts, these tiny robots can navigate through the body’s narrowest capillaries and perform procedures down to the cellular level. These studies have demonstrated the great potential of micro/nanorobots for performing precision surgery at the cellular or even subcellular level. The potential of surgical nanorobots will be greatly improved by their ability to penetrate and resect tissues and to sense specific targets, through the choice of propulsion method and use of real-time localization and mapping with a robust control system.

1.2.3 Biosensing

Owing to their unique features of autonomous motion, easy surface functionalization, effective capture and isolation of target analytes in complex biological media, micro/nanorobots have shown considerable promise for performing various demanding biosensing applications towards precise diagnosis of diseases. The micro/nanorobot sensing strategy relies on the motility of artificial nanomotors, functionalized with different bioreceptors (Fig. 1.5A), through the sample to realize 'on-the-fly' specific biomolecular interactions [12,15]. Such receptor-functionalized micro/nanomotors offer powerful binding and transport capabilities that have led to new routes for detecting and isolating biological targets, such as proteins, nucleic acids, and cancer cells, in unprocessed body fluids [59–61]. The continuous movement of these functionalized synthetic motors leads to built-in solution mixing in microliter clinical samples, which greatly enhances the target binding efficiency and offers major improvements in the sensitivity and speed of biological assays [62]. Furthermore, the efficient cargo towing ability of such self-propelled nanomotors, along with their precise motion control within microchannel networks, can lead to new medical diagnostic microchips powered by active transport [63]. Several examples of such bioreceptor-functionalized micro/nanomotors for the detection and isolation of different types of bioanalytes are displayed in Fig. 1.5B-C. Fig. 1.5B demonstrates efficient "on-the-fly" DNA hybridization in complex media by using oligonucleotide-probe functionalized micromotors, which allows sensitive and selective detection of nanomolar levels of target DNA sequences [64]. Beyond detection and transportation of biological subjects in ambient environments outside of cells, the internalization and movement of nanorobots within cells can also be exploited for intracellular sensing. For example, Esteban *et al.* introduced an attractive intracellular "Off-On" fluorescence strategy for detecting the endogenous content of target miRNA-21 based on the use of a ultrasound-propelled nanomotor functionalized with ssDNA (Fig. 1.5C) [65]. Such nanomotor biosensing approach could find important applications for profiling miRNAs expression at the single-cell level in a variety of clinical scenarios.

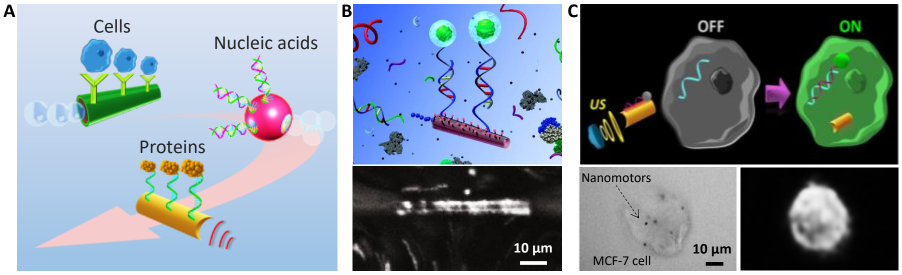

Figure 1.5 Strategies and examples of micro/nanorobots for sensing. (A) Functionalization of micro/nanorobot with different bioreceptors towards biosensing of target analytes, including cells, proteins, and nucleic acids. (B) ssDNA-functionalized microrockets for selective hybridization and isolation of nucleic acids [64]. (C) Specific intracellular detection of miRNA in intact cancer cells using ultrasound-propelled nanomotors [65].

1.2.4 Detoxification

Self-propelled micro/nanorobots have been used also as powerful detoxification tools with high cleaning capability. Similar to biosensing, detoxification strategies rely on self-propelled micro/nanorobot that rapidly capture and remove the toxin to render the environment non-toxic. Efficient motion would facilitate the collision and binding of toxins to the motors, which are coated with desired functional materials. For example, nanomotors have been combined with cell-derived natural materials – capable of mimicking the natural properties of their source cells – toward novel nanoscale biodetoxification devices. Among different cell derivatives, red blood cells (RBCs) have shown excellent capability to function as toxin-absorbing nanosponges to neutralize and remove dangerous “pore-forming toxins” (PFTs) from the bloodstream (Fig. 1.6A) [66]. Motivated by the biological properties of RBCs, several different types of cell-mimicking micromotors have been developed for detoxification. Wu *et al.* presented a cell-mimicking water-powered micromotor based on RBC membrane-coated magnesium microparticles, which were able to effectively absorb and neutralize α-toxin in biological fluids (Fig. 1.6B) [67]. Another detoxification strategy explored the combination of RBC membranes with ultrasound-propelled nanomotors as a biomimetic platform to effectively absorb and neutralize PFTs [37]. Another microrobot-based detoxification approach was based on the use of a self-propelled 3D-printed microfish containing polydiacetylene (PDA) nanoparticles (Fig. 1.6C, top part), which served to attract, capture, and neutralize toxins *via* binding interactions [68]. Self-propelled 3D-microfishes incubated in the toxin solution showed higher fluorescence intensities (Fig. 1.6C, bottom part) compared to static microfishes, highlighting the importance of active motion for enhancing the detoxification processes.

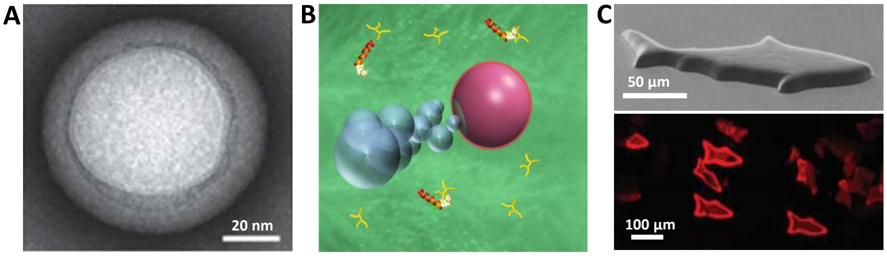

Figure 1.6 Representative examples of micro/nanorobots for detoxification. (A) Transmission electron microscope image of a cell membrane-coated nanosponge used for toxin neutralization [66]. (B) Scheme of the RBC-Mg Janus micromotor moving in biological fluid (left), and their capacity for cleanning of α-toxin [67]. (C) Scanning electron microscope image of a 3D-printed microfish (top) and fluorescent image of the microfish incubated in melittin toxin solution after swimming (bottom part) [68].

1.3 Other applications of micro/nanorobots

1.3.1 Environmental applications

Nanotechnology offer considerable promise for addressing growing environmental sustainability and challenges facing our world. The attractive capabilities of micro/nanorobots can add a new dimension based on motion to environmental remediation processes and lead to greatly enhanced destruction protocols (12, 67). The continuous movement of these tiny motors has been used for transporting reactive materials throughout contaminated samples, and for imparting significant mixing during detoxification processes. These capabilities have led to significantly shorter cleanup times in connection to lower levels of reagents, thus holding considerable promise to lower the decontamination costs. Environmental monitoring, water-quality screening, oil cleaning, heavy metal removal, and CO_2 scrubbing have also greatly benefited from the use of functionalized microrobots. Examples of some of these impressive microrocket-based environmental remediation strategies are displayed in Fig. 1.7A-B.

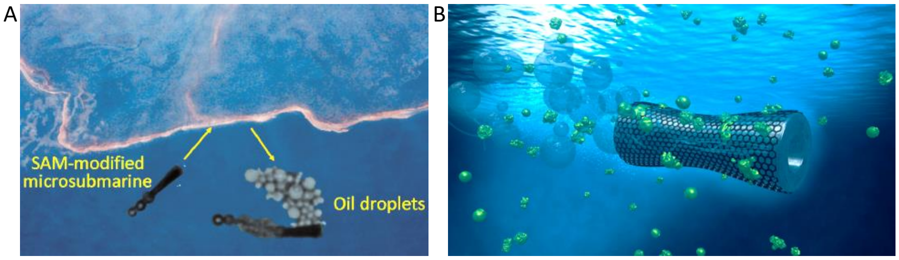

Figure 1.7 Examples of micro/nanorobots for environmental remediation. (A) Alkanethiol-coated microsubmarines for effective removal of oil [71]. (B) Graphene-based microbots for toxic heavy metal removal [72].

1.3.2 Defense applications

Threats of chemical and biological warfare agents (CBWA) represent a serious global concern and require rapid and efficient destruction methods. The advanced micro/nanorobotic tools can offer “on-the-fly” detection and destruction, or ‘capture–transport–release’ separation process. Such active transfer process through high-speed nanoscale location leads to rapid methods to detect and destruct CBWA from environment (Fig. 1.8A-B) [73,74]. Like biological function of human cells could be highly sensitive to the presence of CBWA, the motion dynamics of the micro/nanorobots are also highly related to the toxic agent in the environment. By visualizing the motion behavior of micro/robots, such response to the threats will lead to a rapid “seeing is sensing” platform [75–78]. Intelligent micro/nanorobots could be steered to inaccessible or harsh locations or using trace the source of threats for rapid sensing and destruction. Integrating active reactants on the micro/nanorobots with their rapid motion capacity enables rapid threat destructions without external device to enhance the mass transfer. Therefore, such micro/nanorobot platform is highly practical for *in situ* disarm without any external energy sources or expensive devices. Overall, the micro/nanorobotic platforms could address many obstacles associated with traditional methodologies used in the defense sector, especially for remote and rural location without power supplies and desired setups.

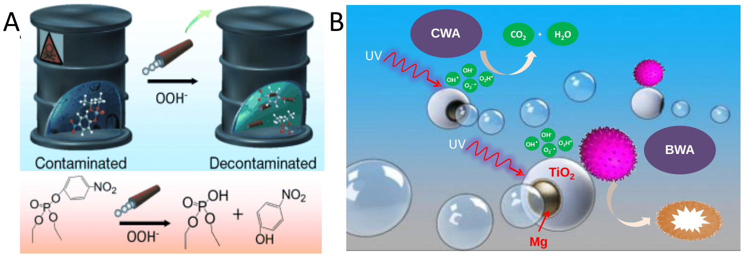

Figure 1.8 Countermeasures delivery with micro/nanorobots. (A) Rapid oxidative neutralization of organophosphorus nerve agents based on self-propelled micromotors [74]. (B)Schematic representation of the self-propulsion and photocatalytic degradation of biological and chemical warfare agent into environmentally-friendly products by water-driven spherical TiO_2/Au/Mg micromotors [73].

1.3.3 Energy applications

The potential of micro/nanorobots of energy application can be achieved by either enhancing the chemical process or directly transfer their mechanical motion into energy. The active transfer process enabled by micro/nanorobots can dramatically enhance the chemical process and reaction related to energy generation. For example, Singh *et al.* have demonstrated that the autonomous motion of these catalytic micromotors, as well as their bubble generation, leads to enhanced mixing and transport of $NaBH_4$ towards the Pt-black catalytic surface (compared to static microparticles or films), and hence to a substantially faster rate of H_2 production as sustainable energy (Fig. 1.9A) [79]. The mechanical energy associated with the motion of micro/nanorobots can also be directly transferred in electricity. For example, Matsui *et al.* demonstrated that peptide–

metal–organic framework (Pep-MOF) motors, whose motions are driven by anisotropic surface tension gradients created via peptide self-assembly around frameworks, can rotate microscopic rotors and magnets fast enough to generate an electric power of 0.1 μW (Fig. 1.9B) [80].

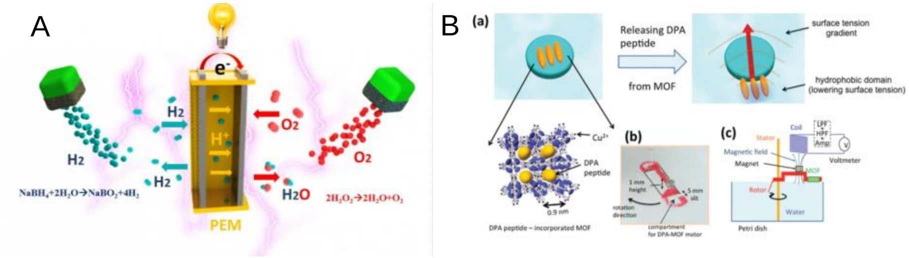

Figure 1.9 Micro/nanorobots for energy production. (A) Micromotor-enhanced H_2 production [79]. (B) MOF micromotor-based electric generator [80].

1.3.4 Nanomanipulation and assembly

Making complex functional materials with three-dimensional micro- or nano-scale dynamic compositional features is highly demanded for diverse applications. The micro/nanorobot can transport both themselves and other passive nanostructures to build complicated assembles. For example, Schmidt *et al.* demonstrated maneuvers of self-propelled microbots can be wirelessly coordinated by an external magnetic to selectively manipulation of different microobjects randomly suspended in solution (Fig. 1.10A) [81]. Sitti *et al.* used an untethered magnetic micro-robot to code complex materials in three-dimensions with tunable structural, morphological and chemical features (Fig. 1.10B) [82]. With advanced control technique, the microrobot can transport any individual building block to the desired location with high precision, thus making three-dimensional structure with arbitrary feature possible.

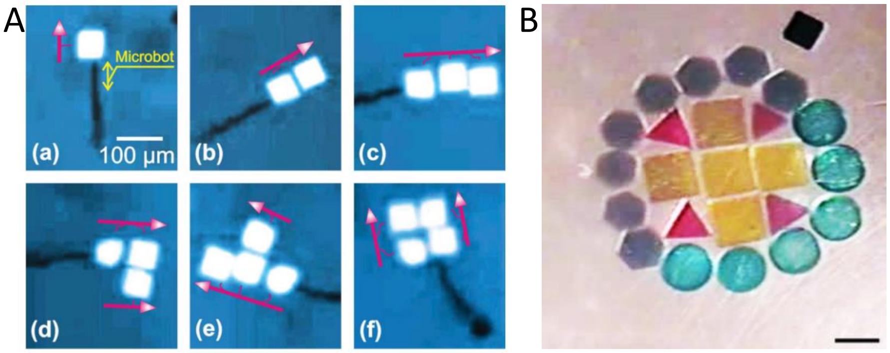

Figure 1.10 Nanomanipulation and assembly with micro/nanorobots. (A) Microbot assembling four nanoplates in different configurations [81]. (B) Micro-robotic coding and reconfiguration of Poly(ethylene glycol) dimethacrylate hydrogels into complex planar constructs [82].

1.3.5 Active and living matter

Complex dynamic systems–from a living cell to neural circuits and swarming bacteria to schooling fishes–have several common features, among which are the autonomous movement of the components of these systems, and the interactions (both attractive and repulsive) among these components in far-from-equilibrium processes. Exploring the dynamics and spatiotemporal complexity at the nanometer scale, which remains a relatively primitive stage, requires designing nanoscale building blocks that actively both move and interact with one another, followed by characterization of the spatial structures and patterns that emerge from groups of these components. The self-organization of micro/nanorobots, usually made with motile colloidal nanoparticles, in a far-from-equilibrium system and to use this system as a new dimension for directing self-assembling dynamics and structures.

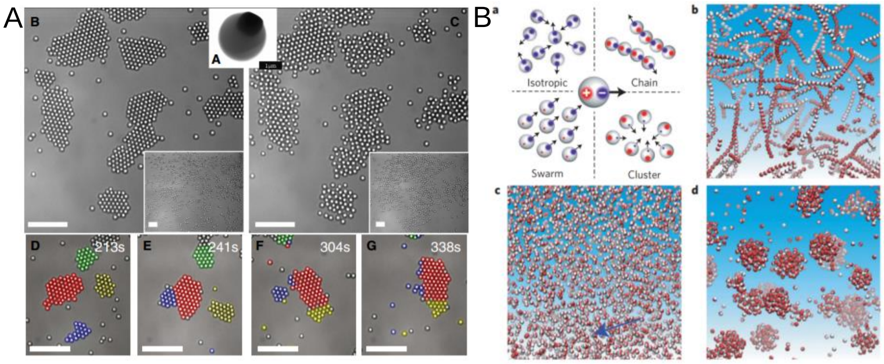

Figure 1.11 Active and living matter based micro/nanorobot which consume energy. (A) Light-activated living crystal made by active colloidal [83]. (B) Examples of collective active states formed by spheres with imbalanced, off-centered charges [84].

The wide range of self-assembled structures by colloidal matter often develops in thermal and structural equilibriums. Micro/nanorobots driven by intrinsic or extrinsic energy sources, rather than thermal fluctuations, can show far-from-equilibrium self-organization with high complexity rivaling that of biological systems. Micro/nanorobots are usually powered by local chemical reactions, external stimuli, or the hybridization of multiple energy sources. Their mobility and complex interactions are new pathways to direct the self-assembly process. These processes are principally regulated by local chemical and diffusion processes, and can be further digitally tuned by external optical, electrical, magnetic or ultrasound fields. In addition, micro/nanorobots can synthesized with controlled anisotropy and crystal geometries, such as Janus nanoparticles or heterogeneous nanocrystals. The obtained anisotropic structure would consist of “active” facets for directional propulsion and “passive” facets which can be functionalized by ligands to direct further chemistry or interparticle interactions. In such a living, dissipative system consisting of active and anisotropic individuals, energy consumption will offer on-demand control of their collective dynamics and behaviors towards active superlattices with higher-level structural complexity and hierarchy (Fig. 11A-B). Particularly, the far-from-equilibrium behavior will lead to nanoscale dynamic orders, including transient assembly [83], reconfigurable patterns [72], stimulus-dependent synchronization, temporal and spatial oscillations, and even self-replicating ensembles.

Chapter 1 is based, in part, on the material as it appears in Science Robotics, 2017, by Jinxing Li, Berta Esteban-Fernández de Ávila, Wei Gao, Liangfang Zhang, Joseph Wang. The dissertation author was the primary investigator and author of these papers.

1.4 References

(1) Ijspeert, A. J. Biorobotics: Using Robots to Emulate and Investigate Agile Locomotion. *Science (80-.).* **2014**, *346*.

(2) A Roadmap for US Robotics 2016 Edition | USA Robotics VO https://robotics-vo.us/node/562 (accessed Apr 14, 2017).

(3) Mack, M. J. Minimally Invasive and Robotic Surgery. *JAMA* **2001**, *285*, 568.

(4) Beasley, R. Medical Robots: Current Systems and Research Directions. *J. Robot.* **2012**.

(5) Alemzadeh, H.; Raman, J.; Leveson, N.; Kalbarczyk, Z. Adverse Events in Robotic Surgery: A Retrospective Study of 14 Years of FDA Data. *PLoS One* **2016**.

(6) Nelson, B. J. B.; Kaliakatsos, I. K. I.; Abbott, J. J. Microrobots for Minimally Invasive Medicine. *Annu. Rev. Biomed. Eng.* **2010**, *12*, 55–85.

(7) Wang, J.; Gao, W. Nano/Microscale Motors: Biomedical Opportunities and Challenges. *ACS Nano* **2012**, *6*, 5745–5751.

(8) Purcell, E. M. E. Life at Low Reynolds Number. *Am. J. Phys.* **1977**, *45*, 3–11.

(9) BERG, H. C.; ANDERSON, R. A. Bacteria Swim by Rotating Their Flagellar Filaments. *Nature* **1973**, *245*, 380–382.

(10) Rikmenspoel, R.; Isles, C. A. Digitized Precision Measurements of the Movements of Sea Urchin Sperm Flagella. *Biophys. J.* **1985**, *47*, 395–410.

(11) Solovev, A. A.; Mei, Y.; Bermúdez Ureña, E.; Huang, G.; Schmidt, O. G. Catalytic Microtubular Jet Engines Self-Propelled by Accumulated Gas Bubbles. *Small* **2009**, *5*, 1688–1692.

(12) Li, J.; Rozen, I.; Wang, J. Rocket Science at the Nanoscale. *ACS Nano* **2016**, *10*, 5619–5634.

(13) Peyer, K. K. E.; Zhang, L.; Nelson, B. J. B.; Ozkale, B.; Zeeshan, M. a.; Lühmann, T.; Nelson, B. J. B.; Pané, S.; Toonder, J. M. J. den; Onck, P. R. Bio-Inspired Magnetic Swimming Microrobots for Biomedical Applications. *Nanoscale* **2013**, *5*, 1259–1272.

(14) Abdelmohsen, L.; Peng, F.; Tu, Y. Micro-and Nano-Motors for Biomedical Applications. *J. Mater.* **2014**.

(15) Guix, M.; Mayorga-Martinez, C. C.; Merkoçi, A. Nano/Micromotors in (Bio)chemical Science Applications. *Chem. Rev.* **2014**, *114*, 6285–6322.

(16) Palagi, S.; Mark, A. G.; Reigh, S. Y.; Melde, K.; Qiu, T.; Zeng, H.; Parmeggiani, C.; Martella, D.; Sanchez-Castillo, A.; Kapernaum, N. Structured Light Enables Biomimetic Swimming and Versatile Locomotion of Photoresponsive Soft Microrobots. *Nat. Mater.* **2016**, *15*, 647–653.

(17) Mei, Y.; Solovev, A. A.; Sanchez, S.; Schmidt, O. G. Rolled-up Nanotech on Polymers:

From Basic Perception to Self-Propelled Catalytic Microengines. *Chem. Soc. Rev.* **2011**, *40*, 2109.

(18) Lin, X.; Wu, Z.; Wu, Y.; Xuan, M.; He, Q. Self-Propelled Micro-/Nanomotors Based on Controlled Assembled Architectures. *Adv. Mater.* **2016**, *28*, 1060–1072.

(19) Duan, W.; Wang, W.; Das, S.; Yadav, V. Synthetic Nano-and Micromachines in Analytical Chemistry: Sensing, Migration, Capture, Delivery, and Separation. *Annu. Rev.* **2015**.

(20) Singh, A. V.; Sitti, M. Targeted Drug Delivery and Imaging Using Mobile Milli/microrobots: A Promising Future towards Theranostic Pharmaceutical Design. *Curr. Pharm. Des.* **2016**.

(21) Wang, H.; Pumera, M. Fabrication of Micro/Nanoscale Motors. *Chem. Rev.* **2015**, *115*, 8704–8735.

(22) Kim, K.; Guo, J.; Xu, X.; Fan, D. L. Recent Progress on Man-Made Inorganic Nanomachines. *Small* **2015**, *11*, 4037–4057.

(23) Moran, J. J. L.; Posner, J. D. J. Phoretic Self-Propulsion. *Annu. Rev. Fluid Mech.* **2017**, *49*, 511–540.

(24) Wang, W.; Duan, W.; Ahmed, S.; Mallouk, T. E.; Sen, A. Small Power: Autonomous Nano- and Micromotors Propelled by Self-Generated Gradients. *Nano Today* **2013**, *8*, 531–554.

(25) Nadal, F.; Lauga, E. Asymmetric Steady Streaming as a Mechanism for Acoustic Propulsion of Rigid Bodies. *Phys. Fluids* **2014**, *26*, 82001.

(26) Dai, B.; Wang, J.; Xiong, Z.; Zhan, X.; Dai, W.; Li, C. Programmable Artificial Phototactic Microswimmer. *Nature* **2016**.

(27) Liu, M.; Zentgraf, T.; Liu, Y.; Bartal, G.; Zhang, X. Light-Driven Nanoscale Plasmonic Motors. **2010**, *5*, 570–573.

(28) Fan, D.; Yin, Z.; Cheong, R.; Zhu, F. F. Q.; Cammarata, R. C.; Chien, C. L.; Levchenko, A. Subcellular-Resolution Delivery of a Cytokine through Precisely Manipulated Nanowires. **2010**, *5*, 545–551.

(29) Loget, G.; Kuhn, A. Electric Field-Induced Chemical Locomotion of Conducting Objects. *Nat. Commun.* **2011**, *2*, 535.

(30) Magdanz, V.; Guix, M. Tubular Micromotors: From Microjets to Spermbots. *Robot.* **2014**.

(31) Ghosh, A.; Fischer, P. Controlled Propulsion of Artificial Magnetic Nanostructured Propellers. *Nano Lett.* **2009**, *9*, 2243–2245.

(32) Garcia-Gradilla, V.; Orozco, J.; Sattayasamitsathit, S. Functionalized Ultrasound-Propelled Magnetically Guided Nanomotors: Toward Practical Biomedical Applications. *ACS* **2013**.

(33) Magdanz, V.; Medina-Sánchez, M. How to Improve Spermbot Performance. *Adv. Funct.*

2015.

(34) Tottori, S.; Zhang, L.; Qiu, F.; Krawczyk, K. Magnetic Helical Micromachines: Fabrication, Controlled Swimming, and Cargo Transport. *Advanced* **2012**.

(35) Leong, T. G.; Randall, C. L.; Benson, B. R.; Bassik, N.; Stern, G. M.; Gracias, D. H. Tetherless Thermobiochemically Actuated Microgrippers. *Proc. Natl. Acad. Sci. U. S. A.* **2009**, *106*, 703–708.

(36) Balasubramanian, S.; Kagan, D.; Jack Hu, C.-M.; Campuzano, S.; Lobo-Castañon, M. J.; Lim, N.; Kang, D. Y.; Zimmerman, M.; Zhang, L.; Wang, J. Micromachine-Enabled Capture and Isolation of Cancer Cells in Complex Media. *Angew. Chemie Int. Ed.* **2011**, *50*, 4161–4164.

(37) Wu, Z.; Li, T.; Gao, W.; Xu, T.; Jurado-Sánchez, B.; Li, J.; Gao, W.; He, Q.; Zhang, L.; Wang, J. Cell-Membrane-Coated Synthetic Nanomotors for Effective Biodetoxification. *Adv. Funct. Mater.* **2015**, *25*, 3881–3887.

(38) Gao, W.; Kagan, D.; Pak, O. S.; Clawson, C.; Campuzano, S.; Chuluun-Erdene, E.; Shipton, E.; Fullerton, E. E.; Zhang, L.; Lauga, E. Cargo-Towing Fuel-Free Magnetic Nanoswimmers for Targeted Drug Delivery. *Small* **2012**, *8*, 460–467.

(39) Wu, Z.; Wu, Y.; He, W.; Lin, X.; Sun, J. Self-propelled Polymer-based Multilayer Nanorockets for Transportation and Drug Release. *Angew. Chemie* **2013**.

(40) Peng, F.; Tu, Y.; van Hest, J. C. M.; Wilson, D. A. Self-Guided Supramolecular Cargo-Loaded Nanomotors with Chemotactic Behavior towards Cells. *Angew. Chemie Int. Ed.* **2015**, *54*, 11662–11665.

(41) Wu, Z.; Lin, X.; Zou, X.; Sun, J.; He, Q. Biodegradable Protein-Based Rockets for Drug Transportation and Light-Triggered Release. *ACS Appl. Mater. Interfaces* **2015**, *7*, 250–255.

(42) Peters, C.; Hoop, M.; Pané, S.; Nelson, B. Degradable Magnetic Composites for Minimally Invasive Interventions: Device Fabrication, Targeted Drug Delivery, and Cytotoxicity Tests. *Advanced* **2016**.

(43) Medina-Sánchez, M.; Schwarz, L.; Meyer, A. K.; Hebenstreit, F.; Schmidt, O. G. Cellular Cargo Delivery: Toward Assisted Fertilization by Sperm-Carrying Micromotors. *Nano Lett.* **2016**, *16*, 555–561.

(44) Katuri, J.; Ma, X.; Stanton, M. Designing Micro-and Nanoswimmers for Specific Applications. *Accounts Chem.* **2017**.

(45) Gao, W.; Kagan, D.; Pak, O.; Clawson, C.; Campuzano, S. Cargo-towing Fuel-free Magnetic Nanoswimmers for Targeted Drug Delivery. *small* **2012**.

(46) Wu, Z.; Wu, Y.; He, W.; Lin, X.; Sun, J.; He, Q. Self-Propelled Polymer-Based Multilayer Nanorockets for Transportation and Drug Release. *Angew. Chemie Int. Ed.* **2013**, *52*, 7000–7003.

(47) Gao, W.; Dong, R.; Thamphiwatana, S.; Li, J.; Gao, W.; Zhang, L.; Wang, J. Artificial

Micromotors in the Mouse's Stomach: A Step toward *in Vivo* Use of Synthetic Motors. *ACS Nano* **2015**, *9*, 117–123.

(48) Li, J.; Thamphiwatana, S.; Liu, W.; Esteban-Fernández de Ávila, B.; Angsantikul, P.; Sandraz, E.; Wang, J. J. J. J. J.; Xu, T.; Soto, F.; Ramez, V. Enteric Micromotor Can Selectively Position and Spontaneously Propel in the Gastrointestinal Tract. *ACS Nano* **2016**, *10*, 9536–9542.

(49) Servant, A.; Qiu, F.; Mazza, M.; Kostarelos, K. Controlled In Vivo Swimming of a Swarm of Bacteria-Like Microrobotic Flagella. *Advanced* **2015**.

(50) Felfoul, O.; Mohammadi, M.; Taherkhani, S.; de Lanauze, D.; Zhong Xu, Y.; Loghin, D.; Essa, S.; Jancik, S.; Houle, D.; Lafleur, M. Magneto-Aerotactic Bacteria Deliver Drug-Containing Nanoliposomes to Tumour Hypoxic Regions. *Nat. Nanotechnol.* **2016**, *11*, 941–947.

(51) Li, J.; Angsantikul, P.; Liu, W.; Esteban-Fernández de Ávila, B.; Thamphiwatana, S.; Xu, M.; Sandraz, E.; Wang, X.; Delezuk, J.; Gao, W. Micromotors Spontaneously Neutralize Gastric Acid for pH-Responsive Payload Release. *Angew. Chemie* **2017**, *129*, 2188–2193.

(52) Lanfranco, A.; Castellanos, A.; Desai, J. Robotic Surgery: A Current Perspective. *Ann.* **2004**.

(53) Barbash, G.; Glied, S. New Technology and Health Care Costs—the Case of Robot-Assisted Surgery. *N. Engl. J. Med.* **2010**.

(54) Chatzipirpiridis, G.; Ergeneman, O.; Pokki, J. Electroforming of Implantable Tubular Magnetic Microrobots for Wireless Ophthalmologic Applications. *Advanced* **2015**.

(55) Kagan, D.; Benchimol, M.; Claussen, J. Acoustic Droplet Vaporization and Propulsion of Perfluorocarbon-Loaded Microbullets for Targeted Tissue Penetration and Deformation. *Angewandte* **2012**.

(56) Solovev, A. A. A.; Xi, W.; Gracias, D. D. H.; Harazim, S. S. M.; Deneke, C.; Sanchez, S.; Schmidt, O. G. Self-Propelled Nanotools. *ACS Nano* **2012**, *6*, 1751–1756.

(57) Srivastava, S. K.; Medina-Sánchez, M.; Koch, B.; Schmidt, O. G. Medibots: Dual-Action Biogenic Microdaggers for Single-Cell Surgery and Drug Release. *Adv. Mater.* **2016**, *28*, 832–837.

(58) Ullrich, F.; Fusco, S.; Chatzipirpiridis, G.; Pané, S. Recent Progress in Magnetically Actuated Microrobotics for Ophthalmic Therapies. *Eur. Ophthalmic Rev.* **2014**.

(59) Campuzano, S.; Orozco, J.; Kagan, D.; Guix, M.; Gao, W. Bacterial Isolation by Lectin-Modified Microengines. *Nano* **2012**.

(60) Nguyen, K. Van; Minteer, S. DNA-Functionalized Pt Nanoparticles as Catalysts for Chemically Powered Micromotors: Toward Signal-on Motion-Based DNA Biosensor. *Chem. Commun.* **2015**.

(61) Yu, X.; Li, Y.; Wu, J.; Ju, H. Motor-Based Autonomous Microsensor for Motion and Counting Immunoassay of Cancer Biomarker. *Anal. Chem.* **2014**.

(62) Wang, J. Self-Propelled Affinity Biosensors: Moving the Receptor around the Sample. *Biosens. Bioelectron.* **2016**, *76*, 234–242.

(63) Wang, J. Cargo-Towing Synthetic Nanomachines: Towards Active Transport in Microchip Devices. *Lab Chip* **2012**.

(64) Kagan, D.; Campuzano, S.; Balasubramanian, S. Functionalized Micromachines for Selective and Rapid Isolation of Nucleic Acid Targets from Complex Samples. *Nano* **2011**.

(65) Ávila, B. E.-F. de; Martín, A.; Soto, F.; Esteban-Fernández de Ávila, B.; Martín, A.; Soto, F.; Lopez-Ramirez, M. A.; Campuzano, S.; Vásquez-Machado, G. M.; Gao, W. Single Cell Real-Time miRNAs Sensing Based on Nanomotors. *ACS Nano* **2015**, *9*, 6756–6764.

(66) Hu, C.-M. J. C.; Fang, R. H. R.; Copp, J.; Luk, B. B. T.; Zhang, L. A Biomimetic Nanosponge That Absorbs Pore-Forming Toxins. **2013**, *8*, 336–340.

(67) Wu, Z.; Li, J.; Ávila, B. de; Li, T.; Gao, W. Water-Powered Cell-Mimicking Janus Micromotor. *Adv. Funct.* **2015**.

(68) Zhu, W.; Li, J.; Leong, Y.; Rozen, I.; Qu, X. 3D-Printed Artificial Microfish. *Advanced* **2015**.

(69) Soler, L.; Sánchez, S. Catalytic Nanomotors for Environmental Monitoring and Water Remediation. *Nanoscale* **2014**, *6*, 7175.

(70) Moo, J. G. S.; Pumera, M. Chemical Energy Powered Nano/Micro/Macromotors and the Environment. *Chem. - A Eur. J.* **2015**, *21*, 58–72.

(71) Guix, M.; Orozco, J.; García, M.; Gao, W.; Sattayasamitsathit, S.; Merkoçi, A.; Escarpa, A.; Wang, J. Superhydrophobic Alkanethiol-Coated Microsubmarines for Effective Removal of Oil. *ACS Nano* **2012**, *6*, 4445–4451.

(72) Vilela, D.; Parmar, J.; Zeng, Y.; Zhao, Y.; Sánchez, S. Graphene-Based Microbots for Toxic Heavy Metal Removal and Recovery from Water. *Nano Lett.* **2016**, *16*, 2860–2866.

(73) Li, J.; Singh, V. V.; Sattayasamitsathit, S.; Orozco, J.; Kaufmann, K.; Dong, R.; Gao, W.; Jurado-Sanchez, B.; Fedorak, Y.; Wang, J. Water-Driven Micromotors for Rapid Photocatalytic Degradation of Biological and Chemical Warfare Agents. *ACS Nano* **2014**, *8*, 11118–11125.

(74) Orozco, J.; Cheng, G.; Vilela, D.; Sattayasamitsathit, S.; Vazquez-Duhalt, R.; Valdés-Ramírez, G.; Pak, O. S.; Escarpa, A.; Kan, C.; Wang, J. Micromotor-Based High-Yielding Fast Oxidative Detoxification of Chemical Threats. **2013**.

(75) Dong, R.; Li, J.; Rozen, I.; Ezhilan, B.; Xu, T.; Christianson, C.; Gao, W.; Saintillan, D.; Ren, B.; Wang, J. Vapor-Driven Propulsion of Catalytic Micromotors. *Sci. Rep.* **2015**, *5*, 13226.

(76) Ezhilan, B.; Gao, W.; Pei, A.; Rozen, I.; Dong, R.; Jurado-Sanchez, B.; Wang, J.; Saintillan, D.; Kan, C.; Wang, J. Motion-Based Threat Detection Using Microrods: Experiments and Numerical Simulations. *Nanoscale* **2015**, *7*, 7833–7840.

(77) Orozco, J.; García-Gradilla, V.; D'Agostino, M.; Gao, W.; Cortés, A.; Wang, J. Artificial Enzyme-Powered Microfish for Water-Quality Testing. *ACS Nano* **2013**, *7*, 818–824.

(78) Kagan, D.; Calvo-Marzal, P.; Balasubramanian, S.; Sattayasamitsathit, S.; Manesh, K. M.; Flechsig, G.-U.; Wang, J. Chemical Sensing Based on Catalytic Nanomotors: Motion-Based Detection of Trace Silver. *J. Am. Chem. Soc.* **2009**, *131*, 12082–12083.

(79) Singh, V. V.; Soto, F.; Kaufmann, K.; Wang, J. Micromotor-Based Energy Generation. *Angew. Chemie Int. Ed.* **2015**, *54*, 6896–6899.

(80) Ikezoe, Y.; Fang, J.; Wasik, T. L.; Uemura, T.; Zheng, Y.; Kitagawa, S.; Matsui, H. Peptide Assembly-Driven Metal-Organic Framework (MOF) Motors for Micro Electric Generators. *Adv. Mater.* **2015**, *27*, 288–291.

(81) Solovev, A. A.; Sanchez, S.; Pumera, M.; Mei, Y. F.; Schmidt, O. G. Magnetic Control of Tubular Catalytic Microbots for the Transport, Assembly, and Delivery of Micro-Objects. *Adv. Funct. Mater.* **2010**, *20*, 2430–2435.

(82) Tasoglu, S.; Diller, E.; Guven, S.; Sitti, M.; Demirci, U. Untethered Micro-Robotic Coding of Three-Dimensional Material Composition. *Nat. Commun.* **2014**, *5*, 1667–1680.

(83) Palacci, J.; Sacanna, S.; Steinberg, A. P.; Pine, D. J.; Chaikin, P. M. Living Crystals of Light-Activated Colloidal Surfers. *Science (80-.).* **2013**, *339*, 936–940.

(84) Yan, J.; Han, M.; Zhang, J.; Xu, C.; Luijten, E.; Granick, S. Reconfiguring Active Particles by Electrostatic Imbalance. *Nat. Mater.* **2016**, *15*, 1095–1099.

Chapter 2 Inspired from the Nature: Wireless Nanorobots Actuated by External Fields

2.1 Template electrosynthesis of tailored-made helical nanoswimmers

2.1.1 Introduction

The synthesis of nanoscale structures capable of moving in liquids represents a major nanotechnological challenge [1–6]. Significant progress has been made recently towards the fabrication of micro/nano motors that rely on local chemical fuel [7–9] or on external electrical [10,11], optical [12], ultrasound [13,14] and magnetic [15–17]stimuli. Among the different types of micro/nanomotors, magnetically actuated ones are extremely promising for diverse *in vivo* biomedical applications owing to their attractive swimming performance [1,18,19]. In particular, helical magnetic micro/nanoswimmers - inspired by bacterial flagellum propulsion [20] - transform a rotation around their helical axis into a translation along the helical axis to offer an efficient locomotion behavior [17,19]. However, till recently the large-scale preparation of helical micro/nanostructures has been challenging, since traditional microfabrication techniques - based on the deposition or removal of thin layers of material - have not been compatible with the preparation of complex three-dimensional (3D) helical micro/nanostructures [19]. The challenges of fabricating 3D helical swimmers have been discussed [17,19]. Several fabrication methods have been proposed recently for addressing these challenges and preparing magnetically-actuated helical micro/nanoswimmers [17,19]. The first magnetically-driven helical corkscrew-shaped microrobot (2-3 μm in diameter, 30-50 μm long) was fabricated by a self-scrolling technique that combines "top-down" lithographic patterning and a "self-organizing" step [16]. Even smaller highly-densed helical nano-propellers were prepared in 2009 by glancing angle deposition (GLAD) [21]. An attractive top-down 3D laser direct writing (DLW) of magnetic helical micromachines was demonstrated recently by Nelson's group [22,23]. Yet, these routes for fabricating helical micro/nanoswimmers require specialized and expensive instrumentation, and the dimensions of these helical magnetic motors are commonly limited by the resolution of optical lithography.

This article describes an effective and simple template electrodeposition approach for the large-scale preparation of extremely small and highly efficient helical magnetic swimmers. For over two decades, template electrosynthesis has been shown to be an attractive approach for the mass production of diverse nanostructures and nanodevices [24]. Such template-assisted electrochemical growth of different nanostructures involves electrodeposition of different materials into the cylindrical nanopores of a host porous membrane template, followed by dissolution of the template [25]. The versatility of the template-directed electrodeposition has been shown to be extremely useful for preparing chemically-powered nanomotors, including catalytic bi-segment (Pt-Au) nanowires [7] and microtubular engines [7,26,27]. Template electrosynthesis has been used also for preparing flexible nanowire swimmers [17], but not for fabricating helical (corkscrew-shaped) magnetic swimmers. Several groups have demonstrated recently the successful template fabrication and assembly of helical composite mesostructures [28,29]. In particular, Park's group described the synthesis of palladium (Pd) nanosprings using anodized aluminum oxide (AAO) templates and electrochemical deposition [29].

Taking advantage of these recent advances in the electrosynthesis of nanosprings, we demonstrate in the following sections that this templating route can lead to the large-scale low-cost preparation of remarkably small magnetically-driven helical nanoswimmers (down to 100 nm in diameter and 600 nm in length) that display efficient propulsion behavior. Our study demonstrates that such template synthesis provides convenient control the dimensions, geometry and composition of the helical swimmers, as desired for optimizing the swimming performance. Geometrically tunable helical nanostructures - with varied diameter, length and spiral pitch - can be readily fabricated via judicious selection of the membrane template pore size, composition of the plating solution and electrodeposition parameters. Thousands of helical nanoswimmers can thus be prepared within few hours. The nanoscale dimensions and efficient propulsion behavior of these template-prepared helical nanoswimmers make them ideal candidates for future miniature devices in the human body.

2.1.2 Experimental Section

Synthesis of magnetic nanohelices

Nanoporous AAO templates membrane (6809-6022, Whatman, Maidstone, UK) with a pore size of 200 nm were used as a template for fabricating 200 nm nanohelices. PC membrane templates (110605 and 110607, Whatman, NJ, USA) with pore sizes of 100 nm and 400 nm were used for fabricating 100 and 400 nm helical nanoswimmers. Al_2O_3 coatings were formed in the PC templates by atomic layer deposition for 800 cycles at 100^oC. Before electrochemical deposition, a 75 nm gold film was sputtered on one side of the porous membrane to serve as a working electrode using the Denton Discovery 18 (Moorestown, NJ). A Pt wire and an Ag/AgCl (with 1 M KCl) were used as counter and reference electrodes, respectively. The membrane was then assembled in a plating cell with an aluminium foil serving as a contact. All electrochemical deposition steps were carried out at room temperature (22 ^oC). For preparing 200 nm nanohelices using an AAO membrane, a sacrificial silver layer was initially electrodeposited at -1.0 V for a total charge of 3 C using a commercial silver plating solution (1025 RTU @ 4.5 Troy/gallon). Gold nanorods were then electrodeposited at -1.0 V for a total charge of 1.5 C from a commercial gold plating solution (Orotemp 24 RTU RACK); subsequently, the Pd/Cu nanorods were deposited at -0.1 V from the

$PdCl_2$ / $CuCl_2$ plating solution mixture. All the Pd/Cu plating solutions contained 20 mM $CuCl_2$ and 0.1 M HCl, while the $PdCl_2$ concentrations varied from 25 mM to 45 mM to prepare nanohelices with different morphologies. After electrochemical deposition, the sputtered gold layer was completely removed by hand polishing with 3–4 µm alumina slurry. The AAO membrane templates were dissolved in 3 M NaOH for 30 min followed by washing with ultrapure water until neutral pH was obtained. Finally, the Ag sacrificial layer and the Cu component (of the Pd/Cu nanorods) were dissolved using an 8 M HNO_3 solution for 10 minutes, resulting in the formation of Pd nanohelices. Fabrication of 100 nm and 400 nm nanohelices, with the PC membrane templates involved the electrodeposition of gold nanorods using a charge of 0.2 C; and subsequent deposition of Pd/Cu nanorods at -0.1 V from a plating solution containing 20 mM $CuCl_2$, 30 mM $PdCl_2$ and 0.1 M HCl for 2 C. The templates were dissolved in methylene chloride for 10 min to completely release the nanostructures. The latter were collected by centrifugation at 9000 rpm for 3 min and washed 3 times with methylene chloride, ethanol and deionized water each, with a 3 min centrifugation after each wash. Finally, Pd/Cu nanorods were soaked in a NaOH (3 M) solution for 30 min to dissolve Al_2O_3 for a complete release of nanorods. The Cu in the Pd/Cu nanorods was then etched as mentioned above. The Pd nanohelices were dispersed on glass slides. Finally, a 10 nm thick Ni layer was deposited onto the Pd nanohelices by electron beam evaporation, using a deposition speed of 0.05 nm/s.

Magnetic actuation and microscopy observation

A Helmholtz coil pair was used to generate the magnetic rotation field for remote actuation. The frequency of the rotating magnetic field can be changed from 1 Hz to 1000 Hz by a sinusoidal wave generator. The above magnetic nanohelices were dispersed in water droplets for rotation and translation motion tests. An inverted optical microscope (Nikon Instrument Inc. Ti-S/L100), coupled to a 40× objective, a Hamamatsu digital camera C11440 and NIS Elements AR 3.2

software, were used for capturing movies of the swimming motion. The speed of the nanoswimmers was tracked using a NIS Elements tracking module.

2.1.3 Template-assisted electrodeposition

As illustrated in Fig. 2.1, the new protocol for fabricating helical nanoswimmers is based on the procedure described by Park and coworkers for creating Pd nanosprings [29]. The preparation of such Pd nanohelices relies on electrochemical co-deposition of Pd^{2+} and Cu^{2+} inside the nanoscopic pores of AAO membrane templates using an acidic environment. Gold nanorods (~1 μm long) were electrodeposited initially within the nanopores to form a uniform solid base essential for the growth of the Pd/Cu nanorods (Fig. 2.1a). Subsequently, a solution containing 30 mM $PdCl_2$, 20 mM $CuCl_2$, and 0.1 M HCl was used for growing the Pd/Cu nanorods (Fig. 2.1b). An OH group terminated Al_2O_3 surface and the H^+ in acidic solution, along with a suitable reduction potential, are essential for the effective reduction of Pd^{2+} (during the co-deposition with Cu) to form crystal structures on the nanopore wall.[32] Dissolution of the membrane template (Fig. 2.1c) and etching of copper from the nanorod (Fig. 2.1d) result in Pd nanohelices. Subsequent electron beam evaporation of a nanometer-thick magnetic nickel layer onto the Pd nanosprings leads to tiny magnetic helical nanoswimmers (as small as 100 nm in diameter and 600 nm in length) (Fig. 2.1e). Applying a continuous torque to the new Ni-coated Pd nanohelices, *via* a rotating magnetic field, transforms the rotation around their helical axis into a translational corkscrew motion along this axis.

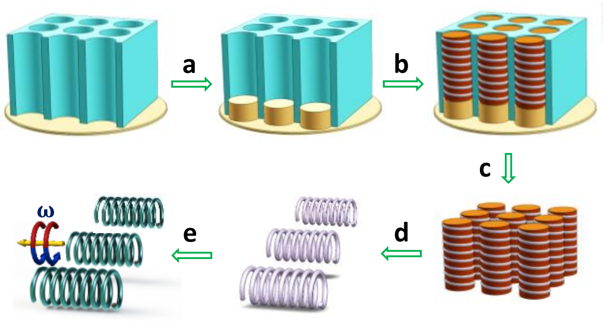

Figure 2.1 Schematic illustration of the template-based fabrication of helical magnetic nanoswimmers. a) Electrodeposition of Au; b) electrochemical codeposition of Pd/Cu rods; c) removal of the membrane template and the Au bottom layer; d) etching of Cu; e) Ni coating for magnetic actuation.

We initially used AAO membrane templates with pore diameter of ~200 nm for preparing the helical nanoswimmers. Stepwise schematic illustrations and SEM images of the nanostructures prepared at the different steps of the synthesis are displayed in Fig. 2.2a-c. For example, the SEM image of Fig. 2.2a depicts the surface morphology of a Pd/Cu alloy nanorod released during the NaOH-induced dissolution of AAO membrane. A close examination of this image indicates the presence of periodical helical dented curvature on the nanorod surface, corresponding to Pd nanodomains curling up on the Cu nanorod, and reflecting the coiled-shaped growth of Pd.[32] Subsequent 10 min exposure of this Pd/Cu rod structure to an 8M nitric acid solution results in etching of the Cu component, leaving behind a helical Pd nanospring structure with a rough surface (SEM image of Fig. 2.2b). Longer etching time can damage (slowly dissolve) the Pd nanospring structures. While the exact reason for the formation of the Pd nanospring is not fully understood, it has been attributed to the spatially different growth processes of Pd and Cu.[32] The circular cross section of the filament of this helical Pd nanostructure has a diameter of about 40 nm. A smoother surface is observed Fig. 2.2c after the electron beam evaporation of a uniform and thin Ni film over the Pd nanohelix. In order to improve the coating uniformity, the deposition rate of the Ni layer was maintained as low as 0.05 nm/s under a very low pressure (10^{-7} torr).

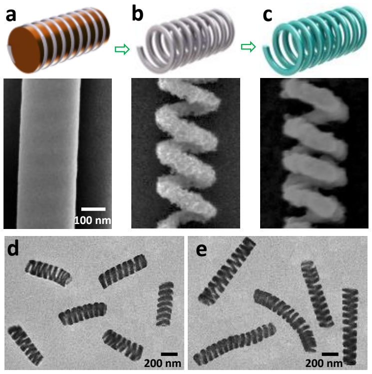

Figure 2.2 Schematic and SEM images of a Pd/Cu nanorod (showing periodical helical indented curvature on the surface) (a), the Pd helical nanospring (b) and the Ni-coated Pd helical nanospring (c). (d,e) TEM characterization of magnetic nanohelices of different lengths: ~800 nm (d) and ~1.5 µm (e), prepared using charge densities of 0.5 and 1 C/cm^2 , respectively.

The template electrosynthesis method can produce helical nanopropellers with tailored-made geometries and dimensions. For example, controlling the charge density during the Pd/Cu deposition has been used for producing nanohelices with different lengths. The transmission electron microscopy (TEM) images of Fig. 2.2d show well-defined nanohelices with a length of around 800 nm, prepared using a charge density of 0.5 C/cm^2. Increasing the charge density to 1 C/cm^2 results in longer helices with an average length of ~1.5 µm, (Fig. 2.2e). It should be noted that nanosprings with aspect ratios larger than 15 display some bending and may compromise the magnetic locomotion. Nanohelices with aspect ratios smaller than 10 were thus used for most subsequent propulsion experiments.

Another attractive feature of the new template electrosynthesis route is its ability to tailor the helical pitch through control of the composition of plating solution. In particular, the morphology of the helices is strongly dependent on the Pd^{2+}/Cu^{2+} concentration ratio in the solution. The absence of copper in the solution leads to the formation of Pd nanotubes due to the higher Pd^{2+} reduction rate at the surface of the nanopore [29]. Similarly, the helical architecture is not observed using plating solutions with very high Cu^{2+} concentrations, since such solutions hinder the nanohelix growth and lead to highly porous Pd nanorods. In order to tailor the helical pitch of the resulting nanohelices, we thus used plating solutions with a Cu^{2+} concentration of 20 mM and Pd^{2+} concentrations ranging from 25 mM to 45 mM. Fig. 2.3a-e displays a series of SEM images of nanohelices prepared with varied Pd^{2+} concentrations: a) 25, b) 30, c) 35, d) 40 and e) 45 mM. Fig. 3.f summarizes the observed effect of the composition of the plating solution and shows the dependence of the helical pitch length upon the Pd^{2+}/Cu^{2+} concentration ratio. These data and images indicate that the pitch length decreases gradually from ~130 nm to ~60 nm upon increasing the Pd^{2+} concentration from 20 mM to 45 mM. The resultant structure finally approaches a nanotube at the highest Pd^{2+} level. Overall, a plating solution containing 30 mM $PdCl_2$, 20 mM $CuCl_2$, and 0.1 M HCl is optimal for preparing well-defined Pd nanosprings towards efficient helical magnetic nanoswimmers.

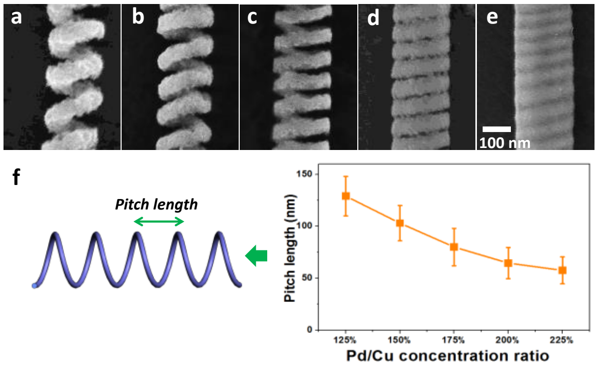

Figure 2.3 Control of the pitch length of the template-prepared magnetic nanohelices. a-e) SEM images of Ni-Pd nanosprinsg. $PdCl_2/CuCl_2$ concentration ratio in the plating solution: a) 25/20, b) 30/20, c) 35/20, d) 40/20, e) 45/20. f) Plot showing the dependence of the pitch length upon the Pd^{2+}/Cu^{2+} concentration ratio.

The electrodeposition strategy allows precise control of the diameter of helical Pd nanostructure, and of the corresponding nanoswimmers, through the use of membrane templates with different pore sizes. Since commercial Polycarbonate (PC) membranes have a larger variety of pore diameters (ranging from 15 nm to 12 µm) than AAO templates, it is possible to use different PC membrane templates for preparing helical nanoswimmers with different diameters. Accordingly, we evaluated polycarbonate membranes with pore diameters of 100 nm and 400 nm (along with the AAO membrane with 200 nm pores). Since hydroxyl (OH) group-terminated alumina surfaces in acidic environment are critical for nanohelix formation due to the interfacial electrostatic double layer formation in nanochannels [29], we used atomic layer deposition (ALD) for incorporating alumina into walls of the PC membrane micropores. Electrodeposition of Pd/Cu alloy nanorods has been subsequently carried out under the optimal conditions (30 mM $PdCl_2$/20 mM $CuCl_2$), followed by dissolution of the PC template and the Cu component using methylene chloride and 8 M nitric acid, respectively. SI Fig. 2.1 displays long Pd nanosprings encapsulated within 400 nm diameter Al_2O_3 nanotubes after the dissolution of the PC membrane. Subsequent NaOH-induced dissolution of the Al_2O_3 nanotubes and electron beam evaporation of Ni layer resulted in the formation of magnetic helical nanoswimmers of different diameters. Fig. 2.4 displays a series of SEM and TEM images of such magnetic nanohelices formed inside nanopores of varying diameters. These images indicate that well-defined nanohelices of diameters ranging from 100 to 400 nm can be prepared using membrane templates possessing nanopores of different diameters. Note also that the cross section of the filament increases from ~30 nm to ~150 nm upon increasing the diameter of the nanopores.

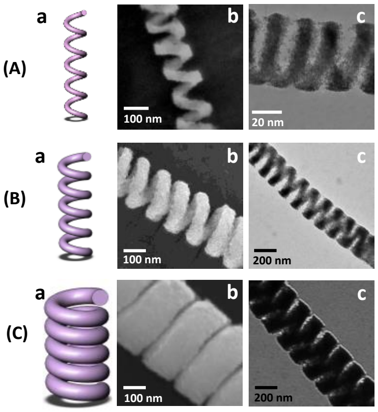

Figure 2.4 Schematic illustrations (a), SEM (b) and TEM (c) images of Ni/Pd nanohelices with different diameters: 100 (A), 200 (B) and 400 (C) nm prepared by using different membrane templates.

2.1.4 Magnetic actuation of the helical nanoswimmers

Following the successful template fabrication of tailored-made magnetic nanohelices, a rotating magnetic field has been used to remotely actuate their directional motion. The new template-prepared torque-driven nanoswimmers display an attractive propulsion behavior: tumbling motion at low magnetic rotation frequency and corkscrew motion at high magnetic rotation frequencies (Fig. 2.5a and 5b, respectively). The change from tumbling to a corkscrew rotation occurs at a specific stabilization frequency. Such frequency-dependent transition motion behavior is illustrated for a 400 nm diameter helical nanoswimmer, upon increasing the magnetic field frequency from 10 to 100 Hz. Subsequent work has focused on the corkscrew motion of the new template-prepared nanoswimmers. The image sequence of Fig. 2.5 c-f displays such movement using a 3 µm long (400 nm diameter) nanoswimmer over the 3 sec period at a rotation frequency of 150 Hz. The nanoswimmer travels over a long path of approximately 45 µm parallel to the magnetic field axis, *i.e.*, at a speed of 15 µm/s, corresponding to a relative speed of ~5 body lengths/s. Such speed compares favorably with those reported for helical swimmers prepared by advanced self-scrolling and GLAD techniques.[16,21,22] The new helical swimmers also displayed effective propulsion in cell culture media, which is in agreement with previously study of the magnetic nanoswimmers in salt-rich media.[18]

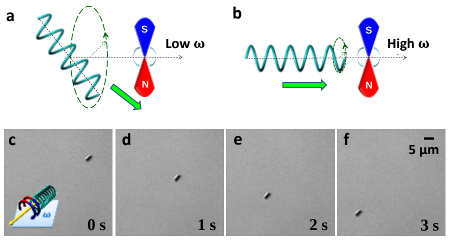

Figure 2.5 Schematic illustration of the tumbling (a) and corkscrew (b) motions of helical nanoswimmer under low and high magnetic rotation frequencies, respectively. (c-f) Time-lapse motion images of a 400 nm helical nanoswimmer under a magnetic rotation frequency of 150 Hz**.**

The translational velocity of helical nanoswimmers with different diameters has been examined using different magnetic rotation frequencies. The trajectories in Fig. 2.6a-c illustrate the defined motion of different helical nanoswimmers with diameters of 100, 200 and 400 nm, respectively, over a 2 second period at a rotation frequency of 120 Hz. Tracking analysis demonstrates that their average speeds are 6, 9 and 13 µm/s, respectively. The influence of the frequency upon the speed of helical nanoswimmers of different diameters is shown in Fig. 6d. These plots indicate that the motor speed increases in a nearly linear fashion with the frequency. Furthermore, it is noted that large nanoswimmers (with a 400 nm diameter) swim nearly 3-fold faster than the smaller (100 nm) ones. The speed of helical swimmers is dependent upon various geometric parameters (including the diameter) and the rotation frequency, in a complex manner described in Equation (2.1) [22,30]:

$$\boldsymbol{v} = \frac{(\xi_{\perp} - \xi_{||}) \sin\boldsymbol{\theta}\ \cos\boldsymbol{\theta}}{2(\xi_{\perp} sin^2\boldsymbol{\theta} + \xi_{||} cos^2\boldsymbol{\theta})} \boldsymbol{d\omega} \tag{2.1}$$

where $\xi_{\perp}$ and $\xi_{||}$ are the drag coefficients perpendicular and parallel to the helical axis, $\boldsymbol{\theta}$ is the helix angle, d is diameter of the helix, and ω is the rotational frequency. Overall, our experimental results follow closely the theoretical prediction of equation.

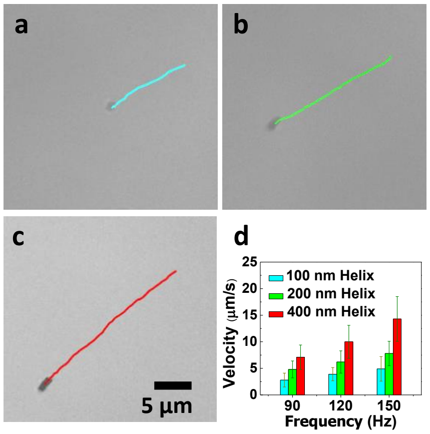

Figure 2.6 Motion trajectories of helical nanoswimmers with different diameters: a) 100 nm; b) 200 nm; c) 400 nm (aspect ratios of ~10) over a 2 sec period. Magnetic field frequency: 120 Hz. d) Dependence of the nanoswimmer velocity on the magnetic frequency and diameter of the motors, calculated from the tracking analysis of the observed motion.

2.1.5 Conclusions

In summary, we have demonstrated an attractive template-electrosynthesis approach for the fabrication of the extremely small yet highly efficient helical magnetic nanoswimmers. The Pd helical nanostructures were fabricated by template electrodeposition of Pd/Cu nanorods into nanoporous membrane templates, followed by removal of Cu, and electron-beam coating the resulting Pd nanohelices with a magnetic Ni layer. The new templating route results extremely small (of 100 nm diameter) and efficient helical nanoswimmers and allows convenient tailoring of the length, diameter and helix pitch of nanohelices. These template-prepared fuel-free helical nanoswimmers display an attractive locomotion behavior and are promising for a plethora of future biomedical applications, such as in vivo targeted drug delivery or biopsy.

2.2 Magneto-acoustic hybrid nanomotor

2.2.1 Introduction

Robotics deals with automated machines that can locomote themselves and perform different tasks in various environments across different scales. One of the most inspiring challenges is achieving efficient propulsion at micro/nanoscales, where viscous forces dominate [31]. The outstanding performance of molecular biomotors has inspired considerable interest in the design of man-made micro-/nanomachines which can mimic their behaviors and operate with locally-supplied chemical fuels [1,2,5,6,32–34]. For instance, researchers have developed catalytic nanomotors which exhibit autonomous self-propulsion in the presence of hydrogen peroxide and perform various advanced functions [9,35–44]. While chemically powered catalytic motors have received tremendous attention, many important applications of nanomotors (particularly *in vivo* biomedical ones) require the elimination of the external fuel. To address these needs, considerable recent efforts have been directed led to development of biocompatible fuel-free propulsion mechanisms based on external stimuli [10–13,15,21,45–51]. Increasing the capabilities and sophistication of such fuel-free nanomotors is essential to design advanced nanosystems for diverse biomedical applications.

Hybrid nanomotors, which use multiple distinct power sources for nanoscale propulsion, could expand the scope of operation of man-made nanomachines in changing environments. Hybrid nanomotors coupling fuel-powered and fuel-free propulsions in a single nanovehicle have thus been described recently [52–54]. For example, Wang's group demonstrated the first example of a hybrid nanomotor which can be powered both magnetically and catalytically [52], as well as a chemically-powered hybrid micromotor that harvests its energy from reactions of three different fuels [53]. Mallouk's group reported recently on bimetallic nanowire hybrid motors driven by chemical and acoustic forces [54]. However, there are no reports on synthetic fuel-free hybrid nanomotors based on different propulsion mechanisms and powered by various external stimuli. The dynamic interplay and collective behaviors of nanomotors under different external fields have not been explored. Achieving hybrid propulsion of nanomotors requires the design and fabrication of multicomponent within a single nanoscale device, along with integrated multifunctionality for dynamic complexity, while ensuring minimal effect upon the individual propulsion modes.

Here we describe a magneto-acoustic hybrid fuel-free nanomotor which can be powered by either a magnetic (Mag) or ultrasound (US) field. Both magnetic and ultrasound fields, which are traditionally used in diagnostic imaging, are playing an ever-increasing role in the delivery of therapeutic agents including genetic material, proteins, and chemotherapeutic agents [55,56]. Owing to their biocompatible energy transduction mechanism, magnetic and ultrasound propulsions have also dominated the operation of fuel-free nanomotors and hold considerable promise for biomedical applications, particularly *in vivo* ones. The magneto-acoustic hybrid nanomotors, described in the present work, thus lead a new generation of versatile and robust fuel-free nanovehicles for on-demand operation with either mode when the other one is failed or has to be suppressed in complex medical treatments. Meanwhile, such functional nanomachines are expected to be coupled with conventional magnetic and ultrasound diagnostic devices for multitask medical treatments including diagnostic, imaging and drug delivery at the same time with the dual-mode operation capacities. Of particular significance, the adaptive and reserved collective behaviors, with fast aggregation and swarm motion, provide a new route to control large-number of nanomotors which could not be achieved by using a single propulsion mode. Such new design and hybrid operation in an integrated manner thus expands the horizon of nanomotors to treat future diverse and complex medical conditions.

2.2.2 Experimental section

Synthesis of magneto-acoustic hybrid nanomotors

PC membrane templates (110607, Whatman, NJ, USA) with pore sizes of 400 nm were used for fabricating the hybrid nanomotors. Before electrochemical deposition, a 75 nm gold film was sputtered on one side of the porous membrane to serve as a working electrode using the Denton Discovery 18 (Moorestown, NJ). A Pt wire and an Ag/AgCl (with 1 M KCl) were used as counter and reference electrodes, respectively. The membrane was then assembled in a plating cell with an aluminium foil serving as a contact. All electrochemical deposition steps were carried out at room temperature (22 °C). Gold nanorods were then electrodeposited at −1.0 V for a total charge of 1.5C from a commercial gold plating solution (Orotemp 24 RTU RACK); subsequently, the Pd/Cu nanorods were deposited at −0.1 V from the $PdCl_2$/$CuCl_2$ plating solution mixture containing 20 mM CuCl2, 30 mM $PdCl_2$, and 0.1 M HCl with a total charge of 3C. After electrochemical deposition, the sputtered gold layer was completely removed by hand polishing with 3–4 μm alumina slurry. The templates were dissolved in methylene chloride for 10 min to completely release the nanostructures. The latter were collected by centrifugation at 9000 rpm for 3 min and washed 3 times with methylene chloride, ethanol and deionized water each, with a 3 min centrifugation after each wash. Then the Cu component (of the Pd/Cu nanorods) were dissolved using an 8 M HNO_3 solution for 10 minutes, resulting in the formation of nanorod-nanospring bi-segment structure. The nanostructures were then dispersed on glass slides. Finally, a 10 nm thick Ni layer was deposited onto the bi-segment structure nanostructures by electron beam evaporation, using a deposition speed of 0.05 nm s^{-1} . The control Au nanorods were electrodeposited at −1.0 V for a total charge of 3.0 C from a commercial gold plating solution (Orotemp 24 RTU RACK); while the control Pd nanosprings Pd/Cu nanorods were deposited at −0.1 V from the PdCl2/CuCl2 plating solution mixture containing 20 mM $CuCl_2$, 30 mM $PdCl_2$, and 0.1 M HCl with a total charge of 6 C. Similarly, a 10 nm thick Ni layer was deposited onto the fabricated control nanostructures by electron beam evaporation, using a deposition speed of 0.05 nm s^{-1}.

Ultrasound and magnetic propulsion

The hybrid propulsion was carried out in a cell made in a covered glass slide (75 × 25 × 1 mm). A piezoelectric transducer (PZT), consisting of a 0.5 mm thick ring with a 10 mm outside diameter and 5 mm inner diameter, was attached to the bottom center of the glass slide to create the ultrasonic field. The continuous ultrasound sine wave was applied through the PZT, via an Agilent 15 MHz arbitrary waveform generator, which was connected to a power amplifier. The continuous sine waveform and a voltage amplitude varied between 0 and 10.0 V, as needed for controlling the intensity of the ultrasonic wave. The electric signal was monitored using a 20 MHz Tektronix 434 storage oscilloscope. A Helmholtz coil pair was used to generate the magnetic rotation field for remote actuation. The frequency of the rotating magnetic field can be changed from 1 Hz to 1000 Hz by a sinusoidal wave generator. The above hybrid nanomotors were dispersed in different media for rotation and translation motion tests. Human serum from human male AB plasma was received from Sigma-Aldrich (St. Louis, MO). Fresh blood was collected from six-week-old male ICR mice and anticoagulated with ethylenediamine tetraacetate and diluted by 20 times. An inverted optical microscope (Nikon Instrument Inc. Ti-S/L100), coupled to a 40 ×objective, a Hamamatsu digital camera C11440 and NIS Elements AR 3.2 software, were used for capturing movies of the swimming motion. The speed of the nanoswimmers was tracked using a NIS Elements tracking module. In this study, each bar represents the mean ± Standard Deviation of 10-20 nanomotors under the same propulsion condition. We also performed statistical calculations using Student’s t test ($P \leq 0.05$). The speed between each bar is statistically different.

2.2.3 Hybrid nanomotor design and fabrication

Using different fields to power a single hybrid motor offers considerable promise for designing multi-modal adaptive nanovehicles that reconfigure their operation on demand based on changing conditions. Combining different fuel-free propulsion modes into a single device represents a nanoengineering challenge in view of the different requirements of the magnetic and acoustic propulsions. It is thus critical that the design and fabrication of the new dual-mode hybrid nanomotor will have a minimal effect upon the individual magnetic and ultrasound propulsions, compared to that of the common magnetic or ultrasound-based nanomotors. To address the challenge of harvesting the propulsion force from both magnetic and acoustic fields, the new class of nanomotors is constructed from bi-segment nanomechanical elements, where concave nanorod segments (essential for the ultrasound actuation), are connected to nanohelical magnetic segments (Fig. 2.7). The creation of such distinct multicomponent (rod-helical) architectures has been realized through a versatile template-assisted electrochemical deposition method followed by segment-selective chemical etching (Fig. 2.7B). Specifically, and as illustrated in Fig. 2.7A, the hybrid nanomotor is based on a bi-segment configuration, with a magnetic nanospring (Ni coated Pd) on one end, and a concave (Ni coated Au) nanorod on the other. The resulting nanostructures offer an attractive fuel-free magneto-acoustic hybrid nanomotor operation with the magnetic helical end serving for the magnetic propulsion and the concave nanorod for acoustic propulsion (Fig. 2.7A, bottom and top, respectively). The magneto-acoustic hybrid nanomotors can thus be powered by either the magnetic or ultrasound field, and change their swimming mode and direction instantaneously upon alternating the applied fields. Tuning the amplitude of the acoustic field or the frequency of the magnetic field leads to rapid speed regulation of such hybrid nanomotors.

Both the magnetic and acoustic fields are highly biocompatible and are widely applied in medicine. As desired for such biomedical applications, we demonstrate that the new hybrid motors display efficient magnetic and acoustic propulsions in various untreated biofluids, including cell culture medium, serum and blood. The exact mode switching would depend on the specific biomedical operation and requirements. The new hybrid nanomotors display also a distinct biomimetic collective behavior in response to alternating the external field. This unique collective behaviors includes a reversible transition between stable aggregation, swarm motion and swarm vortex configurations. Applying the different fields thus leads to three distinct states of the hybrid nanomotors which could be not achieved by using a single propulsion mode.

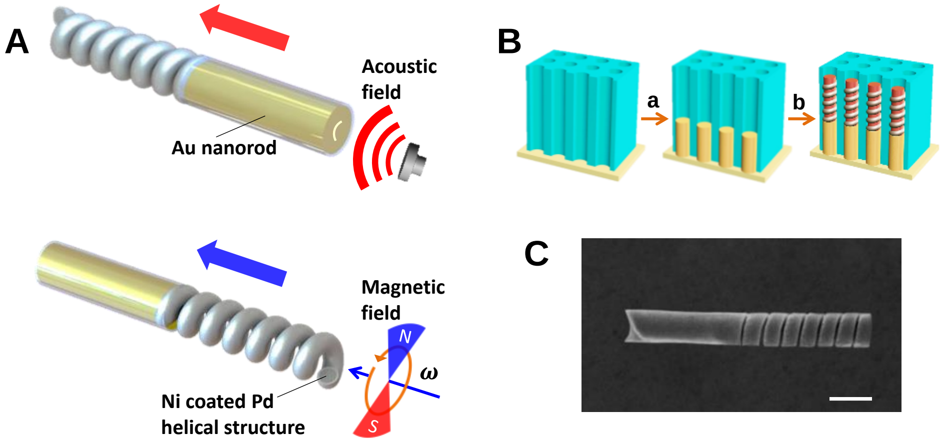

Figure 2.7 (A) Scheme of the design of the magneto-acoustic hybrid nanomotor and its dual propulsion modes under the acoustic and magnetic fields. (B) Schematic illustration of the template-assisted fabrication of the bisegment magneto-acoustic hybrid nanomotors. (C) SEM image of a magneto-acoustic hybrid nanomotor. Scale bar: 500 nm.

To realize such magneto-acoustic hybrid nanomotor, with the requisite geometric complexity and materials properties, we took advantage of recent advances in the electrosynthesis of nanorods and nanosprings [25]. As illustrated in Fig. 2.7B, commercial polycarbonate (PC) membranes with a pore diameter of 400 nm are first sputtered with a thin Au film as the bottom contact electrode. The gold nanorod segment (1.5 µm long) is subsequently electrodeposited within the nanopores (step *a* in Fig. 2.7B). Adding the helical structure involves a template electrochemical approach for creating Pd nanosprings [29]. This relies on the co-deposition of Pd^{2+} and Cu^{2+} within the nanoscopic pores (on top of the gold segment) under an acidic environment (step *b* in Fig. 2.7B). Dissolution of the membrane template, followed by selective wet (nitric-acid) etching of copper from the Pd/Cu segment, result in Pd nanohelices connected to the gold segment. Subsequent electron beam evaporation of a 10nm-thick nickel layer onto the bi-segment nanostructures leads to the 3µm-long hybrid nanomotors, displayed in the scanning electron microscope image (SEM) in Fig. 2.7C. The template-prepared Au segment has a concave end (illustrated also in the TEM images below) essential for efficient ultrasound-powered motion [13], based on the asymmetric steady fluid streaming physical mechanism [57]. Alternatively, by applying a rotational magnetic field, a continuous torque will be exerted on the hybrid nanomotor, transforming the rotation around its helical axis into a translational corkscrew motion along this axis (Fig. 2.7A, bottom). Such preparation of the new hybrid motor ensures efficient ultrasound and magnetic propulsions as well as rapid switching between the two propulsion modes.

2.2.4 Adaptive actutation of hybrid nanomotors

The ability to power the new hybrid nanomotor both magnetically and acoustically is illustrated in Fig. 2.8. The fabricated hybrid nanomotors have been suspended in water, with the suspension added to a capillary cell with an ultrasonic transducer at the bottom. Such this transducer generates a vertical acoustic standing wave at a resonant frequency of about 2.66 MHz. Precise control of the magnetic propulsion of hybrid nanomotors has been achieved using two orthogonal Helmholtz coil pairs that create a uniform rotating magnetic field. Fig. 2.8 compares the movement of the hybrid nanomotor in its acoustic and magnetic modes over a 25 sec period. Using the magnetic mode, with a rotational frequency of 150 Hz, the hybrid nanomotor moves towards its Au end at a speed of 12.2 μm/s (Fig. 2.8A). Similarly, efficient acoustic propulsion, with a speed of 16.8 μm/s, is observed under the ultrasound field (Fig. 2.8C). In order to verify that our hybrid nanomotor design leads to opposite moving directions - along the nanowire axis - under the dual propulsion modes, alignment of a single nanomotor by an external magnet was performed. As expected for such acoustic propulsion, the motor moves “backwards” towards its helical end. The repeated cycles shown in Fig. 2.8D-G illustrate the ability to repeatedly generate movement in opposite directions, and to facilitate an on-demand change in the motor directionality. Only

Brownian motion of the hybrid nanomotor (with no net displacement) is observed in the absence of the both acoustic and magnetic fields (Fig. 2.8B, D and F). The dynamic speed change of the hybrid nanomotor during the multiple propulsion switching of Fig. 2.8A-G is illustrated in Fig. 2.8H. Here we define the acoustic propulsion as a "forward" (positive) motion. The temporal speed change in Fig. 2.8H illustrates the rapid response of the hybrid nanomotor to the different external stimuli. Overall, Fig. 2.8 demonstrates that the hybrid nanomotors offer an attractive performance with an on demand operation switching, including instantaneous achievement of the corresponding steady-state speeds (< 50 ms) and reversal of the movement direction. Beyond fast moving direction switching, such hybrid operation leads a new generation of versatile and robust fuel-free nanovehicles for on-demand operation by a given mode when the second one is failed or suppressed in complex biomedical applications.

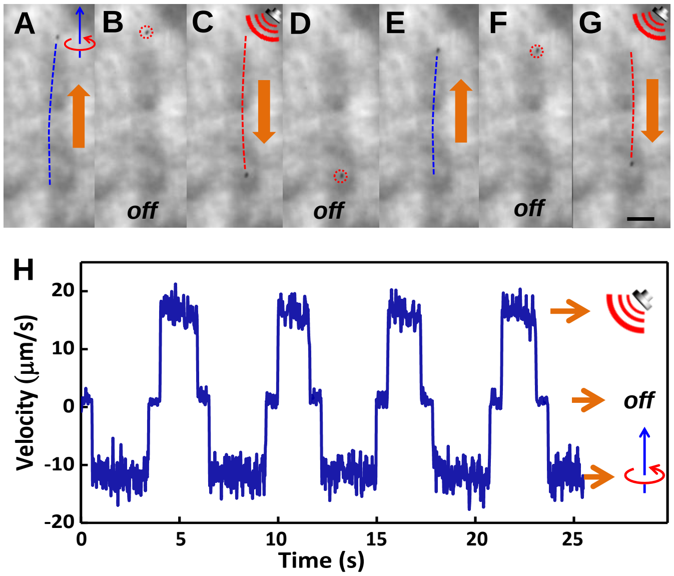

Figure 2.8 Cycling between the magnetic and acoustic actuations while changing the movement direction. (A-G) Tracking lines and (H) speed changes of the movement in the magnetic or acoustic modes over 4 s, as well as without external fields. Conditions: Ultrasound transducer power: 4V with resonant frequency of 2.66 MHz; rotational magnetic field frequency: 150 Hz. The acoustic (forward) and magnetic (backward) propulsions are colored in blue and red, respectively, with the forward speed defined as positive in the speed-time profile plot. Scale bar: 20 μm.

The speed of chemically-powered nanomotors can be controlled by parameters of the chemical environment, such as fuel concentration and temperature [58]. However, real-time and rapid speed regulation is still quite challenging for chemical-powered nanomotors. Since our new hybrid nanomotor is completely fuel free and powered by external fields, its speed could be easily regulated by changing the input parameters of the corresponding field. Under acoustic mode, a nanoparticle can be viewed as a body oscillating in a uniform oscillating velocity field [57]. Based on the physical mechanism of asymmetric steady fluid streaming, the inertial rectification of the time-periodic oscillating flow, generates steady stresses on the nanomotor which, in general, do not average to zero, resulting in a finite propulsion speed along the axis of the symmetry of the particle and perpendicular to the oscillation direction. The dimensional propulsion speed of the nanomotor can be expressed as [57]:

$$v_u = \varepsilon R_e V^{\perp} v^{(1,1)} \tag{2.2}$$

Where ε is the dimensionless small shape parameter, R_e is the Reynolds number, $v^{(1,1)}$ is the leading-order dimensionless propulsion speed, and $V^{\perp}$ is the relative amplitude of the particle oscillations which scales with the amplitude of the ultrasound field. Therefore, the speed of the hybrid nanomotors levitated in solution under a fixed ultrasound wave frequency can be readily controlled by changing the amplitude of the driving voltage.

The speed of helical magnetic swimmers depends upon various geometric parameters (including the diameter) and the rotation frequency, in a complex manner described in Equation 2.3 [22,30]:

$$v_u = \frac{\left(\xi_{\perp} - \xi_{\|}\right)\sin\theta\cos\theta}{2\left(\xi_{\perp}\sin^2\theta + \xi_{\|}\cos^2\theta\right)} d\omega \tag{2.3}$$

where $\xi_{\perp}$ and $\xi_{\|}$ are the drag coefficients perpendicular and parallel to the helical axis, θ is the helix angle, d is diameter of the helix, and ω is the rotational frequency. Therefore, the speed of the hybrid nanomotor in a certain fluid, operated in the magnetic mode, can be regulated by controlling the rotational frequency of the magnetic field. Overall, while the speed of the new hybrid motor under the magnetic and ultrasound actuations could be controlled by controlling the rotation frequency of the magnetic field and the voltage amplitude applied on the piezoelectric transducer, respectively.

We tested the propulsion performance of the hybrid nanomotors under different input parameters of the individual modes. Fig. 2.9A displays track lines of the nanomotor over 4 s periods using different applied voltages of the acoustic mode. As expected from Equation 2.2, the speed increases from 8.1, to 16.4, and 22.3 μm/s upon increasing the applied voltage from 2, to 4 and 6 V, respectively. Similarly, the speed of the hybrid motor operated in the magnetic mode increased from 7.6, 12.3 and 15.9 μm/s upon changing the rotational frequency from 100 to 150 and 200 Hz, respectively (Fig. 2.9B). Considering that the propelling force is balanced by the drag force which is proportional to the speed of the nanomotor, the slightly lower speed of the magnetic movement compared to that observed under the ultrasound field reflects the lower magnetic propelling forces. The average speeds of the hybrid nanomotor under different magnetic rotation frequencies and acoustic voltages are displayed in Fig. 2.9C. We also studied the force competition through a simultaneous application of both ultrasound and magnetic fields. By adjusting the ultrasound and magnetic propelling forces to be balanced with each other, an equilibrium state could be achieved while the net speed of the hybrid nanomotor is approaching zero. Overall, these data follow the theoretical predictions of Equations 2.2 and 2.3. In order to demonstrate the digital and programmable speed regulation of the hybrid nanomotor, it was subjected to a series of predefined field inputs.

An ideal hybrid motor is expected to switch rapidly its propulsion modes upon applying the corresponding actuation. Such capability was examined by applying alternately the magnetic and acoustic fields (every 3 sec) while changing the corresponding ultrasound voltage and the rotational magnetic frequency. Speed-time profile (Fig. 2.9D) demonstrates that the new hybrid nanomotor displays an instantaneous switching between its acoustic and magnetic modes, with steady-state speeds reaching rapidly upon switching the operation mode. Careful analysis indicates that the hybrid nanomotor can rapidly reverse its moving direction within less than 50 msec. Therefore, rapid, on-demand and programmable speed and direction control of the hybrid nanomotors can be achieved with the judicious combination of acoustic and magnetic fields.

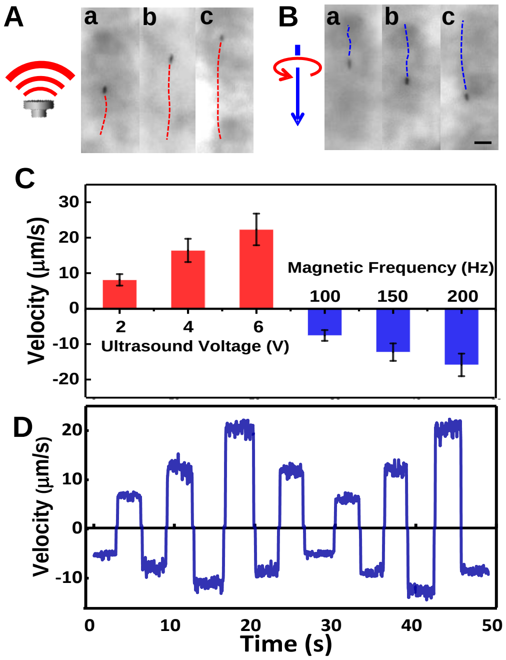

Figure 2.9 (A) Tracking lines over 4 s illustrating the movement of the hybrid nanomotor under the acoustic mode using applied voltage amplitudes of 2(a), 4(b) and 6 (c) V. (B) Tracking lines over 4 s showing the magnetic operation of the hybrid nanomotor using rotational magnetic frequencies of 100 (a), 150 (b) and 200 (c) Hz. Scale bar: 20 μm. (C) Quantitative velocity of the hybrid motor using magnetic frequencies of 100 Hz, 150 Hz and 200 Hz and ultrasound voltage amplitudes of 2V, 4V and 6V. All the speed data are averaged by 20 nanomotors under the same propulsion conditions (D) Digital control of the hybrid motor speed by changing the actuation mode and the corresponding ultrasound voltage and rotational magnetic frequency alternately every 3 seconds using the following sequence: Mag 100 Hz, US 2V, Mag 150 Hz, US 4V, Mag 200 Hz, US 6V, Mag 150 Hz, US 4V, Mag 100 Hz, US 2V, Mag 150 Hz, US 4V, Mag 200 Hz, US 6V, Mag 150 Hz.

In order to test the critical role of the bi-segment configuration for optimal hybrid propulsion in both modes, we compared its hybrid operation with that of a Au nanorod and Pd nanospring (both coated with 10-nm Ni thin layer). The TEM images in Fig. 2.10 display the structure of these (A) nanorod, (B) nanospring, and (C) hybrid nanomotors. Clear concave ends are observed for both the nanorod and hybrid nanomotor. The hybrid propulsion performance of these different nanostructures is illustrated in Fig. 2.10D. The nanorod structure displays an efficient movement, with a speed of 19.2 µm/s under the acoustic propulsion (applied voltage: 6 V). This speed is consistent with previous studies of ultrasound-powered nanowire motors [45]. In contrast, no obvious net displacement of the Au nanorod is observed under magnetic actuation with a rotation frequency of 200 Hz. Since the Au nanorods are coated with a thin Ni layer, they can still tumble at the surface with a very low speed of 3.5 µm/s under the rotational magnetic field; such speed is comparable with that of Brownian motion at this scale. These data confirm that while the concave end of the nanorod leads to the shape asymmetry essential for efficient ultrasound-powered propulsion,[29] such nanorods are not able to transform their rotation into a translational corkscrew motion (in the absence of helical structure). In contrast, applying a rotating magnetic field of 200 Hz onto the nanospring structure results in the expected translational corkscrew motion with a speed of 17.4 µm/s. Interestingly, the nanospring moves under the acoustic actuation, with a speed of 14.9 µm/s. This speed is 22% slower than that of Au nanorods (with the same length), indicating that the nanorod with a concave end offers a more efficient acoustic propulsion than the nanospring. The somewhat surprising acoustic propulsion of the nanospring appears to reflect its inherent geometric asymmetry and hollow structure which results in a finite propulsion speed along the axis of the particle in the time-periodic oscillating flow under acoustic field [57]. The bi-segment hybrid spring-rod nanomotor displays both efficient acoustic and magnetic propulsions, with speeds of 21.9 µm/s and 14.1 µm/s, respectively (Fig. 2.10D). According to the asymmetric steady streaming mechanism for acoustic propulsion of rigid bodies, the speed of a nanomotor under the ultrasound field is strongly related to its geometric dimensions while the symmetry breaking of the particle itself (shape, composition) is essential to achieve propulsion [57]. The dimensionless shape parameter ε in Equation 2.2 quantifies the distance to a perfect sphere. The hybrid motor is constructed with a bi-segment structure with larger shape and composition asymmetry, leading to a larger average speed under ultrasound propulsion. Though the speed of the hybrid nanomotor under magnetic propulsion mode is slightly slower than that of the nanospring structure, the sum of propulsion speeds of the total two modes is larger than that of the nanospring. The above experiments demonstrate that the magnetic nanospring structure can still lead to a useful hybrid operation. However, the hybrid spring-rod nanomotors can harvest and translate the propelled forces more efficiently. Overall, these data indicate that the bisegment nanowire design of the hybrid nanomotor does not compromise the performance of the individual propulsion modes.

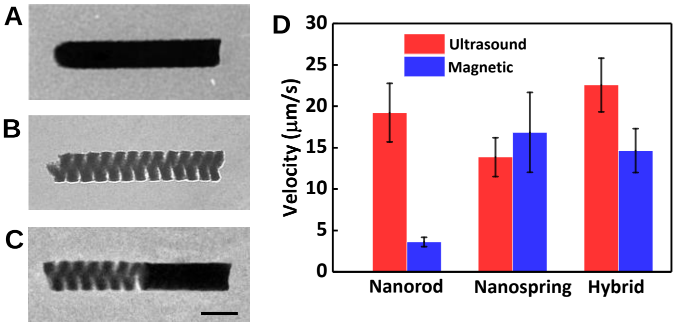

Figure 2.10 TEM image of (A) Ni-coated Au nanorod, (B) Ni-coated Pd nanohelix and (C) hybrid bisegment nanomotor. Scale bar: 500 nm. (D) Quantitative velocity evaluation of the motion of the three motor designs (shown in A-C). Ultrasound transducer power: 6 V, rotational magnetic field: 200 Hz.

For practical biomedical applications of the new hybrid nanomotors, it is critical to test their propulsion behavior in different complex environments. As illustrated in Fig. 2.11, the hybrid nanomotors operate readily in their dual propulsion modes in diverse media, including (A) seawater,

(B) culture medium, (C) serum and (D) blood. The average speeds of the hybrid motor in different biological media are measured and displayed in Fig. 2.11E. The speed of the hybrid motor under the ultrasound mode decreased from 15.4 μm/s in seawater to 11.4, 9.8 and 5.4 μm/s in cell medium, serum and blood, respectively (ultrasound transducer voltage 4V). The speed of the hybrid motor under the magnetic mode also decreased from 12.2 μm/s in seawater to 8.6, 6.8 and 6.0 μm/s in cell medium, serum and blood respectively (magnetic rotational frequency of 150 Hz). These changes reflect the increased environmental viscosity of these biofluids. Chemically-powered nanomotors cannot operate in high ionic-strength environments (such as seawater and blood) because these media interfere with their self-electrophoresis propulsion mechanism. While these environments affect the speed of the hybrid nanomotors, these motors still move efficiently in both modes in the different viscous fluids, reflecting their robustness in complex environments.

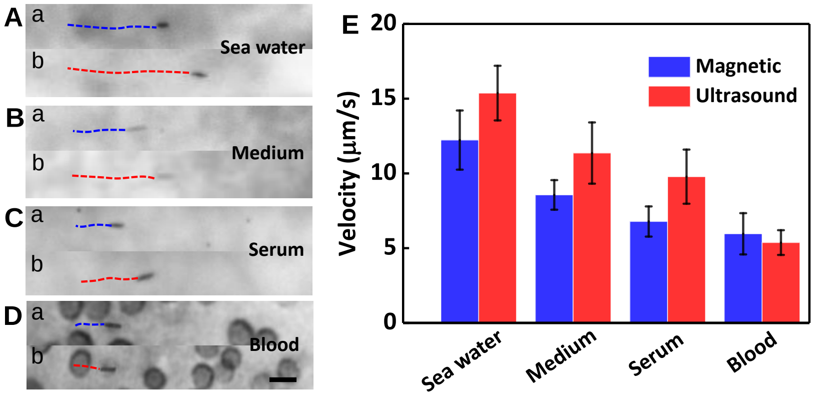

Figure 2.11 Movement of hybrid nanomotors in various media. Images illustrating the 2-second tracking lines of magnetic (blue) and ultrasound (red) propulsions of a hybrid nanomotor in (A) seawater, (B) cell culture medium, (C) serum and (D) blood (50% in PBS buffer); the black circles are fresh red blood cells collected from a six-week-old male ICR mice and anticoagulated with ethylenediamine tetraacetate. Scale bar: 10 μm. (E) Quantitative data of the velocity of the hybrid nanomotor in different modes and media, using an ultrasound transducer voltage of 4 V or a magnetic rotational frequency of 150 Hz.

2.2.5 Collective behaviours of hybrid nanomotors

Collective behavior, which is a very common phenomenon in the biological world [59], inspired us to investigate how groups of the hybrid motors behave under the external field inputs. As illustrated in Fig. 2.12A, the acoustic field (frequency 618 Hz) is able to trigger a fast tight assembly of the hybrid nanomotors. Note that the ultrasound frequency used in Fig. 2.12 for achieving such nanomotor aggregate is different from resonant frequency of the 2.66 MHz commonly used for self-propulsion of single nanomotors (e.g., Fig. 2.8). In contrast, the magnetic actuation induces disassembly of the aggregate and drives the directional motion of the nanomotor swarm. Such compact assembly and directional swarm movement of the hybrid nanomotors can be dynamically reversed by alternating the acoustic and magnetic stimuli. The reversible collective behavior of hybrid nanomotors and defined transitions between the two states are demonstrated in Fig. 2.12B. Initially, all the hybrid nanomotors display a typical corkscrew motion in the presence of rotating magnetic field (t=6 s). Stopping the magnetic actuation and applying the acoustic field leads to rapid aggregation of the hybrid motors towards the acoustic field node, with formation of a tight assembly structure within 5 seconds (t=18 s). Such aggregation is based on the acoustically-generated pressure gradients (generated by the piezoelectric transducer) which trigger spontaneous migration of microparticles towards low-pressure regions (nodes or antinodes) [60]. A similar behavior was reported for the swarming of chemically-powered catalytic nanomotors [61]. The assembling and aggregation persist while the acoustic field is applied. Removal of this acoustic field and activation of the magnetic field trigger the corkscrew propulsion and lead to rapid dispersion of the nanomotor aggregate, and a directional motion of the resulting swarm (t=26 s). Because of the ferromagnetic property of the surface, an attraction force is induced between the nanomotors might induce assembly and aggregation configurations at short-range magnetic order. However, by using a high-frequency rotational magnetic field, the magnetic drag force eventually exceeds the magnetic interaction force between the two nanomotors due to their slight individual structural differences [62]. Therefore, the relative distance between two nanomotor increases with the applied time of the magnetic field, leading to disassembly of the aggregation and to a swarm motion of the nanomotors. The dispersed nanomotors could be re-collected and re-assembled upon applying the acoustic field (t=43 s). Such collective behavior is highly switchable and can be repeated with multiple cycles (two cycles are shown here). A fully reversible swarming, with rapid aggregation and dispersion of the nanomotors, can thus be obtained, with proper application of the acoustic and magnetic fields, respectively. Such fast collective behavior represents a significant improvement in speed and reversibility compared to early studies involving the slow swarming of microparticles [63–65]. The ability of hybrid nanomotors to form dynamic steady states offers considerable promise for creating groups of machines that can perform cooperative tasks which would be impossible by using a single nanomotor. For a given droplet in the ultrasound cell, the locations of pressure nodes and antinodes can be estimated from the wavelength of the acoustic wave [61,66,67]. Therefore, it is anticipated that the resulting nanomotor swarm can be moved in a controlled manner by varying the applied acoustic frequency, which changes the ultrasound wavelength. Such wavelength shift thus changes the location of the pressure nodes and hence leads to migration of the entire swarm toward the new location.

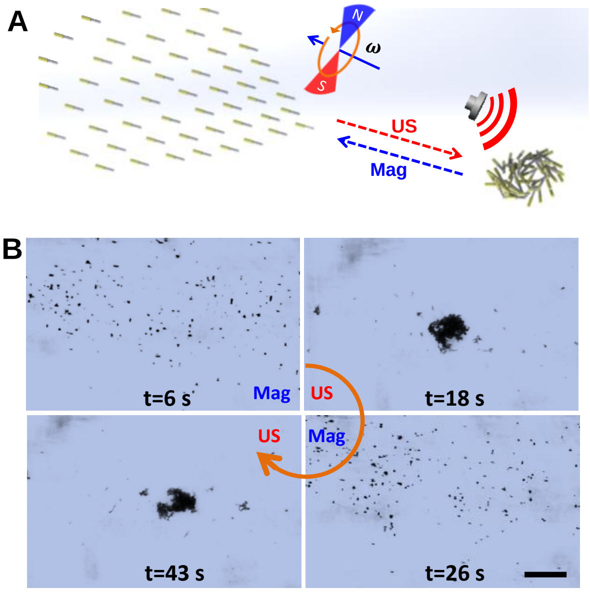

Figure 2.12 Reversible assembly of the magneto-acoustic hybrid nanomotors. (A) Scheme of the reversible switching between swarming nanomotors and assembled nanomotors by alternating the actuating magnetic and acoustic fields. (B) Snapshots of the directional swarm motion (magnetic field ‘on’ at t = 6 s), aggregated nanomotor assembly (ultrasound ‘on’ at t = 18 s), swarm motion (magnetic field ‘on’ at t = 26 s), and re-assembly of the nanomotor aggregate (ultrasound ‘on’ at t = 43 s) at different times. Ultrasound transducer power: 6 V; rotational magnetic field: 200 Hz. Scale bar, 50 μm.

We also examined the collective behavior of hybrid nanomotors in the presence of both of the acoustic and magnetic fields (*i.e.*, a “dual operation mode”) that can lead to three distinct states. Fig. 2.13 illustrates the dynamic behavior of the hybrid nanomotor assemblies and swarms with both acoustic and magnetic fields turned ‘On’. Interestingly, unlike the directional swarm motion observed under the magnetic field alone or the stable aggregation under the acoustic field, a swarm vortex is formed when both of the fields are turned ‘on’ (Fig. 2.13A). Turning the acoustic field ‘off’ in such a state leads to directional moving swarm of the nanomotors under the rotational magnetic field (Fig. 2.13B-C). Application of the acoustic field again leads to rapid migration of the hybrid motors toward the original node position and re-formation of a swarm vortex (Fig. 2.13D-E), although the magnetic field is still ‘on’. Upon removal of the magnetic field, the acoustic field dominates and a stable assembly is formed again (Fig. 2.13F). Applying again both fields results in the re-formation of the swarm vortex. The three different states of the swarm vortex (when both fields 'on'), directional swarm motion (only the Mag is 'on'), and the stable assembly (only the US 'on'), are highly switchable and reversible.

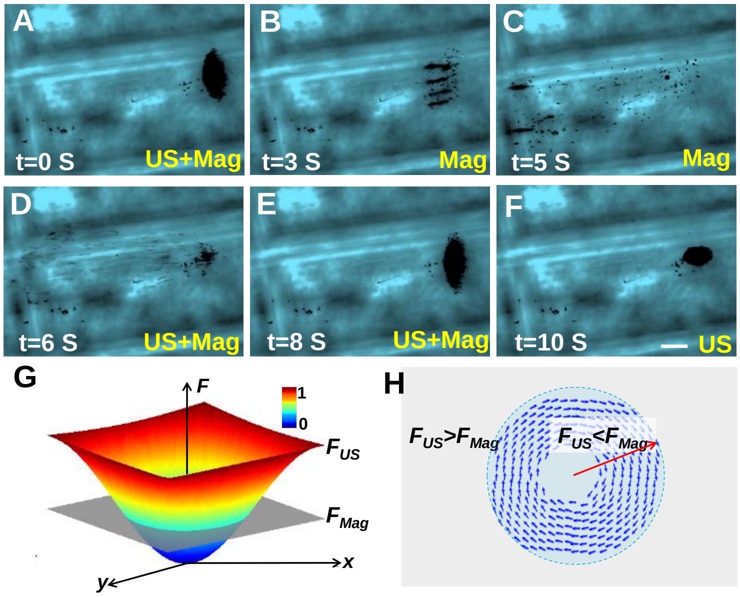

Figure 2.13 Complex spatial-temporal collective behaviors of magneto-acoustic hybrid nanomotors. (A) A swarm vortex is formed when both the ultrasound and magnetic fields are 'on'. (B-C) The hybrid nanomotors display directional swarm motion when only the magnetic field is 'on'. (D-E) Rapid re-formation of the swarm vortex upon turning the ultrasound field 'on' again. (E) A stable aggregation is formed when only the ultrasound field is turned 'on' (G) Normalized distribution of the acoustic force gradient F_{us} and magnetic force F_{mag} near the ultrasound pressure node in the acoustic cell. The magnetic force is considered to have a uniform distribution, shown by the grey plane. (h) Illustration of swarm vortex formation in a round boundary system where the magnetic force and the acoustic force becomes equal. US field: 6 V, 618 kHz, Mag field: 200 Hz, Scale bar: 50 µm.

Such adaptive switching of the collective behavior results primarily from the competition between the magnetic and acoustic forces. At steady-state, the imposed propelling force is always counterbalanced by the Stoke's drag force. From Equation 2.2, one can note that the magnetic propelling force imposed on a hybrid nanomotor is always consistent at a fixed frequency. Under the acoustic actuation with a frequency of 618 kHz, a plane standing wave field arises from the superposition of two waves (one is generated by the transducer, while the other reflected by the cover slide) of equal wavelength and amplitude traveling in opposite directions. The interference between the waves results in the formation of antinodes and nodes, with zero levitation force at the pressure nodes. The acoustic force can be divided into the primary radiation force (PRF) and the secondary radiation force (SRF). The PRF, which is the main force in the field of acoustic waves, can be subdivided into an axial component F_z and a transverse component F_{xy}. [51-52] The F_z component of the PRF is the force that drives the migration of microparticles to the nearest pressure node or antinode plane, while the F_{xy} component leads to their aggregation within the nodal plane. Our experiment depends on the theoretical understanding of the F_z component of the PRF which drives the nanomotor in a standing ultrasound wave field [44,60].

$$F_z = VE_{ac}\frac{2\pi}{\lambda}\mathrm{Q}\sin\left(\frac{4\pi}{\lambda}z\right) \tag{2.4}$$

Here V is the nanomotor volume, z is the axial distance from the transducer to the node or antinode plane, λ is the wavelength, Q is the acoustic contrast factor which is related to the particle fluid interactions. The acoustic energy density E_{ac} is equal to the sum of the average potential and kinetic energy densities. As indicated from the Equation 2.4, the acoustic force exhibits a sinusoidal dependence of the axial distance from the transducer to the node or antinode plane. Therefore, the acoustic force drops rapidly near the node and becomes zero at the node (Fig. 2.13G). In this case, within a certain distance from the node position, the magnetic propelling force is larger than the acoustic radiation force. Once the nanomotor approaches the equilibrium round boundary where the magnetic and acoustic forces become equal, the nanomotors can no longer achieve directional motion, and instead aggregate rapidly into a swarm vortex configuration with zero density in the center. Since the ultrasound radiation force boundaries are reflecting, the velocity perpendicular to the boundary is suppressed in the course of collisions with other nanomotors on the way back from the boundary [68]. As a consequence, the velocity parallel to the wall survives and becomes a natural attractor for the dynamics, which is plotted in Fig. 2.13H. The circular system boundaries conform perfectly to parallel velocity, resulting in a tight vortex formation. At the position beyond the equilibrium boundary, the increased acoustic force will dominate the motion of the nanomotor and tow the nanomotor again towards the node position. Further aggregation with magnetic field off (Fig. 2.13F) is facilitated by the SRF, which is associated with the sound waves that are scattered by individual nanomotors. The SRF is responsible for particle-particle interactions, making them either to attract or repel each other, as well as forming stable multiparticle spherical structures [44,60]. Such diverse and unique collective behaviors, *e.g.,* vortex formation and swarm motion, of the hybrid nanomotor system, can serve as a good model for complex open systems such as bacterial chemotaxis or cell migrations [68,69].

2.2.6 Conclusion

In conclusion, we reported a new magneto-acoustic hybrid nanomotor that could be powered by magnetic or acoustic fields. The use of magnetic and acoustic actuations to power a hybrid device offers a broader scope of operation and holds considerable promise for designing smart nanovehicles that autonomously adapt and reconfigure their operation in response to changes in their surrounding environment. Addressing the different requirements of the magnetic and acoustic propulsions within a single nanoscale device has been achieved by combining the fabrication of the two different swimmer designs (helical and concave rod) via judicious template electrosynthesis of bi-segment nanostructures. The resulting hybrid nanomotor can harvest the propelling forces from both magnetic and acoustic fields for efficient fuel-free dual-mode hybrid motor operation. The speed and directionality of the hybrid nanomotors can be rapidly controlled by changing the parameters of the field inputs. The hybrid nanomotors can also achieve efficient propulsion in biological media and demonstrate attractive and switchable collective behaviors.

Dynamically and reversible change between a tight assembly, swarm motion and swarm vortex state is achieved in response to a change of the acoustic and/or magnetic actuations. Such multi-mode fuel-free propulsion capability offers a broader scope of operation and considerable promise for adaptive performance under different scenarios in dynamically changing environments. Such adaptive and hybrid opeation provides a new versatile route to precisely control a single or a large-number of nanomotors which could not be achieved by using a single propulsion mode. Overall, the new magneto-acoustic hybrid nanomotors can function individually and collectively, with rapid cycling between the magnetic and acoustic modes and precise temporal-spatial control and regulation. Future efforts will lead to intelligent hybrid vehicles to be coupled with conventional magnetic and ultrasound diagnostic devices with real-time autonomous mode switching in response to changing conditions. Meanwhile, various medical functions, such as imaging and drug delivery, could be integrated on the nanomotors for multitask response and operation. Owing to their attractive performance, the new hybrid magneto-acoustic nanomotors are expected to advance the field of artificial nanomachines and to offer considerable promise for a wide range of practical applications ranging from nanoscale manipulation and assembly to nanomedicine.

2.3 Biointerfacing magnetic nanorobots with platelet membrane for biothreat isolation

2.3.1 Introduction

Robots have become commonplace in today's world through their application to diverse domains such as manufacturing, service, defense, and health care. These automated devices can locomote themselves and perform different tasks in various environments across different scales. The efficient locomotion capacity and advanced biological functionality of natural microscopic machines, such as motile cells like leukocyte and spermatozoa, have inspired scientists to recreate this form of locomotion and function using artificial machines with similar dimensions. Over the last decade, considerable progress in materials science and nanotechnology has led to remarkable advances in the development and operation of man-made nanomachines mimicking their natural counterparts [1,5,6,33,43,70–74]. Synthetic nanomachines based on variety of materials and nanostructures have demonstrated efficient locomotion capacity by harvesting thrust from either localized chemical reactions or from external stimuli [13,35,36,50,51,75,76]. Like their natural counterparts, these versatile man-made nanomachines possess advanced locomotive capabilities, including precise speed regulation and spatial motion control, along with self-organization and collective movement, allowing for a variety of practical applications, ranging from targeted drug delivery [77–79], to environmental remediation [80,81], and nanoscale manipulations for lithography and imaging [38,82]. As advanced nanorobot capabilities are being developed, proper attention must be given to overcoming key challenges for their operation in real-life biological environments [83,84]. Though nanomotors have been functionalized with different bio-receptors for imparting specific recognition of target biomolecules [85], the viability of these nanomachines relies largely on synthetic nanomaterials, which are susceptible to immune response or other biological processes in physiological systems, and may eventually hinder their effectiveness. Therefore, new bioinspired and bioengineered approaches, based on the incorporation of natural materials into the nanomachine design, must be considered to address these limitations.

Bioinspired and biomimetic design approaches have recently emerged as a novel paradigm to address the limitations of synthetic nanomaterials for biomedical operation [86,87]. Essential functional biological attributes can be imparted into synthetic systems through the biomimetic design based on innate circulatory cells. Therefore, the circulation and targeting functions designed in synthetic nanomachines are highly desired to be naturally processed by circulating cells, including erythrocytes, leukocytes, and platelets. Particularly, platelets have inspired the design of functional nanocarriers owing to their many functions responsible for immune evasion [88,89], subendothelium adhesion [90,91], and pathogen interactions [92,93], as well as their essential role in hemostasis [94]. Therefore, the platelet membrane cloaking method provides a new approach for developing functional nanoparticles with a bioengineered interface for diverse biomedical applications [95].

Here we demonstrate the preparation of platelet membrane-cloaked nanomotors (PL-motors), by enclosing magnetic helical nanomotors with the plasma membrane of human platelets, for biothreat binding and isolation (Fig. 2.14A). The PL-motors are synthesized using a template-assisted electrochemical deposition method followed by a cell membrane cloaking technique. The prepared PL-motors possess a membrane coating containing a wide variety of functional proteins associated with platelets. Magnetic propulsion offers fuel-free remote actuation and navigation abilities desired of biomimetic nanomotors [6]. Bridging the biological functions of platelet vesicles with the locomotion capacity of synthetic nanomotors thus results in a powerful biomimetic platform. The prepared PL-motors offer remarkable biocompatibility and propulsion in various biological fluids. Significantly, the PL-motors display an efficient locomotion in whole blood with no apparent biofouling, mimicking the movement of natural motile cells, such as leukocytes, which can move in whole blood. Such efficient propulsion and PL coating open the door for attractive detoxification capabilities. To exemplify their biological function, we demonstrate that the PL-motors can be used to effectively absorb Shiga toxin (Stx) using a Vero cell assay, resulting from the strong platelet-Stx binding enabled by the protein receptors presented on the platelet membrane. The PL-motors display also platelet-mimicking properties, such as enhanced binding to platelet-adhering pathogens, which can be used for rapid bacteria isolation. These platelet-camouflaged nanomotors with advanced fuel-free locomotion capabilities are thus expected to dramatically expand the domain of biomedical nanorobotic operations in physiological systems.

2.3.2 Experimental Section

Preparation and Characterization of PL-motor

The PL-motors were prepared by enclosing magnetic helical nanomotors with the plasma membrane of human platelets. Platelet membrane derivations were performed as previously described (37). Briefly, after isolation of platelet from whole blood, the platelets were resuspended in PBS mixed with protease inhibitor tablets. Platelet membrane was derived by a repeated freeze-thaw process and washed by centrifugation in PBS solution mixed with protease inhibitor tablets. Aliquots of platelet suspensions were first frozen at -80 °C, thawed at room temperature, and pelleted by centrifugation at 4000 × g for 3 min. Following three repeated washes, the pelleted platelet membranes were suspended in water and stored at -80 °C until use.

Helical nanomotors were synthesized using a template-assisted electrochemical deposition method. Before electrochemical deposition, a 75 nm gold film was sputtered on one side of a 400-nm-poresize polycarbonate (Millipore, HTTP02500) membrane to serve as a working electrode using the Denton Discovery 18 (Moorestown, NJ). A Pt wire and an Ag/AgCl (with 1 M KCl) were used as counter and reference electrodes, respectively. The sputtered membrane was then assembled in a plating cell with an aluminum foil serving as a contact. All electrochemical deposition steps were carried out at room temperature (22 °C). Pd/Cu nanorods were deposited at

−0.1 V from the $PdCl_2/CuCl_2$ plating solution mixture containing 20 mM $CuCl_2$, 30 mM $PdCl_2$, and 0.1 M HCl with a total charge of 3C. After electrochemical deposition, the sputtered gold layer was completely removed by hand polishing with 3–4 μm alumina slurry. The templates were dissolved in methylene chloride for 10 min to completely release the nanostructures. The latter were collected by centrifugation at 9000 rpm for 3 min and washed 3 times with methylene chloride, ethanol and deionized water each, with a 3 min centrifugation after each wash. Then the Cu (of the Pd/Cu nanorods) was dissolved using an 8 M HNO_3 solution for 10 min, resulting in the formation of Pd nanohelices with 400 nm diameter and 3-5 μm length. The Pd nanostructures were then dispersed on glass slides, and coated with a 5 nm-thick Ni layer by electron beam evaporation (using a deposition speed of 0.05 nm s^{-1}), and sputtered with a 5 nm-Au layer. Afterwards, the resulting magnetic nanomotors were incubated overnight with 3-mercaptopropionic acid (MPA, Sigma Aldrich). Then, the MPA-modified helical nanomotors were incubated with platelet membrane-derived vesicles (diameter 50–100 nm) under ultrasonication for 20 min.

Scanning electron microscopy (SEM) images of bare helical nanomotors and PL-motors were obtained with a Phillips XL30 ESEM instrument, using an acceleration voltage of 10 kV. To further confirm the presence and cloaking of platelets onto the surface of the motor, Platelet vesicles were labeled with 1,2-dimyristoyl-sn-glycero-3-phosphoethanolamine-N-lissamine rhodamine B sulfonyl (DMPE-RhB, Sigma Aldrich), and then incubated with the helical nanomotors. Fluorescence microscopy images were captured using EVOS FL microscope coupled with a 20× and 40× microscope objectives and fluorescence filter with red light excitation. The fluorescence quenching assay to determine the platelet membrane coverage of the PL-motors was performed by combining the PL-motors with a thiolated fluorescent ligand from a synthesized fluorescein isothiocyanate (FITC)–thiol conjugate probe, and measuring the fluorescence spectra of the FITC-thiol, FITC-thiol and PL-motor mixture, and FITC-thiol and bare motor mixture, at 520 nm by a Tecan Infinite M200 microplate reader. The thiolated fluorescent probe was prepared by first conjugating FITC to cysteamine 4-methoxytrityl resin (EMD Millipore) through N - hydroxysuccinimide (NHS, Thermo Scientific)-mediated amine coupling, followed by trifluoroacetic acid (TFA) treatment to cleave the conjugate from the resin. To determine the protein content of the PL-motors, 10 mg/mL of both bare motors and PL-motors were centrifuged and resuspended with 1X PBS for 3 times, and a bicinchoninic acid (BCA) colorimetric assay (Sigma Aldrich) was used to determine the protein content. Briefly, the purple-colored reaction product of this assay is formed by the chelation of two molecules of BCA with one cuprous ion, and this water-soluble complex exhibits a strong absorbance at 562 nm that is nearly linear with increasing protein concentrations. Gel electrophoresis followed by protein staining with Coomassie Blue was also performed. The PL-vesicle and PL-motor samples containing equivalent total proteins were prepared in lithium dodecyl sulfate (LDS) sample loading buffer (Invitrogen). The samples were then separated on a 4–12% Bis-Tris 17-well minigel in MOPS running buffer using a Novex Xcell SureLock Electrophoresis System (Life Technologies). Finally, the protein columns were stained according to manufacturer's protocol.

Propulsion of PL-motor

A Helmholtz coil pair was used to generate the magnetic rotation field for remote actuation. The frequency of the rotating magnetic field (15 mT) can be changed from 1 Hz to 1000 Hz by a sinusoidal wave generator. The above magnetic nanohelices were dispersed in water droplets for rotation and translation motion tests. An inverted optical microscope (Nikon Instrument Inc. Ti-S/L100), coupled 20× and 40× objectives, a Hamamatsu digital camera C11440 and NIS Elements AR 3.2 software, were used for capturing movies of the swimming motion. The speed of the nanoswimmers was tracked using a NIS Elements tracking module (n=20).

Shiga toxin binding and detoxification

For the characterization of the adhesion of PL-motors with Shiga toxin (Stx), Stx (Toxin Technology, INC, lot#62411V1) was labeled with fluorescein dye (FITC) following the specifications of a commercial FITC Labeling kit (MarkerGene™, M0955). To evaluate the adhesion of Stx-FITC to the PL-motors, 1 mg of the PL-motors were immersed in the FITC-labeled Stx solution or in FITC dye solution (used as negative control) during 20-min under magnetic actuation (55 Hz, 15 mT). To calculate the amount of adsorbed toxin, the fluorescence intensity corresponding to the Stx-FITC or FITC solutions was measured (at 495 nm), before and after the PL-motors binding process. After the 20-min magnetic actuation, fluorescence microscopy images of the Stx-FITC@PL-motors and FITC dye solutions were taken, using EVOS FL microscope coupled with a 20× and 40× microscope objectives and a fluorescence filter with green light excitation. Furthermore, cellular toxicity was studied using a Vero cell assay. To perform this experiment, fixed amounts of Stx (0.01 mg/mL or 150 µL, 100 µg/mL as in caption) dissolved in PBS buffer were mixed with equal amounts of PBS buffer containing 1 mg PL-motors, 1 mg bare motors (without platelet coating), or 0.07 mg PL-vesicles (containing equivalent proteins to 1 mg PL-motors). The positive and negative control consisted on PBS buffer with and without Stx, respectively. All the samples were treated for 20 min under magnetic field (55 Hz, 15 mT), and, after this time, each formulation was added to Vero cell cultured wells (1.2×10^5 cells per well, n=3 for each formulation) and incubated for 48 h. After the 48 h incubation, the cell-viability was assessed using the CellTiter 96® Cell Proliferation Assay (Promega Corporation), based on a MTS tetrazolium compound. In brief, 10 µL of the MTS reagent were added into each well, mixed gently, and incubated at 37 °C for 4 h in a humidified CO_2 incubator. This was followed by reading the absorbance of the 96 well-plate at 490 nm using a plate reader. The quantity of formazan product as measured by Abs at 490 nm was directly proportional to the number of living cells. Microscopy images of Vero cells after the corresponding 48-h incubations were captured using a EVOS FL microscope coupled with a 20× and 40× microscope objectives.

Staphylococcus aureus (MRSA252) bacteria adherence and isolation

MRSA252 obtained from the American Type Culture Collection was cultured on tryptic soy broth (TSB) agar (Becton, Dickinson and Company) overnight at 37 ^{o}C. A single colony was inoculated in TSB medium at 37 ^{o}C in a rotary shaker. Overnight culture was refreshed in TSB medium at a 1:100 dilution at 37 ^{o}C under shaking for another 3 h until the OD600 of the culture medium reached approximately 1.0 (logarithmic growth phase). The bacteria were washed and suspended in sterile PBS to a concentration of 1×10^{8} CFU ml^{-1}. For the nanomotor adhesion study, aliquots of 0.8 ml of 1×10^{8} CFU ml^{-1} MRSA252 were mixed with 1 ml of 100 mg ml^{-1} PL-motor, 1 ml of 100 mg ml^{-1} bare motors, 1 ml of 7.5 mg ml^{-1} PL-vesicle, or 1 ml of PBS for 20 min magnetic actuation at room temperature. The suspensions were then left 30 min at room temperature to have the precipitate settle down with a magnet placed below the suspension. After removal of the supernatant, the collected pellets were resuspened in PBS buffer and then fixed with formalin and stained with DAPI subsequently for fluorescence analysis, fluorescence microscopy imaging, and SEM imaging.

2.3.3 Preparation and characterization of PL-motors

To obtain the nanostructures with desired geometric configuration and material components, we combine template-assisted electrodeposition and cell membrane cloaking techniques to synthesize the platelet-cloaked magnetically-actuated helical nanomotors (Fig. 2.14B). First of all, Pd nanohelices, with a diameter of 400 nm and length of 3-5 μm, were synthesized by a template-assisted electrochemical deposition method, followed by segment-selective chemical etching [96,97]. The Pd nanohelices were then coated with a 5 nm-thick nickel layer and a 5 nm-gold layer by electron beam evaporation and sputter, respectively. The resulting bare magnetic nanomotors undergo an *ex situ* stabilization by an overnight incubation with 3-Mercaptopropionic acid (MPA) to introduce negative charges onto the gold surface, thus allowing the platelet membranes to bond to the gold surface of the nanomotor. The negatively charged nanomotors were subsequently incubated with platelet membrane-derived vesicles (diameter 50–100 nm) under ultrasonication. The small nanoscale platelet vesicles, with high surface energy, tend to bind onto the negatively-charged gold surface to minimize the free energy of the system. The ultrasonic mixing further enhanced the adsorption of platelet vesicles onto the gold surface of the nanomotors. This fusion process allowed for the retention of the bilayer structure of the platelet membrane and for the preservation of its protein function. In addition, due to the large asymmetric negative charge between the ectoplasmic and cytoplasmic surfaces of the platelet membranes, the outer surface of the platelet membrane is much more negatively charged than the inner surface. Therefore, electrostatic repulsion allowed the platelet vesicles to fuse onto the negatively charged motors in the right-side-out orientation of the membranes, which was similar to what has been observed using platelet membrane-coated polymeric nanoparticle system [95].

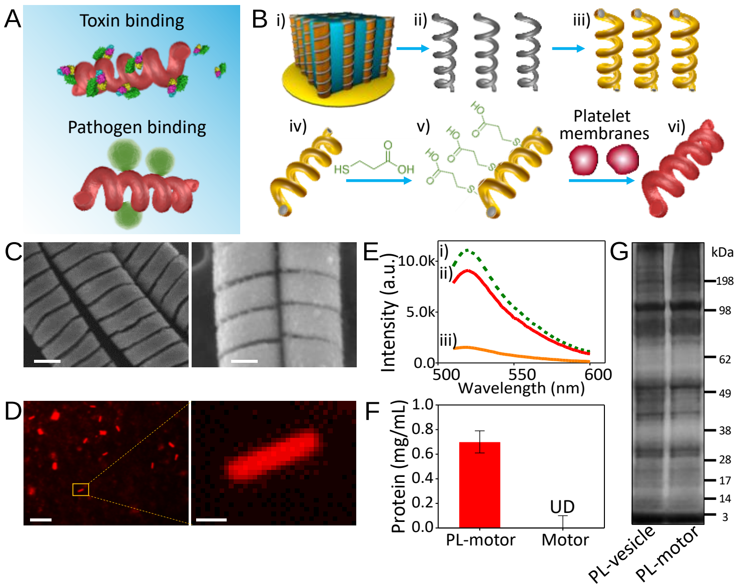

Figure 2.14 Preparation and characterization of platelet-cloaked magnetic helical nanomotors (denoted as PL-motors). (A) Schematic of PL-motors for binding and isolation of toxin and pathogens. (B) Preparation of PL-motors: (i) Pd/Cu co-electrodeposition in a polycarbonate membrane with pore size of 400 nm; (ii) Dissolution of Cu using nitric acid and release of the helical Pd nanostructures; (iii) Deposition of Ni/Au bilayer on the Pd helical nanostructure. (iv) Collection of the helical nanowires. (v) Modification of the bare helical nanomotor surface with 3-Mercaptopropionic acid (MPA). (vi) Fusion of platelet vesicles to the MPA-modified surface of the helical nanomotor. (C) Schematic representation of a nanomotor before and after coating with platelet membranes, with corresponding SEM image of the fabricated bare nanomotors without platelet coating (left) and PL-motors (right). Scale bars, 100 nm. (D) Fluorescent images of PL-motors covered with Rhodamine-labeled platelets. Scale bars, 20 µm and 1 µm. (E) Fluorescence quenching assay to determine the platelet membrane coverage of the PL-motors. Fluorescence spectra of i) FITC-thiol only, ii) FITC-thiol and PL-motor mixture, and iii) FITC-thiol and bare motor mixture. (F) The measured weight of protein content on bare motors and PL-motors (both 10 mg/mL) stored in 1XPBS at 4 °C for 24 h. Error bars represent the standard deviation from three different measurements. (G) SDS-PAGE analysis of proteins present on the platelet vesicles and the PL-motors. The samples were run at equal protein content and stained with Coomassie Blue.

Fig. 2.14C shows the scanning electron microscope (SEM) images of bare helical nanomotors and PL-motors. The characteristic shape of the PL-motor, with its periodic helical structure, is not affected by the platelet coating, which is expected from the negligible thickness of the lipid bilayer on 400 nm diameter gold nanomotors. To further confirm the presence and cloaking of platelets onto the surface of the motor, platelet vesicles were labeled with 1,2-dimyristoyl-sn-glycero-3-phosphoethanolamine-N-lissamine rhodamine B sulfonyl (DMPE-RhB) prior to be coated on the nanomotors. Full coverage of the helical motors is illustrated in the florescence microscopy images in Fig. 2.14D, indicating the successful incorporation of DMPE-RhB-labeled platelet vesicles onto the PL-motors. Further evaluation of the coverage of the helical nanomotors by the platelet membranes was conducted by studying the interactions between the PL-motors with a thiolated fluorescent ligand from a synthesized fluorescein isothiocyanate (FITC)–thiol conjugate probe [98]. As shown in Fig. 2.14E, at the emission peak of 520 nm of the FITC-thiol, the bare motors incubated with the fluorescence probe exhibited a greatly reduced fluorescence intensity in comparison with free FITC-thiol, indicating the presence of fluorescence quenching resulted from the bare gold surface. Such a noticeable quenching effect is absent in the FITC–thiol incubated with the PL-motors. The results clearly indicate high coverage of platelet membranes on the surface of the nanomotors due to the high shielding of the gold-thiol interactions between the nanomotors and the FITC–thiol dye by the presence of the platelet membranes.

Next, the platelet membrane coating on the nanomotors was investigated in terms of protein content. PL-motors were centrifuged and resuspended with 1X phosphate buffer saline (PBS) for 3 times to remove uncoated vesicles and obtain purified PL-motors. A bicinchoninic acid (BCA) protein assay was used to quantitatively measure the membrane protein amount on the surface of nanomotors. PL-motors exhibited an increase in absorbance at 562 nm indicating the presence of protein content, whereas no detectable absorbance was observed from the bare nanomotor at the same motor concentration (10 mg/mL) suggesting no protein was found, shown in Fig. 2.14F. The protein content of PL-motors was determined as 0.72±0.10 mg/mL using protein standards. Analysis of the protein content on the PL-motors was further carried out to confirm the successful functionalization of nanomotors with the platelet membrane antigens. Gel electrophoresis followed by protein staining showed the protein profile of the purified platelet vesicles and PL-motors (Fig. 2.14G).

The protein profile of PL-motors matched closely to the platelet membrane vesicles which evidently demonstrated that platelet membranes can translocate to the nanomotors and that the preparation of PL-motors did not alter the profile of platelet membrane proteins.

2.3.4 Propulsion performance and anti-biofouling capacity of PL-motors

An important feature of the PL-motor is its ability to resist biofouling, thus ensuring lasting and efficient propulsion of the nanomotor in whole blood. After having evaluated the preparation and characteristics of PL-motors, it is important to test their propulsion performance and anti-fouling capacity in various complex biological environments. The 5-s tracking of PL-motor movement in Fig. 2.15A showcase their propulsion performance in water, plasma, serum, and whole blood, respectively. Although the viscosity of each environment affects the propulsion, the resulting movement remains effective for PL-motor operation in biological environments, including whole blood. Fig. 2.15B compares the propulsion performances of the PL-motors with bare nanomotors in different media. It is observed that though their speeds are almost equal in water, the speeds of PL-motors in plasma, serum, and whole blood are significantly faster than the speeds of the bare nanomotors in same solution. The layer of natural platelet membranes covering the nanomotors enables their biocompatible and stable operation in whole blood unaffected by biofouling effects. Thus, these biomimetic nanomotors are expected to resist biofouling and thus remain operational in biological environments over prolonged periods of time. The 10-s tracking trajectory, shown in Fig. 2.15C, illustrates the movement of a bare nanomotor in whole blood, which displays slow propulsion at a speed of ~6 μm/s. The propulsion is further hindered after incubation of the bare nanomotor for 1 h in whole blood. Apparently, the bare nanomotors undergo severe protein fouling that dramatically hinders their propulsion efficiency. In contrast, the PL-motor displays long-term efficient magnetic propulsion in whole blood. The 10-s tracking trajectories in Fig. 2.15D demonstrate the magnetic propulsion of PL-motors in whole blood at 0 and 60 min, respectively. These images illustrate no apparent diminution of the propulsion efficiency over the prolonged actuation in whole blood. The resistance to biofouling and propulsion behavior of the PL-motors were further evaluated by incubating them in undiluted whole blood for 48 h. The 10-s tracking trajectories in Fig. 2.15E illustrate the movement of the PL-motors before and after such 48 h incubation. It was observed that the PL-motors maintain efficient propulsion at similar speeds after such prolonged incubation, indicating that fouling effects are negligible. Apparently, the antifouling properties of the platelet membrane layer shield the nanomotor from fouling effects in untreated biological fluids.

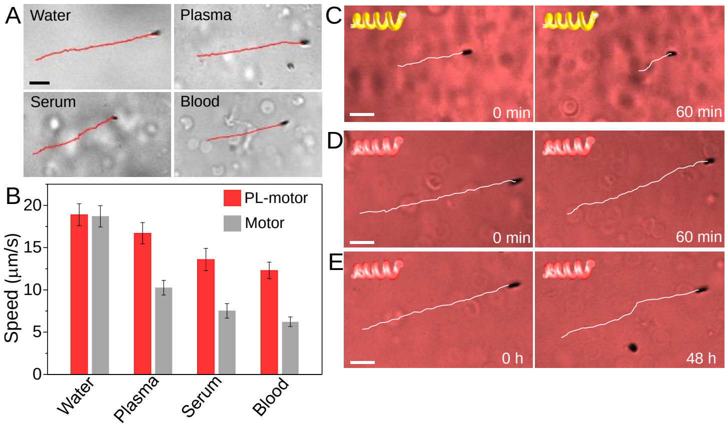

Figure 2.15 Propulsion performance and anti-biofouling capacity of PL-motors. (A) Tracking trajectories showing the propulsion of PL-motors in various medium over a timeframe of 5 s. (B) Speed comparison of PL-motors with bare helical nanomotors in various media. (C) 10-s tracking of the propulsion of a bare motor in whole blood at the beginning and after 60 min. (D) 10-s tracking showing the propulsion of a PL-motor in whole blood at the beginning and after 60 min. (E) 10-s tracking showing the propulsion of a PL-motor in whole blood without being incubated in the blood, and with a 48-h incubation. Scale bars, 10 µm. The nanomotors were propelled using a frequency of 55 Hz and a magnetic field strength of 15 mT. Speed data are averaged for 20 nanomotors under the same propulsion conditions.

2.3.5 Shiga toxin binding and detoxification

The therapeutic potential of PL-motors was firstly evaluated by assessing their selective binding and rapid isolation of Shiga toxin (Stx), a toxin produced by *Escherichia coli* that can induce haemolytic uraemic syndrome [99,100]. Shiga and Shiga-like toxins can bind platelets *via* specific glycosphingolipid receptors, while such binding further contributes to the thrombocytopenia, platelet activation, and microthrombus formation observed in hemolytic-uremic syndrome [101]. To characterize the adhesion of the Stx with the PL-motors, the Stx is labeled with fluorescein (FITC). 1 mg of the PL-motors was immersed in the FITC-labeled Stx PL-motors for a 20-min magnetic actuation. FITC dye for non-specific staining was used as a negative control. The amount of Stx absorbed on the PL-motors was calculated by measuring the Stx-FITC solution florescence intensity before and after the PL-motors binding process. As displayed in Fig. 2.16A, a 60% of fluorescence intensity decrease in the Stx-FITC conjugate solution is measured, compared to only 15% of decrease in the FITC dye with same amount of PL-motors. Fig. 2.16B displays the fluorescence microscopy images of the PL-motors after loading and 20-min propulsion in the Stx-FITC and FITC solution, respectively. A much stronger fluorescence binding is observed for the PL-motors in the Stx-FITC solution. Such results confirm the effective and selective binding of the PL-motors to the Shiga toxin.

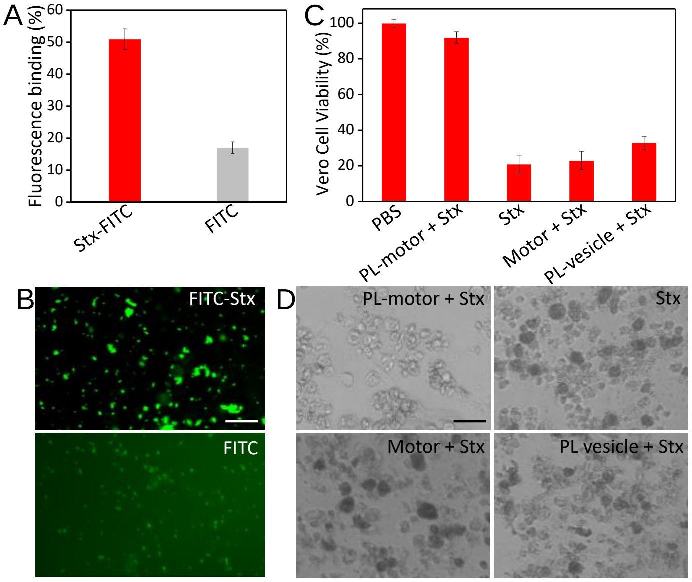

Figure 2.16 Shiga toxin binding and detoxification study. (A) Fluorescence binding percentage (measured at 495 nm) of the FITC-Stx conjugate and FITC dye only with PL-motors (red and grey bars, respectively). (B) Fluorescence images of PL-motors after 20 min incubation in whole blood and propulsion in FITC-Stx and FITC dye solution only. (C) Vero cell viability (1.2×10^5 cells per well, n=3) over 48 h following an incubation with Stx (150 µL, 100 µg/mL), PL-motors + Stx, bare motor + Stx, and platelet vesicles + Stx. PBS without Stx was used as a control. 1 mg of PL-motors was used for the detoxification process along with 20 min of propulsion time. Vero cell viability was checked by using an MTT assay. (D) Microscopy images showing the morphologies of the corresponding Vero cells treated with different formulations. Each image is representative of five examined sections. Scale bars, 50 µm.

To further examine adsorption of Stx to the PL-motors and successful toxin reduction to harmless levels for cellular targets, cellular cytotoxicity was studied using a Vero cell assay, as Stx is cytotoxic in the Vero cell assay (VCA) from 10 pg/mL and above [102]. Experiments were performed by mixing fixed amounts of the toxin, with a concentration of 0.01 mg/mL dissolved in PBS buffer, with equal amounts of PBS buffer containing 1 mg PL-motors, 1 mg bare motors (without platelet coating), and 0.07 mg platelet vesicles (containing equivalent proteins to 1 mg PL-motors). PBS buffer with and without toxin were also added as positive and negative control, respectively. After 20 min of magnetic operation, all of the five formulations were added to Vero cell cultured wells for 48 h incubation. The cell-viability was accessed by a MTT protocol, as illustrated in Fig. 2.16C. The PL-motors treated formulation displayed a cell viability of 92%, which is comparable with the PBS buffer control without toxin. In contrast, the viability of bare nanomotors and static platelet vesicles was only 21% and 31%, respectively. Fig. 2.16D displays the microscopy images showing the morphology of the Vero cells after 48-h incubation with the four formulations. It is clearly observed that the Vero cells are healthy for the formulation treated by the PL-motors, while all other three formulations induce severe damage and lysing to the cells. By cloaking platelet vesicles on the magnetic nanomotors, the PL-motors can serve as moving decoys that attract toxins for cell protection by diverting the toxins away from the solution and rendering the environment non-toxic to cells. In addition, under magnetic actuation, the large-scale collective location of the PL-motors can dramatically accelerate the local interfacing of coated platelets with Stx, thus enhancing the absorption process in comparison to the static platelet vesicles.

2.3.6 Platelet-adhering pathogens binding and isolation

We further examined the therapeutic potential of PL-motors for binding and isolation of platelet-adhering pathogens. Opportunistic bacteria, including several strains of staphylococci and streptococci, are able to bind to platelets either directly through a bacterial surface protein or indirectly by a plasma bridging molecule that links bacterial and platelet surface receptors [103,104]. Such bacteria–platelet interactions further lead to immune evasion and bacteremia [93]. MRSA252, a strain of methicillin-resistant *Staphylococcus aureus* expressing a serine-rich adhesion which can bind to platelets (SraP) [105], was used as a model pathogen for PL-motor adhesion study. After 20 min of incubation and magnetic actuation of the PL-motors (1 mg) in MRSA252 suspension (1×10^8 CFU ml^{-1}), the PL-motors were re-collected through precipitation with a magnet. Bare motors and PL-vesicles were used as negative controls. The retained bacteria on the collected pellets were fixed with formalin and stained with DAPI subsequently. Fig. 2.17A displays the microscopy images, showing the binding of the DAPI-stained bacteria on a DPME-RhB-labeled PL-motor PL-motor. Bare motors and PL-vesicles showed negligible increase in DAPI signal compared to PBS control in Fig. 2.17B. On the other hand, PL-motors exhibit a 10-fold increase in DAPI fluorescence intensity compared to all other groups which manifest a significant adhesion of the bacteria to PL-motors . The SEM images in Fig. 2.17C also clearly shows the preferential binding of the bacteria to the PL-motors, while the microscopy image in Fig. 2.17D displays ‘on-the-fly’ isolation of bacteria by a PL-motor. The new nanorobot platform thus presents a unique approach for meeting the need for rapid, direct, and real time isolation of pathogens.

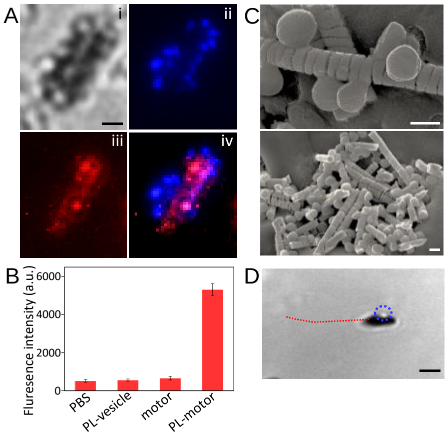

Figure 2.17 Binding and isolation of PL-motors to platelet-adhering pathogens. (A) Microscopic images showing the binding of MRSA 252 bacteria with PL-motor: (i) bright field, (ii) blue florescence channel showing the DAPI stained bacteria, (iii) red florescence channel showing the DMPE-RhB-labeled platelet membrane, and (iv) the overlay. (B) Normalized fluorescence intensity of DAPI stained MRSA252 bacteria retained on the PL-motors (n=3). Bare nanomotors, PL-vesicles, and PBS were used as controls. Scale bars, 500 nm. (C) SEM images of MRSA252 bacteria attached to PL-motors. Scale bars, 500 nm. (D) Microscopy image showing one-the-fly isolation of a bacteria (labeled with blue circle) with a PL-motor. Scale bar, 2 μm.

2.3.7 Conclusions

In summary, we have developed PL-motors, based on magnetically actuated helical nanomotors biointerfaced with a platelet membrane coating, as a new type of biomimetic nanorobot possessing efficient locomotion and biological functions. The intrinsic antifouling properties of the platelet membrane coating shields the nanomotor from common biofouling effects in biological fluids. A comparison study of the propulsion of PL-motors and the bare nanomotors in whole blood demonstrated their distinct anti-fouling properties of platelet membrane coating that lead to efficient propulsion in real complex biological environment. The platelet membranes coated on the PL-motors impart also strong affinity to platelet-adhering toxin and pathogen, along with their efficient movement leading to efficient detoxification capacity, as illustrated by the rapid binding and isolation of Shiga toxin and MRSA252 bacteria. This study validates that the biomembrane interfaces can significantly enhance the binding of nanorobots to pathogens, which may pave the way for using nanorobots for targeted antibiotics delivery to improve infectious disease treatment. Magnetic actuation of a large amount of PL-motors dramatically enhanced the binding and isolation process of these biothreats. Swarms of PL-motors could thus be used for target detoxification in particular locations due to the ease of magnetic navigation. The PL-motors represent a powerful biomimetic platform based on the fusion of biological materials and synthetic nanorobotics. Such bio-inspired engineered nanomachines are expected to offer efficient treatment of diseases in real physiological environments.

Chapter 2.1, in full, is a reprint of the material as it appears in Nanoscale, 2014, by Jinxing Li, Sirilak Sattayasamitsathit, Renfeng Dong, Wei Gao, Ryan Tam, Xiaomiao Feng, Stephen Ai, Joseph Wang; Chapter 2.2, in full, is a reprint of the material as it appears in Nano Letters, 2015, by Jinxing Li, Tianlong Li, Tailin Xu, Melek Kiristi, Wenjuan Liu, Zhiguang Wu, Joseph Wang. The dissertation author was the primary investigator and author of these papers.

2.4 References

(1) Wang, J. *Nanomachines : Fundamentals and Applications*.

(2) Mallouk, T. E.; Sen, A. Powering Nanorobots. *Sci. Am.* **2009**, *300*, 72–77.

(3) Ozin, G. A.; Manners, I.; Fournier-Bidoz, S.; Arsenault, A. Dream Nanomachines. *Adv. Mater.* **2005**, *17*, 3011–3018.

(4) Wang, J.; Gao, W. Nano/Microscale Motors: Biomedical Opportunities and Challenges. *ACS Nano* **2012**, *6*, 5745–5751.

(5) Mei, Y.; Solovev, A. A.; Sanchez, S.; Schmidt, O. G. Rolled-up Nanotech on Polymers: From Basic Perception to Self-Propelled Catalytic Microengines. *Chem. Soc. Rev.* **2011**, *40*, 2109.

(6) Nelson, B. J. B.; Kaliakatsos, I. K. I.; Abbott, J. J. Microrobots for Minimally Invasive Medicine. *Annu. Rev. Biomed. Eng.* **2010**, *12*, 55–85.

(7) Kline, T. R.; Paxton, W. F.; Mallouk, T. E.; Sen, A. Catalytic Nanomotors: Remote-Controlled Autonomous Movement of Striped Metallic Nanorods. *Angew. Chemie Int. Ed.* **2005**, *44*, 744–746.

(8) Gao, W.; Sattayasamitsathit, S.; Orozco, J.; Wang, J. Highly Efficient Catalytic Microengines: Template Electrosynthesis of Polyaniline/Platinum Microtubes. *J. Am. Chem. Soc.* **2011**, *133*, 11862–11864.

(9) Li, J.; Zhang, J.; Gao, W.; Huang, G.; Di, Z.; Liu, R.; Wang, J.; Mei, Y. Dry-Released Nanotubes and Nanoengines by Particle-Assisted Rolling. *Adv. Mater.* **2013**, *25*, 3715–3721.

(10) Loget, G.; Kuhn, A. Propulsion of Microobjects by Dynamic Bipolar Self-Regeneration. *J. Am. Chem. Soc.* **2010**, *132*, 15918–15919.

(11) Chang, S. T.; Paunov, V. N.; Petsev, D. N.; Velev, O. D. Remotely Powered Self-Propelling Particles and Micropumps Based on Miniature Diodes. *Nat. Mater.* **2007**, *6*, 235–240.

(12) Liu, M.; Zentgraf, T.; Liu, Y.; Bartal, G.; Zhang, X. Light-Driven Nanoscale Plasmonic Motors. **2010**, *5*, 570–573.

(13) Wang, W.; Castro, L. A.; Hoyos, M.; Mallouk, T. E. Autonomous Motion of Metallic Microrods Propelled by Ultrasound. *ACS Nano* **2012**, *6*, 6122–6132.

(14) Kagan, D.; Benchimol, M. J.; Claussen, J. C.; Chuluun-Erdene, E.; Esener, S.; Wang, J. Acoustic Droplet Vaporization and Propulsion of Perfluorocarbon-Loaded Microbullets for Targeted Tissue Penetration and Deformation. **2012**.

(15) Dreyfus, R.; Baudry, J.; Roper, M. L.; Fermigier, M.; Stone, H. A.; Bibette, J. Microscopic Artificial Swimmers. *Nature* **2005**, *437*, 862–865.

(16) Zhang, L.; Abbott, J. J.; Dong, L.; Kratochvil, B. E.; Bell, D.; Nelson, B. J. Artificial

Bacterial Flagella: Fabrication and Magnetic Control. *Appl. Phys. Lett.* **2009**, *94*, 64107.

(17) Gao, W.; Sattayasamitsathit, S.; Manesh, K. M.; Weihs, D.; Wang, J. Magnetically Powered Flexible Metal Nanowire Motors. *J. Am. Chem. Soc.* **2010**, *132*, 14403–14405.

(18) Fischer, P.; Ghosh, A. Magnetically Actuated Propulsion at Low Reynolds Numbers: Towards Nanoscale Control. *Nanoscale* **2011**, *3*, 557–563.

(19) Peyer, K. E.; Tottori, S.; Qiu, F.; Zhang, L.; Nelson, B. J. Magnetic Helical Micromachines. *Chem. - A Eur. J.* **2013**, *19*, 28–38.

(20) BERG, H. C.; ANDERSON, R. A. Bacteria Swim by Rotating Their Flagellar Filaments. *Nature* **1973**, *245*, 380–382.

(21) Ghosh, A.; Fischer, P. Controlled Propulsion of Artificial Magnetic Nanostructured Propellers. *Nano Lett.* **2009**, *9*, 2243–2245.

(22) Tottori, S.; Zhang, L.; Qiu, F.; Krawczyk, K. K.; Franco-Obregón, A.; Nelson, B. J. Magnetic Helical Micromachines: Fabrication, Controlled Swimming, and Cargo Transport. *Adv. Mater.* **2012**, *24*, 811–816.

(23) Kim, S.; Qiu, F.; Kim, S.; Ghanbari, A.; Moon, C.; Zhang, L.; Nelson, B. J.; Choi, H. Fabrication and Characterization of Magnetic Microrobots for Three-Dimensional Cell Culture and Targeted Transportation. *Adv. Mater.* **2013**, *25*, 5863–5868.

(24) Liu, Y.; Goebl, J.; Yin, Y. Templated Synthesis of Nanostructured Materials. *Chem. Soc. Rev.* **2013**, *42*, 2610–2653.

(25) Wang, J. Template Electrodeposition of Catalytic Nanomotors. *Faraday Discuss.* **2013**, *164*, 9.

(26) Huang, G.; Wang, J.; Mei, Y. Material Considerations and Locomotive Capability in Catalytic Tubular Microengines. *J. Mater. Chem.* **2012**, *22*, 6519.

(27) Zhao, G.; Pumera, M. Concentric Bimetallic Microjets by Electrodeposition. *RSC Adv.* **2013**, *3*, 3963.

(28) Wu, Y.; Cheng, G.; Katsov, K.; Sides, S. W.; Wang, J.; Tang, J.; Fredrickson, G. H.; Moskovits, M.; Stucky, G. D. Composite Mesostructures by Nano-Confinement. *Nat. Mater.* **2004**, *3*, 816–822.

(29) Liu, L.; Yoo, S.-H.; Lee, S. A.; Park, S. Wet-Chemical Synthesis of Palladium Nanosprings. *Nano Lett.* **2011**, *11*, 3979–3982.

(30) Lauga, E.; Powers, T. R. The Hydrodynamics of Swimming Microorganisms. *Reports Prog. Phys.* **2009**, *72*, 96601.

(31) Purcell, E. M. E. Life at Low Reynolds Number. *Am. J. Phys.* **1977**, *45*, 3–11.

(32) Schliwa, M.; Woehlke, G. Molecular Motors. *Nature* **2003**, *422*, 759–765.

(33) Guix, M.; Mayorga-Martinez, C. C.; Merkoçi, A. Nano/Micromotors in (Bio)chemical Science Applications. *Chem. Rev.* **2014**, *114*, 6285–6322.

(34) Moo, J. G. S.; Pumera, M. Chemical Energy Powered Nano/Micro/Macromotors and the Environment. *Chem. - A Eur. J.* **2015**, *21*, 58–72.

(35) Paxton, W. F.; Kistler, K. C.; Olmeda, C. C.; Sen, A.; St. Angelo, S. K.; Cao, Y.; Mallouk, T. E.; Lammert, P. E.; Crespi, V. H. Catalytic Nanomotors: Autonomous Movement of Striped Nanorods. *J. Am. Chem. Soc.* **2004**, *126*, 13424–13431.

(36) Solovev, A. A.; Mei, Y.; Bermúdez Ureña, E.; Huang, G.; Schmidt, O. G. Catalytic Microtubular Jet Engines Self-Propelled by Accumulated Gas Bubbles. *Small* **2009**, *5*, 1688–1692.

(37) Wilson, D. A.; Nolte, R. J. M.; van Hest, J. C. M. Autonomous Movement of Platinum-Loaded Stomatocytes. *Nat. Chem.* **2012**, *4*, 268–274.

(38) Li, J.; Gao, W.; Dong, R.; Pei, A.; Sattayasamitsathit, S.; Wang, J. Nanomotor Lithography. *Nat. Commun.* **2014**, *5*, 5026.

(39) Lee, T.-C.; Alarcón-Correa, M.; Miksch, C.; Hahn, K.; Gibbs, J. G.; Fischer, P. Self-Propelling Nanomotors in the Presence of Strong Brownian Forces. *Nano Lett.* **2014**, *14*, 2407–2412.

(40) Solovev, A. A. A.; Xi, W.; Gracias, D. D. H.; Harazim, S. S. M.; Deneke, C.; Sanchez, S.; Schmidt, O. G. Self-Propelled Nanotools. *ACS Nano* **2012**, *6*, 1751–1756.

(41) Wu, Z.; Wu, Y.; He, W.; Lin, X.; Sun, J.; He, Q. Self-Propelled Polymer-Based Multilayer Nanorockets for Transportation and Drug Release. *Angew. Chemie Int. Ed.* **2013**, *52*, 7000–7003.

(42) Palacci, J.; Sacanna, S.; Steinberg, A. P.; Pine, D. J.; Chaikin, P. M. Living Crystals of Light-Activated Colloidal Surfers. *Science (80-.).* **2013**, *339*, 936–940.

(43) Wang, W.; Duan, W.; Ahmed, S.; Mallouk, T. E.; Sen, A. Small Power: Autonomous Nano- and Micromotors Propelled by Self-Generated Gradients. *Nano Today* **2013**, *8*, 531–554.

(44) Xu, T.; Soto, F.; Gao, W.; Garcia-Gradilla, V.; Li, J.; Zhang, X.; Wang, J. Ultrasound-Modulated Bubble Propulsion of Chemically Powered Microengines. *J. Am. Chem. Soc.* **2014**, *136*, 8552–8555.

(45) Garcia-Gradilla, V.; Orozco, J.; Sattayasamitsathit, S.; Soto, F.; Kuralay, F.; Pourazary, A.; Katzenberg, A.; Gao, W.; Shen, Y.; Wang, J. Functionalized Ultrasound-Propelled Magnetically Guided Nanomotors: Toward Practical Biomedical Applications. *ACS Nano* **2013**, *7*, 9232–9240.

(46) Schamel, D.; Mark, A. G.; Gibbs, J. G.; Miksch, C.; Morozov, K. I.; Leshansky, A. M.; Fischer, P. Nanopropellers and Their Actuation in Complex Viscoelastic Media. *ACS Nano* **2014**, *8*, 8794–8801.

(47) Qiu, T.; Lee, T.-C.; Mark, A. G.; Morozov, K. I.; Münster, R.; Mierka, O.; Turek, S.; Leshansky, A. M.; Fischer, P. Swimming by Reciprocal Motion at Low Reynolds Number. *Nat. Commun.* **2014**, *5*, 5119.

(48) Venugopalan, P. L.; Sai, R.; Chandorkar, Y.; Basu, B.; Shivashankar, S.; Ghosh, A. Conformal Cytocompatible Ferrite Coatings Facilitate the Realization of a Nanovoyager in Human Blood. *Nano Lett.* **2014**, *14*, 1968–1975.

(49) Wu, Z.; Li, T.; Li, J.; Gao, W.; Xu, T.; Christianson, C.; Gao, W.; Galarnyk, M.; He, Q.; Zhang, L. Turning Erythrocytes into Functional Micromotors. *ACS Nano* **2014**, *8*, 12041–12048.

(50) Loget, G.; Kuhn, A. Electric Field-Induced Chemical Locomotion of Conducting Objects. *Nat. Commun.* **2011**, *2*, 535.

(51) Wu, Z.; Lin, X.; Wu, Y.; Si, T.; Sun, J.; He, Q. Near-Infrared Light-Triggered "On/Off" Motion of Polymer Multilayer Rockets. *ACS Nano* **2014**, *8*, 6097–6105.

(52) Gao, W.; Manesh, K. M.; Hua, J.; Sattayasamitsathit, S.; Wang, J. Hybrid Nanomotor: A Catalytically/Magnetically Powered Adaptive Nanowire Swimmer. *Small* **2011**, *7*, 2047–2051.

(53) Gao, W.; D'Agostino, M.; Garcia-Gradilla, V.; Orozco, J.; Wang, J. Multi-Fuel Driven Janus Micromotors. *Small* **2013**, *9*, 467–471.

(54) Wang, W.; Duan, W.; Zhang, Z.; Sun, M.; Sen, A.; Mallouk, T. E.; Schmidt, O. G.; Sattayasamitsathit, S.; Zhang, L.; Wang, J. A Tale of Two Forces: Simultaneous Chemical and Acoustic Propulsion of Bimetallic Micromotors. *Chem. Commun.* **2015**, *51*, 1020–1023.

(55) Mitragotri, S. Healing Sound: The Use of Ultrasound in Drug Delivery and Other Therapeutic Applications. *Nat. Rev. Drug Discov.* **2005**, *4*, 255–260.

(56) Veiseh, O.; Gunn, J. W.; Zhang, M. Design and Fabrication of Magnetic Nanoparticles for Targeted Drug Delivery and Imaging. *Adv. Drug Deliv. Rev.* **2010**, *62*, 284–304.

(57) Nadal, F.; Lauga, E. Asymmetric Steady Streaming as a Mechanism for Acoustic Propulsion of Rigid Bodies. *Phys. Fluids* **2014**, *26*, 82001.

(58) Wang, J.; Manesh, K. M. Motion Control at the Nanoscale. *Small* **2010**, *6*, 338–345.

(59) Vicsek, T.; Zafeiris, A. Collective Motion. *Phys. Rep.* **2012**, *517*, 71–140.

(60) Laurell, T.; Petersson, F.; Nilsson, A. Chip Integrated Strategies for Acoustic Separation and Manipulation of Cells and Particles. *Chem. Soc. Rev.* **2007**, *36*, 492–506.

(61) Xu, T.; Soto, F.; Gao, W.; Dong, R.; Garcia-Gradilla, V.; Magaña, E.; Zhang, X.; Wang, J. Reversible Swarming and Separation of Self-Propelled Chemically Powered Nanomotors under Acoustic Fields. *J. Am. Chem. Soc.* **2015**, *137*, 2163–2166.

(62) Tottori, S.; Zhang, L.; Peyer, K. E.; Nelson, B. J. Assembly, Disassembly, and Anomalous Propulsion of Microscopic Helices. *Nano Lett.* **2013**, *13*, 4263–4268.

(63) Ibele, M.; Mallouk, T. E.; Sen, A. Schooling Behavior of Light-Powered Autonomous Micromotors in Water. *Angew. Chemie Int. Ed.* **2009**, *48*, 3308–3312.

(64) Kagan, D.; Balasubramanian, S.; Wang, J. Chemically Triggered Swarming of Gold

Microparticles. *Angew. Chemie Int. Ed.* **2011**, *50*, 503–506.

(65) Peng, F.; Tu, Y.; van Hest, J. C. M.; Wilson, D. A. Self-Guided Supramolecular Cargo-Loaded Nanomotors with Chemotactic Behavior towards Cells. *Angew. Chemie Int. Ed.* **2015**, *54*, 11662–11665.

(66) Ding, X.; Lin, S.-C. S.; Kiraly, B.; Yue, H.; Li, S.; Chiang, I.-K.; Shi, J.; Benkovic, S. J.; Huang, T. J. On-Chip Manipulation of Single Microparticles, Cells, and Organisms Using Surface Acoustic Waves. *Proc. Natl. Acad. Sci. U. S. A.* **2012**, *109*, 11105–11109.

(67) Chen, Y.; Ding, X.; Steven Lin, S.-C.; Yang, S.; Huang, P.-H.; Nama, N.; Zhao, Y.; Nawaz, A. A.; Guo, F.; Wang, W. Tunable Nanowire Patterning Using Standing Surface Acoustic Waves. *ACS Nano* **2013**, *7*, 3306–3314.

(68) Grossman, D.; Aranson, I. S.; Ben Jacob, E. Emergence of Agent Swarm Migration and Vortex Formation through Inelastic Collisions. *New J. Phys.* **2008**, *10*, 23036.

(69) Ingham, C. J.; Jacob, E. Swarming and Complex Pattern Formation in Paenibacillus Vortex Studied by Imaging and Tracking Cells. *BMC Microbiol.* **2008**, *8*, 36.

(70) Sánchez, S.; Soler, L.; Katuri, J. Chemically Powered Micro- and Nanomotors. *Angew. Chemie Int. Ed.* **2015**, *54*, 1414–1444.

(71) Kim, K.; Guo, J.; Xu, X.; Fan, D. L. Recent Progress on Man-Made Inorganic Nanomachines. *Small* **2015**, *11*, 4037–4057.

(72) Wang, H.; Pumera, M. Fabrication of Micro/Nanoscale Motors. *Chem. Rev.* **2015**, *115*, 8704–8735.

(73) Wu, Z.; Lin, X.; Si, T.; He, Q. Recent Progress on Bioinspired Self-Propelled Micro/Nanomotors via Controlled Molecular Self-Assembly. *Small* **2016**, *12*, 3080–3093.

(74) Abdelmohsen, L. K. E. A.; Peng, F.; Tu, Y.; Wilson, D. A. Micro- and Nano-Motors for Biomedical Applications. *J. Mater. Chem. B* **2014**, *2*, 2395–2408.

(75) Fan, D.; Yin, Z.; Cheong, R.; Zhu, F. F. Q.; Cammarata, R. C.; Chien, C. L.; Levchenko, A. Subcellular-Resolution Delivery of a Cytokine through Precisely Manipulated Nanowires. **2010**, *5*, 545–551.

(76) Palagi, S.; Mark, A. G.; Reigh, S. Y.; Melde, K.; Qiu, T.; Zeng, H.; Parmeggiani, C.; Martella, D.; Sanchez-Castillo, A.; Kapernaum, N. Structured Light Enables Biomimetic Swimming and Versatile Locomotion of Photoresponsive Soft Microrobots. *Nat. Mater.* **2016**, *15*, 647–653.

(77) Li, J.; Rozen, I.; Wang, J. Rocket Science at the Nanoscale. *ACS Nano* **2016**, *10*, 5619–5634.

(78) Peyer, K. E.; Zhang, L.; Nelson, B. J. Bio-Inspired Magnetic Swimming Microrobots for Biomedical Applications. *Nanoscale* **2013**, *5*, 1259–1272.

(79) Felfoul, O.; Mohammadi, M.; Taherkhani, S.; de Lanauze, D.; Zhong Xu, Y.; Loghin, D.; Essa, S.; Jancik, S.; Houle, D.; Lafleur, M. Magneto-Aerotactic Bacteria Deliver Drug-

Containing Nanoliposomes to Tumour Hypoxic Regions. *Nat. Nanotechnol.* **2016**, *11*, 941–947.

(80) Soler, L.; Sánchez, S. Catalytic Nanomotors for Environmental Monitoring and Water Remediation. *Nanoscale* **2014**, *6*, 7175.

(81) Singh, V. V.; Wang, J.; Leong, Y. J.; Rozen, I.; Qu, X.; Dong, R.; Wu, Z.; Gao, W.; Chung, P. H.; Wang, J. Nano/micromotors for Security/defense Applications. A Review. *Nanoscale* **2015**, *7*, 19377–19389.

(82) Li, J.; Liu, W.; Li, T.; Rozen, I.; Zhao, J.; Bahari, B.; Kante, B.; Wang, J. Swimming Microrobot Optical Nanoscopy. *Nano Lett.* **2016**, *16*, 6604–6609.

(83) Li, J.; Esteban-Fernández de Ávila, B.; Gao, W.; Zhang, L.; Wang, J. Micro/nanorobots for Biomedicine: Delivery, Surgery, Sensing, and Detoxification. *Sci. Robot.* **2017**, *2*, eaam6431.

(84) Wang, J. Can Man-Made Nanomachines Compete with Nature Biomotors? *ACS Nano* **2009**, *3*, 4–9.

(85) García, M.; Orozco, J.; Guix, M.; Gao, W.; Sattayasamitsathit, S.; Escarpa, A.; Merkoçi, A.; Wang, J. Micromotor-Based Lab-on-Chip Immunoassays. *Nanoscale* **2013**, *5*, 1325–1331.

(86) Yoo, J.-W.; Irvine, D. J.; Discher, D. E.; Mitragotri, S. Bio-Inspired, Bioengineered and Biomimetic Drug Delivery Carriers. *Nat. Rev. Drug Discov.* **2011**, *10*, 521–535.

(87) Hu, C.-M. J. C.; Fang, R. H. R.; Copp, J.; Luk, B. B. T.; Zhang, L. A Biomimetic Nanosponge That Absorbs Pore-Forming Toxins. **2013**, *8*, 336–340.

(88) Olsson, M.; Bruhns, P.; Frazier, W. A.; Ravetch, J. V; Oldenborg, P.-A. Platelet Homeostasis Is Regulated by Platelet Expression of CD47 under Normal Conditions and in Passive Immune Thrombocytopenia. *Blood* **2005**, *105*, 3577–3582.

(89) Sims, P. J.; Rollins, S. A.; Wiedmer, T. Regulatory Control of Complement on Blood Platelets. Modulation of Platelet Procoagulant Responses by a Membrane Inhibitor of the C5b-9 Complex. *J. Biol. Chem.* **1989**, *264*, 19228–19235.

(90) Nieswandt, B.; Watson, S. P. Platelet-Collagen Interaction: Is GPVI the Central Receptor? *Blood* **2003**, *102*, 449–461.

(91) Kieffer, N.; Phillips, D. R. Platelet Membrane Glycoproteins: Functions in Cellular Interactions. *Annu. Rev. Cell Biol.* **1990**, *6*, 329–357.

(92) Yeaman, M. R. Platelets in Defense against Bacterial Pathogens. *Cell. Mol. Life Sci.* **2010**, *67*, 525–544.

(93) Fitzgerald, J. R.; Foster, T. J.; Cox, D. The Interaction of Bacterial Pathogens with Platelets. *Nat. Rev. Microbiol.* **2006**, *4*, 445–457.

(94) Walsh, P. N. Platelet Coagulant Activities and Hemostasis: A Hypothesis. *Blood* **1974**, *43*.

(95) Hu, C.-M. J.; Fang, R. H.; Wang, K.-C.; Luk, B. T.; Thamphiwatana, S.; Dehaini, D.;

Nguyen, P.; Angsantikul, P.; Wen, C. H.; Kroll, A. V. Nanoparticle Biointerfacing by Platelet Membrane Cloaking. *Nature* **2015**, *526*, 118–121.

(96) Li, J.; Li, T.; Xu, T.; Kiristi, M.; Liu, W.; Wu, Z.; Wang, J. Magneto–Acoustic Hybrid Nanomotor. *Nano Lett.* **2015**, *15*, 4814–4821.

(97) Li, J.; Sattayasamitsathit, S.; Dong, R.; Gao, W.; Tam, R.; Feng, X.; Ai, S.; Wang, J.; Stucky, G. D. Template Electrosynthesis of Tailored-Made Helical Nanoswimmers. *Nanoscale* **2014**, *6*, 9415–9420.

(98) Gao, W.; Hu, C.-M. J.; Fang, R. H.; Luk, B. T.; Su, J.; Zhang, L. Surface Functionalization of Gold Nanoparticles with Red Blood Cell Membranes. *Adv. Mater.* **2013**, *25*, 3549–3553.

(99) Tarr, P. I.; Gordon, C. A.; Chandler, W. L. Shiga-Toxin-Producing Escherichia Coli and Haemolytic Uraemic Syndrome. *Lancet* **2005**, *365*, 1073–1086.

(100) Paton, J. C.; Paton, A. W. Pathogenesis and Diagnosis of Shiga Toxin-Producing Escherichia Coli Infections. *Clin. Microbiol. Rev.* **1998**, *11*, 450–479.

(101) Cooling, L. L.; Walker, K. E.; Gille, T.; Koerner, T. A. Shiga Toxin Binds Human Platelets via Globotriaosylceramide (Pk Antigen) and a Novel Platelet Glycosphingolipid. *Infect. Immun.* **1998**, *66*, 4355–4366.

(102) Sekino, T.; Kiyokawa, N.; Taguchi, T.; Takenouchi, H.; Matsui, J.; Tang, W.-R.; Suzuki, T.; Nakajima, H.; Saito, M.; Ohmi, K. Characterization of a Shiga-Toxin 1-Resistant Stock of Vero Cells. *Microbiol. Immunol.* **2004**, *48*, 377–387.

(103) O'Brien, L.; Kerrigan, S. W.; Kaw, G.; Hogan, M.; Penadés, J.; Litt, D.; Fitzgerald, D. J.; Foster, T. J.; Cox, D. Multiple Mechanisms for the Activation of Human Platelet Aggregation by Staphylococcus Aureus: Roles for the Clumping Factors ClfA and ClfB, the Serine-Aspartate Repeat Protein SdrE and Protein A. *Mol. Microbiol.* **2002**, *44*, 1033–1044.

(104) Kerrigan, S. W.; Douglas, I.; Wray, A.; Heath, J.; Byrne, M. F.; Fitzgerald, D.; Cox, D. A Role for Glycoprotein Ib in Streptococcus Sanguis-Induced Platelet Aggregation. *Blood* **2002**, *100*, 509–516.

(105) Siboo, I. R.; Chambers, H. F.; Sullam, P. M. Role of SraP, a Serine-Rich Surface Protein of Staphylococcus Aureus, in Binding to Human Platelets. *Infect. Immun.* **2005**, *73*, 2273–2280.

Chapter 3 State of the Art:

Technical Applications of Micro/Nanorobots

3.1 Nanorobot to write: nanomotor lithography

3.1.1 Introduction

A variety of lithographic techniques are now available for direct processing of materials at the nanoscale [1–3]. While the resolution of these techniques has continued to improve, the cost of their implementation and system complexity have also increased substantially. For example, traditional photolithographic nanofabrication techniques rely on costly masks, while electron and focused ion beam writing require expensive beam sources and elaborate control systems [4,5]. Similarly, sophisticated equipment is required for lithographic techniques based on scanning probes and optical tweezers [6–9]. Alternate strategies, involving self-assembling nanostructures, have been explored to improve the versatility and lower the fabrication costs [10–13]. However, arbitrary direct writing cannot be performed by these methods due to the lack of mobility of these nano components.

Inspired by natural biological systems [14,15], the recent development of synthetic nanomotors has paved the way towards major advances in nanoscience [16–22]. These self-propelled nanoscale devices can convert various energies into autonomous movement and overcome miniaturization challenges governed by force-scaling laws. Like their natural counterparts, these versatile man-made nanomotors have demonstrated advanced capabilities, including precise speed regulation and spatial motion control, along with self-organization and collective movement, for a wide range of practical applications [23–27]. The advanced performance of such self-propelled nanomotor systems can address the challenges encountered with existing nanopatterning techniques and lead to powerful tools for direct surface writing at the nanoscale.

We report here a new versatile and cost-effective direct-write nano-patterning methodology, named “nanomotor lithography” (NML), using nanomotors that “swim” over photoresist surfaces for creating spatially-defined complex surface patterns. This approach is made possible by developing an “on-the-fly” strategy for manipulating the light incident on the moving nanomotors. Self-propelled metallic nanowire motors and Janus sphere motors with distinct optical properties are used here as the moving optical elements. Once light reaches the moving nanomotors, they can effectively perform near-field lithography: the opaque metallic nanowire motors allow for the nanoscale blocking of light while the transparent Janus sphere motors allow for efficient near-field concentration of light. Using such a versatile method, various nanoscale features are generated through modular nanomotor design. Due to the small dimension of the nanowire motors and the near-field focusing effect of the Janus sphere motors, sub-wavelength resolution can be achieved. The self-propelled motion along with magnetically guided control makes the new nanomotor approach simple, cost-effective, and obviates the requirements of elaborate control systems used in common surface patterning techniques. Spatially-defined nanofeatures are obtained by remote magnetic guidance of the nanomotors, while parallel writings are achieved through organized assembly and controlled motion of multiple nanomotors. This transformative combination preserves the high spatial resolution of near-field optical lithography while gaining the ability to control the patterns in a predefined and parallel fashion, creating a unified tool for constructing and studying nanomaterials and nanodevices.

3.1.2 Experimental methods

Synthesis of magnetic-guided catalytic nanomotors

The magnetic-guided catalytic nanomotors composed of Au, Ni, Au and Pt segments were prepared by electrodepositing the corresponding metals into 200 nm alumina membrane template (Catalog no. 6809-6022; Whatman, Maidstone, UK) and 400 nm and 1 μm polycarbonate (PC) membrane template (Catalog no. 800282 and 7060-2510; Whatman, New Jersey, USA). A thin silver film was first sputtered on the branched side of the alumina membrane or back side of PC membrane to serve as a working electrode. The membrane was assembled in a plating cell with aluminum foil serving as an electrical contact for the subsequent electrodeposition. For 200 nm alumina membrane template, a sacrificial silver layer was electrodeposited into the branched area of the membrane using a silver plating solution (1025 RTU@4.5 Troy/ Gallon; Technic Inc., Anaheim, CA) and a total charge of 3.0 C at -0.90 V (vs. Ag/AgCl, in connection to a Pt wire counter electrode). This was followed by an electrodeposition of gold for 0.75 C from a gold plating solution (Orotemp 24 RTU RACK; Technic Inc.) at −1.0 V. Subsequently, nickel was electrodeposited at −1.0 V from a nickel plating solution (20 g L^{-1} $NiCl_2{\cdot}6H_2O$, 515 g L^{-1} $Ni(H_2NSO_3)_2{\cdot}\ 4H_2O$, and 20 g L^{-1} H_3BO_3) using a total charge of 2.0 C. The second gold segment was then electrodeposited for 0.75 C, followed by the Pt segment employing galvanostatically deposited at −2 mA for 50 min using a platinum plating solution (Platinum RTP; Technic Inc.). For 400 nm and 1 μm PC membrane templates, a sacrificial silver layer was first electrodeposited for a total charge of 1.0 C at −0.9 V. Subsequently, gold layer was electroplated for a total charge of 0.25 C at −1.0 V, followed by nickel layer for 2 C at −1.0 V and 0.25 C of gold at -1.0 V. Finally, Pt segment was electroplated at −2 mA for 20 min. The sputtered and sacrificial silver layers were simultaneously removed by mechanical polishing using cotton tip applicators soaked with 35% HNO_3. The alumina membrane was removed in 3 M NaOH for 30 min. The resulting nanowires were collected by centrifugation at 7000 rpm for 5 min and washed repeatedly with DI water until a neutral pH was achieved. The PC membrane was removed in methylene chloride for 5 min to completely release the nanowires. The corresponding nanowires were collected by centrifugation at 6000 rpm for 1 min and washed repeatedly with methylene chloride, followed by ethanol (2 times) and ultrapure water (3 times).

Synthesis of Janus micromotors

The Janus micromotors were prepared using silica microspheres (1.21 µm, and 4.74 mean diameter, Bangs Laboratories, Fishers, IN, USA) and polystyrene microspheres (0.72 µm and 2.16 µm mean diameter, Bangs Laboratories, Fishers, IN, USA) as the base particles. 20 µL of microspheres solution was first dispersed into water and centrifuged. Then, the microspheres were redispersed in 200 µL water. The sample was then spread onto glass slides and dried uniformly to form microsphere monolayers. These spheres were closely packed in contact with each other due to the van der Waals forces. The microspheres were sputter coated with a 10 nm Pt layer using a Denton Discovery 18 sputtering system. The deposition was performed at room temperature with a DC power of 200 W and Ar pressure of 2.5 mT for 10 s. To ensure a uniform Janus half-shell coating, rotation was turned off and the sample slides were set up at an angle to be parallel to the Pt target. Subsequently, the Janus particles were detached from the substrate via sonication or pipette pumping and were dispersed in water again to form the micromotor solution. The singlet Janus motors were obtained by a long sonication time (>1 min), while doublet and triplet Janus motors were created using significantly shorter sonication periods (~5 seconds).

Lithography process

The photoresist (MicroPosit SC-1827) was spin-coated onto a silicon wafer at 3,000 rpm for 40 s. The wafer was prebaked for 1 min at 115 °C. A 20 µl drop of nanomotor solution was placed on the coated photoresist followed by a 20 µl drop of hydrogen peroxide fuel (with concentrations varying from 0.25% to 10%). The sample cell was then translated to a Karl Suss MA6 Mask Aligner (wavelength range UV400 350-450 nm, Power 11 mW/cm^2). The exposure time varied from 2 s to 16 s, depending upon the predefined pattern. A neodymium magnet was used for the remote magnetic guidance during exposure. After exposure, the solution on the photoresist was removed by water rinsing and the sample was developed in MF-321.

Equipment

Template electrochemical deposition of the micromotors was carried out with a CHI 660D potentiostat (CH Instruments, Austin, TX). Scanning electron microscopy (SEM) images were obtained with a Phillips XL30 ESEM instrument, using an acceleration potential of 20 kV. Atomic force microscopy images were taken with Veeco Scanning Probe Microscope. Videos were captured at 45 frames per second by an inverted optical microscope (Nikon Instrument Inc. Ti-S/L100), coupled with a 40x objective, a Hamamatsu digital camera C11440, using the NIS-Elements AR 3.2 software.

3.1.3 Nanomotor lithography concept and optical simulation

Fig. 3.1 illustrates the basic concepts of NML using the self-propelled metallic nanowire motors as nanomasks (a-c) and Janus sphere motors as near-field nanolenses (d-f). In the first case, a motile, remote-controlled metallic nanowire motor replaces the traditional photomask and acts as dynamic nanoscale optical element that locally shields the photoresist beneath it from the UV exposure, and hence generates a surface pattern that mirrors its moving trajectory due to a lower exposure dosage over the predetermined guided path (Fig. 3.1a). After development, the directional trajectories of the nanomotors will be revealed on the polymer surface as raised ridge lines. The Au/Ni/Au/Pt four-segment nanowire motor 'masks', fabricated by a template-assisted electrochemical deposition protocol, are self-propelled over the photoresist surface by self-electrophoresis in the presence of H_2O_2 fuel [16–18]. Finite-difference time-domain (FDTD) numerical simulation of such localized light blocking is displayed in Fig. 3.1b. The AFM image of Fig. 3.1c displays a ridge line created by a 200-nm-diameter nanowire motor swimming with a speed of 15 μm/s. The width of the ridge line (measured as full-width at half maximum, FWHM) is ~300 nm, demonstrating a successful autonomous patterning of a feature smaller than the wavelength (400 nm) of incident light.

In the second case, NML relies on Janus sphere motors as near-field nanolenses (Fig. 3.1d-f). When light at optical frequencies is scattered by a spherical nanoscale lens, it exhibits curvilinear trajectories, resulting in remarkably strong near-field magnification that produces a photonic nanojet [28–30]As such, complementary to light-blocking metallic nanowire motors, self-propelled Janus spherical motors can be used as motile optical lenses to effectively concentrate the processing light and harness near-field optical effects for direct writing. Such near-field magnification leads to the creation of features with resolution beyond the diffraction limit. The Janus motors are prepared by coating transparent polystyrene or silica spheres with a thin hemispherical platinum layer for catalytic propulsion in H_2O_2 solution. FDTD simulations provided evidence that a half-coated Janus microsphere (Fig. 3.1e) can still generate a narrow, high-intensity, subdiffraction-waist beam that propagates into the background medium. This effect is illustrated by the nanoholes obtained using stationary Janus motors as near-field lenses. The simultaneous movement and light-focusing abilities of Janus sphere motors allow for the rapid and controlled transfer of the nanomotor trajectory to distinct sub-micron features in aqueous environments. Fig. 3.1f displays a trench line created by such movement of a 2.16-μm-diameter Janus sphere motor on a positive photoresist. The FWHM of this trench is only 420 nm, which is significantly smaller than the size of the Janus motor, reflecting the effective light focusing effect of such microspheres.

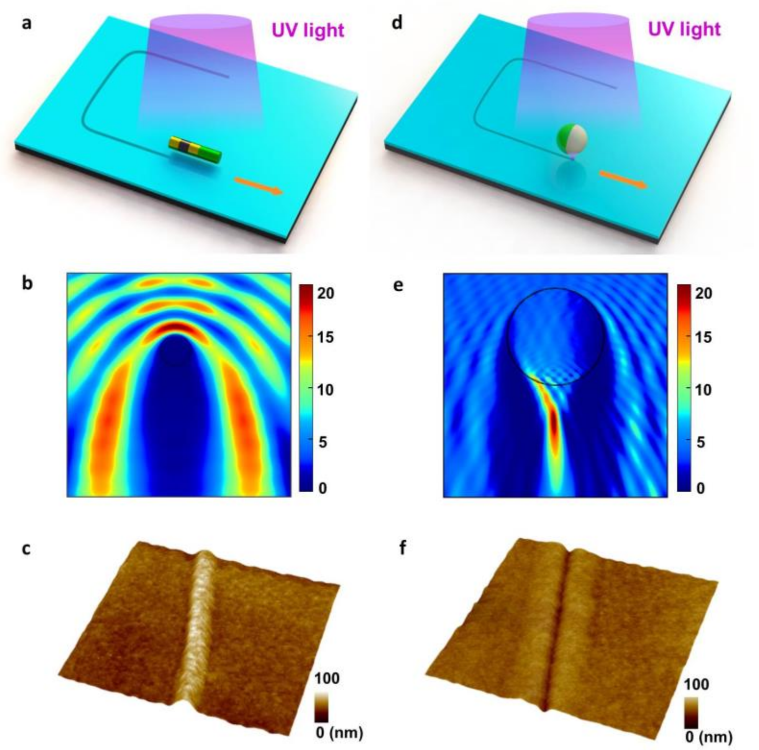

Figure 3.1 (a) Schematic of nanomotor lithography by using a nanowire motor as a self-propelled nanomask. (b) FDTD model of the intensity of light blocking by a 200-nm-diameter Pt nanowire in water (refraction index n=1.34). The plane shown is parallel to the light propagation direction. Wavelength of light, 400 nm. The black circle represents the cross-section of the nanowire. (c) Atomic force microscopy (AFM) topographical three-dimensional (3D) patterns of a ridge line feature created by a 200-nm-diameter wire nanomotor swimming in a 1% H_2O_2 solution. (d) Schematic of nanomotor lithography by using a Janus sphere motor as a self-propelled nanolens. (e) FDTD model of the intensity of light passing through a 2.16-μm-diameter Janus sphere (n=1.62 for polystyrene) in water (n=1.34). The black circle represents the contour of the sphere and the right hemisphere is coated with a 10-nm Pt film. (f) AFM topographical 3D pattern of a trench line feature created by a 2.16-μm-diameter Janus sphere motor swimming in a 5% H_2O_2 solution. Scanning areas are 6×6 μm^2.

3.1.4 Patterning by metallic nanowire motors

In The versatility of nanomotors gives NML the freedom for varying a wide range of experimental parameters for creating a myriad of distinct nanopatterned features. For example, the size of the nanowire motor mask can be tailored using membrane templates with different pore sizes. Here, nanomotors with diameters of 200 nm, 400 nm and 1000 nm were prepared for use as swimming nano-masks (Fig. 3.2 a-c). The AFM images of Fig. 3.2 d-f illustrate the morphologies of ridge lines obtained using self-propelled nanowire motors of the above diameters. As expected, nanomotor masks with smaller diameters result in higher resolution patterns, as indicated from the changes in the corresponding feature height and width. The slightly larger feature size (compared to the diameter of the swimming nanomask) is attributed to increased Brownian motion and light scattering. While these effects could compromise the positional accuracy and light masking ability for smaller motors, the FWHM of the lines drawn by 200-nm nanomotors is still in the sub-wavelength regime. An investigation of ridgeline profiles from motors with various propulsion velocities indicates that the height of the ridge decreases with increasing motor speed; intuitively, slower swimming speeds result in longer light blocking times over their moving path (Fig. 3.2d). Meanwhile, the FWHM decreases slightly for faster motors due to the weaker influence of the Brownian motion (Fig. 3.2h). These results indicate that using nanomotors with smaller dimensions leads to an increased patterning resolution due to the nanomask shadowing effects. The resolution can also be slightly improved by increasing the motor speed, due to the reduced exposure time and influence of Brownian motion. FDTD simulations indicate that the resolution could be enhanced further by adopting a UV laser with a shorter wavelength than that of the UV lamp used here (350-450 nm).

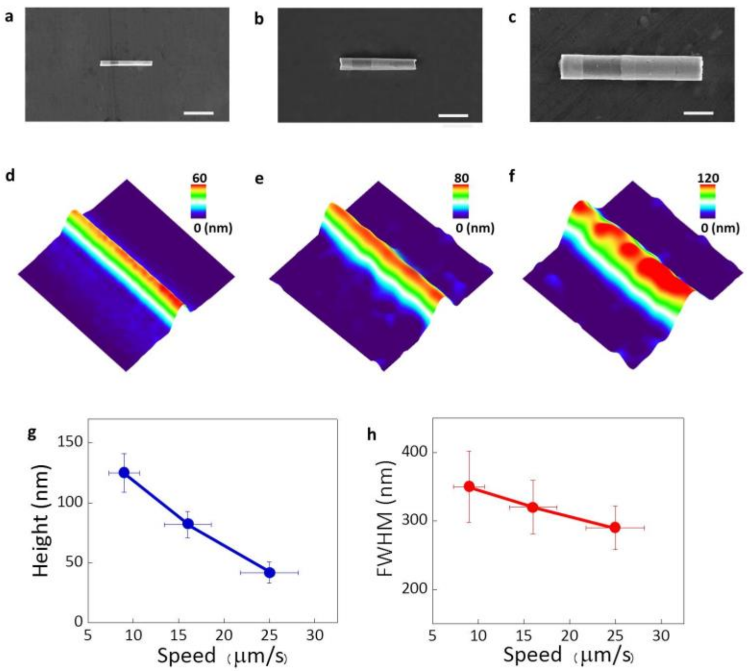

Figure 3.2 Patterning by nanowire motors. Scanning electron microscope (SEM) images illustrating the nanowire motors with diameters of (a) 200 nm, (b) 400 nm, and (c) 1000 nm, Scale bar, 1000 nm. AFM images of topographical 3D line morphologies generated by nanowire motors with diameters of (d) 200 nm, (e) 400 nm, and (f) 1000 nm and speed of 15 μm/s. Scanning areas for the 3D perspective images, $3\times3\ \mu m^2$. Maximum height (g) and FWHM (h) of a number of single lines ‘drawn’ by the nanowire motors swimming at different speeds obtained using H_2O_2 concentrations of 0.25%, 1% and 5%. Error bars represent one standard deviation (N=20).

3.1.5 Remote magnetically-guided writing

Directional magnetic orientation of the nanowire motors can be achieved by incorporating a ferromagnetic Ni segment into the motor structure. Precise control of the nanomotor paths allows for the rapid prototyping of their trajectories to predefined patterns. Fig. 3.3a displays a double-ridge line feature fabricated by the simultaneous lateral movement of two individual nanomotors along the applied magnetic field. This feature illustrates the uniformity and highly parallel capabilities of the controlled nanomotor patterning concept. Fig. 3.3b displays two crossed lines obtained as a result of one nanomotor crossing over the path of another one after turning the magnetic field. This illustrates the potential of using multiple motors to generate complex patterns through superposition of different motor paths. Fig. 3.3c and d display surface features of parallel lines and a 90-degree turn, respectively, over large areas (60×60 µm2). Note that the length scale of the patterned lines in Fig. 3.3c-d is over 20 times longer than the length of the nanomotors, illustrating the capability for large-scale well-defined spatial control of the nanomotors. Fig. 3.3e and f displays a square-wave pulse pattern, and a letter "D" pattern, respectively. Such ability to execute discrete and continuous turns through an external magnetic field enables the patterning of both sharp vertices and smooth curves, thus leading to a wide variety of possible surface features. Additionally, the magnetic field and trajectory of the nanomotors can be controlled and pre-programmed, allowing for the automatic patterning of substrates by identical motor movements.

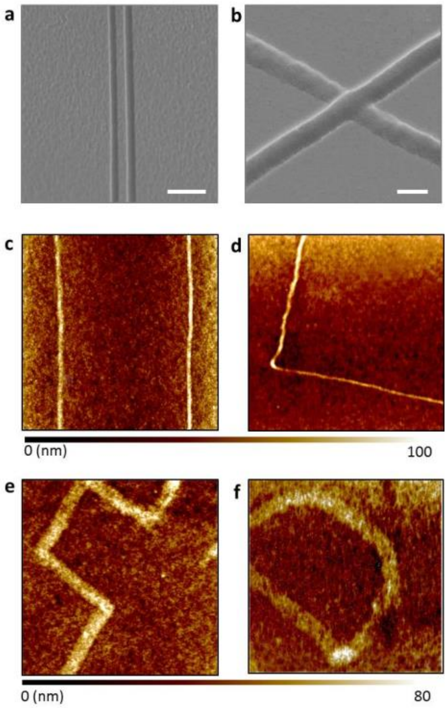

Figure 3.3 Remote magnetically-guided writing. (a) SEM images of two ridge lines generated from parallel (magnetically-guided) motion of two individual nanowire motors. Diameter of nanowire motor, 400 nm. Scale bar, 5 μm. (b) Two crossed ridge lines produced from two individual staggered nanomotors under an external magnetic field. Scale bar, 1 μm. The second line resulted from the path of one nanomotor crossing over the path of another motor after turning the magnetic field. AFM images of parallel ridge lines (c) and of a right angle ridge pattern (d) generated from a longer exposure period. Scanning areas, 60×60 μm^2. AFM images of a square-wave (e) and the letter 'D' (f) patterns obtained using moving nanomotors. Scanning areas, 10×10 μm^2. Hydrogen peroxide concentration: 1%.

3.1.6 Patterning by Janus sphere motors

Janus microsphere motors, which are half-coated with a Pt layer, move autonomously in a hydrogen peroxide fuel solution due to the catalytic fuel decomposition reaction[34]. When the photoresist surface is exposed to UV light, the Janus sphere motor acts as a near-field lens for nanopatterning (Fig. 3.4a). While the processing UV light illuminates a large area, it reaches a much higher intensity for photoresist exposure directly beneath the microsphere lens. The Janus sphere motors with diameter of 2.16 μm can move stably at a fixed height above the photoresist surface for uniform and consistent patterning. Due to their catalytic hemispheric patch, Janus microsphere motors can lead to unique and complex optical effects unavailable for bare spheres. By carefully tuning the thickness of the platinum patch, we demonstrate that the optical properties of these motors can be intrinsically tailored from near-transparent nano-lenses to semi-opaque nano-masks, thus offering further possibilities for engineering the topography of the patterned surface features. A FDTD 2D model (Fig. 3.4b-d) was used to predict how the incident light is manipulated by the engineered Janus spheres with Pt patches of different thicknesses: b) 5 nm, c) 40 nm, and d) 120 nm. It can be observed that the peak intensity of the photonic nanojet diminishes slightly upon increasing the Pt thickness while the opposite hemisphere remains transparent. Solvent-mediated electrostatic repulsions between the charged surfaces of the sphere and the substrate balance with van der Waals forces, resulting in an equilibrium sphere-substrate spacing. Very small Janus spheres (less than 500 nm in diameter) experience a much stronger Brownian motion that can cause fluctuations in their vertical distance from the substrate and influence the resulting patterns. Accordingly, we focus on the 4.74-μm Janus sphere motors which always remain close to the surface and move stably at a fixed plane. The AFM images of Fig. 3.4e-g illustrate the ability to tailor the morphology of the generated features using Janus spheres with Pt films of different thicknesses, while Fig. 3.4h-j display the corresponding cross-section profiles. The 5-nm thin Pt coating displays minimal attenuation of the incident light and thus exhibits a lower influence on the sphere’s near-field focusing, resulting in a trench line pattern (Fig. 3.4e). Note that a wider raised area surrounding the trench line was formed simultaneously as a result of light blocking effects from the Pt patch. Increasing the thickness of the Pt film to 40 nm results in surface features of multiple symmetric ridges (Fig. 3.4f), reflecting the varied intensities of the scattered light. Further increasing the film thickness to 120 nm leads to a single ridge, consistent with results expected from an opaque mask (Fig. 3.4g). The height of the ridge line can reach 200 nm, which is comparable to heights obtained with nanowire motors. Nanopatterns with improved aspect ratio are expected by increasing the exposure dose through a higher light intensity. This versatility of

Janus motors, through control of the thickness of the catalytic layer, greatly enhances the patterning capability and leads to the creation of a wide variety of distinct surface features. Further studies will focus on exploring even more complex high-aspect ratio surface patterns by changing the geometry and coverage of the Pt catalytic patch.

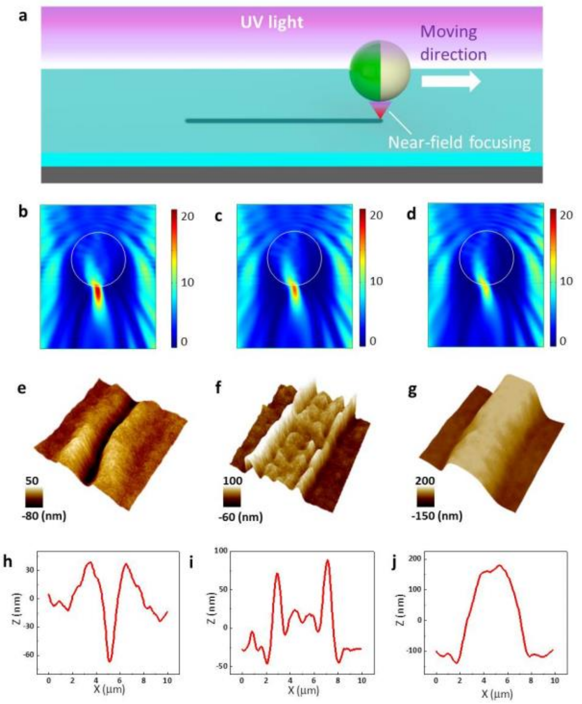

Figure 3.4 Patterning by Janus sphere motors. (a) Schematic showing a moving Janus microsphere motor near the photoresist surface under exposure to UV light. 2D plots of the steady-state intensity of light passing through a 4.74-μm-diameter Janus sphere (silica n=1.55) with Pt thickness of (b) 5 nm, (c) 40 nm, (d) 120 nm in water (n=1.34). The circle represents the contour of the sphere and the right hemisphere is coated with a Pt film. Surface morphologies and corresponding cross-section profile of the created features by using 4.74-μm Janus spheres, coated with Pt films of different thicknesses: (e) 5 nm, (f) 40 nm, (g) 120 nm scanning areas, 10×10 μm^2. (h), (i) and (j) Representative cross-section profiles of images (d), (e) and (f), respectively.

Meanwhile, the integration of a ferromagnetic Ni layer in the Janus sphere motor can facilitate remote magnetic control for predefined writing. As illustrated in Fig 3.5a, the Janus motors align such that the Janus boundary is perpendicular to the applied magnetic field, allowing for a magnetically guided patterning illustrated from AFM images of Fig. 3.5b,c. Under an optical microscope, the Janus boundaries of the motors are clearly and consistently observed when they are moving, indicating that the orientation of such nanolenses is preserved. Using assemblies and arrays of dynamic patterning tools is a promising pathway for the parallel fabrication of complex devices consisting of many small components. Although a variety of complex configurations are possible for assembled Janus particles, we focus here on the "side-by-side" paradigmatic case to illustrate the patterning capability of such assemblies. Fig. 3.5d-f display the continuous patterns obtained by such singlet, doublet and triplet Janus-sphere assemblies moving together under magnetic guidance. The various peaks in the pattern correspond to the optical field from individual Janus spheres overlapping with each other and superimposing to form higher ridge features. These data indicate that further improvements in the pattern complexity are possible via advanced self-assembly protocols [31,32], and that the diversity of the patterned features can be increased by tailoring the patch morphology of the individual Janus motors in the assembly.

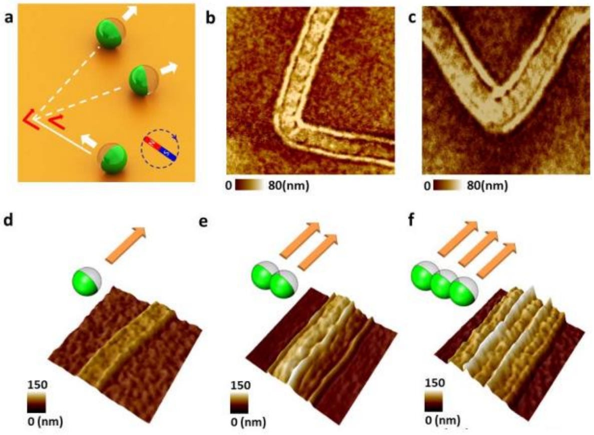

Figure 3.5 Controlled and parallel patterning by Janus sphere motors. (a) Illustration of the magnetic guidance of Janus sphere motion. (b) A pattern created by turning the magnetic field by 90°; scanning area, 30×30 μm^2. (c) A pattern created by turning the magnetic field by 120°; scanning area, 20×20 μm^2. Continuous patterns obtained by using (d) single, (e) double and (f) triple Janus spheres moving alongside under magnetic guidance. Scanning areas, 20×20 μm^2.

3.1.7 Conclusion

We have introduced a simple and efficient nanomotor-based nanopatterning technique based on self-propelled nanomasks and nanolenses that brings a twist to conventional static optical fabrication systems. This nanomotor-fabrication strategy combines controlled movement with unique light-focusing or blocking abilities for direct surface writing and provides researchers with considerable freedom for creating diverse features with different shapes and sizes. Spatially-defined surface-patterns, corresponding to the predetermined path of the nanomotors, have thus been generated. We expect that directional propulsion and variation of nanomotor parameters can be used to generate more elaborate functional features. For example, the shape and number of the catalytic patches of the microsphere lenses can be customized to further increase the pattern complexity. Higher order motor organization and modular motor design should lead to further improvements in pattern intricacy. Diverse pattern morphologies can thus be achieved by rationally designing each component in the Janus motor assembly. As proof of concept, we demonstrated here that such nanomachines could effectively manipulate the processing light beams for optical-based nanopatterning. Future research and development of the nanomotor patterning method can be realized by combining advanced nanomotor designs with diverse functionalities. For example, it could be possible to use thermal, mechanical, electrical, plasmonic, and chemical effects for such dynamic nanomotor lithographic techniques by incorporating specific physical functionality or surface chemistry into the nanomotor. These current capabilities and future possibilities offered by motile optically-active nanomachines lead to the new "on the fly" nanomanufacturing platform and create new opportunities for surface science.

3.2 Nanorobot to read: swimming microrobot optical nanoscopy

3.2.1 Introduction

The ability to resolve small structures with high resolution has been a topic of enormous interest and importance [28,33–39]. Scanning probe microscopy (SPM) has been widely used to map local nanoscale information with functionalized tips, but such tip scanning processes are hampered by the perturbation induced at the near field and slow imaging speeds within limited scanning areas, especially for operation in liquids and biologically relevant environments [40]. The large forces induced by the sharp tip and rigid cantilever usually make it challenging to scan over soft samples [41]. Fluorescence nanoscopy approaches have been rapidly advanced recently as powerful super-resolution tools [42–45]but might still require sophisticated labeling and image processing algorithms. Recently, micro-/nanostructured lenses, such as metamaterials and microsphere lenses [28,33–39], have shown considerable promise for resolving surface structures below the diffraction limit. While metamaterials have been limited by losses, microspheres lenses are particularly attractive as they are essentially loss-free [46,47]. However, the lack of mobility of microsphere lenses impedes their operation for site-specific probing or large-area scanning of real-life samples.

Artificial micro-/nanomachines, which are tiny devices that overcome low Reynolds number viscous drag and Brownian motion by converting local fuels or external energies into nanoscale locomotion, have recently emerged as powerful nanotechnology tools for biomedical and environmental sciences [17,18,20–22,48–50]. The operation of micro-/nanoscale machines and robots have proved be useful for cell penetration [26], environmental remediation [51], active materials assembly [52], and nanoscale lithography [53]. Engineering small robots with nano-optical elements will provide an alternative paradigm for scanning probe techniques to overcome roadblocks in optical imaging devices.

Here, we introduce a new nanoscopy methodology, denoted swimming micro-robot optical nanoscopy (SMON), based on autonomously moving micro-robots that rapidly scan over the sample surface. These untethered micro-robots, comprised of high-refractive-index microsphere lens, utilize chemical locomotion and magnetic guidance for non-destructive ‘on-the-fly’ scanning and imaging over large areas, obviating unwanted tip-sample interactions, macroscopic cantilevers, and complex control systems common to conventional SPM techniques. High-resolution imaging below 50 nm of large areas can be achieved with a conventional white-light or fluorescence microscope. The imaging throughput can be further improved by parallel operation of multiple micro-robots. Such self-propelled micro-robots with integrated nanophotonic functionality provide a new paradigm for surface imaging towards high-performance, user-friendly, cost-efficient, and readily accessible nanoscopy.

3.2.2 Experimental section

Fabrication of Micro-robot Lenses

The Janus micro-robots were prepared using different sizes of spherical polystyrene (PS) and titania (TiO2) base particles. Three diameters of PS microspheres were used: 2.16, 4.86, and 10 μm (Bangs Laboratories, Fisher, IN, USA), while the mean diameter of the TiO¬2 microspheres is 15 μm (Microspheres-Nanospheres, Corpuscular, NY, USA). First, 100 μL of each particle suspension was centrifuged and washed with ultrapure water (18.2 MΩ□cm) three times. Then, the microsphere suspensions were spread onto glass slides and dried uniformly to form particle monolayers. At this point, the spheres are closely packed due to attractive van der Waals forces.

An adhesive 2-nm layer of titanium (Ti) followed by a 5-nm layer of nickel (Ni) and a 5-nm layer of platinum (Pt) were sequentially deposited by electron-beam evaporation (Temescal BJD 1800) at a 75º angle of incidence to minimize the coating area. After the fabrication, the Janus micro-robots were detached from the substrate via sonication or pipette pumping, and then centrifuged and washed with ultrapure water two times. Sonication was used to disperse the micro-robot water suspension. Dimers, trimers, and other larger assemblies were obtained by reducing the sonication time from >1 min to ~5 s. All micro-robots were stored in ultrapure water at room temperature and tested prior to each experiment to verify their motion capabilities.

Imaging Samples Fabrication and Preparation

The 45-nm “UC” letter array, 20-nm nanogap patterns, and 200-nm nanodot array were fabricated using electron beam lithography (Vistec EBPG5200 Electron Beam Writer). The samples each consist of 200-nm HSQ thin films coated on a Si substrate. The 320-nm nanograting structures were obtained by peeling the soft protective film from the edge of a blank Blu-ray disc, exposing the grooved recording layer.

The neuron axon samples were obtained from mouse brain slices. Horizontal slices 300-μm thick were cut from the hippocampus of 15–19 day-old C57BL6 mice in an ice-cold artificial cerebrospinal fluid (ACSF) containing: 125 mM NaCl, 2.5 KCl, 2 mM CaCl2, 1 mM MgCl2, 25 mM NaHCO3, 1.25 mM NaH2PO4, and 25 mM glucose, bubbled with 95% O2 and 5% CO2 and incubated for 30 min at 34ºC. Afterwards, the slices were stored in ACSF at room temperature (22–23ºC) until use.

The fluorescent nanobeads were purchased commercially (Polysciences, Fluoresbrite® YG Carboxylate Microspheres 0.05µm, 16661-10). 1 μL of nanobead suspension was washed with ultrapure water (18.2 MΩ□cm) three times, then diluted in 100 μL water. Then, the diluted nanobead suspension was spread onto glass slides and dried uniformly to form nanobead monolayers.

An annealing process was used to fabricate DNA nanotubes from DNA strand which was prepared with oligonucleotides (IDT, Inc). In brief, 5 µM DNA was firstly dissolved in TAE/Mg2+ buffer composed of tris(hydroxymethyl) aminomethane (Tris) base (40 mM, pH 8.0), acetic acid (20 mM), ethylenediaminetetraacetate (EDTA; 2 mM), and MgAc2 (12.5 mM) and slowly cooled from 95 to 20 °C over 48 h, then diluted to 500 nM with PBS/10 mM MgCl2 solution. Prior to fluorescence SMON imaging, 100 μL of 100 mM YOYO-1 (Molecular Probes) solution (in PBS buffer) was directly loaded onto DNA nanotubes and incubated for 3 min at room temperature.

Rhodamine-labeled protein microtubules were prepared by polymerizing rhodamine-tubulin (Cytoskeleton, Inc) and native tubulin (molar ratio: 0.5:99.5; [tubulin] = ~400 μM) in BRB80 buffer (80 mM PIPES-2K; 5 mM MgCl2; 1 mM EGTA; pH 6.8) with 1 mM guanosine-5′-triphosphate (GTP) at 37°C for 15 min. A BRB80 buffer, including 1 mM GTP was used to dilute the obtained microtubule solution 100 times. A thin layer of microtubules was prepared by placing a cover glass (18 mm × 18 mm) on a sample droplet on a slide glass.

The B. globigii spores (solid biomaterial with 3.52 × 1012 cell/g, from The U.S. Army-Dugway Proving Ground) were diluted and cleaned to eliminate some silica added to the cells to increase followability (for dispersion purposes). The spores were centrifuged at low speeds of 1000 rpm for 1 min to separate the supernatant (the spores) from the precipitate (the silica). The spores were centrifuged again at 14000 rpm for 10 min to remove the supernatant, and the spore pellets were subsequently used to prepare 1 mL of spore solution for imaging experiments.

Imaging and Propulsion Experiments

To determine the relationship between the micro-robot speed and fuel concentration, aqueous H2O2 solutions (H325-500, Fisher) with concentrations ranging from 5% to 15% were prepared. A 1 μL droplet containing the micro-robots was placed first on a glass slide. After the micro-robots settled into focus of the microscope, a 1 μL droplet of peroxide solution was mixed directly into the micro-robot droplet. Particle tracking was subsequently performed in Metamorph to capture the average micro-robot speed for each micro-robot sample.

In each imaging experiment, a similar procedure was followed as above. Here, the micro-robot droplet was placed directly onto the sample substrate surface. After the micro-robot settled into focus near the objects of interest, an equal volume of the appropriate peroxide solution was directly mixed in for propulsion. Additionally, a remote magnet was used to align the micro-robots and control their direction.

For the bright field microscopy videos, we used an upright optical microscope (Nikon Eclipse 80i), coupled with a 40× objective (CFI Plan Fluor, Nikon, N.A. 0.75) and a CoolSNAP HQ2 camera (Photometrics) under white light illumination (MKII Fiber Optic Light Illuminator, Nikon). For the fluorescence microscopy videos, an identical setup was used in conjunction with a Sola Light Engine (SM5-LCR-VA, Lumencor) for florescence excitation. Nikon fluorescence filter cubes 96225 and 96312 were used for UV and green light excitation, respectively. An exposure time of 200 ms was used for the florescence imaging. An external magnet was used to align and control the moving direction of the micro-robots. All videos were captured up to 45 frames per second. Scanning electron microscopy (SEM) images of the micro-robots and the imaging samples were obtained with a Phillips XL30 ESEM instrument, using an acceleration potential of 20 kV.

Software

Single particle tracking was accomplished using Metamorph software (developed by Molecular Devices). ImageJ (developed by National Institue of Health) was used to generate the relative intensity profiles. Image reconstruction from the acquired videos was done using Matlab (Mathworks, Natick, MA, USA). Light simulations were made using FEM simulations in COMSOL Multiphysics (COMSOL, Stockholm, Sweden).

3.2.3 Scanning with Single Microrobot

As illustrated in Fig. 3.6a,b, the micro-robot swims autonomously over the sample surface in aqueous solution containing the chemical fuel, focusing light through a high-intensity optical field directly beneath. Sub-diffraction surface features scatter this light as near-field evanescent waves, which are magnified and focused by the moving microsphere. The magnified virtual images are captured by the CCD camera behind the objective lens as a video with high-resolution frames, which can be reconstructed as a stitched image with large view. To make the Janus micro-robot, high-refractive index colloidal polystyrene (PS) (n = 1.59) or TiO2 (n = 2.1) microspheres (diameter 2-20 µm) are partially coated with a thin Ti/Ni/Pt (2/5/5 nm) metallic tri-layer. As illustrated in Fig. 3.6b, the micro-robot swims autonomously in aqueous solution by generating a local oxygen gradient through the asymmetric Pt-catalyzed decomposition of the hydrogen peroxide fuel [54]. The Ni layer enables remote control of the direction by an external magnet. Deposition of the tri-layer at a steep glancing angle is used to reduce the area of the metallic patch, thus minimizing light scattering (Fig. 3.6c). Finite Element Method (FEM) simulations verify the negligible effect of the thin metallic coating on the collection efficiency of the microsphere near a point source (Fig. 3.6d).

As a first demonstration of SMON imaging, we acquired an imaging video of a “UC” pattern with 45-nm line width (Fig. 3.6e) by a 10-µm PS micro-robot. Fig. 3.6f displays a 3-frame overlay image of the micro-robot swimming straight, under magnetic alignment, to clearly magnify and resolve multiple sub-diffraction features. In Fig. 3.6g,h, a 15-µm TiO2 micro-robot resolves 20-nm nanogaps that are far below the diffraction limit. Fig. 3.6i displays two frames of a 10-µm PS micro-robot scanning over fixed neuron axons of a mouse’s brain tissue. Clear magnified 50-nm neuron axons are resolved by the micro-robot without damage to the axon fibers. Fig. 3.6j-l shows that a 20-nm gap could be distinguisted by a TiO2 microrobot.

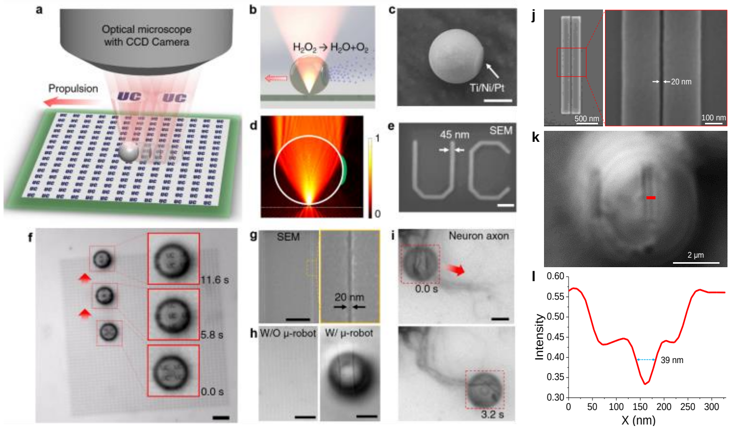

Figure 3.6 Swimming micro-robot optical nanoscopy (SMON). (a) Schematic illustration of SMON. A swimming micro-robot scans and magnifies near-field information on the object plane underneath. The virtual images are captured by an objective coupled with a CCD camera as a microscopy video containing high-resolution frames, which can be reconstructed as a stitched image with large area of view. (b) Schematic illustration of the chemically-powered propulsion and light amplification through the micro-robot nanoscope. (c) SEM image of a micro-robot, composed of a 10-µm polystyrene microsphere, partially coated with a thin Ti/Ni/Pt (2/5/5 nm) magnetic/catalytic patch. Scale bar: 5 µm. (d) FEM model of a point light source (wavelength: 400 nm) passing through a 10-µm micro-robot lens (n = 1.59) in water (n = 1.33). The 12-nm thin Ti/Ni/Pt metallic coating is indicated in green color. (e) SEM image of a “UC” nanopattern with a line width of 45 nm made by electron beam lithography. Scale bar: 200 nm. (f) Overlaying image of three frames from a microscopy video of a 10-µm PS micro-robot swimming over the “UC” nanopattern. The three insets highlight the magnified areas from each frame. Scale bar: 10 µm. (g) SEM image of 2-µm stripes separated by 20-nm nanogaps fabricated by electron beam lithography. Scale bar: 1 µm. (h) Microscopy images showing the 20-nm nanogap without and with a 15-µm TiO2 micro-robot scanning on it. Scale bars: 10 µm. (i) Microscopy images of scanning and imaging of neurons axon (including 50-nm fibers) by a swimming 10-µm PS micro-robot. Scale bar: 5 µm. All fuel concentrations: 5%. (j) SEM images of 200-nm stripes separated by a 20-nm nanogap. (k) Micro-robot nanoscopy image of 15-µm TiO2 micro-robot scanning over the nanogap feature. (l) Relative intensity profile and FWHM of the highlighted segment in (k).

3.2.4 Large-area and parallel scanning

The large-area scanning capacity of SMON has been examined by using a disc with grating nanostructures of 320 nm-wide lines separated 420 nm apart (Fig. 3.7a). The tracking line of Fig. 3.7b displays the motion of a 10-µm PS micro-robot scanning the nanograting surface over 3.6 s. Fig. 3.7c displays a reconstructed image of the magnified surface feature, obtained by stitching the magnified scanning area of the micro-robot from each frame. By comparing the intensity profiles of the scanned and un-scanned areas, we see that SMON significantly enhances the light contrast more than fivefold, clearly distinguishing the grating structure with 1.8× lateral magnification (Fig. 3.7d,e). The potential scanning area of the micro-robots is essentially unlimited within the aqueous environment, allowing the micro-robots to approach and scan any location in the whole view of the microscope. Compared to scanning tips, which might induce image artifacts due to the shape inconstancy, the micro-robot lens produce stable and reliable high-resolution images in each frame throughout the scanning process.

The simplicity of SMON enables straightforward parallelization imaging schemes by using multiple imaging micro-robots swarm together or using micro-robot ensembles. Fig. 3.7f-h show the parallel scanning of two magnetically-aligned micro-robots aligned to greatly accelerate the scan rate of a sample, analogous to parallel AFM cantilevered tips [55]. Colloidal microspheres, capable of forming self-assembled configurations for building complex devices and structures [31,32], have been used to explore the parallelized imaging capabilities of micro-robot assemblies. Fig. 3.7i-k display a ‘side-by-side’ paradigmatic dimer assembly of a dual-lens micro-robot, enlarging the magnified area in each frame for efficient scanning. This self-assembly is not limited to doublets, fast imaging can be achived using triplet and quadruplet micro-robot ensembles. These parallelization and self-assembly strategies could dramatically improve the scanning throughput at a large scale.

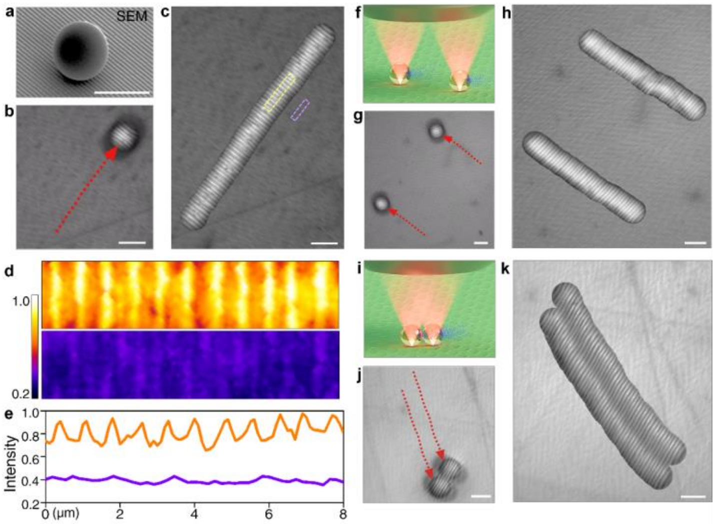

Figure 3.7 Large area scanning and parallel operation of micro-robot nanoscopes. (a) SEM image of a 10-µm PS micro-robot on a 320-nm nanograting structure to be scanned. (b) Tracking line showing the motion of a 10-µm imaging microrobot scanning over 5.6 s and (c) reconstructed image by stitching the magnified area from individual video frames. (d) False color images and (e) the corresponding relative intensity profiles of the reconstructed image (orange) to the original microscopy image (blue) of equal length labeled in c. (f) Schematic illustration of two micro-robot nanoscopes scanning in parallel. (g) Tracking lines showing the motion of two 10-µm PS micro-robots scanning the nanograting over 6.2 s; (h) the corresponding reconstructed image. (i) Schematic illustration of a self-assembled doublet micro-robot scanning. (j) Tracking lines showing the motion of an assembled doublet 10-µm PS micro-robot scanning the nanograting over 8.6 s; (k) the corresponding reconstructed image. All scale bars: 10 µm. All fuel concentrations: 5%.

3.2.5 Magnification capacity and scanning rate

The magnification capacity and lateral resolution of SMON are modeled and experimentally verified using PS and TiO_2 microspheres with different sizes. Fig. 3.8a shows the FEM simulation of light focused by a 10-µm PS microsphere (n = 1.59) in water (n = 1.33), which we analyzed with the ray optics method to locate the image plane and calculate the magnification [56]. Fig. 3.8b,c show the focal distances and magnification factors respectively, for microsphere lens with different refractive indices and sizes. We validated these results experimentally by imaging a 200-nm nanodot array with PS microspheres of three sizes (2.16, 4.86, and 10-µm) and 15-µm TiO_2 microspheres, as displayed in Fig. 3.8d. The corresponding 3D intensity profiles of the magnified portions over equal-pixel areas are shown in Fig. 3.8e. In agreement with our simulation results, the refractive index plays a more critical role in the lateral magnification, with TiO_2 microsphere swimmers offering a magnification factor higher than 4×.

We then estimated the scanning throughput of SMON. As illustrated in Fig. 3.8f, for a micro-robot with a diameter of d and a magnification factor of m, the lateral scanning length is d/m in each frame. To avoid missing local information between two consecutive frames, the maximum micro-robot speed should be fd/m, where f is frame rate, providing a maximum scanning rate of fd^2/m^2. Experimentally, the micro-robot speed is highly dependent on the fuel concentration and ranges from 5-35 μm/s. These micro-robot swimming speeds are faster than the regular scanning speeds of AFM, where a typical fast speed of up to 10 μm/s is used for a largest scanning distance of ~100 μm [57]. The corresponding scanning rates, based on our experimental results for different micro-robots, are shown Fig. 3.8g. Fig. 3.8h displays reconstructed images obtained during a 2 s scanning period using a 10-µm PS nanoscope and fuel concentrations of 2.5%, 5.0% and 7.5%. The larger stitched images indicate that higher fuel concentrations can dramatically increase the scanning speed without compromising the image quality. Overall, coupling a high-frame-rate microscope with high-speed parallelized micro-robots would be optimal for high-resolution high-throughput scanning and imaging. In our current SMON set-up, an experimental video rate of 45 frames/s with a 3-µm by 3-µm field of view in each frame, could be achieved using the 15-µm TiO_2 micro-robot. Such a data acquisition throughput is faster than the recently developed video-rate of far-field optical nanoscopy [58].

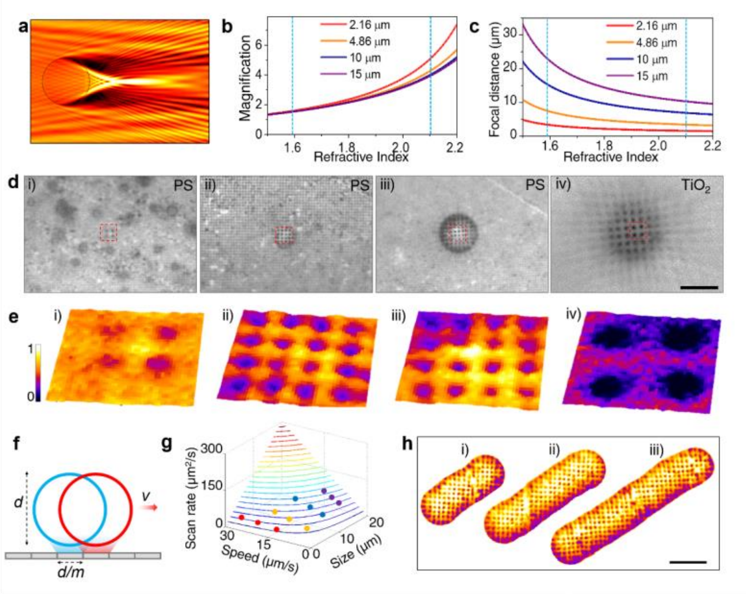

Figure 3.8 Super-resolution focal distance, virtual magnification factor and imaging speed. (a) FEM simulated electric field distribution of a plane wave passing through a 10-μm PS (n = 1.59) sphere in water (n = 1.33). (b) Virtual magnification factors and (c) focal distances of spherical lenses with different refractive indices and diameters. Blue dotted lines correspond to refractive indices of PS (n = 1.59) and TiO_2 (n = 2.1) used in experiments. (d) Magnification of a periodic dot array by spherical lenses made of PS micro-robot with diameter of (i) 2.16, (ii) 4.86 and (iii) 10 μm as well as (iv) a 15-μm TiO_2 micro-robot. Scale bar: 10 μm. (e) The intensity profiles corresponding to the magnified areas indicated in d. (f) Scheme showing the maximum scanning speed without missing surface information. (g) Dependence of the scan rate upon the micro-robot speed and size. Experimental results for scanning rates of different lenses are depicted with circle markers. (h) SMON image of a periodic dot array obtained using a 10-μm PS microrobot and different fuel concentrations: (i) 2.5%; (ii) 5%; (iii) 7.5% over a 2 s swimming time. Scale bar: 10 μm.

3.2.6 Imaging of fluorescent and biological samples

SMON can easily achieve high-resolution imaging of fluorescent and biological samples. Fig. 3.9a,b display fluorophore-labeled 50-nm PS nanobeads imaged by a 10-μm PS micro-robot. Beyond resolving the individual nanobeads, the nanoscope also dramatically enhances the fluorescent intensity by 20-25 fold, as highlighted in the fluorescence intensity profile in Fig. 3.9a, while the comparison in Fig. 3.9b highlights the 4× lateral magnification by SMON. The SMON image of a typical nanobead shows a FWHM of 81 nm. The strong fluorescence enhancement and photon collection efficiency through the high-refractive index microlens eliminate the long exposure time common to florescence microscopy, allowing fast florescence scanning with an exposure time of only 20 ms, without compromising the imaging quality. Similar to the fast stochastic optical reconstruction microscopy [59], such time resolution is very promising for imaging biological dynamics at the nanoscale. Fig. 3.9c compares an expanded fluorescence microscopy image of a nanobead string to a stitched SMON image of the same sample at the same scale. This degree of magnification and fluorescence enhancement is highly appealing for future single molecule imaging [39]. This technique has also been applied to biological samples, using fluorescence SMON to image rhodamine-labeled protein microtubules (Fig. 3.9d). Normalized intensity profiles of the microtubules shows a FWHM of ~75 nm, which is comparable to the value of 30-90 nm obtained by advanced super-resolution fluorescence microscopy techniques [60–62]. A comparison of microscopy and SMON images of fluorophore-labeled DNA nanotubes illustrates how the micro-robot nanoscope can distinguish individual signals from significant background noise (Fig. 3.9e). Note that the strong background noise from the DNA nanotube imaging is from the YOYO-1 dyeing solution, which is directly added to the DNA solution prior to the SMON imaging. Fig. 3.9f illustrates that under white-light illumination, SMON can clearly resolve individual *B. globigii* spores within large aggregates, indicating potential application within microbiome research. In our imaging experiments, we observed that the biological samples are quite stable without any deformation or cracking after continuous micro-robot scanning back and forth for over 50 times. For micromotors swimming in fluid, there is still a small sedimentation height between the micromotor surface and the sample surface[63]. Therefore, the spherical micro-robot does not come into direct contact with the samples and hence avoiding damage to soft structures. The smooth and stable scanning motion of the micro-robot has negligible interactions with the underlying biological samples, while the high resolution and photon-collection efficiency offered by SMON make it attractive for real-time tracking of sub-diffraction cellular structures and biological processes.

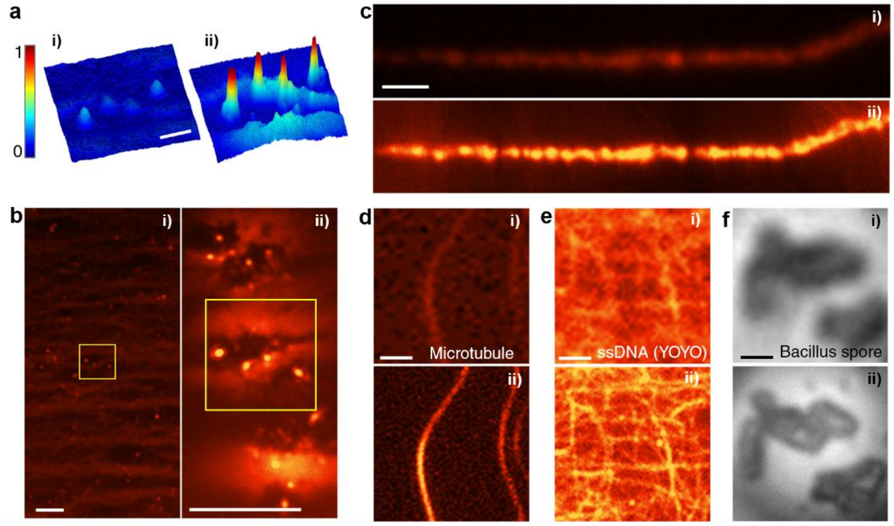

Figure 3.9 Imaging of fluorescent and biological samples by SMON. (a) Fluorescent intensity profiles of an identical region of florescence nanobeads imaged by microcopy (i) and SMON (ii). (b) Fluorescence microscopy (i) and SMON (ii) images showing lateral magnification of fluorescence nanobeads. (c) Fluorescence microscopy (i) and reconstructed SMON (ii) images of a large-area fluorescent nanobead string pattern. (d) Microscopy (i) and SMON (ii) images of microtubules labelled with the rhodamine. (e) Microscopy (i) and SMON (ii) images of ssDNA labelled with YOYO-1. (f) Microscopy (i) and SMON (ii) images of Bacillus globigii spores. Images are representative of >20 data sets of similar quality. Scale bars: 500 nm (a, c, f); 2 µm (b) and 1 µm (d, e).

3.2.7 Conclusion

In summary, we have reported swimming micro-robot optical nanoscopy (SMON) as an efficient and high-resolution imaging technique. This micro-robot imaging approach relies on controlled and rapid autonomous movement of untethered nano-optical elements over large areas for high-resolution and high-throughput surface imaging. The scalable parallelization schemes and self-assembly of the micro-robots can further enhance the imaging throughput. SMON represents a user-friendly, non-destructive and low-cost alternative to complex micromanipulation techniques, and can be used for real-time high-resolution imaging of soft biological samples. Furthermore, chemicals such as glucose or urea could potentially be used as biocompatible fuel sources for the micro-robots [64], replacing the currently toxic peroxide fuel. Moreover, a fuel-free operation of the micro-robot -- based on magnetic or acoustic actuation -- can replace the catalytic propulsion for digital control and imaging of many live samples. The trajectory of fuel-free micro-robots could be readily pre-programmed towards automatic high-throughput surface imaging. Although the current SMON method cannot achieve the atomic-level resolution offered by scanning probe microscopy, replacing scanning tips with micro-/nanoscale robots and enabling mobility of nano-optical devices create new opportunities for a variety of applications requiring high-resolution optical imaging and surface topography of large sample areas. We envision that metamaterial superlenses and hyperlenses could also be employed as future microscale imaging robot for site-specific probing and large-area scanning. Beyond improving the resolution of regular white-light and fluorescence microcopy, SMON can also be coupled with other high-resolution techniques, such as stimulated emission depletion (STED) microscopy and structural illumination, to further enhance the resolution synergistically. SMON also offers site-specific optical signal enhancement, thus expanding the parameter space of applicable optical intensities, pulse energies, durations and wavelengths of spectrometers and optical detectors. The photonic micro-robots described in this work should also find applications in reconfigurable nanophotonic systems.

3.3 Nanorobot to repair: Self-propelled nanomotors autonomously seek and repair cracks

3.3.1 Introduction

Microscopic cracks and physical defects can drastically alter the macroscopic optoelectronic, thermal, and mechanical properties of materials, and can propagate to induce catastrophic failure in valuable devices. It would be highly desirable to create devices that not only monitor their own structural integrity, but also autonomously repair incipient damage; achieving such self-regulating, self-repairing behavior in synthetic systems, however, remains a considerable challenge. Notably, biological organisms display remarkable abilities to autonomously heal and regenerate after being wounded. These self-healing abilities are vital to survival because they confer a level of physical robustness, and hence, increase the organism's lifetime. Inspired by this biological behavior, researchers have recently developed self-healing materials and chemistries [65–74] for applications towards functional surfaces [75–78], electrical conductors [79–84], electronic skin [71,85] and other complex synthetic systems with enhanced lifetimes and durability [86–88]. Materials that undergo autonomous repair could dramatically improve the sustainability of manufactured parts and systems [89]. Biomimetic self-healing processes are particularly desirable for integrated circuits and microelectronic devices because nano- and microscopic mechanical damage along a conductive pathway can noticeably limit the device performance, causing its electronic failure and ultimately limiting its lifetime. Recent research efforts have been directed towards the development of biomimetic self-healing processes to address this critical issue [79–84]. Some of these self-healing mechanisms involve the incorporation of healing agents directly into the material [80]; once these agents are depleted, however, the system cannot provide repeated restoration of conductive failure [84]. Moreover, this invasive approach can compromise the device performance and is limited to only certain classes of materials. Other approaches require external stimuli that can cause additional damage to the devices [84]. Furthermore, conventional repair techniques (such as those involving soldering and conductive inks) are not ideal for mending nanoscale/microscale cracks since these approaches are somewhat limited in providing localized delivery of the healing agents or repairing specific cracks without affecting nearby functioning parts.

For a system to perform autonomous repair, it must be capable of delivering the healing agents precisely to specific defect sites. Such healing agents must carry out the following three key functions: convert environmental energy into mechanical work for directed motion, autonomously sense and detect the damage, and possess engineered repairing capabilities. These tasks are particularly challenging in the case of microscopic defects because the damage is often hard to detect, making selective repair especially difficult (especially *via* conventional techniques such as soldering). Biological cells are highly proficient at sensing and adapting their motion to the presence of microscopic defects. For example, neutrophils autonomously migrate and chemotax toward the site of inflammation to mitigate the spread of infection [90], while circulated platelets attach to the collagen fibers of a wound to stop bleeding [91]. To perform these vital tasks, the cells not only respond to signals in their environment, but also transduce energy from their surroundings. Recently, there has been considerable effort towards designing artificial nanomachines that mimic the ability of biological motors to harvest and convert energy from their surroundings into directed motion [17,18,20,48,49,92,93]. These nanomotor systems share many properties with their biological counterparts, including speed regulation and collective movement in response to different environmental stimuli [19,63,94–97]. Microscopic surface defects might trigger useful changes in the dynamic behavior of artificial nanomotors, allowing for the autonomous detection of damaged sites. Given the recent advances in bio-inspired nanomachines, self-propelled nanomotors are attractive candidates for mimicking biological self-healing systems, where the nanomotors can effectively seek and locate defects, and thus, enable *in situ* repair.

Inspired by biological self-healing processes, we introduce a new mode of repairing microscopic defects that harnesses the properties of self-propelled nanomotors. We demonstrate that these active nanomotors, with excellent mobility, damage detection capacity, and engineered repairing functionality, can autonomously search, detect and repair microscale surface cracks. On a conceptual level, the behavior of these nanomotors mimics the chemotaxis of neutrophils towards inflammation sites and the aggregation of platelets at interrupted endothelium [90,91]. The presence of surface cracks introduces obstructions and gaps, presenting both energetic barriers and potential wells to the random walk trajectories of the nanomotors. The fast localization of the nanomotors at the cracks results from both geometric confinement and an attractive interaction between the surface of the exposed crack and the functionalized surface of the nanomotors. The latter features interrupt the nanomotors' directed propulsion and constrain them in the potential well of the crack. Quantitative agreement between the experimental data and a numerical model is achieved in studying the dynamics of the nanomotors swimming in an environment with such a surface defect. We demonstrate that spherical Au/Pt Janus nanomotors, with high mobility, surface functionality, and good conductivity, are able to restore autonomously the electrical conductivity of severely damaged electric pathways by forming conductive "patches" within the damaged regions (Fig. 3.10). We examine factors that influence the rate of the nanomotor accumulation and hence the efficiency of the repair process, and demonstrate that motor suspensions with high mobility and density exhibit a more efficient localization and repair capability. Such a bio-inspired healing system constitutes a step toward engineering advanced biomimetic nanomotors for the autonomous, nondestructive detection and repair of defects in a variety of materials, as well as applications involving targeted drug delivery. Finally, we note that the concept described here can be extended to encompass other nanomotor-crack interactions (e.g., involving charged particles and surfaces) and applied to surface cracks of different dimensions. Importantly, the healing provided by the self-propelled nanomotors does not affect the inherent properties of the device material. Moreover, the approach can be reapplied to provide repeatable repair in subsequent instances of damage.

3.3.2 Experimental section

Synthesis of Janus Nanomotors

The Janus nanomotors were prepared using spherical gold particles (diameter 0.8-1.6 μm, Alfa Aesar, Ward Hill, MA, USA) as the base particles. 10 μg of gold particles were first dispersed into ethyl alcohol (A407-4, Fisher, Pittsburgh, PA, USA) and centrifuged. Then, the gold particles were modified by immersion in 0.5 mM octadecanethiol in absolute ethanol (from Sigma-Aldrich) for 30 min. To remove any unreacted reagents, the particles were isolated by centrifugation and washed four times in double-distilled water. The sample was then spread onto glass slides and dried uniformly to form particle monolayers. The particles were sputter coated with a 15 nm Pt layer using a Denton Discovery 18. The deposition was performed at room temperature with a DC power of 200 W and Ar pressure of 2.5 mT for 15s. In order to obtain a uniform Janus half-shell coating, stage rotation was disabled and the sample slides were set up at an angle to be parallel to the Pt target. After the fabrication, the Janus particles were detached from the substrate via sonication or pipette pumping and were dispersed into double-distilled water.

Speed and Mean Squared Displacement

To determine the relationship between the Au/Pt motor speed and fuel concentration, aqueous hydrogen peroxide solutions (H325-500, Fisher, Pittsburgh, PA, USA) of 5.0%, 10%, and 15% (w/v) were prepared and directly mixed with equal volumes of droplets of nanomotor suspensions, attaining final hydrogen peroxide concentrations of 2.5%, 5.0%, and 7.5% respectively. Speeds of multiple ($n \geq 30$) nanomotors were tracked and averaged for each nanomotor sample, as well as their mean-squared displacements over 5 s. The propulsion experiments were performed by mixing 1 μL of the motors and 1 μL of the hydrogen peroxide solutions.

Localization Experiments

Nanomotors were prepared as above, with desired densities (motors per unit area of the droplet on the glass slide) achieved by either concentration or dilution of the suspension. The densities were measured by placing a 1 μL droplet of the nanomotors and 1 μL droplet of water on a glass slide to simulate experimental conditions, allowing the motors to settle into the plane of focus of the microscope, and counting the number of nanomotors within a random sample of $n \geq 30$ areas of size 100×100 μm^2. Two densities were prepared in this manner: a low density of 7.3 ± 0.8 motors per 100×100 μm^2, and a high density of 16.3 ± 1.5 motors per 100×100 μm^2. In each nanomotor density and fuel concentration, the experiments are repeated and 5 times to calculate the averaged percentages of the free and localized nanomotors.

Gold electrodes with hydrophilic surfaces were patterned on hydrophobic glass slides (Fisherbrand Microscope Cover Glass, 12-545-E). Lift-off lithography was used to pattern the Au electrode on the glass slides. The slides were coated with a thin layer of Au (100 nm) using electron-beam deposition, and then submerged in acetone to lift-off the remaining photoresist and unwanted Au, leaving only the desired Au electrodes behind on the surface. These electrodes were scratched down the middle with a diamond tip glass cutter, with crack widths ranging from 0.5 to 2.2 μm. For each of the six experimental configurations (two motor densities, three fuel concentrations) a 1 μL droplet of the motor suspension was first placed over the crack, and allowed to settle into the plane of focus. Then, a 1 μL droplet of the hydrogen peroxide solution was directly mixed into the motor droplet.

Conductivity Restoration Experiments

Lift-off lithography was used to pattern the Au electrode on the Si wafer with a 300 nm SiO_2 insulating layer. The substrates were coated with a thin layer of Au (100 nm) using electron-beam deposition, and then submerged in acetone to lift-off the remaining photoresist and unwanted Au, leaving only the desired Au electrodes behind on the surface. Electrical contacts at each end of the electrodes were made by employing stainless steel wires coated with silver epoxy.

For each conductivity restoration experiment, the resting resistance of each electrode (width 5 mm) was measured. Then, a diamond tip glass cutter was used to crack the electrode down the middle, severing conductivity completely and exposing the SiO_2 insulating layer. Low and high densities of nanomotors were prepared as above for these experiments, along with the three different hydrogen peroxide solutions of 5.0%, 10%, and 15% (w/v) and one control without adding hydrogen peroxide. A 3 μL droplet of the motor suspension was first placed over the crack, and allowed to settle into the plane of focus. Then, a 3 μL droplet of the hydrogen peroxide solution was directly mixed into the motor droplet. During this period, the resistance was continuously monitored between the two ends of the electrode. After the droplet dried (generally after 30 min), a thermal treatment was used to reduce the contact resistance. The final resistance of the repaired electrode was measured with a digital multimeter. In each nanomotor density and fuel concentration, the experiments are repeated and 10 times to get the final averaged conductivity.

Equipment

Videos were captured by an inverted optical microscope (Nikon Instrument Inc. Ti-S/L100), coupled with 40× objectives, and a Hamamatsu digital camera C11440 using the NIS-Elements AR 3.2 software. SEM images were made obtained on Philips XL30 ESEM. Conductivity and resistance measurements were made using a Radioshack PC Interface Digital Multimeter.

3.3.3 Simulation Section

To understand main features of the experimentally observed behavior of the Janus nanomotors influenced by the cracked surface, we simulate a collective dynamics of interacting self-propelled particles, moving with average speed u_0. The two-dimensional motion of N

nanomotors, labeled by index i, is described by velocity vectors $\mathbf{u}_i(t) = (u_i(t), v_i(t))$ where x- and y-components $u(t)_i$, $v(t)_i$, and angle $\phi_i(t)$ (with respect to x-axis) obey Langevin equations in the overdamped limit:

$$
\begin{aligned}
u_i &= u_0 \cos\phi_i - \mu \sum_{\substack{j=1 \\ j\neq i}}^{N} F_x^{p-p}(r_{ij}) - \mu \sum_{j=1}^{N} F_x^{p-t}(r_i) + \mu\sqrt{2q_u}\,\xi_i^x(t), \\
v_i &= u_0 \sin\phi_i - \mu \sum_{\substack{j=1 \\ j\neq i}}^{N} F_y^{p-p}(r_{ij}) - \mu \sum_{j=1}^{N} F_y^{p-t}(r_i) + \mu\sqrt{2q_u}\,\xi_i^y(t), \\
\dot{\varphi}_i &= \sqrt{q_\varphi}\,\xi_i^\phi(t), \qquad 1 \le i, j \le N.
\end{aligned}
\tag{3.1}
$$

The stochastic fluctuations are characterized by strength parameters q_u and q_ϕ, which we define below. The variables ξ_i^x, ξ_i^y and ξ_i^ϕ are assumed to be Gaussian white noise:

$$\left\langle \xi_i^x(t) \right\rangle = 0, \quad \left\langle \xi_i^y(t) \right\rangle = 0, \quad \left\langle \xi_i^x(t_1)\xi_j^y(t_2) \right\rangle = \delta_{ij}\delta_{xy}\delta(t_1 - t_2),$$

$$\left\langle \xi_i^\phi(t) \right\rangle = 0, \quad \left\langle \xi_i^\phi(t_1)\xi_j^\phi(t_2) \right\rangle = \delta_{ij}\delta(t_1 - t_2).$$

In equations (1), μ is the nanomotor mobility, $r_{ij} = \sqrt{(x_i - x_j)^2 + (y_i - y_j)^2}$ is the vector from particle j to particle i, r_i is the shortest vector from the trough to motor i, $F^{p-p}(r_{ij}) = -\dfrac{\partial U^{p-p}(r_{ij})}{\partial r_{ij}}$, and $F^{p-t}(r_i) = -\dfrac{\partial U^{p-t}(r_i)}{\partial r_i}$ are forces due to interactions with other particles and with the trough respectively. To model interactions between motors we use Morse potential

$$U^{p-p}(r) = \frac{\varepsilon^p}{\mu}\left(1 - \exp[-\lambda^p(r - r^p)]\right)^2 \tag{3.2}$$

where parameters ε^p, λ^p, and r^p characterize the potential strength, width, and equilibrium inter-particle distance respectively and $r=\sqrt{x^2+y^2}$ is the distance between the pair of motors. The process of accumulation of particles in the trough is controlled by the balance of particle fluxes *in* and *out* of the trough. One possible physical mechanism to provide such balance is to use a force, between the nanomotors and the trough, generated by superposition of Morse potentials:

$$U^{p-t}(r)=\frac{\varepsilon_1^t}{\mu}\left(1-\exp[-\lambda^t r]\right)^2-\frac{\varepsilon_2^t}{\mu}\left(1-\exp[-\lambda^t\left|r-r^b\right|]\right)^2 \tag{3.3}$$

where the height of the repulsive barrier ε_2^t controls the influx of particles and the depth of the potential well ε_1^t controls particle flux out of the trough. λ^t characterizes the width of such potential and r^b specifies the location of the repulsive potential barriers on each side of the trough.

The dynamics of the non-interacting nanomotors can be characterized by approximating the mean-squared displacement as:

$$\left\langle r^2(t)\right\rangle=4Dt+2u_0^2\tau^2\left(\frac{t}{\tau}+\mathrm{e}^{-t/\tau}-1\right). \tag{3.4}$$

The attractive interactions, resulting in the cluster formation, slow down the particle dynamics. To study the dynamics of interacting particles, we parameterize our model (1)-(3). Using the experimental average motor radius $R=0.6$ μm provides the Brownian (passive) diffusion coefficient

$$D=\mu^2 q_u=\frac{k_B T}{6\pi R\eta}=4.1\cdot 10^{-13}\ \ \mathrm{m^2/s}, \tag{3.5}$$

where k_B is the Boltzmann constant, $T=300\,\mathrm{K}$ is temperature, and $\eta=8.94\cdot 10^{-4}$ kg/s m is the dynamic viscosity of water. The nanomotor mobility $\mu=1/6\pi\eta R=10^8$ s/kg provides the fluctuation strength $q_u=4.1\cdot 10^{-29}$ Jkg/s. Measuring in the experiment the average motor speed,

u_0, the torsional diffusivity $\frac{q_\phi}{2} = \frac{1}{\tau}$ was chosen so that our simulations would reproduce the mean square displacement $\langle r^2(t) \rangle$ observed the experimentally values. The values of u_0 and q_ϕ are given for representative hydrogen peroxide concentrations (2.5%, 5.0%, and 7.5%) in the following: u_0 (7.53, 8.55, and 10.54 μm/s); q_ϕ (18.2, 7.25 and 4.55 rad^2/s)

The parameters ε^p and λ^p, accounting for inter-particle interactions, were set to ensure formation of clusters of nanomotors similar to those observed in experiment. Parameters ε_2^t and ε_1^t, controlling the particle interaction with the trough, were chosen to reproduce the evolution of number of particles accumulating in the trough. Parameters responsible for the inter-particle and trough-nanomotor interactions are summarized in the table below: $\varepsilon^p = 0.8 \cdot 10^{-19}$ J; $\lambda^p = 1.5$ μm^{-1}; $r^p = 1.3$ μm; $\varepsilon_1^t = 1.4 \cdot 10^{-19}$ J; $\varepsilon_2^t = 1.1 \cdot 10^{-19}$ J; $\lambda^t = 4$ μm^{-1}; $r^b = 0.75$ μm.

Simulations were performed in a square computational domain of area $A = 1\text{mm}^2$ with periodic boundary conditions. A trough, described by potential (3), was placed crossing the domain through the middle parallel to one of the walls. To start evolution, N nanomotors were randomly distributed in the domain, with number $N = \rho A$ determined by the experimentally observed motor areal density ρ. To integrate equations (1), we used a first order numerical scheme with time step $5 \cdot 10^{-4}$ s. To count numbers N_f and N_t of freely moving motors and those absorbed in the trough as functions of time, a square observation region of size $348 \times 261\,\mu\text{m}^2$ was chosen in the middle of the computational domain. The nanomotors located within $0.5\,\mu\text{m}$ distance from the trough were considered to be absorbed (N_t), the rest were considered free (N_f).The accumulation of the nanomotors in the trough, described by the percentages of the localized $\frac{100 N_t}{N_t + N_f}$ and free

$\frac{100N_f}{N_t + N_f}$ nanomotors is presented in Fig. 3.12 of the manuscript for the 7.5% of hydrogen peroxide concentration. Shown in these figures, the mean values and the standard deviations for each evolution of the percentage of nanomotors were obtained by averaging 8 independent simulations.

3.3.4 Nanomotor localization

To demonstrate autonomous repair by nanomotors experimentally and to characterize the localization process of the repair mechanism, we created a system of self-propelled nanomotors swimming over the damaged surface of an electronic circuit. Gold electrodes with a thickness of 100 nm were patterned on a glass substrate. The untreated surfaces of the pure gold electrodes, prepared by physical vapor deposition, are highly hydrophilic [98], while the surface of the glass substrate is relatively hydrophobic. Microscopic cracks on the gold surface were made by mechanical scratching with a diamond tip, removing the gold layer and exposing the underlying hydrophobic glass substrate. Scanning electron microscopy (SEM) characterization of the damaged substrate revealed cracks with widths ranging from 0.5 to 2.2 μm. The cracks of this size and shape are representative of those expected in microelectronic devices and circuits. As schematically displayed in Fig. 3.10A, we fabricated conductive Au/Pt Janus nanomotors by depositing a hemispheric platinum film (15 nm thick) on the gold spheres (diameter 0.8-1.6 μm). Such bimetallic Au/Pt catalytically-powered nanomotors self-propel efficiently in the presence of hydrogen peroxide (H_2O_2) fuel [99,100]. Both gold and platinum are stable noble metals with high electrical conductivity. We further functionalized the surface of the gold hemisphere of the nanomotors with a self-assembled monolayer of octadecanethiol, as schematically illustrated in Fig. 3.10A. This modification was performed for two purposes: first, these alkanethiol hydrophobic monolayers enhance the motor interactions with the exposed hydrophobic cracks [101]; second, these hydrophobic surfaces strengthen hydrophobic interactions between the gold hemispheres of different motors, leading to the formation of motile nanomotor clusters that can be confined within the crack [31].

Repair is achieved by the autonomous transport and aggregation of metallic nanomotors into the cracks, which act as new conductive “patches” in the broken circuit to restore the electrical current, as illustrated conceptually in Fig. 3.10B-C. When mixed with the H_2O_2 chemical fuel, a suspension of the Janus nanomotors can undergo self-propelled motion over the electrode, and thereby encounter cracks and other defects. The relative difference in surface energies between the hydrophilic electrode surface and the hydrophobic exposed substrate enables the nanomotors to effectively sense the microscale gaps created by the mechanical cracking. Notably, similar interactions were used to localize nanoparticle-filled microcapsules into microscale surface cracks [78]. In the latter study, an imposed flow was used to drive the capsules over the damaged surface, and hence, into hydrophobic cracks. The capsules had thin walls and when lodged in the crack, hydrophobic nanoparticles diffused from the capsules’ interior to fill and repair the damaged region. Sen and coworkers used ion gradients to trigger the motion of charged nanoparticles for bone repair [102]. The present system, in contrast, relies on self-propelled, tailor-made nanomotors in a quiescent solution that are trapped in the damaged location via engineered surface interactions.

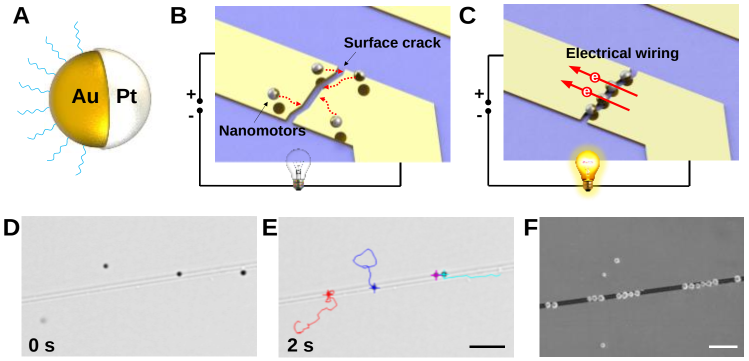

Figure 3.10 Schematic and actual process of autonomous repair of broken electronic pathways by artificial nanomotors that autonomously seek and repair microscopic mechanical cracks to effectively restore conductivity. (A) Structure of the functionalized Au/Pt Janus spherical nanomotor. (B-C) Nanomotor-based autonomous conductivity restoration concept. Localization of nanomotors at the crack site restores a conductive pathway, lighting up the lightbulb. (D-E)

Time-lapse microscopy images showing the nanomotors swimming and localizing in a surface crack within 2 sec. (F) SEM image illustrating the spherical nanomotors confined in the crack. Scale bar: 5 µm.

In addition to hydrophobic interactions, the motion of the nanomotors along the surface is further restricted by geometric confinement within the microscale cracks. The time-lapse images of Fig. 10D-E, illustrate the propulsion and subsequent localization of Au/Pt nanomotors in an exposed crack on a conductive gold-coated glass substrate in the presence of 5% H_2O_2. It was observed that the defect obstructed the motion of the nanomotors and confined them in the crack. SEM characterization in Fig. 3.10F reveals that multiple nanomotors are localized in the surface crack; this provides further evidence that such surface cracks can act as potential wells to confine and trap the nanomotors.

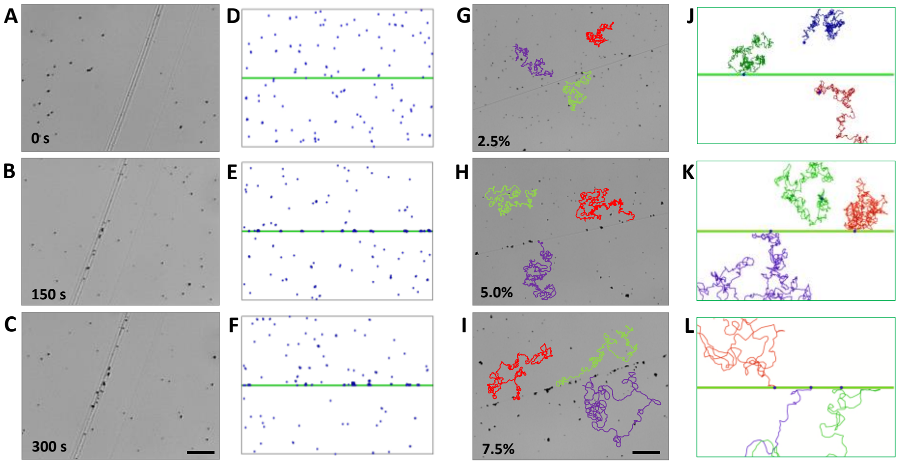

Figure 3.11 (A-C) Time-lapse microscopy images and (D-F) simulated video snapshots showing the nanomotor propulsion and localization process with an H_2O_2 fuel concentration of 7.5% and average motor density of 16.3 motors per 100×100 µm^2 at times 0 s (A), 150 s (B) and 300 s (C) from adding the fuel solution. (G-I) Time-lapse microscopy images showing the influence of the motor speed, controlled by the fuel concentration, on the propulsion and localization process of multiple nanomotors. Fuel concentrations, (G) 2.5% (H) 5.0% and (I) 7.5%. Average motor density: 16.3/100×100 µm^2. (J-L) Simulated video snapshots showing the propulsion and localization process of multiple nanomotors, moving at speeds corresponding to H_2O_2 fuel concentrations of (J) 2.5%, (K) 5.0% and (L) 7.5%. Scale bar (A-C; G-I): 50 µm.

To observe directly how a group of self-propelled nanomotors swim and accumulate at the crack of a damaged surface, we have monitored the self-propulsion process of a relatively large number of nanomotors on the damaged gold surface under a microscope. In the microscopy experiments, we ensured that the nanomotor droplet was exposed only to the hydrophilic electrode surface or to the hydrophobic crack, and not to the rest of the hydrophobic substrate (in order to maximize the concentration of particles at the crack). Fig. 11A-C show the time-lapse microscopy images of a group of nanomotors swimming over the cracked surface in the presence of 7.5% H_2O_2 fuel with an average nanomotor density of 16.3 motors per 100×100 μm^2. Immediately after fuel addition (corresponding to Fig. 3.11A), a negligible number of nanomotors are observed to have accumulated in the crack, owing to limited displacements under pure Brownian motion.

In the presence of the peroxide fuel, the nanomotors exhibit isotropic self-propulsion at consistent average speeds throughout the experiment (indicating negligible fuel depletion); over long time periods, the self-propulsion of the motors is combined with their Brownian reorientation to behave as a random walk [54]. Such enhanced random walk trajectories (see discussion below) increase the probability of nearby motors to encounter surface cracks over a sufficiently long time period, i.e., on the order of minutes. These surface defects introduce irregularities that disrupt the random walk through physical interactions that can entrench the nanomotors in a potential well within the crack. Furthermore, the hydrophobic hemispheres of the nanomotors can adhere to these exposed hydrophobic crack surfaces. Hence, the dynamics of the nanomotors at the crack are drastically altered by the hydrophobic surface interaction between the modified nanomotor surface and the crack, along with the physical defect itself. In addition, higher speeds correspond to greater collision rates between motors, where hydrophobic-hydrophobic surface interactions can lead to self-assembly of nanomotor clusters that can move and accumulate at the cracks as entire groups. The change in the crack can be clearly observed after 5 min of the particle motion (Fig. 3.11C), with the originally dispersed swimming nanomotors gradually accumulating and aggregating into the surface crack.

Our observations reveal complex dynamic interactions at the cracks that lead to such gradual accumulation: the nanomotors decelerate at the surface obstacle, where some of the motors are fully stopped and confined in the crack, while others move alongside the crack before entering. In addition, we observed that some of the trapped nanomotors can migrate within the crack and even overcome the energy barrier to exit the potential well and become free again. There were also instances in which the motors passed over the crack with no discernible interaction, or changed direction upon encountering the crack. Furthermore, we noticed that the nanomotors that became confined tended to self-assemble and aggregate around those already entrapped, such that even singular localized nanomotors could nucleate entire clusters of motors that stretch outside of the cracks. We also observed the rare opposite effect, where sufficiently energetic nanomotors could occasionally break free from these localized clusters. Higher viscous drag forces on the larger clusters, however, generally prevented them from overcoming the interior energy barriers to detach from the crack as a group, contributing to a net swarming effect. Overall, these observations indicate that the crack is a preferable site for confinement of nanomotors.

To analyze the mechanisms contributing to the observed accumulation of nanomotors in the crack, we developed a computational model describing the random walks of self-propelled interacting particles influenced by the presence of a trough. This approach relies on techniques developed to describe the clustering of Brownian walkers in the presence of an external potential [103,104]. In our case, the attractive potential is associated with the relative hydrophobicity of the crack and this attractive interaction leads to the motors being localized in the crack with a finite probability. The motor's trajectories were obtained by numerical integration of stochastic differential equations describing the propulsion of the nanomotors. We assumed that the nanomotor dynamics are governed by a combination of self-propulsion, random forces originating from thermal noise, and forces resulting from the inter-particle and particle-trough interactions.

The catalytic reactions at the surface of the Au/Pt Janus nanomotors can propel the motors at a constant speed through the fluid solution. Besides fluctuations in the nanomotor position, Brownian forces cause fluctuations in the direction of the propulsion vector. The self-propulsion of the nanomotors is described by the average speed u_0, the directional fluctuations, and the characteristic rotational time τ and yields dynamics in which particle displacement is ballistic (linear in time) at short times, and diffusive (proportional to the square root of time) at longer times.[48,51] The observed localization process occurs on a time scale of minutes (much longer than $\tau \sim 1\text{ s}$), suggesting enhanced motor diffusion dynamics with an effective diffusion coefficient $D_{\text{eff}} = D + \frac{1}{2} u_0^2 \tau$. The straightforward estimates for a 1.2 μm size motor with diffusion coefficient $D = 0.4 \cdot 10^{-12}\text{ m}^2/\text{s}$, moving with a speed $u_0 \sim 10\ \mu\text{m/s}$, give an increase in the effective diffusion coefficient $\frac{D_{\text{eff}}}{\text{D}} \sim 100$ (relative to thermally-driven Brownian motion characterized by D) and correspond to a 10-fold increase in the distances accessible by random walk. For each of the three fuel concentrations, 2.5%, 5.0%, and 7.5% H_2O_2 (w/v), we measured the average speed u_0 and then fitted τ such that the mean squared displacement of the simulated random walks reproduced the observed values.

The clustering of nanomotors is primarily due to the hydrophobic coating on their hemispheric gold surfaces. The formation of such clusters reduces the net motor surface exposed to the fuel solution. Since the individual motors within a cluster are randomly oriented, the propulsion vectors largely cancel out and the net motion of the cluster tends to be slower as the cluster size increases. This phenomenon exhibits two opposing effects: clustering outside the crack depletes the number of fast free motors and slows down the repair dynamics; clustering inside the crack helps to bridge the gap between conducting surfaces, improving the localization process. To account for the clustering phenomenon, we modeled the attractive interactions between nanomotors using a Morse potential, which is frequently used to model the self-assembly of nanoparticles [104]. This form of the interaction was chosen for simplicity and stability of the numerical procedure. Other potentials that account for a hard-core repulsion and a short-range attraction that smoothly vanishes at large distances (to stabilize the numerical simulations), could also be chosen to model clustering of nanomotors [105,106], and would yield qualitatively similar results. The experimental observation of nanomotor accumulation suggests that the crack is a preferable site for confinement, due to the larger hydrophobicity of the crack relative to the undamaged hydrophilic conductive surfaces. On average, the flux of nanomotors entering the crack is larger than that of nanomotors exiting this region. The balance between the two fluxes determines the rate of the nanomotor accumulation and ultimately affects the efficiency of the repair process. As one possible physical mechanism of controlling inward and outward nanomotor fluxes, we chose to model the nanomotor-crack interactions with a superposition of Morse potentials, consisting of a well in the middle of the crack flanked on either side by potential barriers, providing a higher energy cost for nanomotors to exit the well than to enter it. This model was developed based on our observations of the nanomotor behavior around the crack, and built on work characterizing such adhesive hydrophobic interactions between surface-modified microcapsules and a microscale crack [107,108]. A related study on nanoparticle localization similarly detailed the use of such potential barriers to model these adhesive/repulsive interactions between nanoparticles and a microscopic crack [109]. Increasing the height of the barriers reduces the probability of an approaching nanomotor entering the crack, and hence decreases the accumulation rate. Equilibrium is reached when the flux into the crack balances the flux out of the crack. Increasing the depth of the well decreases the frequency of nanomotors escaping from the crack. Therefore, by adjusting the depth of the well and the heights of the barriers, we can tune the accumulation rate and equilibrium point in the simulations to match the experimentally observed localization rates..

The simulated random walks of a collection of interacting self-propelled nanomotors moving with average speed of 10.4 µm/s (corresponding to a fuel concentration of 7.5%) around a crack is shown in Fig. 11D-F. Good agreement is observed between the simulations and the corresponding experiments (Fig. 11A-C). Over time, we observed the gradual accumulation of individual and assembled nanomotors within the crack. In the experiments, an average of 51% of the nanomotors was trapped in the crack after 20 minutes under these conditions. Many of the nanomotors had assembled into clusters that bridged the gap of the crack.

Increasing the peroxide fuel concentration increases the nanomotor speed and allows trajectories to reach greater distances over a given time, thus making the repair procedure more efficient. Representative samples of the experimental and simulated trajectories, demonstrating the motor localization over time as a function of their average speed, are shown in Fig. 11G-I and Fig. 11J-L, respectively. The increased length of the trajectories (over the 10 s period) reflects the increase in the speed of nanomotors due to higher fuel concentrations. In the experimental Fig. 11G-I, the faster nanomotor speeds, at higher fuel concentrations, result in the significantly greater accumulation within the cracks, as well as a greater degree of clustering. These results indicate that the greater mobility afforded by higher fuel concentrations has a two-fold effect on the nanomotor accumulation. The direct effect of increasing the fuel concentration is that the longer nanomotor trajectories, corresponding to larger mean squared displacements, increase the probability of encountering the crack. Indirectly, the faster speeds contribute to more collision events between motors, promoting cluster formation. Clusters formed outside the crack bind highly mobile free motors and slow down the dynamics, whereas clusters accumulating inside the crack facilitate the bridging of the gap. The combination of these effects is that higher speeds drastically enhance the localization process of the nanomotors over shorter time periods, which is crucial to achieving the highest repair efficiencies.

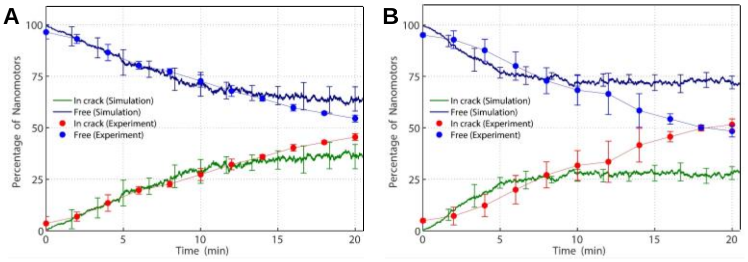

Figure 3.12 Experimental and simulated values of percentages of the free and localized nanomotors over 20 min (at 2 min intervals) using (A) low (average 7.3 motors per 100×100 μm^2) and (B) high (average 16.3 motors per 100×100 μm^2) motor density populations. Fuel level: 7.5%.

Denser nanomotor populations have more nanomotors available to interact with the crack and with each other compared to sparser ones. We investigated the effects of nanomotor density upon their accumulation within a representative segment of the crack throughout the first 20 minutes after adding the fuel. We performed multiple experiments with three different fuel concentrations – 2.5%, 5.0%, and 7.5% H_2O_2 (w/v) – at a low and high densities of 7.3±0.8 and 16.3±1.5 motors per 100×100 μm^2, respectively, totaling six unique experimental configurations. At each 2 min time interval, we counted the number of free and localized motors within the field of view of the microscope. In each case, we opted to compare the percentages of motors inside the crack versus outside the crack rather than raw counts because the total number of motors slightly varied over time, owing to nanomotors moving in and out of the field of view. Fig. 3.12 compares swimmer accumulation versus time between multiple (n = 5) low density (3A) and high density (3B) experiments at the 7.5% fuel level. We observed an average of 34 localized motors at the low density compared to an average of 60 localized motors at the high density over a 340 μm portion of the crack after 20 min, representing nearly a two-fold increase in localized motors at this fuel concentration. We observed similar, but smaller, differences in the number of localized motors between the two densities at the 2.5% and 5.0% fuel levels.

Our experimental results showed that denser populations correspond to significantly greater percentages of localized motors, indicating a larger than linear relationship between density and the number of localized motors. This behavior can be explained by noting that an increase in the number of nanomotors leads to an increase in the number of nanomotor collision events, resulting in more clusters that can accumulate as groups on the crack. In agreement with this hypothesis, we observed that in each of our high density experiments, the degree of nanomotor self-assembly was significantly higher at each fuel concentration. This also underscores the importance of the self-assembly process in the nanomotor localization: in the low density experiments using 2.5% fuel, corresponding to minimal accumulation of under 20% by 20 min, we found that few to no clusters had been formed relative to either higher fuel concentration or higher density experiments.

We also performed simulations of each of the six experimental configurations that we used to extract motor counts from an equal-area representative segment, and compared these findings to our experimental results. These comparisons are presented in Fig. 3.12 (7.5% H_2O_2). The numerical model was parameterized based on the case with the 7.5% fuel level, where the high motor density yielded the best accumulation results, with over 50% of the motors successfully localized in the crack within 20 min. Note a slight deviation between the experimental and modeling localization rates results at longer time scales; this deviation is more pronounced at the higher motor density, where clustering effects are more prominent. The discrepancy may result from the assumption of constant motor speed (implying constant fuel concentration), which may be inaccurate in larger clusters of motors. However, both modeling and experimental results pointed to the greatest localization using the motor suspension with the highest mobility and density; this combination was used to demonstrate the most efficient circuit repair process.

3.3.5 Restoring conductivity of cracked circuits

To demonstrate the autonomous healing potential of the nanomotors, we measured the conductivity of a number of gold electrodes before and after the propulsion and localization process. The gold electrode was patterned over a Si wafer, with a 300 nm SiO_2 insulating layer and a width of 5 mm. The average original resistance of the electrodes was found to be 3.2 Ω. After cracking the electrodes with a diamond tip and exposing the hydrophobic SiO_2 layer, we found that in each experiment, there was no conductivity at all between the two ends of the electrode, as shown in Fig. 3.13A prior to the 0 minute mark. To investigate the time scale for restoring the conductivity, we monitored the resistance between the two ends of the broken electrode after placing the nanomotor solution over the crack. As displayed in Fig. 3.13A, after placing the suspension of the high density of Janus nanomotors with a peroxide fuel concentration of 7.5%, we noted that the resistance of the circuit had leveled out at a maximum of 10 MΩ. This trace conductivity in the circuit at the start of the experiment is a result of the weak conductivity of water, which forms the droplets used to add both the nanomotors and fuel over the crack. This high resistance begins to decrease steadily to roughly 5 MΩ over the next 20-25 minutes, but the presence of the water droplet still interferes with accurate resistance measurements. In each experiment, we found that our low volumes of droplets eventually dried after 30 minutes on average, and resistances under 100 Ω were finally obtained, proving the successful healing of broken circuits by localization of nanomotors in the cracks. An additional thermal annealing process could further reduce the contact resistance and thereby improve the conductivity.

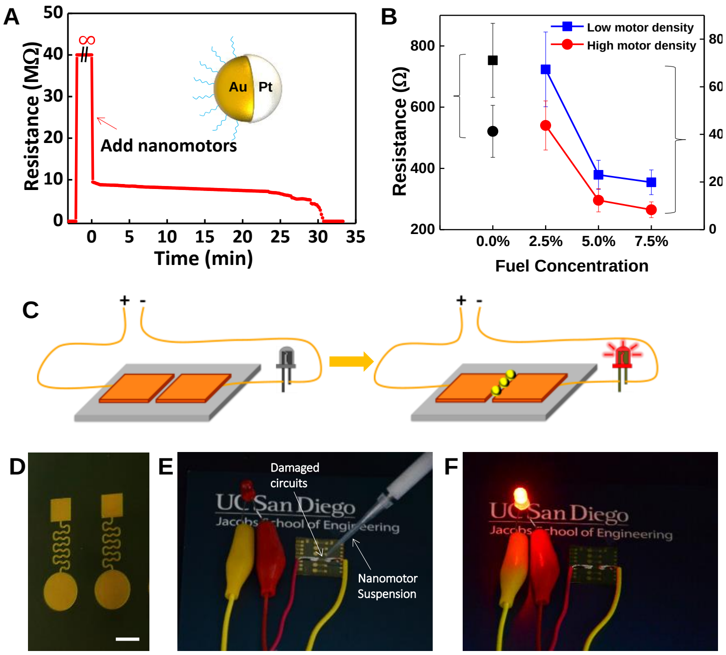

Figure 3.13 Autonomous restoration of the electrical conductivity using self-propelled nanomotors. (A) Variation of the resistance of the electrode during a representative connection/disconnection/reconnection experiment. Fuel level: 7.5%; average motor density: 16.3/100×100 μm^2. (B) Measured resistance of a gold electrode after repairing with nanomotors at four different fuel concentrations and low and high nanomotor densities. Original average resistance: 3.2 Ω. (C) Schematics illustrating the disconnection and reconnection of a simple electronic circuit using self-propelled nanomotors. (D) Image of gold electrodes patterned on a Si wafer. Scale bar: 1 mm. (E-F) Photographs of a simple circuit consisting of a damaged electrode wired to a power source and a red LED, followed by successful recovery of the conductance after placing the nanomotors solution over the crack. Fuel level: 7.5%; average motor density: 16.3/100×100 μm^2.

In line with our previous experiments and modeling of the localization process, we performed multiple conductivity restoration experiments (n = 10) for each of the aforementioned six experimental configurations to examine the effects of the nanomotor density and fuel concentration on the healing process; the results are summarized in Fig. 3.13B. A control experiment without adding hydrogen peroxide was also conducted; in the absence of the fuel and efficient self-propulsion of the nanomotor, the electrode exhibited a very large resistance (>500 Ω) after the drying of nanomotor suspension at both nanomotor density. Motor suspensions with either low fuel concentrations or low densities repaired the electrode to higher final resistances, reflecting the inferior localization and hence impaired repair. At the slowest nanomotor speeds, corresponding to 2.5% fuel concentration, even the high density suspensions repaired the damaged electrode less efficiently than the low density suspensions at the 5.0% and 7.5% fuel concentrations. But at these higher fuel levels, we found that increasing the motor density provided greater gains in the repair capacity. Motor suspensions with high mobility and high density exhibit a more efficient repair due to the improved localization capability; utilizing these conditions yielded an average final resistance of 8.9 Ω. Our experimental results closely matched the model predictions, where higher motor densities and speeds greatly contributed to improved conductivity; this conveys the critical importance of motor mobility and density upon the efficiency of the motor-based repair process.

To further demonstrate the capability of the autonomous healing system, as a proof-of-concept these nanomotors were used to repair a simple circuit consisting of a gold electrode, a direct power source and a red LED, as schematically illustrated in Fig. 3.13C. The lithographically patterned gold electrode, with a width of 200 μm, is displayed in Fig. 3.13D. After severing and damaging the electrode with a diamond tip, there was no light emitted by the red LED. We then placed a high density suspension of nanomotors with 7.5% H_2O_2 fuel over the cracked site (Fig. 3.13E). After the solution evaporated following 30 min of propulsion, the voltage was reapplied, and the conductivity of the circuit was restored by the nanomotors, as evidenced by the light emission shown in Fig. 3.13F.

The above results illustrate that such a nanomotor-based repair capability can be achieved in conductive materials, obviating the need to modify the materials themselves. These findings also indicate that the present nanomotor repair system could be adapted for use in a wide range of materials and devices. Considering that the depth of the crack-induced potential well may vary with the width of the crack, we envision that a suspension consisting of a mixture of nanomotors with different diameters could rapidly repair cracks of different widths. Note that, as in our experiments, the nanomotor diameter need not be as large as the crack width. The tendency for nanomotors to aggregate allows larger gaps to be bridged by clusters of nanomotors. In addition, the new nanomotor-based repair process is fully independent of the time after damage, allowing for restoration at any time afterwards. Such behavior demonstrates that these nanomotors can be used to autonomously repair broken conductive pathways, thus potentially expanding the utility of current nanorobotics for diverse applications in microelectronics and repairing complex integrated circuits. Furthermore, these surface energy- and geometry-based sensing mechanisms could be applied to a wide range of other nanomotor repair systems, such as the healing of diverse artificial and biological materials through defect-triggered localization or targeted drug delivery.

3.3.6 Conclusion

In conclusion, we have engineered synthetic nanomotors that self-propel and autonomously detect surface cracks to localize in these defects and rapidly restore the conductive pathway. These nanomotors convert chemical fuel in their surrounding environment into directed motion to autonomously seek the surface cracks on the substrate. Mimicking natural sensing mechanisms, the motors probe the surface for defects by utilizing the differences in surface energies, as well as geometric obstructions, which interfere with the dynamic driving forces acting on the nanomotors to trigger localization within the cracks. These nanomotors can also spontaneously self-assemble into clusters that can travel as groups towards these cracks. The surface cracks act as potential wells, which confine and localize both individual nanomotors and clusters of such motors. The restorative nature of the autonomous nanomotor system has been quantitatively examined by multiple experimental configurations and modeled by numerical simulations, leading to a good agreement between experiment and theory.

A direct application of this bio-inspired nanomotor repair system is demonstrated with the formation of conductive ‘patches’ that restore electrical conductivity in a mechanically damaged circuit. Autonomously healed circuits will lead to increased longevity and enhanced device reliability in adverse mechanical environments, enabling new applications in microelectronics, advanced batteries, and electrical systems. Although the repair functionality demonstrated here involves the selective localization of conductive nanoparticles at cracked electrodes, the self-propelled nanomotor concept can be extended to repair the biological, mechanical, optical and/or electronic properties of a wide range of damaged materials. The use of self-propelled nanomotors to probe nano- and microscale environmental changes and to promote autonomous and precise localization at desired sites opens the door for artificial responsive nanosystems with advanced biomimetic functionalities for a wide variety of applications, ranging from targeted drug delivery to self-healing nanodevices.

Chapter 3.1, in full, is a reprint of the material as it appears in Nature Communications, 2014, by Jinxing Li, Wei Gao, Renfeng Dong, Allen Pei, Sirilak Sattayasamitsathit, Joseph Wang. Chapter 3.2, in full, is a reprint of the material as it appears in Nano Letters, 2016, by Jinxing Li, Wenjuan Liu, Tianlong Li, Isaac Rozen, Jason Zhao, Babak Bahari, Boubacar Kante, Joseph Wang. Chapter 3.3, in full, is a reprint of the material as it appears in Nano Letters, 2015, by Jinxing Li, Oleg E Shklyaev, Tianlong Li, Wenjuan Liu, Henry Shum, Isaac Rozen, Anna C Balazs, Joseph Wang. The dissertation author was the primary investigator and author of these papers.

3.4 References

(1) Ito, T.; Okazaki; Okazaki, S. Pushing the Limits of Lithography. *Nature* **2000**, *406*.

(2) Service, R. F. Optical Lithography Goes to Extremes--And Beyond. *Science (80-.).* **2001**, *293*.

(3) Madou, M. J. *Fundamentals of Microfabrication : The Science of Miniaturization*; CRC Press, 2002.

(4) Vieu, C.; Carcenac, F.; Pépin, A.; Chen, Y.; Mejias, M.; Lebib, A.; Manin-Ferlazzo, L.; Couraud, L.; Launois, H. Electron Beam Lithography: Resolution Limits and Applications. *Appl. Surf. Sci.* **2000**, *164*, 111–117.

(5) Melngailis, J. Focused Ion Beam Technology and Applications. *J. Vac. Sci. Technol. B Microelectron. Nanom. Struct.* **1987**, *5*, 469.

(6) Huo, F.; Zheng, Z.; Zheng, G.; Giam, L. R.; Zhang, H.; Mirkin, C. A. Polymer Pen Lithography. *Science* **2008**, *321*, 1658–1660.

(7) Liao, X.; Brown, K. A.; Schmucker, A. L.; Liu, G.; He, S.; Shim, W.; Mirkin, C. A. Desktop Nanofabrication with Massively Multiplexed Beam Pen Lithography. *Nat. Commun.* **2013**, *4*, 1458–1464.

(8) Piner, R. D.; Zhu, J.; Xu, F.; Hong, S.; Mirkin, C. A.; Zhu; Xu; Hong; Mirkin. No Title. **1999**, *283*, 661–663.

(9) Mcleod, E.; Arnold, C. B. Subwavelength Direct-Write Nanopatterning Using Optically Trapped Microspheres. *Nat. Nanotechnol.* **2008**, *3*, 413–417.

(10) Younan Xia, †; John A. Rogers, ‡; Kateri E. Paul, § and; George M. Whitesides*, §. Unconventional Methods for Fabricating and Patterning Nanostructures. **1999**.

(11) Barth, J. V.; Costantini, G.; Kern, K. Engineering Atomic and Molecular Nanostructures at Surfaces. *Nature* **2005**, *437*, 671–679.

(12) Srituravanich, W.; Pan, L.; Wang, Y.; Sun, C.; Bogy, D. B.; Zhang, X. Flying Plasmonic Lens in the near Field for High-Speed Nanolithography. *Nat. Nanotechnol.* **2008**, *3*, 733–737.

(13) Pan, L.; Park, Y.; Xiong, Y.; Ulin-Avila, E.; Wang, Y.; Zeng, L.; Xiong, S.; Rho, J.; Sun, C.; Bogy, D. B. Maskless Plasmonic Lithography at 22 Nm Resolution. *Sci. Rep.* **2011**, *1*, 175.

(14) Schliwa, M.; Woehlke, G. Molecular Motors. *Nature* **2003**, *422*, 759–765.

(15) Bath, J.; Turberfield, A. J. DNA Nanomachines. *Nat. Nanotechnol.* **2007**, *2*, 275–284.

(16) Ismagilov, R. F.; Schwartz, A.; Bowden, N.; Whitesides, G. M. Autonomous Movement and Self-Assembly. *Angew. Chemie Int. Ed.* **2002**, *41*, 652–654.

(17) Mallouk, T. E.; Sen, A. Powering Nanorobots. *Sci. Am.* **2009**, *300*, 72–77.

(18) Ozin, G. A.; Manners, I.; Fournier-Bidoz, S.; Arsenault, A. Dream Nanomachines. *Adv. Mater.* **2005**, *17,* 3011–3018.

(19) Wang, J.; Manesh, K. M. Motion Control at the Nanoscale. *Small* **2010**, *6*, 338–345.

(20) Mei, Y.; Solovev, A. A.; Sanchez, S.; Schmidt, O. G. Rolled-up Nanotech on Polymers: From Basic Perception to Self-Propelled Catalytic Microengines. *Chem. Soc. Rev.* **2011**, *40*, 2109.

(21) Loget, G.; Kuhn, A. Electric Field-Induced Chemical Locomotion of Conducting Objects. *Nat. Commun.* **2011**, *2*, 535.

(22) Wilson, D. A.; Nolte, R. J. M.; van Hest, J. C. M. Autonomous Movement of Platinum-Loaded Stomatocytes. *Nat. Chem.* **2012**, *4*, 268–274.

(23) Wang, J.; Gao, W. Nano/Microscale Motors: Biomedical Opportunities and Challenges. *ACS Nano* **2012**, *6*, 5745–5751.

(24) Soler, L.; Magdanz, V.; Fomin, V. M.; Sanchez, S.; Schmidt, O. G. Self-Propelled Micromotors for Cleaning Polluted Water. *ACS Nano* **2013**, *7,* 9611–9620.

(25) Manesh, K. M.; Campuzano, S.; Gao, W.; Lobo-Castañón, M. J.; Shitanda, I.; Kiantaj, K.; Wang, J.; Fullerton, E. E.; Zhang, L.; Lauga, E. Nanomotor-Based Biocatalytic Patterning of Helical Metal Microstructures. *Nanoscale* **2013**, *5*, 1310–1314.

(26) Wang, W.; Li, S.; Mair, L.; Ahmed, S.; Huang, T. J.; Mallouk, T. E. Acoustic Propulsion of Nanorod Motors Inside Living Cells. *Angew. Chemie* **2014**, *126*, 3265–3268.

(27) Fischer, P.; Ghosh, A.; Felfoul, O.; Zhao, L.; Pouponneau, P.; Pileni, M. P.; Kim, M. J.; Nelson, B. J.; Crespi, V. H.; Soulez, G. Magnetically Actuated Propulsion at Low Reynolds Numbers: Towards Nanoscale Control. *Nanoscale* **2011**, *3*, 557–563.

(28) Lee, J. Y.; Hong, B. H.; Kim, W. Y.; Min, S. K.; Kim, Y.; Jouravlev, M. V.; Bose, R.; Kim, K. S. K. S.; Hwang, I.-C.; Kaufman, L. J. Near-Field Focusing and Magnification through Self-Assembled Nanoscale Spherical Lenses. *Nature* **2009**, *460*, 498–501.

(29) Dong, L.; Agarwal, A. K.; Beebe, D. J.; Jiang, H. Adaptive Liquid Microlenses Activated by Stimuli-Responsive Hydrogels. *Nature* **2006**, *442*, 551–554.

(30) McCloskey, D.; Wang, J. J.; Donegan, J. F. Low Divergence Photonic Nanojets from Si_3N_4 Microdisks. *Opt. Express* **2012**, *20*, 128.

(31) Gao, W.; Pei, A.; Feng, X.; Hennessy, C.; Wang, J. Organized Self-Assembly of Janus Micromotors with Hydrophobic Hemispheres. *J. Am. Chem. Soc.* **2013**, *135*, 998–1001.

(32) Chen, Q.; Whitmer, J. K.; Jiang, S.; Bae, S. C.; Luijten, E.; Granick, S. Supracolloidal Reaction Kinetics of Janus Spheres. *Science (80-.).* **2011**, *331*, 199–202.

(33) Pendry, J. B. Negative Refraction Makes a Perfect Lens. *Phys. Rev. Lett.* **2000**, *85*, 3966–3969.

(34) Zhang, X.; Liu, Z. Superlenses to Overcome the Diffraction Limit. *Nat. Mater.* **2008**, *7*, 435–441.

(35) Salandrino, A.; Engheta, N. Far-Field Subdiffraction Optical Microscopy Using Metamaterial Crystals: Theory and Simulations. *Phys. Rev. B* **2006**, *74*, 75103.

(36) Jacob, Z.; Alekseyev, L. V.; Narimanov, E. Optical Hyperlens: Far-Field Imaging beyond the Diffraction Limit. *Opt. Express* **2006**, *14*, 8247.

(37) Atre, A. C.; García-Etxarri, A.; Alaeian, H.; Dionne, J. A. A Broadband Negative Index Metamaterial at Optical Frequencies. *Adv. Opt. Mater.* **2013**, *1*, 327–333.

(38) Mason, D. R.; Jouravlev, M. V.; Kim, K. S. Enhanced Resolution beyond the Abbe Diffraction Limit with Wavelength-Scale Solid Immersion Lenses. *Opt. Lett.* **2010**, *35*, 2007.

(39) Schwartz, J. J.; Stavrakis, S.; Quake, S. R. Colloidal Lenses Allow High-Temperature Single-Molecule Imaging and Improve Fluorophore Photostability. *Nat. Nanotechnol.* **2010**, *5*, 127–132.

(40) Adams, J. D.; Erickson, B. W.; Grossenbacher, J.; Brugger, J.; Nievergelt, A.; Fantner, G. E. Harnessing the Damping Properties of Materials for High-Speed Atomic Force Microscopy. *Nat. Nanotechnol.* **2015**, *11*, 147–151.

(41) Friedrich, L.; Rohrbach, A. Surface Imaging beyond the Diffraction Limit with Optically Trapped Spheres. *Nat. Nanotechnol.* **2015**, *10*, 1064–1069.

(42) Hell, S. W. Far-Field Optical Nanoscopy. *Science (80-.).* **2007**, *316*, 1153–1158.

(43) MOERNER, W. E. Microscopy beyond the Diffraction Limit Using Actively Controlled Single Molecules. *J. Microsc.* **2012**, *246*, 213–220.

(44) Hell, S. W.; Wichmann, J. Breaking the Diffraction Resolution Limit by Stimulated Emission: Stimulated-Emission-Depletion Fluorescence Microscopy. *Opt. Lett.* **1994**, *19*, 780.

(45) Huang, B.; Babcock, H.; Zhuang, X. Breaking the Diffraction Barrier: Super-Resolution Imaging of Cells. *Cell* **2010**, *143*, 1047–1058.

(46) Xiao, S.; Drachev, V. P.; Kildishev, A. V.; Ni, X.; Chettiar, U. K.; Yuan, H.-K.; Shalaev, V. M. Loss-Free and Active Optical Negative-Index Metamaterials. *Nature* **2010**, *466*, 735–738.

(47) Wang, Z.; Guo, W.; Li, L.; Luk'yanchuk, B.; Khan, A.; Liu, Z.; Chen, Z.; Hong, M. Optical Virtual Imaging at 50 Nm Lateral Resolution with a White-Light Nanoscope. *Nat. Commun.* **2011**, *2*, 218.

(48) Wang, J. *Nanomachines : Fundamentals and Applications*.

(49) Wang, H.; Pumera, M. Fabrication of Micro/Nanoscale Motors. *Chem. Rev.* **2015**, *115*, 8704–8735.

(50) Palagi, S.; Mark, A. G.; Reigh, S. Y.; Melde, K.; Qiu, T.; Zeng, H.; Parmeggiani, C.; Martella, D.; Sanchez-Castillo, A.; Kapernaum, N. Structured Light Enables Biomimetic Swimming and Versatile Locomotion of Photoresponsive Soft Microrobots. *Nat. Mater.*

2016, *15*, 647–653.

(51) Orozco, J.; Cheng, G.; Vilela, D.; Sattayasamitsathit, S.; Vazquez-Duhalt, R.; Valdés-Ramírez, G.; Pak, O. S.; Escarpa, A.; Kan, C.; Wang, J. Micromotor-Based High-Yielding Fast Oxidative Detoxification of Chemical Threats. **2013**.

(52) Palacci, J.; Sacanna, S.; Steinberg, A. P.; Pine, D. J.; Chaikin, P. M. Living Crystals of Light-Activated Colloidal Surfers. *Science (80-.).* **2013**, *339*, 936–940.

(53) Li, J.; Gao, W.; Dong, R.; Pei, A.; Sattayasamitsathit, S.; Wang, J. Nanomotor Lithography. *Nat. Commun.* **2014**, *5*, 5026.

(54) Howse, J. R.; Jones, R. A. L.; Ryan, A. J.; Gough, T.; Vafabakhsh, R.; Golestanian, R. Self-Motile Colloidal Particles: From Directed Propulsion to Random Walk. *Phys. Rev. Lett.* **2007**, *99*, 48102.

(55) Eichelsdoerfer, D. J.; Liao, X.; Cabezas, M. D.; Morris, W.; Radha, B.; Brown, K. A.; Giam, L. R.; Braunschweig, A. B.; Mirkin, C. A. Large-Area Molecular Patterning with Polymer Pen Lithography. *Nat. Protoc.* **2013**, *8*, 2548–2560.

(56) Hecht, E. *Optics*; Addison-Wesley, 2002.

(57) Bhushan, B. *Springer Handbook of Nanotechnology*; Springer, 2010.

(58) Westphal, V.; Rizzoli, S. O.; Lauterbach, M. A.; Kamin, D.; Jahn, R.; Hell, S. W. Video-Rate Far-Field Optical Nanoscopy Dissects Synaptic Vesicle Movement. *Science (80-.).* **2008**, *320*, 246–249.

(59) Zhu, L.; Zhang, W.; Elnatan, D.; Huang, B. Faster STORM Using Compressed Sensing. *Nat. Methods* **2012**, *9*, 721–723.

(60) Vicidomini, G.; Moneron, G.; Eggeling, C.; Rittweger, E.; Hell, S. W. STED with Wavelengths Closer to the Emission Maximum. *Opt. Express* **2012**, *20*, 5225.

(61) Dyba, M.; Jakobs, S.; Hell, S. W. Immunofluorescence Stimulated Emission Depletion Microscopy. *Nat. Biotechnol.* **2003**, *21*, 1303–1304.

(62) Jia, S.; Vaughan, J. C.; Zhuang, X. Isotropic Three-Dimensional Super-Resolution Imaging with a Self-Bending Point Spread Function. *Nat. Photonics* **2014**, *8*, 302–306.

(63) Palacci, J.; Sacanna, S.; Abramian, A.; Barral, J.; Hanson, K.; Grosberg, A. Y.; Pine, D. J.; Chaikin, P. M. Artificial Rheotaxis. *Sci. Adv.* **2015**, *1*, e1400214–e1400214.

(64) Ma, X.; Jannasch, A.; Albrecht, U.-R.; Hahn, K.; Miguel-López, A.; Schäffer, E.; Sánchez, S. Enzyme-Powered Hollow Mesoporous Janus Nanomotors. *Nano Lett.* **2015**, *15*, 7043–7050.

(65) Bergman, S. D.; Wudl, F. Mendable Polymers. *J. Mater. Chem.* **2008**, *18*, 41–62.

(66) White, S. R.; Sottos, N. R.; Geubelle, P. H.; Moore, J. S.; Kessler, M. R.; Sriram, S. R.; Brown, E. N.; Viswanathan, S. Autonomic Healing of Polymer Composites. *Nature* **2001**, *409*, 794–797.

(67) Ghosh, B.; Urban, M. W. Self-Repairing Oxetane-Substituted Chitosan Polyurethane Networks. *Science (80-.).* **2009**, *323*, 1458–1460.

(68) Balazs, A. C. Modeling Self-Healing Materials. *Mater. Today* **2007**, *10*, 18–23.

(69) Cordier, P.; Tournilhac, F.; Soulié-Ziakovic, C.; Leibler, L. Self-Healing and Thermoreversible Rubber from Supramolecular Assembly. *Nature* **2008**, *451*, 977–980.

(70) Kolmakov, G. V.; Matyjaszewski, K.; Balazs, A. C. Harnessing Labile Bonds between Nanogel Particles to Create Self-Healing Materials. *ACS Nano* **2009**, *3*, 885–892.

(71) Tee, B. C.-K.; Wang, C.; Allen, R.; Bao, Z. An Electrically and Mechanically Self-Healing Composite with Pressure- and Flexion-Sensitive Properties for Electronic Skin Applications. *Nat. Nanotechnol.* **2012**, *7*, 825–832.

(72) Burnworth, M.; Tang, L.; Kumpfer, J. R.; Duncan, A. J.; Beyer, F. L.; Fiore, G. L.; Rowan, S. J.; Weder, C. Optically Healable Supramolecular Polymers. *Nature* **2011**, *472*, 334–337.

(73) Chen, Y.; Kushner, A. M.; Williams, G. A.; Guan, Z. Multiphase Design of Autonomic Self-Healing Thermoplastic Elastomers. *Nat. Chem.* **2012**, *4*, 467–472.

(74) Wang, C.; Wu, H.; Chen, Z.; McDowell, M. T.; Cui, Y.; Bao, Z. Self-Healing Chemistry Enables the Stable Operation of Silicon Microparticle Anodes for High-Energy Lithium-Ion Batteries. *Nat. Chem.* **2013**, *5*, 1042–1048.

(75) Li, Y.; Li, L.; Sun, J. Bioinspired Self-Healing Superhydrophobic Coatings. *Angew. Chemie Int. Ed.* **2010**, *49*, 6129–6133.

(76) Andreeva, D. V.; Fix, D.; M¨□ohwald, H.; Shchukin, D. G. Self-Healing Anticorrosion Coatings Based on pH-Sensitive Polyelectrolyte/Inhibitor Sandwichlike Nanostructures. *Adv. Mater.* **2008**, *20*, 2789–2794.

(77) Wong, T.-S.; Kang, S. H.; Tang, S. K. Y.; Smythe, E. J.; Hatton, B. D.; Grinthal, A.; Aizenberg, J. Bioinspired Self-Repairing Slippery Surfaces with Pressure-Stable Omniphobicity. *Nature* **2011**, *477*, 443–447.

(78) Kratz, K.; Narasimhan, A.; Tangirala, R.; Moon, S.; Revanur, R.; Kundu, S.; Kim, H. S.; Crosby, A. J.; Russell, T. P.; Emrick, T. Probing and Repairing Damaged Surfaces with Nanoparticle-Containing Microcapsules. *Nat. Nanotechnol.* **2012**, *7*, 87–90.

(79) Williams, K. A.; Boydston, A. J.; Bielawski, C. W. Towards Electrically Conductive, Self-Healing Materials. *J. R. Soc. Interface* **2007**, *4*, 359–362.

(80) Blaiszik, B. J.; Kramer, S. L. B.; Grady, M. E.; McIlroy, D. A.; Moore, J. S.; Sottos, N. R.; White, S. R. Autonomic Restoration of Electrical Conductivity. *Adv. Mater.* **2012**, *24*, 398–401.

(81) Li, Y.; Chen, S.; Wu, M.; Sun, J. Polyelectrolyte Multilayers Impart Healability to Highly Electrically Conductive Films. *Adv. Mater.* **2012**, *24*, 4578–4582.

(82) Palleau, E.; Reece, S.; Desai, S. C.; Smith, M. E.; Dickey, M. D. Self-Healing Stretchable

Wires for Reconfigurable Circuit Wiring and 3D Microfluidics. *Adv. Mater.* **2013**, *25*, 1589–1592.

(83) Garnett, E. C.; Cai, W.; Cha, J. J.; Mahmood, F.; Connor, S. T.; Greyson Christoforo, M.; Cui, Y.; McGehee, M. D.; Brongersma, M. L. Self-Limited Plasmonic Welding of Silver Nanowire Junctions. *Nat. Mater.* **2012**, *11*, 241–249.

(84) Kang, H. S.; Kim, H.-T.; Park, J.-K.; Lee, S. Light-Powered Healing of a Wearable Electrical Conductor. *Adv. Funct. Mater.* **2014**, *24*, 7273–7283.

(85) Benight, S. J.; Wang, C.; Tok, J. B. H.; Bao, Z. Stretchable and Self-Healing Polymers and Devices for Electronic Skin. *Prog. Polym. Sci.* **2013**, *38*, 1961–1977.

(86) Cui, J.; Daniel, D.; Grinthal, A.; Lin, K.; Aizenberg, J. Dynamic Polymer Systems with Self-Regulated Secretion for the Control of Surface Properties and Material Healing. *Nat. Mater.* **2015**, *14*, 790–795.

(87) Liu, H. A.; Gnade, B. E.; Balkus, K. J. A Delivery System for Self-Healing Inorganic Films. *Adv. Funct. Mater.* **2008**, *18*, 3620–3629.

(88) Patrick, J. F.; Hart, K. R.; Krull, B. P.; Diesendruck, C. E.; Moore, J. S.; White, S. R.; Sottos, N. R. Continuous Self-Healing Life Cycle in Vascularized Structural Composites. *Adv. Mater.* **2014**, *26*, 4302–4308.

(89) Yuan, Y. C.; Yin, T.; Rong, M. Z.; Zhang, M. Q. Self Healing in Polymers and Polymer Composites. Concepts, Realization and Outlook: A Review. *Express Polym. Lett.* **2008**, *2*, 238–250.

(90) Greenhalgh, D. G. The Role of Apoptosis in Wound Healing. *Int. J. Biochem. Cell Biol.* **1998**, *30*, 1019–1030.

(91) Clemetson, K. J. Platelets and Primary Haemostasis. *Thromb. Res.* **2012**, *129*, 220–224.

(92) Guix, M.; Mayorga-Martinez, C. C.; Merkoçi, A. Nano/Micromotors in (Bio)chemical Science Applications. *Chem. Rev.* **2014**, *114*, 6285–6322.

(93) Nelson, B. J. B.; Kaliakatsos, I. K. I.; Abbott, J. J. Microrobots for Minimally Invasive Medicine. *Annu. Rev. Biomed. Eng.* **2010**, *12*, 55–85.

(94) Kim, K.; Guo, J.; Xu, X.; Fan, D. L. Recent Progress on Man-Made Inorganic Nanomachines. *Small* **2015**, *11*, 4037–4057.

(95) Ibele, M.; Mallouk, T. E.; Sen, A. Schooling Behavior of Light-Powered Autonomous Micromotors in Water. *Angew. Chemie Int. Ed.* **2009**, *48*, 3308–3312.

(96) Wang, J. Can Man-Made Nanomachines Compete with Nature Biomotors? *ACS Nano* **2009**, *3*, 4–9.

(97) Sánchez, S.; Soler, L.; Katuri, J. Chemically Powered Micro- and Nanomotors. *Angew. Chemie Int. Ed.* **2015**, *54*, 1414–1444.

(98) Smith, T. The Hydrophilic Nature of a Clean Gold Surface. *J. Colloid Interface Sci.* **1980**, *75*, 51–55.

(99) Paxton, W. F.; Sen, A.; Mallouk, T. E. Motility of Catalytic Nanoparticles through Self-Generated Forces. *Chem. - A Eur. J.* **2005**, *11*, 6462–6470.

(100) Lee, T.-C.; Alarcón-Correa, M.; Miksch, C.; Hahn, K.; Gibbs, J. G.; Fischer, P. Self-Propelling Nanomotors in the Presence of Strong Brownian Forces. *Nano Lett.* **2014**, *14*, 2407–2412.

(101) Guix, M.; Orozco, J.; García, M.; Gao, W.; Sattayasamitsathit, S.; Merkoçi, A.; Escarpa, A.; Wang, J. Superhydrophobic Alkanethiol-Coated Microsubmarines for Effective Removal of Oil. *ACS Nano* **2012**, *6*, 4445–4451.

(102) Yadav, V.; Freedman, J. D.; Grinstaff, M.; Sen, A. Bone-Crack Detection, Targeting, and Repair Using Ion Gradients. *Angew. Chemie Int. Ed.* **2013**, *52*, 10997–11001.

(103) Schweitzer, F.; Schimansky-Geier, L. Clustering of "active" Walkers in a Two-Component System. *Phys. A Stat. Mech. its Appl.* **1994**, *206*, 359–379.

(104) Wang, J.-C.; Neogi, P.; Forciniti, D. On One-Dimensional Self-Assembly of Surfactant-Coated Nanoparticles. *J. Chem. Phys.* **2006**, *125*, 194717.

(105) Brugués, J.; Casademunt, J. Self-Organization and Cooperativity of Weakly Coupled Molecular Motors under Unequal Loading. *Phys. Rev. Lett.* **2009**, *102*, 118104.

(106) Downton, M. T.; Zuckermann, M. J.; Craig, E. M.; Plischke, M.; Linke, H. Single-Polymer Brownian Motor: A Simulation Study. *Phys. Rev. E* **2006**, *73*, 11909.

(107) Verberg, R.; Dale, A. T.; Kumar, P.; Alexeev, A.; Balazs, A. C. Healing Substrates with Mobile, Particle-Filled Microcapsules: Designing a "repair and Go" System. *J. R. Soc. Interface* **2007**, *4*, 349–357.

(108) Kolmakov, G. V.; Revanur, R.; Tangirala, R.; Emrick, T.; Russell, T. P.; Crosby, A. J.; Balazs, A. C. Using Nanoparticle-Filled Microcapsules for Site-Specific Healing of Damaged Substrates: Creating a "Repair-and-Go" System. *ACS Nano* **2010**, *4*, 1115–1123.

(109) Lee, J. Y.; Buxton, G. A.; Balazs, A. C. Using Nanoparticles to Create Self-Healing Composites. *J. Chem. Phys.* **2004**, *121*, 5531–5540.

Chapter 4 Towards the *Fantastic Voyage*: Micromotor based Autonomous Medicine

4.1 *In vivo* use of synthetic motors in mouse's stomach

4.1.1 Introduction

The development of small-scale synthetic motors that convert energy into movement and forces has been a fascinating research area [1–8]. Impressive progress made over the past decade has led to a variety of powerful microscale motors based on different propulsion mechanisms and design principles. New functionalities and capabilities have been added to these micromotors, leading to advanced microscale machines that offer a wide range of important applications. In particular, the movement of man-made micromachines in biological fluids can benefit biomedical fields such as directed drug delivery, diagnostics, nanosurgery, and biopsy [9–11]. For example, functional micromotors have shown considerable promise for isolating circulating tumor cells and bacteria from raw biological fluids [12,13]. Mallouk *et al.* have recently reported the ultrasound-driven propulsion of nanowire motors in living cells [14], while Nelson *et al.* have explored targeted drug delivery based on magnetically-propelled artificial flagella [15]. *In vitro* testing by Pumera's team found no apparent toxicity effects of catalytic microngines on cell viability [16]. Although tremendous progress has been made toward such biomedical applications, there are no reports so far illustrating and examining the *in vivo* operation and behavior of these tiny micromotors. Lacking the characterization and evaluation of these synthetic motors in whole living organisms greatly hinders their further development towards practical and routine biomedical applications.

Here we demonstrate the first study of synthetic motors under *in vivo* conditions, involving acid-powered zinc-based micromotors in a living organism. Among the variety of recently developed artificial micromotors, our recently reported zinc-based motors hold great promise for *in vivo* use, particularly for gastric drug delivery, because of their unique features, including acid-powered propulsion, high loading capacity, autonomous release of payloads, and non-toxic self-destruction [17,18]. Fabricated through established membrane templating processes, the zinc-based micromotors can display efficient propulsion in harsh acidic environment without an additional fuel and transport fully-loaded cargoes at high speeds. As the zinc body is dissolved by the acid fuel, the motors are self-destroyed, leaving no harmful chemicals behind [17,18]. Such attractive behavior makes these zinc-based micromotors useful for movement and operation in the harsh stomach environment, hence opening the door to the first *in vivo* operation of micro/nanomotors in living animals.

In this study, the zinc-based micromotors are applied to the stomach of living mice through gavage administration. The autonomous movement of these motors in gastric acid and the motion-induced biodistribution and retention of the micromotors on the stomach wall are carefully evaluated, along with their *in vivo* toxicity profile. Our results demonstrate that the self-propulsion of the micromotors leads a dramatically improved retention of their payloads in the stomach lining compared to the common passive diffusion and dispersion of orally administrated payloads. These findings, along with the absence of toxic effects in stomach, indicate that the movement of micromotors in the stomach fluid offers potentially distinct advantages for *in vivo* biomedical applications and pave the way for their future clinical studies.

4.1.2 Experimental Section

Synthesis of zinc-based micromotors

The PEDOT/Zn micromotors were prepared using a template-directed electrodeposition protocol. The Cyclopore polycarbonate membranes, containing 5 µm diameter (Catalog No 7060-2513; Whatman, Maidstone, U. K.) conical-shaped micropores, were employed as the templates. A 75 nm thick gold film was first sputtered on one side of the porous membrane to serve as working electrode using the Denton Discovery 18. Sputtering was performed at room temperature for 90 s under vacuum of 5×10^{-6} Torr, DC power 200 W, Ar flow of 3.1 mT, and rotation speed of 65 rpm. A Pt wire and an Ag/AgCl electrode (with 3 M KCl) were used as counter and reference electrodes, respectively. The membrane was then assembled in a plating cell with an aluminum foil serving as a contact. First, the outer PEDOT layer of the microtubes was prepared by electropolymerization at +0.80 V using a charge of 0.06 C from a plating solution containing 15 mM EDOT, 7.5 mM KNO_3 and 100 mM sodium dodecyl sulfate (SDS). Subsequently, the inner zinc tube was deposited galvanostatically at -6 mA for 1 hour from a commercial zinc plating solution containing 80 g l^{-1} $ZnSO_4$ and 20 g l^{-1} H_3BO_3 (buffered to pH = 2.5 with sulfuric acid). For the PEDOT/Pt control micromotors, the inner Pt tube was deposited galvanostatically at -2 mA for 10 min from a commercial platinum plating solution (Platinum RTP; Technic Inc, Anaheim, CA). The sputtered gold layer was removed by hand polishing with 3-4 µm alumina slurry. The membrane was then dissolved in methylene chloride for 10 min to completely release the microtubes. The microtubes were collected by centrifugation at 6000 rpm for 3 min and washed repeatedly with methylene chloride, followed by ethanol and ultrapure water (18.2 MΩ cm), three times of each. Finally, the microtubes from the whole piece of membrane were dispersed into 1.2 mL ultrapure water. The simulated gastric acid (pH 1.2) was prepared by adding 2.0 g NaCl and 7 ml HCl (12 M) in 1.0 L of ultrapure water (18.2 MΩ cm).

Stomach retention of PEDOT/Zn micromotors

To measure the retention of the PEDOT/Zn micromotors, ICR male mice at 6 weeks of age were randomly assigned to 4 groups (n=3) and orally administered with 0.3 mL of the PEDOT/Zn micromotor or PEDOT/Pt micromotor solution by oral-gavage. Mice were sacrificed at 2, 6, or 12 hours post administration of PEDOT/Zn micromotors and 2 hours post administration of PEDOT/Pt micromotors, and their stomachs were removed from the abdominal cavity. The stomachs were cut open along the greater curvature, the gastric content was removed, and the gastric fluid containing excess micromotors was washed away. The micromotors retained on stomach lining of the mice from each group were counted under optical microscope.

Cargo delivery by PEDOT/Zn micromotors

To study the capability of PEDOT/Zn micromotors as a carrier for cargo delivery, AuNPs was chosen as a model payload. AuNPs were prepared as previously described. Briefly, sodium citrate solution (2.2 mM) was dissolved into DI water (150 mL) in a three-neck round-bottom flask and heated to 100°C, followed by addition of $HAuCl_4$ aqueous solution (1.0 mL, 25 mM). The reaction mixture was maintained at the boiling temperature for additional 3.5 min followed by cooling to room temperature. The resulting AuNPs (20 mL) were poured into $HAuCl_4$ (8 mL, 2.5 mM, 0.008g) under magnetic stirring. Then, freshly prepared NH_2OH solution (40 mg in 4 mL) was added dropwise and stirred for 30 min to allow the reduction of $HAuCl_4$ to form AuNP with diameters of 50 nm. Particle size (diameter, nm) was measured by DLS on a Zetasizer Nano ZS (model ZEN3600 from Malvern Instruments). To prepare the AuNPs-loaded micromotors, the PEDOT outer layer was electropolymerized first in the 5 μm diameter membrane template at +0.80 V using a charge of 0.06 C from a plating solution containing 15 mM EDOT, 7.5 mM KNO_3 and 100 mM sodium dodecyl sulfate (SDS). Then, AuNPs were loaded into the membranes by encapsulation method. Solutions of AuNPs were passed through membrane pores by vacuum infiltration before the zinc deposition. A polycarbonate membrane with pore sizes of 15 nm was placed below the sputtered Au film of the membrane containing PEDOT microtubes to retain the AuNPs within the upper 5 μm membrane pores. The membrane was then assembled in a plating cell for electrodeposition of zinc.

For the *in vivo* cargo delivery experiments, ICR male mice at 6 weeks of age were randomly assigned to 3 groups (n=4) to receive free AuNPs, AuNPs-loaded PEDOT/Zn micromotors, and PBS as control. Each mouse in the first two groups was administered orally (by oral-gavage) 0.3 mL of the free AuNPs solution, and of the AuNPs-loaded PEDOT/Zn micromotors containing the same amount of AuNPs. After 2 hours of administration, the mice were sacrificed and the stomach was removed from the abdominal cavity. The stomach was cut along the greater curvature and rinsed with PBS. Gastric tissue of the mouse from each group was weighted. The tissue was added to 3 mL aqua regia consisting of concentrated nitric acid and hydrochloric acid (Sigma-Aldrich, trace element analysis grade) in a volume ratio of 1:3. The mixture was left at room temperature for 12 hours, followed by annealing at 80°C for 6 hours to remove the acids. The sample was then resuspended with 3 mL DI water. Inductively-Coupled Plasma Mass-Spectrometry (ICP-MS) was used to quantify the amount of AuNPs delivered and retained in the stomach tissue.

In Vivo Toxicity Study

To evaluate the toxicity of PEDOT/Zn micromotors *in vivo*, ICR male mice at 6 weeks of age were orally administered with 0.3 mL of the PEDOT/Zn micromotors, as well as with free AuNPs or AuNPs-loaded PEDOT/Zn micromotors. Mice administered with PBS were used as a negative control. At 6 hours after the administration, the mice were sacrificed and the stomachs were collected for histological analysis. The longitudinal sections of the gastric tissue were fixed in neutral-buffered 10% formalin and then embedded in paraffin. The tissue sections were stained with hematoxylin and eosin (H&E). Epithelial cell apoptosis was evaluated by the terminal deoxynucleotidyl transferase-mediated deoxyuridine triphosphate nick-end labeling (TUNEL) assay (Boehringer Mannheim, Indianapolis, IN). Sections were visualized by Hamamatsu NanoZoomer 2.0HT and the images were processed using NDP viewing software. All animal experiments were in compliance with institutional animal use and care regulations.

Equipment

Template electrochemical deposition of micromotors was carried out with a CHI 661D potentiostat (CH Instruments, Austin, TX). SEM images were obtained with a Phillips XL30 ESEM instrument, using an acceleration potential of 20 kV. The SEM images were taken using fresh micromotor samples. Mapping elemental analysis was carried out using an Oxford EDX attached to the SEM instrument and operated by Inca software. Microscope images and videos were captured by an inverted optical microscope (Nikon Instrument Inc. Ti-S/L100), coupled with a 10x objective, using a Hamamatsu digital camera C11440 along with the NIS-Elements AR 3.2 software. The size of the gold particle (diameter, nm) was measured by DLS on a Zetasizer Nano ZS (model ZEN3600 from Malvern Instruments). The amount of the released AuNPs retaining on the mouse stomach was quantified using an ICP-MS analyzer (Perkin-Elmer Optima 3000 DV).

4.1.3 Preparation and characterization of PEDOT/Zn micromotors

Fig. 4.1a illustrates the self-propulsion and tissue penetration of acid-driven poly(3,4-ethylenedioxythiophene)(PEDOT)/zinc(Zn) micromotors in the stomach environment. The PEDOT/Zn bilayer micromotors were fabricated using Cyclopore polycarbonate membrane templates containing microconical pores (Fig. 4.1b). Due to solvophobic and electrostatic effects, the monomers initially polymerized on the inner wall of the membrane pores, leading to a rapid formation of the outer PEDOT layer [19]. A zinc layer was subsequently deposited galvanostatically within the PEDOT microtube. The resulting PEDOT/Zn bilayer microstructures were then released by dissolving the membrane templates. Fig. 4.1c (left) displays a side-view SEM image of two typical PEDOT/Zn micromotors. Such biconical micromotors have a length of 20 μm and a diameter of 5 μm. Energy-dispersive X-ray spectroscopy (EDX) mapping analysis, carried out to confirm the motor composition (Fig. 4.1c, right), illustrates the presence of zinc throughout the motor body. Immersion of the PEDOT/Zn micromotors in the gastric acid resulted in a spontaneous redox reaction involving the Zn oxidation and the generation of hydrogen bubbles essential for the propulsion thrust. Fig. 4.1d displays time-lapse images, taken from the supporting video S1, for the movement of the PEDOT/Zn micromotor in a simulated gastric acid (pH 1.2) over a 3 s period at 1 s intervals (I-IV). These images illustrate a defined tail of hydrogen microbubbles generated on the inner Zn surface and released from one side of the micromotors, propelling the micromotors at a high speed of ~60 μm/s. Such efficient propulsion of the zinc-based micromotors at the gastric pH indicates considerable promise for *in vivo* evaluation and operation, as envisioned in Fig. 4.1a.

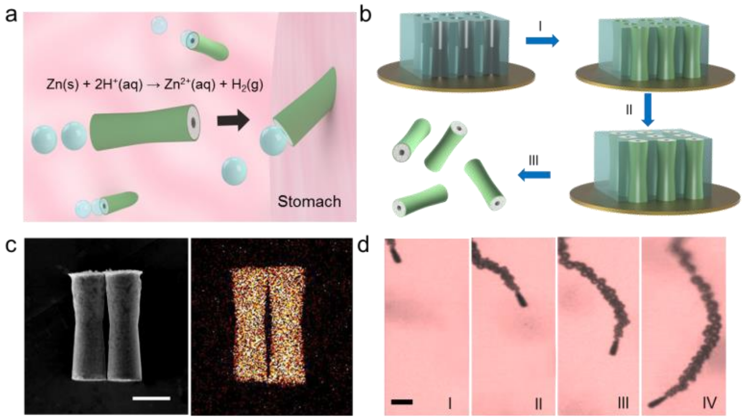

Figure 4.1 Preparation and characterization of PEDOT/Zn micromotors. (a) Schematic of the in-vivo propulsion and tissue penetration of the zinc-based micromotors in mouse stomach. (b) Preparation of PEDOT/Zn micromotors using polycarbonate membrane templates: (I) deposition of the PEDOT microtube, (II) deposition of the inner zinc layer, and (III) dissolution of the membrane and release of the micromotors. (c) Scanning electron microscopy (SEM) image (left) of the PEDOT/Zn micromotors and the corresponding energy-dispersive X-ray spectroscopy (EDX) data (right) of elemental Zn in the micromotors. Scale bar, 5 μm. (d) Time lapse images (1 s intervals, I-IV) of the propulsion of PEDOT/Zn micromotors in gastric acid under physiological temperature (37 °C). Scale bar, 20 μm.

4.1.4 Tissue Retention of micromotors in mouse stomch

In order to demonstrate that the zinc-based micromotors hold such distinct advantages for *in vivo* operation and potential for biomedical applications, we first examined their retention properties on the stomach tissues using a mouse model. The micromotors were administered to the mice orally after the mice were fasted overnight (in order to avoid the influence of food). To examine the effect of the micromotor propulsion upon the tissue penetration, we compared the retention behavior of PEDOT/Zn micromotors with that of PEDOT/Pt micromotors (which cannot move in the stomach environment and thus serve as a control). Following 2 hours of the micromotors administration, the mice were sacrificed and their entire stomach was excised and opened. Subsequently, the luminal lining was rinsed with PBS and flattened for imaging and micromotors counting. The gastric tissue obtained from the mice treated with PEDOT/Zn micromotors displayed a large amount of micromotors retained on the stomach lining 2 hours post administration (Fig. 4.2a). In contrast, a significantly smaller amount of the control PEDOT/Pt micromotors (which are very stable in the stomach environment and do not exhibit autonomous propulsion) was retained on the stomach wall using the same experimental conditions (Fig. 4.2d). Apparently, the propulsion of the Zn-based micromotors in the acidic stomach environment greatly improved their tissue penetration and retention. It is well documented that the inner surface of the stomach is covered by a 170 µm thick mucus layer, which is composed primarily of crosslinked and entangled mucin fibers [20]. When the conical motors are actively propelled in the stomach, they have a great chance to penetrate into the porous, gel-like mucus layer and be trapped within the mucus. The retention of PEDOT/Zn micromotors in the gastric tissue was further examined at 6 and 12 hours after their administration (Fig. 4.2b,c). The number of micromotors retained in the stomach tissues decreased gradually from 285 per mm^2 to 70 per mm^2 and to 25 per mm^2 at 2, 6 and 12 hours post oral administration, respectively (Fig. 4.2e). Such time-dependent decrease of motor retention in the mouse stomach is likely due to further degradation of the anchored motors under gastric conditions as well as their transfer to the subsequent digestive systems such as the small intestine. Nevertheless, the results clearly demonstrate that even after 12 hours micromotors are still observed in the stomach tissue, indicating the efficient tissue penetration of the motors.

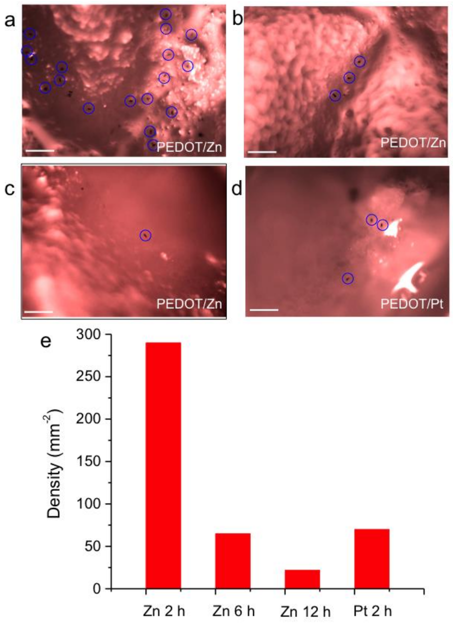

Figure 4.2 Tissue retention of PEDOT/Zn micromotors. (a-d) Microscopic images illustrate the retained micromotors on the stomach tissues collected at (a) 2 hours, (b) 6 hours, and (c) 12 hours post oral administration of PEDOT/Zn micromotors, and (d) 2 hours post oral administration of PEDOT/Pt micromotors (serving as a negative control). Scale bars, 100 µm. (e) Enumeration of the density of PEDOT/Zn and PEDOT/Pt micromotors retained on the stomach tissues at the different times after the administration.

4.1.5 Cargo delivery in mouse stomach

Next, we tested the *in vivo* functionalities of such PEDOT/Zn micromotors for possible applications, particularly for cargo delivery in living organisms. In our previous study [18], we reported the *in vitro* capabilities of Zn-based micromotors for combinational cargo delivery and multifunctional operation, including autonomous release of cargo and self-destruction of the motors during the acid-driven movement of the zinc motors. Taking advantages of these attractive capabilities, we demonstrated here that PEDOT/Zn micromotors could effectively deliver the cargoes *in vivo*. Compared to the previously reported fully-loaded zinc micromotors that could operate only in extremely strong acid and had very short lifetimes (<1 min) [18], the presence of the outer PEDOT polymeric layer here greatly enhances the propulsion performance and lifetime of the zinc micromotors under a broad spectrum of acidic conditions characteristic of the stomach environment. Such PEDOT based micromotors can be self-propelled for ~10 mins in the stomach environment under physiological temperature (pH up to 2). In this study, gold nanoparticles (AuNPs) were employed as a model cargo because of their widespread use as imaging agents and drug carriers [21]. Fig. 4.3a (left) shows an SEM image of a PEDOT/Zn micromotors loaded with AuNPs (~50 nm diameter) through vacuum infiltration before the zinc deposition. The corresponding EDX mapping analysis indicates a uniform distribution of elemental Zn and Au over the entire micromotor body (Fig. 4.3a, center and right panel, respectively), which confirms the successful encapsulation of the AuNP cargoes. Note that the AuNPs are hardly observed in the SEM image because of their extremely small size and confinement within the Zn body. Supporting video S2 displays the autonomous propulsion of two AuNPs loaded PEDOT/Zn micromotors in gastric acid at physiological temperature (37 °C). No obvious difference in the propulsion behavior was observed between regular and AuNPs-loaded micromotors. Oral administration of these AuNPs-loaded PEDOT/Zn micromotors into the mouse stomach led to their movement in the gastric fluid and binding to the mucus layer on the stomach wall. The zinc dissolution at the gastric acidic condition is accompanied with autonomous release and delivery of the encapsulated AuNPs cargo to the stomach tissue during this *in vivo* operation. The motor-based active delivery strategy resulted in distinct improvement in the delivery efficiency compared to the common passive diffusion of orally administrated AuNPs. The amount of the released AuNPs retaining on the mouse stomach was quantified by inductively-coupled plasma/mass spectrometry (ICP-MS). As shown in

Fig. 4.3b, this spectroscopic metal analysis demonstrates that under the same experimental conditions the mice treated orally with AuNPs alone retained 53.6 ng Au per gram tissue compared to 168 ng Au per gram tissue for the mice treated with PEDOT/Zn micromotors loaded with an equivalent amount of AuNPs. Regular PEDOT/Zn micromotors, without AuNPs loading, were used as control. Apparently, loading the AuNPs cargo onto the self-propelled "mother ship" micromotor leads to a significantly (>3 fold) larger retention of AuNPs on the stomach tissue compared to the orally administrated NPs. The high retention of AuNPs can be attributed to the effective penetration and retention of the micromotors that will concentrate and localize the AuNP payloads on the stomach wall. Moreover, the subsequent self-dissolution of the Zn-based motors will release the AuNPs to the mucus layer, which will further trap and retain the released AuNPs. These finding clearly illustrate the importance of the micromotor propulsion for enhancing the delivery efficiency compared to the common passive diffusion. While the concept of *in vivo* cargo delivery of PEDOT/Zn micromotors was illustrated through the loading of model AuNPs, it could be readily expanded to the simultaneous encapsulation and rapid delivery of a wide variety of payloads possessing different functions such as therapy, diagnostics, and imaging. Unlike most existing micromotors, Zn-basedmicromotors destroy themselves upon completing their cargo delivery mission [18].[20] It is also possible to add additional functionalities to these micromotors through bulk or surface modifications [17,22] toward diverse biomedical applications.

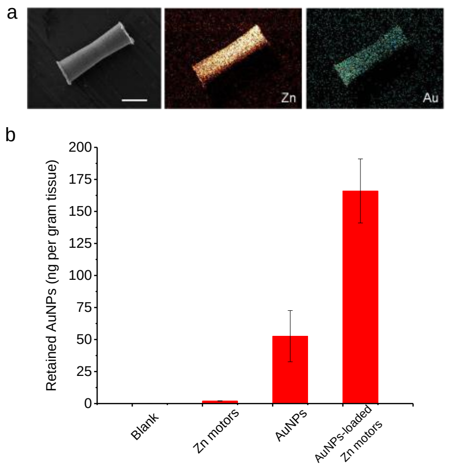

Figure 4.3 In vivo cargo delivery. (a) SEM image of a AuNP-loaded PEDOT/ZN micromotor (left) and EDX analysis illustrating the presence of Zn (middle) and Au (right) within the motor. Scale bar, 5 µm. (b) Inductively coupled plasma - mass spectrometry (ICP-MS) analysis of the amount of gold retained on the stomach tissues. The AuNP-loaded PEDOT/Zn micromotors or AuNPs were administered orally to the mice and the stomach tissues were collected 2 hours post the administration.

4.1.6 Toxicity evaluation of micromot

Finally, we evaluated the acute toxicity of the biodegradable micromotors on healthy mice. Toxicity is a primary issue in any live animal experiment and hence in practical real-world *in vivo* applications of micromotors. The main degradation product of the present micromotors is Zn^{2+}, which is an essential multipurpose nutrient involved in many aspects of metabolism and found in all body tissues [23]. In the study, mice were orally administered with PEDOT/Zn micromotors, AuNPs-loaded PEDOT/Zn micromotors, free AuNPs, or PBS. Mice were fasted overnight before administrating these samples to avoid the influence of food in the digestive tracts. All the mice were sacrificed 6 hours after administrating the micromotors or the AuNPs. The longitudinal sections of gastric tissues obtained from mice were collected and rinsed three times with PBS. The tissue sections were stained with hematoxylin and eosin (H&E). The gastric tissue treated with PEDOT/Zn micromotors maintained an intact structure with a clear layer of epithelial cells (Fig.

4.4c), which was similar to the gastric samples treated with PBS (Fig. 4.4a). The gastric tissue treated with free AuNPs (Fig. 4.4e) and with AuNPs-loaded PEDOT/Zn micromotors (Fig. 4.4g) showed no apparent toxicity as well. The potential toxicity of the PEDOT/Zn micromotors was further evaluated using gastric tissue sections by a terminal deoxynucleotidyl transferase-mediated deoxyuridine triphosphate nick-end labeling (TUNEL) assay to examine the level of gastric epithelial apoptosis as an indicator of gastric mucosal homeostasis [24]. No apparent increase in gastric epithelial apoptosis was observed for treatment groups involving PEDOT/Zn micromotors (Fig. 4.4b), free AuNPs (Fig. 4.4f) and AuNPs-loaded PEDOT/Zn micromotors (Fig. 4.4h), compared to the PBS control group (Fig. 4.4d). The absence of any detectable gastric histopathologic change and toxicity indicates that the orally administrated PEDOT/Zn micromotors and AuNPs-loaded PEDOT/Zn micromotors are safe to the model mouse. While these Zn-based micromotors can penetrate the mucus layer on the stomach wall and thus improve the retention of the motors in the mouse's stomach, such penetration and retention do not induce destructive effect on the gastric epithelial cells. The PEDOT polymer is a known non-cytotoxic material which shows no apparent immunological response [25]. Similarly, zinc is a biocompatible "green" nutrient trace element, vital for numerous body functions and processes. Accordingly, the PEDOT/Zn micromotors leave no harmful products following their movement, cargo delivery and self destruction in the stomach fluid, making them attractive nanoshuttles in living organisms. The absence of toxic effects in the stomach is in agreement with the *in-vitro* study of the influence of micromotors on cell viability [16]. It should be pointed out that changing the micromotor composition would require re-assessment of the toxic response.

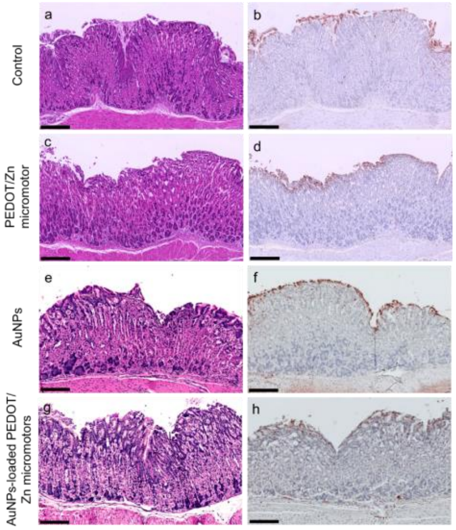

Figure 4.4 Toxicity evaluation of PEDOT/Zn micromotors. The mouse stomach was treated with PBS buffer (a, b), PEDOT/Zn micromotor (c, d), AuNPs (e, f), and AuNP-loaded PEDOT/Zn micromotors (g, h). At 6 hours post treatment, the mice were sacrificed and sections of the mouse stomach were processed as described in Materials and Methods section and stained with H&E assay (a, c, e, and g) or TUNEL assay (b, d, f, and h). Scale bars, 250 μm.

4.1.7 Conclusion

In summary, we reported the first *in vivo* study of artificial micromotors using a live mouse model, and characterized their distribution, retention, cargo delivery and toxicity profile in mouse stomach. These acid-powered micromotors were applied to the stomach of living mice through gavage administration and their retention on the gastric tissue was investigated, along with related toxicity profile. The self-propulsion in the local stomach environment led to greatly improved tissue penetration and retention. Autonomous and efficient *in vivo* release and delivery of cargo payloads upon the self-destruction of the motors were also demonstrated. Such active motor-based delivery strategy offers dramatic improvement in the efficiency compared to the common passive diffusion of orally administrated cargoes. While additional *in vivo* characterizations are warranted to further evaluate the performance and functionalities of various man-made micromotors in living organisms, this study represents the very first step towards such goal. Our new findings and insights are thus expected to advance the field of synthetic nano/micromotors and to promote interdisciplinary collaborations towards expanding the horizon of man-made nanomachines in medicine.

4.2 Enteric Micromotor Can Selectively Position and Spontaneously Propel in the Gastrointestinal Tract

4.2.1 Introduction

Microbiomes play important roles in the health of many animals, including human beings, thus have attracted intense research interest [26,27]. While most of the GI microbes live in harmony with the host, some are hostile and cause a variety of diseases. These bacteria colonize in different segments of the GI tract, dependent on local factors [28,29]. Therefore, selectively locating therapeutic or imaging agents to specific segments of the GI tract is of considerable interest [30]. Ideal GI delivery system should protect the cargos en-route and accurately locate them to the site of action. Upon arrival at destination, the carrier should retain there for unloading the cargos. Fulfilling this goal is hampered by the body's natural physiological and structural barriers. As a result, it still remains an unmet need to develop a biocompatible nano/micro-scale device that can selectively position in a specific segment of the GI tract and actively penetrate into the tissue for prolonged retention.

Over the past decade, remarkable advances have been made in the development of artificial micromotors, which are tiny devices that convert locally supplied fuels or externally provided energy to propelling force and movement [1,3,8,11,31–34]. These micromotors have proved useful for performing diverse biomedical tasks, including transport of cargos, biosensing and imaging, and target isolation [9,35–37]. After nearly ten years of basic research on the synthesis and characterization of artificial micromotors in test-tubes, the field has recently reached a new milestone where the performance and functionality of the motors were being evaluated in live bodies. For instance, the *in vivo* evaluation of synthetic micromotors demonstrated that acid-powered motors can function in a live mouse's stomach for gastric cargo delivery without causing toxic effects [38]. Magnetic actuation and navigation were also applied to control the swarming of artificial bacterial flagella *in* *vivo* [39]. These studies demonstrate that motor-based active delivery approaches offer attractive features for localized cargo delivery.

In this study, we developed an enteric micromotor consisting of a magnesium (Mg)-based motor body with an enteric polymer coating. The Mg body allows for spontaneous propulsion in intestinal fluid while the coating, which is stable in acidic conditions but soluble in neutral or alkaline media [40,41], enables accurate positioning in the GI tract. The enteric coating can shield the motors from acidic gastric fluid environment (pH 1~3), but dissolves in intestinal fluid (pH 6~7) to expose the motors to their fuel and start the movement. By tailoring the thickness of the enteric coating, we can tune the time required to dissolve the polymer layer, thereby controlling the distance that the motors can travel in the GI tract before their propulsion is activated. Upon activation the motors will propel and penetrate into the local tissue and retain there to release payloads. The properties and functions of the synthesized enteric magnesium micromotors (EMgMs) are evaluated in a mouse model. The *in vivo* results demonstrate that these motors can safely pass through the gastric fluid and accurately activate in the GI tract without causing noticeable acute toxicity.

4.2.2 Experimencal Section

Synthesis of EMgMs

Polycarbonate (PC) membrane templates (110607, Whatman, NJ, USA) with pore sizes of 5 μm were used for fabricating the Mg-based micromotors. A 75 nm gold film was sputtered on one side of the porous membrane to serve as a working electrode using the Denton Discovery 18 (Moorestown, NJ, USA). A Pt wire and an Ag/AgCl (with 1 M KCl) were used as counter and reference electrodes, respectively. The membrane was then assembled in a plating cell with aluminum foil serving as a contact. All electrochemical deposition steps were carried out at room temperature (22 °C). First, the outer PEDOT layer of the microtubes was prepared by electropolymerization at +0.80 V using a charge of 0.2 C from a plating solution containing 15 mM

EDOT, 7.5 mM KNO_3, and 100 mM sodium dodecyl sulfate (SDS); subsequently, a gold layer was deposited at −0.9 V from a commercial gold plating solution (Orotemp 24 RTU RACK; Technic Inc., USA) with a total charge of 0.6 C. After electrochemical deposition, the sputtered gold layer was completely removed by mechanical polishing with 3 μm alumina slurry. In order to get the Mg microparticles with favorable size to be loaded in the prepared PEDOT/Au microtube with a diameter of ~5 μm, the microparticles were collected from the commercial ones (size 0.2-50 μm catalog #FMW20, TangShanWeiHao Magnesium Powder Co., China). Vacuum infiltration process by a 5 μm Polycarbonate membrane (110607, Whatman, NJ, USA) was used to remove the Mg microparticles with size larger than 5 μm, then another vacuum infiltration process using a 1 μm Polycarbonate membrane (110607, Whatman, NJ, USA) was used to remove the Mg microparticles with size smaller than 1 μm. The obtained Mg microparticles with size of 1-5 μm were then dispersed in isopropanol with a concentration of 10 mg/mL. Thereafter, the Mg microparticle suspension was pumped into the polished polycarbonate templates with electrodeposited PEDOT/Au microtubes using vacuum infiltration. A polycarbonate membrane with a pore size of 15 nm was placed below the 5 μm diameter PC membrane to retain the magnesium microparticles within the upper PEDOT/Au microtubes. The vacuum infiltration process was performed for 2 hours to ensure full loading of Mg microparticles in the microtubes. The polycarbonate membrane was then dissolved in methylene chloride for 2 h to completely release the micromotors, *e.g.* the Mg microparticles loaded PEDOT/Au microtubes. The micromotors were then collected by a sediment process and washed with methylene chloride and isopropanol (3 times each one). Fluorescent Mg-based micromotors were prepared by using the Mg microparticle suspension dissolved with a Rhodamine 6G dye (83697, SIGMA, USA) with a concentration of 2 μg/mL.

A commercial enteric polymer (Eudragit L100-55; Evonik Industries, Germany) was chosen to be coated on the Mg-based micromotors to prevent the Mg microparticles from reacting in stomach fluid thus ensuring their safe reaching to the GI tract. First, a batch of Mg-based micromotors (dissolved from one whole piece of PC membrane) was collected in 0.1 mL isopropanol solution. Then Eudragit L 100-55 was dissolved into isopropanol solution with three different concentrations of 6.5%, 10.0% and12.5 % (w/v) to prepare the EMgMs with different coating thicknesses. The micromotor suspension was then mixed with Eudragit L100-55 solution with the above three different concentrations, and then dispersed in to a paraffin matrix for a solvent evaporation process. The obtained structures were then solidified with hexanes and a following freeze drying process. Finally, a soft annealing of 130 °C for 10 min to ensure the complete sealing of the Mg-based micromotors. The original diameter of the micromotors without polymer coating is 5 μm, as defined by the micropores of the polycarbonate membrane template. The enteric coating thicknesses were examined by SEM. For the three enteric polymer concentration of 6.5%, 10.0% and 12.5 % (w/v), a coating thickness of 0.3, 0.8 and 1.2 μm was calculated by polymer-coated micromotors with an average diameter of 5.6, 6.8 and 7.4 μm, respectively.

To make the silica microspheres-loaded control micromotors, a suspension of silica microspheres (diameter 1.21 μm, Bangs Lot# 8348, Fisher, IN, USA) were added into the PEDOT/Au microtubes, instead of Mg microparticles. An enteric polymer coating, with a thickness of 0.8 μm, was then coated on these silica-microspheres loaded micromotors by same method described above using a polymer concentration of 10.0%. The resulting coated silica-microspheres loaded micromotors were then used as control micromotors without movement in the intestinal fluid.

In vitro release study

In vitro release of the EMgMs was performed using gastric fluid simulant and intestinal fluid simulant, respectively. Videos of micromotor propulsion were captured by an inverted optical microscope (Nikon Instrument Inc. Ti-S/L100), coupled with a 40X microscope objective, a Hamamatsu digital camera C11440 using the NIS-Elements AR 3.2 software. In each test of the release study, EMgMs were dispersed on a glass slide with PDMS cell to prevent the evaporation of the liquid during the observation. Normally about 400 micromotors were in the view under the 4X microscope objective. The CCD camera is set to take a microscopy image every minute, while the micromotor which is generating bubble or moved from its original place in the imaging is consider as being released. The time-dependent release rate is calculated in each test then averaged as the statistical results (n=6).

In vivo GI tract site-specific localization and retention studies

For *in vivo* GI tract site-specific localization study, 8 weeks old ICR male mice were purchased from Harlan Laboratory (Indianapolis, IN). Mice were gavaged with 0.3 mL of suspension of uncoated Mg-based micromotors or EMgMs with thin, medium, or thick enteric coatings (n=6). GI tracts including stomach, duodenum, jejunum, and ileum from each mouse were collected at 6 hours after administration. The tissues were rinsed with PBS. Each section was placed in a glass vial and 3 mL of aqua regia consisting of concentrated nitric acid and hydrochloric acid (Sigma-Aldrich, St. Louis, MO, USA) in the ratio of 1:3 was added into the tissue for 12 hours at room temperature; this was followed by annealing at 80 °C for 6 hours in order to remove the acids and then resuspended with 5 mL DI water. Analysis of the amount of micromotors retained in each part of GI tract was carried out by measuring their embedded Au content using inductively coupled plasma-mass spectrometry (ICP-MS). For *in vivo* retention study, mice (n=6) were fed with alfalfa-free food from LabDiet (St. Louis, MO, USA) for 2 weeks prior to the experiment. A 0.3 mL suspension of fluorescence-labeled EMgMs with medium thickness of enteric coating was administered orally. At 6 and 12 hours after administration, the GI tracts were dissected, rinsed with PBS, and then imaged using an intelligent visual inspection system (IVIS). A 0.3 mL PBS was given to control mice and tissues were collected and imaged at 6 hours after administration. For *in vivo* retention study comparing the propulsive EMgMs with inert silica microspheres loaded micromotors, one group of the mice were orally administrated with a 0.3 mL suspension of fluorescence-labeled EMgMs with medium thickness of enteric coating, while another group were orally administrated with a 0.3 mL suspension of silica-microsphere loaded PEDOT/Au microtubes coated with medium thickness of enteric coating. At 6 hours after administration, the GI tracts were dissected, rinsed with PBS, and then imaged using an intelligent visual inspection system (IVIS).

In vivo toxicity study

To investigate the acute toxicity of EMgMs, 8 weeks old ICR male mice were oral-gavaged with 0.3 mL suspension of EMgMs with medium thickness of enteric coating. Healthy mice treated with PBS were used as a negative control. Mice were sacrificed at 24 hours after the administration. The stomach and small intestine were collected. The stomach was cut open along the greater curvature, and the gastric content was removed. The small intestine was cut to small sections as duodenum, jejunum, and ileum, and rinsed inside with PBS to remove internal residues. The tissues were put in tissue cassettes and fixed with 10% buffered formalin for 15 hours, then moved into 70% ethanol, and then embedded in paraffin. The tissue sections were cut with 5 μm thickness and stained with hematoxylin and eosin (H&E) assay. The apoptosis cells were evaluated by terminal deoxynucleotidyl transferase-mediated dUTP nick-end labeling (TUNEL) assay using ApopTag® from EMD Millipore (Billerica, MA, USA). The stained sections were visualized by the Hamamatsu NanoZoomer 2.0HT.

4.2.3 Synthesis and characterization of enteric magnesium micromotors

Fig. 4.5a illustrates the operation principle of the EMgMs that can selectively position and spontaneously propel in the GI tract by using the pH-sensitive coating which dissolves in intestinal fluid (pH 6~7). Fig. 4.5b shows the fabrication processes of EMgMs, where a template-electrodeposition method is combined with a particle-infiltration technique by packing Mg microparticles within template-synthesized PEDOT/Au microtubes with a uniform diameter of 5 µm (Supporting Video 2). The template-synthesized PEDOT/Au microtubes serve as robust microcontainers for loading the Mg microparticles while Au is used as a model cargo for *in vivo* biodistribution study. Note that Mg is a biocompatible trace element vital for many bodily functions and that the reaction of Mg microparticles with water is used to generate propulsion [42,43].

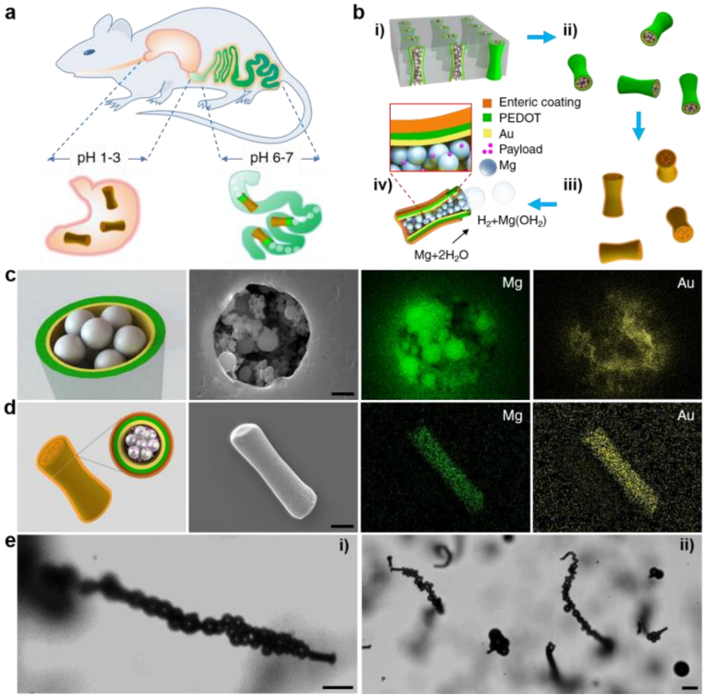

Figure 4.5 Synthesis and characterization of enteric magnesium micromotors (EMgMs). (a) Schematic illustration of *in vivo* operation of the EMgMs for propulsion and localized delivery to the GI tract. (b) Preparation of EMgMs: (i) loading of Mg microspheres and payload into PEDOT/Au microtubes electrodeposited in microporous polycarbonate (PC) membrane with pore size of 5 µm and pore length of 15 µm; (ii) dissolution of PC membrane and release the Mg micromotors; (iii) coating Mg micromotors with enteric polymer; (iv) dissolution of the enteric coating and propulsion of Mg micromotors in solution with neutral pH. (c) Top view of a Mg micromotor with SEM characterization and EDX images of the Mg and Au in the micromotor. Scale bar: 1 µm. (d) Side view of an EMgM with SEM characterization and EDX images of the Mg and Au in the micromotor. Scale bar: 5 µm. (e) Propulsion snapshot of a single (i) and multiple (ii) EMgMs in the intestinal fluid. Scale bars, 20 µm.

Fig. 4.5c and Supporting Fig. 4.5 display the top and side views, respectively, of Mg particles infiltrated into a PEDOT/Au microtube. These SEM images and EDX mapping confirm that the microtube can be successfully loaded with Mg particles, while the interparticle space could be potentially filled with therapeutic or imaging payloads. The motors are subsequently coated with methacrylate-based polymer Eudragit L100-55, which has been used for protecting oral drug capsules from the acidic gastric fluid [40,41,44]. The SEM image and EDX mapping in Fig. 4.5d show the side view of a micromotor with a smooth enteric polymer coverage. Upon fabrication of the EMgMs, we first evaluated their propulsion performance in intestinal fluid. The microscopy images of Fig. 4.5e (corresponding to Supporting Videos 3), demonstrate effective movement of a single and multiple EMgMs in intestinal fluid simulant. Hydrogen bubbles propel the motors for approximately 1 min with average speed of 60 μm/s, demonstrating water-powered microtubular motors that can efficiently propel and function in intestinal fluid.

4.2.4 *In vitro* evaluation

To evaluate the feasibility of precisely tuning the activation time of EMgMs after entering the GI tract, the micromotors - with an original diameter of 5 μm – were modified with enteric polymer coatings of three different thicknesses (0.3, 0.8 and 1.2 μm) and were tested in gastric and intestine fluids. The thickness of the polymeric coating was adjusted by using three enteric polymer concentrations of 6.5%, 10.0% and12.5 % (w/v), which resulted in average EMgMs diameters of 5.6, 6.6 and 7.4 μm, respectively. Fig. 4.6a shows that EMgMs with thin coating display no bubble generation upon immersing in gastric acid for over 150 minutes, reflecting the shielding ability of the polymer in strongly acidic gastric environment. Upon changing to intestinal fluid, these EMgMs display a burst of bubble generation and efficient propulsion within 20 minutes (Fig. 4.6b). The efficient propulsion eventually leads to a dynamic distribution of the micromotors to different locations. Medium and thick enteric coatings are able to delay the bubble generation and micromotor propulsion to 60 minutes and 150 minutes after immersion in intestinal fluid, respectively (Fig. 4.6c and d). Supporting Video 4 shows the delayed actuation of EMgMs in the intestinal fluid.

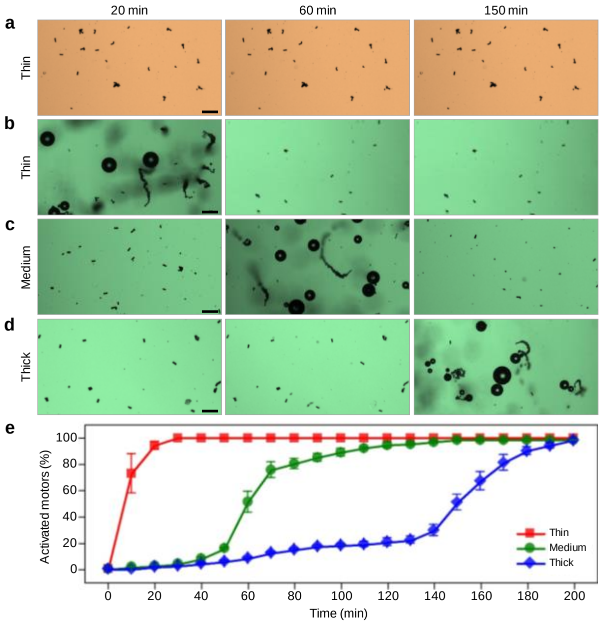

Figure 4.6 *In vitro* evaluation of EMgMs in gastric and intestinal fluids. (a) Microscopy images of EMgMs with thin thickness of enteric polymer coating immersed in gastric fluid for 20 min, 60 min and 150 min. (b-d) Microscopy images of EMgMs with thin (b), medium (c) and thick (d) enteric polymer coating immersed in intestinal fluid for 20 min, 60 min and 150 min. Scale bar, 50 μm. The three coating thicknesses are 0.3, 0.8 and 1.2 μm, respectively. (e) Quantitative analysis of the percentage of activated micromotors in intestinal fluid at different time points (n=6 with 400 micromotors in each test).

Fig. 4.6e shows the quantitative results of the release and activation of EMgMs with different enteric coatings in intestinal fluid. Based upon the statistical analysis of about 400 motors for each group, thin polymer coating results in over 75% of EMgMs activated in intestinal fluid within 10 min, indicating that the propulsion occurs in the upper segment of the GI tract. In contrast, for a medium-thickness coating, a very slow activation is observed between 30 and 45 minutes, followed by a rapid activation of about 75% of EMgMs between 50 to 70 minutes, indicating the motors localize at the middle segment of the GI tract. EMgMs coated by a thick polymer layer display very slow activation up to 2 hours, followed by rapid activation of 80% EMgMs at 3 hours, indicating that these motors can reach the lower segment of the GI tract. These results verify the possibility of selectively position the motors in different regions of the GI tract by controlling the coating thickness.

4.2.5 *In vivo* localization

The ability of EMgMs to selectively localize at desirable segments of the GI tract was evaluated *in vivo* using a mouse model. In the study, four groups (n=3) of mice were assigned to receive EMgMs with three different polymer thicknesses and uncoated micromotors, respectively. Upon oral administration of the motors for 6 hours, the mice were euthanized, and their stomach and entire GI tract were collected to evaluate the biodistribution and retention of the motors. Specifically, the mouse GI tract was sliced into three segments corresponding to duodenum, jejunum and ileum of the GI tract (Fig. 4.7a) for separate inspection. Fig. 4.7b displays the distribution of the micromotors in these three GI segments and the stomach for the four tested groups. The uncoated micromotors display significant (79%) retention in the stomach, reflecting their efficient activation and propulsion in the stomach (Fig. 4.7b i). The enteric polymer coatings offer robust protection of the micromotors in the stomach and thus enhance their delivery efficiency to the GI tract. A small fraction (16%) of EMgMs with thin enteric coating retained in the stomach (Fig. 4.7b ii) while minimal micromotors were detected in the stomach for EMgMs with medium and thick coatings (Fig. 4.7b iii and iv). In contrast, Fig. 4.7b ii-iv illustrate that 75%, 67% and 54% of the motors retained in the duodenum, jejunum and ileum for EMgMs with thin, medium and thick enteric coatings, respectively. These results demonstrate that controlling the coating thickness, and hence the exposure and activation times of the motors, has a profound effect upon the biodistribution of EMgMs within the GI tract.

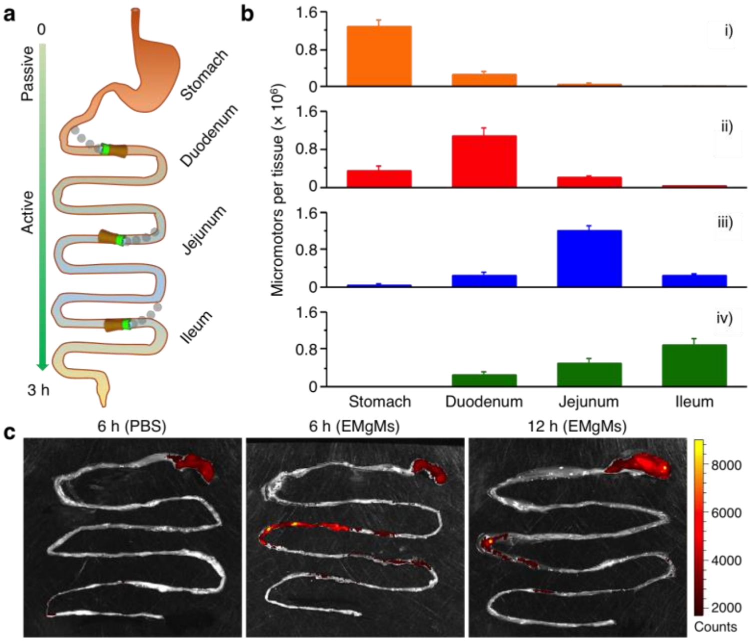

Figure 4.7 *In vivo* biodistribution and retention of EMgMs in the GI tract. (a) Schematic representation of the localization and retention of the micromotors in the stomach and GI tract. (b) ICP-MS analysis of the number of micromotors with different enteric coating thickness retained in the stomach, duodenum, jejunum, and ileum 6 hours post oral administration. The samples include (i) bare Mg micromotors without enteric coating, (ii) EMgMs with thin polymer coating, (iii) EMgMs with medium polymer coating, and (iv) EMgMs with thick polymer coating (n = 6 mice per group; estimation of number of the motors in each administration can be found in Supporting Note). (c) Superimposed fluorescent images of mouse GI tracts at 6 hours and 12 hours post-administration of EMgMs loaded with the dye Rhodamine 6G and covered with medium polymer coating. PBS was used as a control.

We further studied the retention of the EMgMs with medium coating in mouse GI tract by orally administrating fluorescently labeled EMgMs. At 6 and 12 hours after EMgMs administration, the entire GI tract was excised for fluorescence imaging, as shown in Fig 4.7c. The image obtained from GI tract collected at 6 hours showed the strongest fluorescence in jejunum and the signal remained at the site at 12 hours, which was about four-fold longer than typical gastric emptying times in mouse GI tract [45]. In contrast, when mice were treated with phosphate-buffered saline (PBS) control, there was no detectable fluorescence signal in the GI tissue; some signal observed in the stomach is attributed to the food self-fluorescence. The luminal surfaces of the intestines are covered by a mucus layer, consisting of large and highly glycosylated proteins, which serve as the front line of protection of GI tract [45]. When the cylindrical Mg-loaded motors are locally released and activated in the GI tract, they will propel and collide with the porous, slimy mucus layer and can be readily trapped within the gel-like mucus, leading to an enhanced local retention. To test our hypothesis that the active propulsion of the motors is critical for the enhanced local retention, we compared the retention of EMgMs with medium polymer coating with that of inert silica-microsphere loaded PEDOT/Au microtubes (with the same polymer coating). The latter are inert in the intestinal environment fluid and do not exhibit autonomous propulsion when released. These control micomotors displayed a significantly lower fluorescence intensity, compared to the EMgMs, reflecting their greatly reduced retention in the jejunum under the same experimental conditions and coatings. Such observations are similar to our early work which demonstrated that the propulsion of Zn-based micromotors in the acidic stomach environment greatly improved their tissue penetration and retention [38]. In the present work, we obtained similar results with highly enhanced retention (up to 24 hrs) associated with propulsive micromotors. Overall, self-propelled micromotors lead to a dramatically improved localized retention of their payloads in the intestine compared to the passive diffusion and dispersion of inert payloads. These data verify that both the enteric polymer coating and the propulsion of the Mg-based micromotors are critical for their accurate position and enhanced retention in desired segment of the GI tract.

4.2.6 Toxiciy evaluation of enteric micromotors

Finally, the toxicity profile of the EMgMs in the GI tract was investigated. Mice were orally administrated with PBS buffer (Fig. 4.8a-c) or suspension of EMgMs with medium polymer coating thickness (Fig. 4.8d-f) and monitored for general toxicity signs every 2 hours for the first

10 hours post administration. No physiological symptoms such as lethargy, rough fur, or diarrhea were observed in both groups. Then, the GI tract was dissected and sectioned for histological evaluation 24 hours after administration. The tissues were first stained with hematoxylin and eosin (H&E) (Fig. 4.8 a, b, d, e). We did not observe apparent alteration of gastric and intestinal mucosal epithelial architectures or differences in the crypt and villus length and number, or mucosal thickness, between the PBS and motors-treated groups. There was also no infiltration of immune cells such as neutrophils, lymphocytes, or macrophages into the mucosa and submucosa, indicating no sign of tissue inflammation. Furthermore, the deparaffinized mouse gastric tissue sections of motor-treated mice showed no difference in apoptotic gastric and intestinal epithelial compared to the PBS control, as indicated by positive staining cells in TUNEL assay (Fig. 4.8 c, f) [46,47]. Overall, the *in vivo* toxicity studies demonstrate no apparent GI mucosal epithelial morphology change or inflammation, suggesting that the EMgMs are biocompatible and safe for oral administration in mouse model.

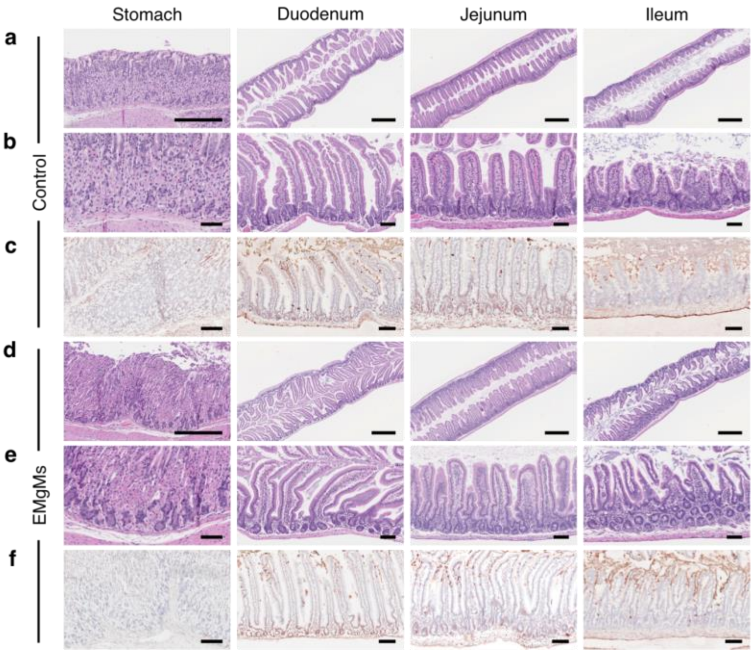

Figure 4.8 Toxicity evaluations of EMgMs. The stomach, duodenum, jejunum and ileum of mice treated with (a-c) PBS buffer or (d-f) EMgMs with medium polymer coating thickness were collected and analyzed. At 24 hours post-treatment, the mice were sacrificed and GI tract tissue sections were stained with H&E assay (a, b, d, and e) and TUNEL assay (c, and f). Scale bar (a, d: 500 μm; b, c, e, and f: 100 μm).

4.2.7. Conclusion

A desirable GI delivery system should be able to protect the cargos en-route and accurately locate them to the site of action. Upon arrival at destination, the carrier should retain at the site for complete unloading of the cargos. The reported enteric magnesium micromotors provide an exciting thrust towards achieving such goal. By simply tuning the thickness of the pH-sensitive polymer coating it is feasible to selectively activate the propulsion of the water-powered micromotors, and thus to control their tissue penetration and retention at desired regions of the GI tract. Such combination of accurate positioning and active propulsion demonstrate that a microscale robot can achieve desired biodistribution and enhanced retention simultaneously in the GI tract; it is therefore of particular importance for the emerging microbiome research. Furthermore, the use of advanced pH-sensitive materials for precise local manipulation of microrobot for site-specific active delivery (compared to conventional passive-diffusion-driven delivery vehicles) is expected to pioneer novel delivery approaches and advance the emerging field of medical nano/micromotors and nanorobotics. While future studies are warranted to validate the delivery efficiency and therapeutic efficacy, the micromotor-based GI transporter system offers innovative combination of accurate positioning and active propulsion towards effective localized GI delivery of cargos and personalized treatment of GI diseases and disorders.

4.4 Micromotor-Enabled Active Drug Delivery for In Vivo Treatment of Stomach Infection

4.4.1 Introduction

Recent advances in the nano/micromotor field[3,4,6,31] in terms of improvement of biocompatibility and biological function have led to their growing use in biomedicine[10,34,48], including therapeutic payload delivery[11,39,49–52], micro-surgery[53,54], isolation of biological targets[12], operation within living cells[1,37], and removal of toxicant molecules and organisms[55–57]. Although significant progress has been accomplished to demonstrate the *in vitro* capabilities of nano/micromotors to transport therapeutic cargos to target destinations, tremendous effort is still required to translate the proof-of-concept research to *in vivo* biomedical applications.

In recent years, the utility and performance of these motor-based active transport systems have been tested in live animals. For example, our group has demonstrated the biocompatibility and attractive *in vivo* performance of zinc-based and magnesium (Mg)-based micromotors under *in vivo* conditions[38,58,59]. These studies have shown that artificial micromotors can self-propel in the stomach and intestinal fluids for enhanced retention in the gastric *mucous* layer[38] and targeted delivery in the gastrointestinal tract[58]. Walker *et al.* presented the ability of magnetic micropropellers to move through gastric mucin gels, by mimicking the mucus penetration strategy of *Helicobacter pylori (H. pylori)*[60]. In addition, Nelson and Martel demonstrated that magnetically actuated nanoswimmers could lead to active and directional drug delivery in a mouse model[39,51]. These prior *in vivo* studies of synthetic motors have significantly advanced motor research and cleared a path towards direct evaluation of disease-oriented therapeutic efficacy associated with motor-enabled active drug delivery. However, this still remains an alluring but unmet goal for biomedical researchers.

This work demonstrates the first attempt to apply Mg-based micromotors, loaded with antibiotic drug clarithromycin (CLR), for *in vivo* treatment of *H. pylori* infection in a mouse model. Given the built-in proton depletion function, this motor-based therapy is able to undergo the harsh gastric environment to achieve remarkable antibacterial efficacy without involving the commonly used proton pump inhibitors (PPIs). The *H. pylori* bacteria, found in about half of the world's population, can cause stomach infection and subsequently lead to diverse gastric and extragastric diseases[61,62]. In most cases, the administration of antibiotics for the treatment of *H. pylori* infection is combined with the use of PPIs to reduce the production of gastric acid[63], because the gastric acid could make antibiotics less effective. The effectiveness of PPIs is attributed to the irreversible binding to proton pumps and thus to suppress acid secretion[64,65], which in long term use can lead to adverse effects such as headache and diarrhea and in more serious scenarios cause anxiety or depression[66–69]. Therefore, it would be highly beneficial to develop an alternative therapeutic regimen with equivalent or advantageous therapeutic efficacy as the current antibiotic treatments while excluding the use of PPIs.

The reported Mg-based micromotors rely on the combination of a CLR-loaded poly(lactic-co-glycolic acid) (PLGA) layer and a chitosan polymer layer covering on a propellant Mg core to offer high drug loading capacity, along with biodegradability and biocompatibility. The positively-charged chitosan outer coating enables adhesion of the motor onto the stomach wall [70], facilitating efficient localized autonomous release of CLR from the PLGA polymer coating. In contrast to acid suppression by PPIs, Mg-based micromotors can temporally and physically alter the local acidic environment by quickly depleting protons while propelling within the stomach[24]. Such elimination of the PPI administration is coupled with significant reduction of bacteria burden, as demonstrated *in vivo* in a mouse model. Using a mouse model of *H. pylori* infection, the propulsion of the drug-loaded Mg-based micromotors in gastric fluid along with their outer chitosan layer are shown to greatly enhance the binding and retention of the drug-loaded motors on the stomach wall. As these micromotors are propelled in the gastric fluid, their Mg cores are dissolved, leading to self-destruction of these motors without harmful residues, as is demonstrated by the toxicity studies.

Overall, we take advantage of the efficient propulsion of Mg-based micromotors in the acidic stomach environment, their built-in proton depletion ability, their active and prolonged retention within the stomach wall, and their high drug-loading capacity, to demonstrate the first actual *in vivo* therapeutic application of chemically-powered micromotors. *In vivo* studies examine the therapeutic efficacy, distribution and retention of the micromotors in the mouse stomach compared to passive drug-loaded microparticles and other control groups, along with corresponding *in vivo* toxicity profile. These results illustrate the attractive therapeutic capabilities of acid-driven micromotors, which open the door for *in vivo* therapeutic applications of body-fluid propelled micromotors towards the treatment of a variety of diseases and disorders.

4.4.2 Experimental Section

Synthesis of Mg-based micromotors

The Mg-based micromotors were prepared using magnesium (Mg) microparticles (catalog #FMW20, TangShan WeiHao Magnesium Powder Co.; average size, 20±5 µm) as the core. The Mg microparticles were initially washed with acetone to eliminate the presence of impurities. After being dried under a N_2 current, the Mg microparticles were dispersed onto glass slides (2 mg of Mg microparticles per glass slide), followed by atomic layer deposition (ALD) of TiO_2 (at 100 °C for 120 cycles) using a Beneq TFS 200 system. Since such an ALD process utilizes gas phase reactants, it leads to uniform coatings over the Mg microparticles, while still leaving a small opening at the contact point of the particle to the glass slide. After that, the Janus micromotors were coated with 120 µL of 1% (w/v) PLGA (Sigma-Aldrich, P2191) prepared in ethyl acetate (Sigma-Aldrich, 270989) and containing 40 mg mL^{-1} clarithromycin (CLR) (TCI CO., LTD. C220). It should be noted that different CLR amounts (between 4 mg and 6 mg) were tested in order to optimize the drug loading. The PLGA@CLR coating was dried fast to avoid crystallization of the drug. Finally, the Janus micromotors were coated with a thin layer of 0.05 % (w/v) Chit (Sigma-Aldrich, C3646) prepared in water and containing 0.1% (w/v) sodium dodecyl sulfate (SDS) (Sigma-Aldrich, 62862) and 0.02% (v/v) acetic acid (Sigma-Aldrich, 695092), forming the outermost layer coated on the Mg microparticles. Finally, the Mg-based micromotors were collected by lightly scratching the microparticles off the glass slide.

Synthesis of dye-loaded Mg-based micromotors

For performing the characterization of the Mg-based micromotors along with the *in vivo* retention studies, fluorescent Mg-based micromotors were prepared by combining both 1% PLGA and 0.05% Chit solutions with 5 µg mL^{-1} 1,1'-dioctadecyl-3,3,3',3'-tetramethylindodicarbocyanine, 4-chlorobenzenesulfonate salt (DiD, λ_{ex}=644 nm/ λ_{em}=665 nm, Life Technologies, D7757) and 1 µg mL^{-1} fluorescein isothiocyanate-dextran (FITC, λ_{ex}=492 nm/ λ_{em}=520 nm, Sigma-Aldrich, 46945) dyes, respectively. To compare with the Mg-based micromotors, inert silica (Si) microparticles (Nanocs, Inc., Cat. No.Si01-20u-1; 20 µm size) were used as core particles, following the same protocol described above.

Micromotor characterization

Bright field and fluorescent images of the Mg-based micromotors and inert silica microparticles were captured using a EVOS FL microscope coupled with a 20× and 40× microscope objectives and fluorescence filters for red and green light excitation.

Scanning electron microscopy (SEM) images of the Mg-based micromotors were obtained with a Phillips XL30 ESEM instrument, using an acceleration voltage of 10 kV. Energy-dispersive X-ray mapping analysis was performed using an Oxford EDX detector attached to SEM instrument and operated by INCA software.

Micromotor propulsion studies

Autonomous Mg-based micromotors propulsion in simulated gastric fluid (Sigma-Aldrich, 01651) was obtained by diluting 25 times the simulated gastric fluid according to the commercial specifications (final pH~1.3), and adding 1% Triton X-100 (Fisher Scientific, FairLawn, NJ) as surfactant. An inverted optical microscope (Nikon Eclipse 80i upright microscope) coupled with different microscope objectives (10×, 20× and 40×) and a QuantEM:512SC camera were used for recording the autonomous micromotor propulsion in the gastric fluid simulant. The speed of the Mg-based micromotors was characterized using the MetaMorph 7.1 software (Molecular Devices, Sunnyvale, CA).

In vitro anti-H. pylori activity

H. pylori Sydney strain 1 (HPSS1) was cultured from frozen stock and routinely maintained on Columbia agar supplemented with 5% (vol/vol) laked horse blood at 37 °C under microaerobic conditions (10% CO_2, 85% N_2, and 5% O_2). For experiments, broth cultures of *H. pylori* were prepared by subculturing fresh colonies from agar plates into Brain heart infusion (BHI) supplemented with 5% fetal bovine serum (FBS) and incubated overnight at 37 °C under microaerobic conditions with moderate reciprocal shaking. An overnight broth culture of *H. pylori* was centrifuged at 5000g for 10 min to obtain a bacterial pellet. After removal of culture medium by centrifugation, the obtained bacteria pellet was then suspended in an appropriate amount of fresh BHI with 5% FBS for future use.

The bactericidal activity against *H. pylori* of free CLR and CLR-loaded Mg-based micromotors (PLGA@CLR/TiO_2/Mg) were tested *in vitro.* Samples were treated in 0.1 N HCl for 1 h and serially diluted to desired concentrations with PBS. Bare Mg-based micromotors (PLGA/TiO_2/Mg) with corresponding amount of micromotors were used as negative control.
The samples were added with 1×10^6 CFU/mL *H. pylori* in BHI with 5% FBS to make final concentrations of 0-16μg/mL CLR, followed by incubation at 37°C under microaerobic conditions with moderate reciprocal shaking for 24 h. Then a series of 10-fold dilutions of the bacterial suspension was prepared, and inoculated onto a Columbia agar plates supplemented with 5% laked horse blood. The plates were cultured for 4 days before the colony-forming unit (CFU) of *H. pylori* was quantified. All measurements were made in triplicate.

In vivo micromotor retention

Prior to the experiment, C57BL/6 mice (n = 3) were fed with alfalfa-free food from LabDiet (St. Louis, MO, USA) for 2 weeks. The *in vivo* retention study was performed by using dye-loaded Mg-based micromotors prepared by the protocol described above. A 0.3 mL suspension of Mg-based micromotors with DiD-labeled PLGA and FITC-labeled chitosan coatings were intragastrically administered. A group of mice was administered with DI water as a negative control. Following 30 min and 2 h of oral administrations, the mice were sacrificed and their entire stomachs were excised and cut opened along the greater curvature. Then, the tissues were rinsed with PBS, flattened, and visualized using a Keyence BZ-X700 fluorescence microscope. The bright field and corresponding fluorescence images were obtained at 665 nm and 520 nm (DiD and FITC, respectively) for each sample. Subsequently, the tissues were transferred to 1 mL PBS and homogenized. Analysis of the amount of micromotors retained in the stomachs was carried out by measuring the fluorescence intensity of their embedded DiD-labeled PLGA and FITC-labeled chitosan using Synergy Mx fluorescent spectrophotometer (Biotek, Winooski, VT).

In vivo therapeutic efficacy against H. pylori infection

Six-week-old C57BL/6 male mice were purchased from the Jackson Laboratory (Bar Harbor, ME). Each C57BL/6 mouse received 0.3 mL of 1 × 10^9 CFU/mL *H. pylori* in BHI broth administered intragastrically through oral gavage every 48 h, repeated three times (on day 3, 5 and 7, respectively), and the infection was allowed to develop for 2 weeks. For the *in vivo* anti-*H. pylori* therapeutic study, mice were randomly divided in five treatment groups (n=6) to be orally administered with CLR-loaded Mg-based micromotors, CLR-loaded inert silica microparticles, free CLR+PPI, blank Mg-based micromotors or DI water. For free CLR+PPI group, mice were first administered with omeprazole (a proton pump inhibitor) through oral gavage at a dose of 400 μmol/kg, followed by a lag time of 30 min before administration of CLR. CLR-loaded Mg-based micromotors, CLR-loaded inert silica microparticles and free CLR (with 30 mg/kg clarithromycin dosage) were administered through oral gavage once daily for 5 consecutive days. Blank Mg-based micromotors and DI water served as movement control and negative control, respectively. Forty-eight hours after last administration, mice were sacrificed and stomachs were excised from the abdominal cavity. The stomachs were cut along the greater curvature, and the gastric content were removed and rinsed with PBS. For *H. pylori* recovery, each gastric tissue was weighed before suspended in 200 μL PBS and homogenized. The homogenate was serially diluted and spotted onto

Columbia agar plate with 5% laked horse blood and Skirrow's supplement (10 μg/mL vancomycin, 5 μg/mL trimethoprim lactate, 2,500 IU/L polymyxin B; Oxiod). The plates were then incubated at 37 °C under microaerobic conditions for 5 days, and bacterial colonies were enumerated. Statistical analysis was performed using one-way ANOVA. No statistical methods were used to predetermine sample size. Studies were done in a non-blinded fashion. Replicates represent different mice subjected to the same treatment (n=6).

Toxicity evaluation of Mg-based micromotors

To evaluate the acute toxicity of the Mg-based micromotors *in vivo*, uninfected C57BL/6 male mice were orally administered with CLR-loaded micromotors once daily for 5 consecutive days. Mice administered with DI water were tested in parallel as a negative control. On day 6, mice were sacrificed and sections of the mouse stomach tissue were processed for histological examination. The longitudinal sections of gastric tissue were fixed in neutral-buffered 10% (vol/vol) formalin for 15 h, transferred into 70% ethanol, and embedded in paraffin. The tissue sections were cut with 5 μm thickness and stained with hematoxylin and eosin (H&E) assay. Sections were visualized by Hamamatsu NanoZoomer 2.0HT and the images processed using NDP viewing software.

4.4.3 Preparation and characterization of drug-loaded Mg-based micromotors.

Fig. 4.9a schematically illustrates the preparation steps of the drug-loaded Mg-based micromotors. The cores of the micromotors are made of Mg microparticles with an average size of ~20 μm. In the study, a layer of Mg microparticles was dispersed onto a glass slide (Fig. 4.19a, I), followed by an asymmetrical coating of the microspheres with a thin TiO_2 layer using atomic layer deposition (ALD) (Fig. 4.9a, II). The ALD process leads to a TiO_2 uniform coating over the Mg-microspheres, while leaving a small opening (essential for contact with the acid fuel) at the sphere-glass contact point[71], which forms a Janus microstructure. Such biocompatible TiO_2 layer acts as a shell scaffold that maintains the micromotor spherical shape and the opening size during the propulsion, leading to consistent and prolonged operation. The Mg/TiO_2 Janus microparticles were then coated with a PLGA film containing the CLR antibiotic payload (Fig. 4.9a, III). After the drug loading step, the microparticles were coated with an outer thin chitosan layer (thickness ~100 nm) that ensures efficient electrostatic adhesion of the micromotors to the mucosal layer on the stomach wall while protecting the CLR-loaded PLGA layer (Fig. 4.9a, IV). Finally, the resulting CLR-loaded Mg-based micromotors were separated and collected by soft mechanical scratching of the glass slide, leaving a small opening for spontaneous Mg-acid reaction when the motors are placed in an acidic solution. This reaction generates hydrogen microbubbles and leads to efficient propulsion in the stomach fluid [59]. The small opening enables also a slow reaction process and gradual dissolution of the Mg core, leading to a prolonged micromotor lifetime of approximately 6 min. The *in vivo* self-propulsion in the gastric fluid of a stomach and the corresponding drug delivery process from the PLGA layer of the Mg-based micromotors are illustrated schematically in Fig. 4.9b and Supplementary Movie 2.

The ability of drug-loaded Mg-based micromotors to efficiently propel in gastric acid was first tested *in vitro* by using a simulated gastric fluid (pH ~1.3). The microscopic images in Fig. 4.9c (taken from Supplementary Movie 3 at 2 min intervals) illustrate the fast and prolonged autonomous propulsion of a CLR-loaded Mg-based micromotor in the gastric fluid simulant. The efficient hydrogen bubble generation propels the micromotors rapidly, with an average speed of ~120 µm/s, and indicates that the Mg-based micromotors can react and move fast in the gastric fluid. Such efficient micromotor propulsion is essential for the motors to reach stomach wall and thus achieving high therapeutic efficacy. Importantly, the acid-Mg reaction responsible for the autonomous propulsion also spontaneously depletes protons in gastric fluid and thus neutralizes the stomach pH without using PPIs[59].

Fig. 4.9d schematically illustrates the structure of a drug-loaded Mg-based micromotor, showing the Mg core, covered mostly with the TiO_2 shell layer, drug-loaded PLGA layer, and an outer chitosan layer. The drug-loaded Mg-based micromotors were carefully characterized. The scanning electron microscopy (SEM) image of a drug-loaded micromotor (shown Fig. 4.9e) confirms the presence of a small opening (~2 µm) on the spherical micromotor, produced during the coating process, that exposes the Mg core of the micromotor to the gastric fluid and facilitates the hydrogen bubble thrust. Energy-dispersive X-ray (EDX) spectroscopy mapping analysis was carried out to confirm the motor composition. The resulting EDX images, shown in Fig. 4.9f-g, illustrate the presence and distribution of magnesium and titanium, respectively.

A fluorescence study was carried out to confirm efficient drug-loading within the PLGA layer and the coating of the micromotor with the protective and adhesive chitosan layer. This was accomplished by preparing Mg-based micromotors with the PLGA and chitosan coatings containing the fluorescent dyes 1,1'-dioctadecyl-3,3,3',3'-tetramethylindodicarbocyanine, 4-chlorobenzenesulfonate salt (DiD, λ_{em}=665 nm) and fluorescein isothiocyanate-dextran (FITC, λ_{em}=520 nm), respectively. An optical image of a dye-loaded micromotor is displayed in Fig. 4.9h. The corresponding fluorescence images show the dye-loaded Mg-based micromotor in the DiD and FITC channels (Fig. 4.9i, j, respectively); an overlay of the two channels is displayed in Fig. 4.9k. The high fluorescent intensity of the loaded dyes confirms the successful coating of the micromotor with both PLGA and chitosan layers, along with the high cargo-loading capacity of the micromotor.

Prior to *in vivo* therapeutic application of the Mg-based micromotors, several *in vitro* studies were performed. Initially, the ability of drug-loaded micromotors to efficiently propel in gastric acid was tested *in vitro*. The micromotor speed drastically decreases upon changing the pH of the gastric fluid solution from pH 1.5 to 1.75. Assuming that the stomach pH is 1.3, the drug-loaded Mg-based micromotors can efficiently move at this condition with an average speed of ~120 µm/s.

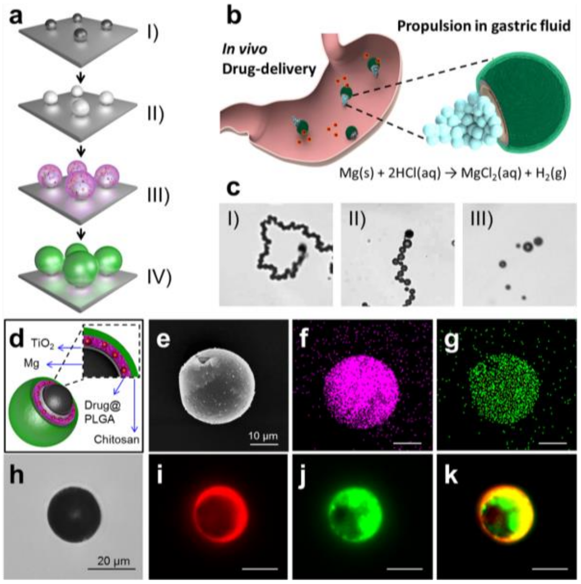

Figure 4.9 Synthesis, characterization and *in vitro* propulsion of drug-loaded Mg-based micromotors. (a) Schematic preparation of the micromotors: (I) Mg microparticles dispersion over a glass slide, (II) TiO_2 atomic layer deposition (ALD) over the Mg microparticles, (III) drug-loaded PLGA deposition over the Mg/TiO_2 microparticles, and (IV) Chitosan polymer deposition over the Mg/TiO_2/PLGA microparticles. (b) Schematic of *in vivo* propulsion and drug delivery of the Mg-based micromotors in a mouse stomach. (c) Time-lapse images (2 min intervals, I-III; taken from Supplementary Movie 3) of the propulsion of the drug-loaded Mg-based micromotors in simulated gastric fluid (pH~1.3). (d) Schematic dissection of a drug-loaded micromotor consisting of a Mg core, a TiO_2 shell coating, a drug-loaded PLGA layer, and a chitosan layer. (e) Scanning electron microscopy (SEM) image of a drug-loaded Mg-based micromotor. (f-g) Energy-dispersive X-ray spectroscopy (EDX) images illustrating the distribution of (f) magnesium and (g) titanium in the micromotor. (h-k) Microscopy images of dye-loaded Mg-based micromotor: (h) optical image, and fluorescence images showing the dye-loaded Mg-based micromotors in the (i) DiD channel (PLGA layer), (j) FITC channel (chitosan layer), along with an overlay of the two channels (k).

4.4.4 Drug loading optimization and *in vitro* bactericidal activity

The CLR loading onto the Mg-based micromotors was optimized to achieve a clinically-relevant therapeutic concentration of the drug (15-30 mg/kg/day)[72]. Fig. 4.10a shows a schematic displaying the loading of CLR onto the micromotors. Briefly, the Mg/TiO_2 microparticles dispersed onto a glass slide (~2mg of Mg microparticles per glass slide) were coated with a PLGA solution prepared in ethyl acetate, which was mixed with CLR (see detailed experimental protocol in Methods section). Rapid evaporation under nitrogen current leads to the formation of a homogeneous PLGA/CLR coating over the Mg/TiO_2 microparticles (microscope images of the coated micromotors are displayed in Fig. 4.10b). The microparticles were further coated with chitosan before quantifying the CLR loading efficiency of the micromotors. In order to optimize the drug loading, Mg-based micromotors were coated with PLGA solutions containing different amounts of CLR (between 4 mg and 6 mg). By studying different combinations of the PLGA/CLR solution volume and CLR concentration, the highest CLR loading efficiency (26%), corresponding to 1032±37 µg per 2 mg micromotor, was obtained when coating the microparticles with 120 µL of the PLGA solution containing 4.8 mg of CLR (Fig. 4.10c, II). This formulation offered optimal CLR loading and was selected for subsequent *in vitro* and *in vivo* anti-*H. pylori* studies.

Once confirmed that the micromotors were capable to load antibiotic cargo with high loading efficiency, an *in vitro* bactericidal activity of CLR-loaded Mg-based micromotors against *H. pylori* was performed. To mimic the gastric environment, samples were treated in 0.1 N HCl for 1 h prior to incubation with bacteria. This also ensured the dissolution of micromotors and consecutive drug release. Fig. 4.10d shows the enumerated amount of bacteria after being treated by CLR-loaded Mg-based micromotors or free CLR solution with varying concentrations of CLR. According to the results, drug-loaded micromotors exhibited a comparable bactericidal activity to free drug solution over the whole range of concentrations used in the study. Specifically, we determined the minimal bactericidal concentration (MBC) values of the samples, defined as the minimal concentration of an antimicrobial agent that kills 3 logs (99.9%) of the bacteria. The MBC value for CLR-loaded Mg-based micromotors was found to be 0.25 µg/mL, which was unaltered from the MBC value of free CLR. Moreover, bare Mg-based micromotors with corresponding amount of motors were used as negative controls. From Fig. 4.10d, the bare motors had negligible effect on the viability of *H. pylori* over the studied range, which supports that the bactericidal effect of CLR-loaded Mg-based micromotors is solely due to the loaded antibiotics, not the other compositions of the micromotor carrier. Overall, Fig. 4.10d verifies that the activity of the loaded drug was not compromised compared to free drug. The findings validate the potential use of these drug-loaded micromotors for therapeutic applications.

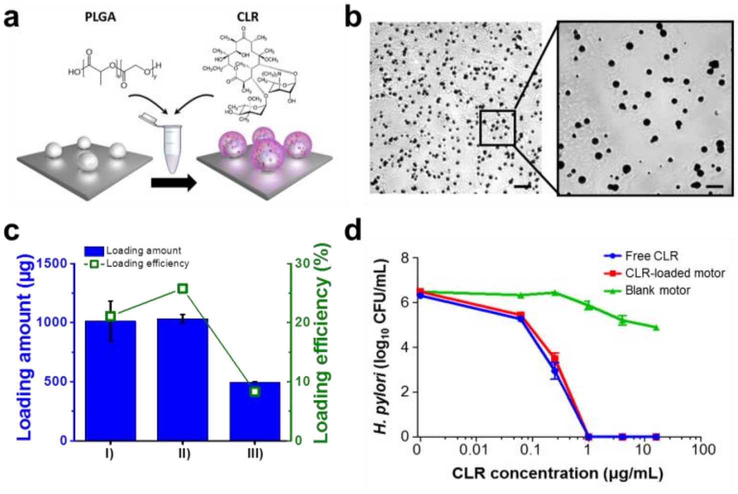

Figure 4.10 Antibiotic drug loading of the Mg-based micromotors and *in vitro* bactericidal activity. (a) Schematic displaying the loading clarithromycin (CLR) onto the Mg-based micromotors. PLGA polymer dissolved in ethyl acetate is mixed with CLR, and the solution is deposited over the Mg/TiO_2 microparticles resulting in the formation of a thin PLGA/CLR coating. (b) Microscope images showing the PLGA/CLR film over the Mg-based micromotors. Scale bars, 100 µm and 40 µm, respectively. (c) Quantification of CLR loading amount and yield of the micromotors prepared with different CLR solutions: (I) 100 µL of 40 mg/mL CLR solution, (II) 120 µL of 40 mg/mL CLR solution, and (III) 200 µL of 30 mg/mL CLR solution. All the CLR-loaded Mg-based micromotors were coated with a thin chitosan layer; all samples were dissolved in acid for 24 h before the drug loading measurement. (d) *In vitro* bactericidal activity of free CLR, CLR-loaded Mg-based micromotors and blank Mg-based micromotors (without CLR drug) against *H. pylori* bacteria.

4.4.5 *In vivo* micromotor retention in mouse stomach

After the optimization of drug loading onto the Mg-based micromotors and the confirmation of effective *in vitro* bactericidal activity, the micromotors were further investigated under *in vivo* setting. First, the *in vivo* retention properties of the Mg-based micromotors on stomach tissue were examined at different post-administration times, and compared with control groups administered with DI water (Fig. 4.11). For this purpose, Mg-based micromotors prepared with DiD-labeled PLGA and FITC-labeled chitosan coatings were administered to a group of mice (n=3), and following 30 min and 2 h of the samples administration, the mice were sacrificed and the entire stomach was excised and opened. Subsequently, the luminal lining was rinsed with PBS and flattened for imaging. Accordingly, Fig. 4.11a shows bright-field and fluorescence images of the luminal lining of freshly excised mouse stomach at 0 min after oral gavage of DI water, and at 30 min and 2 h after oral gavage of Mg-based micromotors. As can be observed, the images corresponding to the dye-loaded Mg-based micromotors show an intense fluorescent signal in both red and green light channels, which indicates efficient distribution and retention of the micromotors in the mouse stomach. The continuous propulsion of the micromotors and the adhesive properties of the chitosan coating help to achieve a homogeneous distribution of the micromotors in the stomach. The corresponding fluorescence quantification of the dye-loaded micromotors retained in the mouse stomach after 30 min and 2 h oral gavage of the sample is displayed in Fig. 4.11b. The graphic represents the higher fluorescence signals obtained at 665 nm and 520 nm (corresponding to DiD and FITC dyes, respectively) for each sample. These results indicate that the micromotors can effectively propel in gastric fluid and are retained in the stomach wall, where the *H. pylori* bacteria reside.

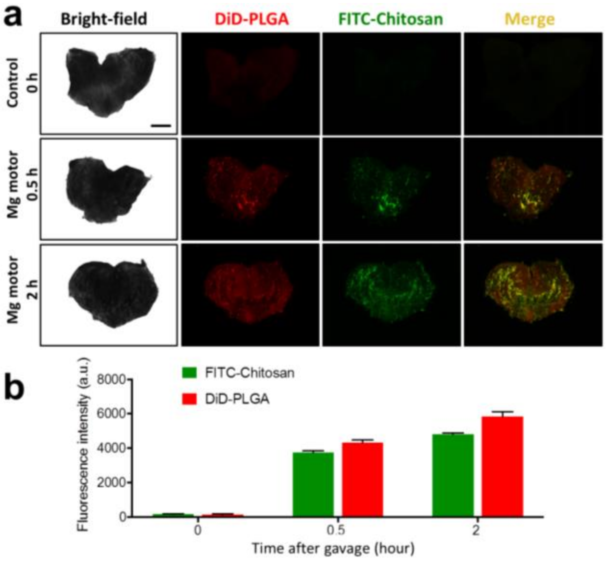

Figure 4.11 Retention of the Mg-based micromotors in mouse stomachs. (a) Bright-field and fluorescence images of the luminal lining of freshly excised mouse stomachs at 0 min after oral gavage of DI water (control), and at 30 min and 2 h after oral gavage of the Mg-based micromotors. Scale bar, 500 mm. (b) Corresponding fluorescence quantification of all the images shown in (a).

4.4.6 *In vivo* anti-*H. pylori* therapeutic efficacy

We proceeded to test the *in vivo* therapeutic efficacy of the drug-loaded Mg-based micromotors against *H. pylori* infection. Prior to the therapeutic study, we developed *H. pylori* infection in a mouse model using C57BL/6 mice. Each mouse was inoculated with 3 × 10^8 CFU *H. pylori* SS1 in brain–heart infusion (BHI) broth by oral gavage three times on day 3, 5, and 7 (Fig. 4.12a)[28,46]. Two weeks after inoculation, the *H. pylori* infected mice were divided into five groups (n = 6 for each group) and treated with DI water, blank Mg-based micromotors (without CLR drug), free CLR drug with PPI (CLR+PPI), CLR-loaded silica microparticles, or CLR-loaded Mg-based micromotors once a day for 5 days. Mice in the free CLR+PPI group received proton pump inhibitor (PPI) 30 min before administrating CLR to neutralize gastric acid and prevent potential degradation of CLR. After the treatment course, the bacterial burden was evaluated by enumerating and comparing *H. pylori* counts recovered from each mouse stomach. The mean bacterial burden from two negative control groups treated with DI water and blank Mg-based motors were 2.1×10^7 and 1.4×10^7 CFU/g of stomach tissue, respectively (Fig. 4.12b, black and orange colour, respectively). Meanwhile, a bacterial burden of 3.0×10^6 CFU/g was measured from the mice treated with CLR-loaded silica microparticles, which did not show statistical difference to the negative controls. In contrast, when the mice were treated with CLR-loaded Mg-based micromotors, the bacterial burden was quantified as 2.9×10^5 CFU/g, a significant reduction compared to the negative control and CLR-loaded silica microparticle groups. The substantial improvement in *H. pylori* reduction demonstrates the benefit of acid-powered Mg-based micromotors compared to static micron-sized carriers. A bacterial burden of 2.8×10^6 CFU/g was obtained for the positive control mice with free CLR+PPI treatment. The difference between CLR-loaded Mg-based micromotors and the free CLR+PPI groups were not statistically significant. However, the CLR-loaded micromotors reduced the *H. pylori* burden in mice compared with in the negative controls by ~1.8 orders of magnitude, whereas the free CLR+PPI group reduced it only by ~0.8 orders of magnitude. More importantly, looking at the bacterial burden in each tested mice, we found that 2 out of 6 mice from the CLR-loaded micromotors group displayed a significant reduction by 4 order of magnitude of bacteria burden which are the lowest among all other treatment groups. These analyses highlight the enhanced performance of Mg-based micromotors compared to free drug and emphasize the benefit of the propulsion-enabled active drug delivery in the stomach. These results demonstrate that the Mg-based micromotors can effectively propel and distribute throughout the stomach of living mice, and perform effective therapeutic activity.

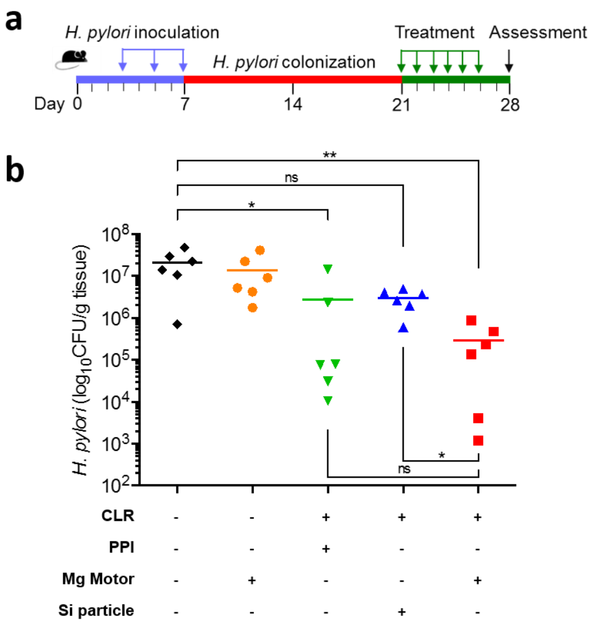

Figure 4.12 *In vivo* anti-*H. pylori* therapeutic efficacy. (a) The study protocol including *H. pylori* inoculation and infection development in C57BL/6 mice, followed by the treatments. (b) Quantification of bacterial burden in the stomach of *H. pylori*-infected mice treated with DI water (black colour), bare Mg-based micromotors (orange colour), free CLR+PPI (green colour), CLR-loaded silica microparticles (blue colour), and CLR-loaded Mg-based micromotors (red colour), respectively (n = 6 per group). Bars represent median values. *P < 0.05, **P < 0.01, ns= no statistical significance.

4.4.7 *In vivo* toxicity evaluation of Mg-based micromotors

Finally, the gastric toxicity of the administrated Mg-based micromotors was evaluated. Healthy mice were orally administered with Mg-based micromotors or DI water once daily for 5 consecutive days. Throughout the treatment, no signs of distress such as squinting of eyes, hunched posture, unkempt fur, or lethargy were observed in both groups. On day 6, mice were sacrificed and their stomachs were processed for histological staining. Longitudinal sections of the glandular stomach were stained with hematoxylin and eosin (H&E), shown in Fig. 4.13. The stomach section of the micromotor-treated group showed undamaged structure of columnar epithelial cells with no signs of superficial degeneration or erosion (Fig. 4.13, left). There was no noticeable difference in the gastric mucosal integrity, in terms of thickness as well as size and number of crypt and villus, between the motor-treated and DI water-treated groups (Fig. 4.13, right). No lymphocytic infiltration into the mucosa and submucosa was observed, implicating no sign of gastric inflammation. The *in vivo* toxicity study of Mg-based micromotors showed no alteration of gastric histopathology or observable inflammation, indicating that the treatment of Mg-based micromotors is safe in the mouse model.

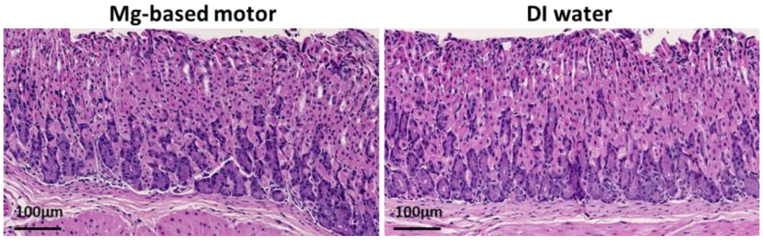

Figure 4.13 *In vivo* toxicity evaluation of the Mg-based micromotors. Uninfected mice were orally administered with the Mg-based micromotors or DI water once daily for 5 consecutive days. On day 6, mice were sacrificed and sections of the mouse stomach tissue were processed for histological staining with hematoxylin and eosin (H&E). Scale bars, 100 μm.

4.4.8 Conclusions

In this work we conducted the first study to evaluate the therapeutic efficacy of a drug-loaded Mg-based micromotor for *in vivo* treatment of *H. pylori* infection in a mouse model. Through these *in vivo* experiments we demonstrated that acid-powered Mg-based micromotors could efficiently be loaded with clinical doses of drugs, retain in the mouse stomach wall, and perform effective *in vivo* bactericidal activity. Our results showed that the active propulsion of drug-loaded Mg-based micromotors in the acidic media of the stomach and motor-tissue interaction lead to efficient drug delivery and hence to a significant reduction of bacteria burden compared to passive drug carriers. Furthermore, such drug-loaded micromotors were able to rapidly deplete the protons in the gastric fluid to reach a neutral pH, thereby excluding the use of PPIs for the *H. pylori* infection treatment. We also demonstrated that there were no toxicological consequences of the micromotors in the mouse models. Overall, our results indicate that micromotors holds great promise for effective and safe therapeutic treatment of *H. pylori* infection. Such micromotor-based therapy represents an exciting new therapeutic regimen for the treatment of stomach diseases such as *H. pylori* infection. While this work is still at early stage and requires more intensive evaluations of the motors prior to their potential practical use, it opens the door to the use of synthetic motors as an active delivery platform for *in vivo* treatment of diseases and will likely trigger intensive research interests in this area.

Chapter 4.1, in full, is a reprint of the material as it appears in ACS Nano, 2015, by Wei Gao, Renfeng Dong, Soracha Thamphiwatana, Jinxing Li, Weiwei Gao, Liangfang Zhang, Joseph Wang. Chapter 4.2, in full, is a reprint of the material as it appears in ACS Nano, 2016, by Jinxing Li, Soracha Thamphiwatana, Wenjuan Liu, Berta Esteban-Fernández de Ávila, Pavimol Angsantikul, Elodie Sandraz, Jianxing Wang, Tailin Xu, Fernando Soto, Valentin Ramez, Xiaolei Wang, Weiwei Gao, Liangfang Zhang, Joseph Wang. Chapter 4.3, in full, is a reprint of the material as it appears in Nature Communications, 2017, by Berta Esteban-Fernández de Ávila, Pavimol Angsantikul, Jinxing Li, Miguel Angel Lopez-Ramirez, Doris E. Ramírez-Herrera, Soracha Thamphiwatana, Chuanrui Chen, Jorge Delezuk, Richard Samakapiruk, Valentin Ramez, Liangfang Zhang, Joseph Wang. The dissertation author was the primary investigator and author of these papers.

4.5 References

(1) Mallouk, T. E.; Sen, A. Powering Nanorobots. *Sci. Am.* **2009**, *300*, 72–77.

(2) Mirkovic, T.; Zacharia, N. S.; Scholes, G. D.; Ozin, G. A. Fuel for Thought: Chemically Powered Nanomotors Out-Swim Nature's Flagellated Bacteria. *ACS Nano* **2010**, *4*, 1782–1789.

(3) Wang, J. *Nanomachines : Fundamentals and Applications*.

(4) Mei, Y.; Solovev, A. A.; Sanchez, S.; Schmidt, O. G. Rolled-up Nanotech on Polymers: From Basic Perception to Self-Propelled Catalytic Microengines. *Chem. Soc. Rev.* **2011**, *40*, 2109.

(5) Paxton, W. F.; Kistler, K. C.; Olmeda, C. C.; Sen, A.; St. Angelo, S. K.; Cao, Y.; Mallouk, T. E.; Lammert, P. E.; Crespi, V. H. Catalytic Nanomotors: Autonomous Movement of Striped Nanorods. *J. Am. Chem. Soc.* **2004**, *126*, 13424–13431.

(6) Guix, M.; Mayorga-Martinez, C. C.; Merkoçi, A. Nano/Micromotors in (Bio)chemical Science Applications. *Chem. Rev.* **2014**, *114*, 6285–6322.

(7) Wilson, D. A.; Nolte, R. J. M.; van Hest, J. C. M. Autonomous Movement of Platinum-Loaded Stomatocytes. *Nat. Chem.* **2012**, *4*, 268–274.

(8) Loget, G.; Kuhn, A. Electric Field-Induced Chemical Locomotion of Conducting Objects. *Nat. Commun.* **2011**, *2*, 535.

(9) Wang, J.; Gao, W. Nano/Microscale Motors: Biomedical Opportunities and Challenges. *ACS Nano* **2012**, *6*, 5745–5751.

(10) Nelson, B. J. B.; Kaliakatsos, I. K. I.; Abbott, J. J. Microrobots for Minimally Invasive Medicine. *Annu. Rev. Biomed. Eng.* **2010**, *12*, 55–85.

(11) Wu, Z.; Wu, Y.; He, W.; Lin, X.; Sun, J.; He, Q. Self-Propelled Polymer-Based Multilayer Nanorockets for Transportation and Drug Release. *Angew. Chemie Int. Ed.* **2013**, *52*, 7000–7003.

(12) Balasubramanian, S.; Kagan, D.; Jack Hu, C.-M.; Campuzano, S.; Lobo-Castañon, M. J.; Lim, N.; Kang, D. Y.; Zimmerman, M.; Zhang, L.; Wang, J. Micromachine-Enabled Capture and Isolation of Cancer Cells in Complex Media. *Angew. Chemie Int. Ed.* **2011**, *50*, 4161–4164.

(13) Campuzano, S.; Orozco, J.; Kagan, D.; Guix, M.; Gao, W.; Sattayasamitsathit, S.; Claussen, J. C.; Merkoçi, A.; Wang, J. Bacterial Isolation by Lectin-Modified Microengines. *Nano Lett.* **2012**, *12*, 396–401.

(14) Wang, W.; Li, S.; Mair, L.; Ahmed, S.; Huang, T. J.; Mallouk, T. E. Acoustic Propulsion of Nanorod Motors Inside Living Cells. *Angew. Chemie* **2014**, *126*, 3265–3268.

(15) Peyer, K. E.; Tottori, S.; Qiu, F.; Zhang, L.; Nelson, B. J. Magnetic Helical Micromachines. *Chem. - A Eur. J.* **2013**, *19*, 28–38.

(16) Chng, E. L. K.; Zhao, G.; Pumera, M. Towards Biocompatible Nano/microscale Machines: Self-Propelled Catalytic Nanomotors Not Exhibiting Acute Toxicity. *Nanoscale* **2014**, *6*, 2119–2124.

(17) Kuralay, F.; Sattayasamitsathit, S.; Gao, W.; Uygun, A.; Katzenberg, A.; Wang, J. Self-Propelled Carbohydrate-Sensitive Microtransporters with Built-In Boronic Acid Recognition for Isolating Sugars and Cells. *J. Am. Chem. Soc.* **2012**, *134*, 15217–15220.

(18) Sattayasamitsathit, S.; Kou, H.; Gao, W.; Thavarajah, W.; Kaufmann, K.; Zhang, L.; Wang, J. Fully Loaded Micromotors for Combinatorial Delivery and Autonomous Release of Cargoes. *Small* **2014**, *10*, 2830–2833.

(19) Gao, W.; Sattayasamitsathit, S.; Uygun, A.; Pei, A.; Ponedal, A.; Wang, J. Polymer-Based Tubular Microbots: Role of Composition and Preparation. *Nanoscale* **2012**, *4*, 2447.

(20) Lai, S. K.; Wang, Y.-Y.; Hanes, J. Mucus-Penetrating Nanoparticles for Drug and Gene Delivery to Mucosal Tissues. *Adv. Drug Deliv. Rev.* **2009**, *61*, 158–171.

(21) Daniel, M.-C.; Astruc, D. Gold Nanoparticles: Assembly, Supramolecular Chemistry, Quantum-Size-Related Properties, and Applications toward Biology, Catalysis, and Nanotechnology. *Chem. Rev.* **2004**, *104*, 293–346.

(22) Orozco, J.; Cortés, A.; Cheng, G.; Sattayasamitsathit, S.; Gao, W.; Feng, X.; Shen, Y.; Wang, J. Molecularly Imprinted Polymer-Based Catalytic Micromotors for Selective Protein Transport. *J. Am. Chem. Soc.* **2013**, *135*, 5336–5339.

(23) King, J. C. Zinc: An Essential but Elusive Nutrient. *Am. J. Clin. Nutr.* **2011**, *94*, 679S–684S.

(24) Que, F.; Gores, G. Cell Death by Apoptosis: Basic Concepts and Disease Relevance for the Gastroenterologist. *Gastroenterology* **1996**, *110*, 1238–1243.

(25) Asplund, M.; Thaning, E.; Lundberg, J.; Sandberg-Nordqvist, A. C.; Kostyszyn, B.; Inganäs, O.; von Holst, H. Toxicity Evaluation of PEDOT/biomolecular Composites Intended for Neural Communication Electrodes. *Biomed. Mater.* **2009**, *4*, 45009.

(26) Huttenhower, C.; Gevers, D.; Knight, R.; Abubucker, S.; Badger, J. H.; Chinwalla, A. T.; Creasy, H. H.; Earl, A. M.; FitzGerald, M. G.; Fulton, R. S. Structure, Function and Diversity of the Healthy Human Microbiome. *Nature* **2012**, *486*, 207–214.

(27) Biteen, J. S.; Blainey, P. C.; Cardon, Z. G.; Chun, M.; Church, G. M.; Dorrestein, P. C.; Fraser, S. E.; Gilbert, J. A.; Jansson, J. K.; Knight, R. Tools for the Microbiome: Nano and Beyond. *ACS Nano* **2016**, *10*, 6–37.

(28) Obonyo, M.; Guiney, D. G.; Harwood, J.; Fierer, J.; Cole, S. P. Role of Gamma Interferon in Helicobacter Pylori Induction of Inflammatory Mediators during Murine Infection. *Infect. Immun.* **2002**, *70*, 3295–3299.

(29) Goodrich, J. K.; Di Rienzi, S. C.; Poole, A. C.; Koren, O.; Walters, W. A.; Caporaso, J. G.; Knight, R.; Ley, R. E. Conducting a Microbiome Study. *Cell* **2014**, *158*, 250–262.

(30) Traverso, G.; Langer, R. Perspective: Special Delivery for the Gut. *Nature* **2015**, *519*,

S19–S19.

(31) Sánchez, S.; Soler, L.; Katuri, J. Chemically Powered Micro- and Nanomotors. *Angew. Chemie Int. Ed.* **2015**, *54*, 1414–1444.

(32) Wang, H.; Pumera, M. Fabrication of Micro/Nanoscale Motors. *Chem. Rev.* **2015**, *115*, 8704–8735.

(33) Palagi, S.; Mark, A. G.; Reigh, S. Y.; Melde, K.; Qiu, T.; Zeng, H.; Parmeggiani, C.; Martella, D.; Sanchez-Castillo, A.; Kapernaum, N. Structured Light Enables Biomimetic Swimming and Versatile Locomotion of Photoresponsive Soft Microrobots. *Nat. Mater.* **2016**, *15*, 647–653.

(34) Li, J.; Rozen, I.; Wang, J. Rocket Science at the Nanoscale. *ACS Nano* **2016**, *10*, 5619–5634.

(35) Peyer, K. K. E.; Zhang, L.; Nelson, B. J. B.; Ozkale, B.; Zeeshan, M. a.; Lühmann, T.; Nelson, B. J. B.; Pané, S.; Toonder, J. M. J. den; Onck, P. R. Bio-Inspired Magnetic Swimming Microrobots for Biomedical Applications. *Nanoscale* **2013**, *5*, 1259–1272.

(36) Baylis, J. R.; Yeon, J. H.; Thomson, M. H.; Kazerooni, A.; Wang, X.; St. John, A. E.; Lim, E. B.; Chien, D.; Lee, A.; Zhang, J. Q. Self-Propelled Particles That Transport Cargo through Flowing Blood and Halt Hemorrhage. *Sci. Adv.* **2015**, *1*, e1500379–e1500379.

(37) Ávila, B. E.-F. de; Martín, A.; Soto, F.; Esteban-Fernández de Ávila, B.; Martín, A.; Soto, F.; Lopez-Ramirez, M. A.; Campuzano, S.; Vásquez-Machado, G. M.; Gao, W. Single Cell Real-Time miRNAs Sensing Based on Nanomotors. *ACS Nano* **2015**, *9*, 6756–6764.

(38) Gao, W.; Dong, R.; Thamphiwatana, S.; Li, J.; Gao, W.; Zhang, L.; Wang, J. Artificial Micromotors in the Mouse’s Stomach: A Step toward *in Vivo* Use of Synthetic Motors. *ACS Nano* **2015**, *9*, 117–123.

(39) Servant, A.; Qiu, F.; Mazza, M.; Kostarelos, K.; Nelson, B. J. Controlled In Vivo Swimming of a Swarm of Bacteria-Like Microrobotic Flagella. *Adv. Mater.* **2015**, *27*, 2981–2988.

(40) Zhang, S.; Bellinger, A. M.; Glettig, D. L.; Barman, R.; Lee, Y.-A. L.; Zhu, J.; Cleveland, C.; Montgomery, V. A.; Gu, L.; Nash, L. D. A pH-Responsive Supramolecular Polymer Gel as an Enteric Elastomer for Use in Gastric Devices. *Nat. Mater.* **2015**, *14*, 1065–1071.

(41) Zhu, Q.; Talton, J.; Zhang, G.; Cunningham, T.; Wang, Z.; Waters, R. C.; Kirk, J.; Eppler, B.; Klinman, D. M.; Sui, Y. Large Intestine–targeted, Nanoparticle-Releasing Oral Vaccine to Control Genitorectal Viral Infection. *Nat. Med.* **2012**, *18*, 1291–1296.

(42) JONES, D. D. G.; MASTERSON, H. G. Effect of Chloride Concentration on the Aqueous Corrosion of a Magnesium Alloy. *Nature* **1961**, *191*, 165–166.

(43) Gao, W.; Feng, X.; Pei, A.; Gu, Y.; Li, J.; Wang, J. Seawater-Driven Magnesium Based Janus Micromotors for Environmental Remediation. *Nanoscale* **2013**, *5*, 4696.

(44) Lautenschläger, C.; Schmidt, C.; Fischer, D.; Stallmach, A. Drug Delivery Strategies in the Therapy of Inflammatory Bowel Disease. *Adv. Drug Deliv. Rev.* **2014**, *71*, 58–76.

(45) Johansson, M. E. V.; Sjövall, H.; Hansson, G. C. The Gastrointestinal Mucus System in Health and Disease. *Nat. Rev. Gastroenterol. Hepatol.* **2013**, *10*, 352–361.

(46) Thamphiwatana, S.; Gao, W.; Obonyo, M.; Zhang, L. In Vivo Treatment of Helicobacter Pylori Infection with Liposomal Linolenic Acid Reduces Colonization and Ameliorates Inflammation. *Proc. Natl. Acad. Sci. U. S. A.* **2014**, *111*, 17600–17605.

(47) Banerjee, A.; Thamphiwatana, S.; Carmona, E. M.; Rickman, B.; Doran, K. S.; Obonyo, M. Deficiency of the Myeloid Differentiation Primary Response Molecule MyD88 Leads to an Early and Rapid Development of Helicobacter-Induced Gastric Malignancy. *Infect. Immun.* **2014**, *82*, 356–363.

(48) Abdelmohsen, L. K. E. A.; Peng, F.; Tu, Y.; Wilson, D. A. Micro- and Nano-Motors for Biomedical Applications. *J. Mater. Chem. B* **2014**, *2*, 2395–2408.

(49) Sundararajan, S.; Lammert, P. E.; Zudans, A. W.; Crespi, V. H.; Sen, A. Catalytic Motors for Transport of Colloidal Cargo. *Nano Lett.* **2008**, *8*, 1271–1276.

(50) Gao, W.; Wang, J. Synthetic Micro/nanomotors in Drug Delivery. *Nanoscale* **2014**, *6*, 10486.

(51) Felfoul, O.; Mohammadi, M.; Taherkhani, S.; de Lanauze, D.; Zhong Xu, Y.; Loghin, D.; Essa, S.; Jancik, S.; Houle, D.; Lafleur, M. Magneto-Aerotactic Bacteria Deliver Drug-Containing Nanoliposomes to Tumour Hypoxic Regions. *Nat. Nanotechnol.* **2016**, *11*, 941–947.

(52) Ávila, B. E.-F. de; Angell, C.; Soto, F.; Esteban-Fernández de Ávila, B.; Angell, C.; Soto, F.; Lopez-Ramirez, M. A.; Báez, D. F.; Xie, S.; Wang, J. Acoustically Propelled Nanomotors for Intracellular siRNA Delivery. *ACS Nano* **2016**, *10*, 4997–5005.

(53) Kagan, D.; Benchimol, M. J.; Claussen, J. C.; Chuluun-Erdene, E.; Esener, S.; Wang, J. Acoustic Droplet Vaporization and Propulsion of Perfluorocarbon-Loaded Microbullets for Targeted Tissue Penetration and Deformation. **2012**.

(54) Leong, T. G.; Randall, C. L.; Benson, B. R.; Bassik, N.; Stern, G. M.; Gracias, D. H. Tetherless Thermobiochemically Actuated Microgrippers. *Proc. Natl. Acad. Sci. U. S. A.* **2009**, *106*, 703–708.

(55) Srivastava, S. K.; Guix, M.; Schmidt, O. G. Wastewater Mediated Activation of Micromotors for Efficient Water Cleaning. *Nano Lett.* **2016**, *16*, 817–821.

(56) Hoop, M.; Shen, Y.; Chen, X.-Z.; Mushtaq, F.; Iuliano, L. M.; Sakar, M. S.; Petruska, A.; Loessner, M. J.; Nelson, B. J.; Pané, S. Magnetically Driven Silver-Coated Nanocoils for Efficient Bacterial Contact Killing. *Adv. Funct. Mater.* **2016**, *26*, 1063–1069.

(57) Soler, L.; Magdanz, V.; Fomin, V. M.; Sanchez, S.; Schmidt, O. G. Self-Propelled Micromotors for Cleaning Polluted Water. *ACS Nano* **2013**, *7*, 9611–9620.

(58) Li, J.; Thamphiwatana, S.; Liu, W.; Esteban-Fernández de Ávila, B.; Angsantikul, P.; Sandraz, E.; Wang, J. J. J. J. J.; Xu, T.; Soto, F.; Ramez, V. Enteric Micromotor Can Selectively Position and Spontaneously Propel in the Gastrointestinal Tract. *ACS Nano* **2016**, *10*, 9536–9542.

(59) Li, J.; Angsantikul, P.; Liu, W.; Esteban-Fernández de Ávila, B.; Thamphiwatana, S.; Xu, M.; Sandraz, E.; Wang, X.; Delezuk, J.; Gao, W. Micromotors Spontaneously Neutralize Gastric Acid for pH-Responsive Payload Release. *Angew. Chemie* **2017**, *129*, 2188–2193.

(60) Walker, D.; Käsdorf, B. T. B.; Jeong, H.-H. H.; Lieleg, O.; Fischer, P. Enzymatically Active Biomimetic Micropropellers for the Penetration of Mucin Gels. **2015**, *1*.

(61) Salama, N. R.; Hartung, M. L.; Müller, A. Life in the Human Stomach: Persistence Strategies of the Bacterial Pathogen Helicobacter Pylori. *Nat. Rev. Microbiol.* **2013**, *11*, 385–399.

(62) Sachs, G.; Weeks, D. L.; Melchers, K.; Scott, D. R. The Gastric Biology of *Helicobacter Pylori*. *Annu. Rev. Physiol.* **2003**, *65*, 349–369.

(63) Holtmann*, G.; Cain‡, C.; Malfertheiner§, P. Gastric Helicobacter Pylori Infection Accelerates Healing of Reflux Esophagitis during Treatment with the Proton Pump Inhibitor Pantoprazole. *Gastroenterology* **1999**, *117*, 11–16.

(64) Olbe, L.; Carlsson, E.; Lindberg, P. A Proton-Pump Inhibitor Expedition: The Case Histories of Omeprazole and Esomeprazole. *Nat. Rev. Drug Discov.* **2003**, *2*, 132–139.

(65) Richardson, P.; Hawkey, C. J.; Stack, W. A. Proton Pump Inhibitors. Pharmacology and Rationale for Use in Gastrointestinal Disorders. *Drugs* **1998**, *56*, 307–335.

(66) Moayyedi, P.; Leontiadis, G. I. The Risks of PPI Therapy. *Nat. Rev. Gastroenterol. Hepatol.* **2012**, *9*, 132–139.

(67) Ho, P. M.; Maddox, T. M.; Wang, L.; Fihn, S. D.; Jesse, R. L.; Peterson, E. D.; Rumsfeld, J. S. Risk of Adverse Outcomes Associated With Concomitant Use of Clopidogrel and Proton Pump Inhibitors Following Acute Coronary Syndrome. *JAMA* **2009**, *301*, 937.

(68) Sheen, E.; Triadafilopoulos, G. Adverse Effects of Long-Term Proton Pump Inhibitor Therapy. *Dig. Dis. Sci.* **2011**, *56*, 931–950.

(69) Yang, Y.-X.; Lewis, J. D.; Epstein, S.; Metz, D. C. Long-Term Proton Pump Inhibitor Therapy and Risk of Hip Fracture. *JAMA* **2006**, *296*, 2947.

(70) Martirosyan, A.; Olesen, M. J.; Howard, K. A. Chitosan-Based Nanoparticles for Mucosal Delivery of RNAi Therapeutics. In; 2014; pp. 325–352.

(71) Li, J.; Singh, V. V.; Sattayasamitsathit, S.; Orozco, J.; Kaufmann, K.; Dong, R.; Gao, W.; Jurado-Sanchez, B.; Fedorak, Y.; Wang, J. Water-Driven Micromotors for Rapid Photocatalytic Degradation of Biological and Chemical Warfare Agents. *ACS Nano* **2014**, *8*, 11118–11125.

(72) Watanabe, K.; Murakami, K.; Sato, R.; Kashimura, K.; Miura, M.; Ootsu, S.; Miyajima, H.; Nasu, M.; Okimoto, T.; Kodama, M. Effect of Sucralfate on Antibiotic Therapy for Helicobacter Pylori Infection in Mice. *Antimicrob. Agents Chemother.* **2004**, *48*, 4582–4588.

Chapter 5 Conclusions and Future Perspectives

Over the past decade, micro/nanorobotics has emerged as a novel and versatile platform to integrate the advantages of nanotechnologies and robotic sciences. A diverse set of design principles and propulsion mechanisms have thus led to the development of highly capable and specialized micro/nanorobots. These micro/nanorobots have unique and multivalent functionalities, including fast motion in complex biological media, large cargo-towing force for directional and long-distance transport, easy surface functionalization for precise capture and isolation of target individuals, and excellent biocompatibility for in vivo operation. These attractive functionalities and capabilities of micro/nanorobots have facilitated biomedical applications, ranging from targeted delivery of payloads and precise surgery on a cellular level to ultrasensitive detection of biological molecules and rapid removal of toxic compounds. These developments have advanced the micro/nanorobots from chemistry laboratories and test tubes to whole living systems. Such *in vivo* studies serve as an important step forward toward clinical translation of the micro/nanorobots.

The ability of micro/nanorobots to address health care issues is just in its infancy. Overcoming knowledge gaps in nanorobotics could have a profound impact on different medical domains. Tremendous efforts and innovations are required for realizing the full potential of these tiny robots for performing complex operations within body locations that were previously inaccessible. Future micro/nanorobots must mimic the natural intelligence of their biological counterparts (e.g., microorganisms and molecular machines) with high mobility, deformable structure, adaptable and sustainable operation, precise control, group behavior with swarm intelligence, sophisticated functions, and even self-evolving and self-replicating capabilities.

A significant challenge is to identify new energy sources for prolonged, biocompatible, and autonomous *in vivo* operation. Although different chemical fuels and external stimuli have been explored for nanoscale locomotion in aqueous media [1], new alternative fuels and propulsion mechanisms are necessary for safe and sustainable operation in the human body. Most of the catalytic micromotors rely on hydrogen peroxide fuel and hence can only be used in vitro. Micromotors powered by active material propellants (e.g., Mg, Zn, Al, and $CaCO_3$) have relatively short lifetimes because of rapid consumption of their propellant during their propulsion. Recent efforts have indicated that enzyme-functionalized nanomotors could be powered by bodily fluid constituents, such as blood glucose or urea [2,3]. The power and stability of these enzyme-based motors require further improvements for practical implementation. Magnetic and acoustic nanomotors can provide fuel-free and on-demand speed regulation, which is highly suitable for nanoscale surgery but may hinder autonomous therapeutic interventions.

Moving nanorobots from test tubes to living organisms would require significant future efforts. The powerful performance of micro/nanorobots has already been demonstrated in viscous biological fluids such as gastric fluid or whole blood [4–8]. Operating these tiny devices in human tissues and organs that impose larger barriers to motion requires careful examination. Magnetically powered microswimmers have been successfully actuated in the peritoneal cavity of a mouse using a weak rotating magnetic field of 9 mT [9]. Magneto-aerotactic bacteria were able to migrate into tumor hypoxic regions under a focalized directional magnetic field of only 15 G [10]. Ultrasound-powered micromotors with powerful “ballistic” capabilities have enabled deep tissue penetration [11]. Powering nanorobot within tissues and organs could greatly benefit from their small size. Such “small is better” philosophy has already been verified using nanoscale magnetic propellers, which display a significant advantage for propulsion in viscoelastic hyaluronan gels because they are of the same size range as the openings in the gel’s mesh, compared with the impeded motion of larger propellers [12]. These results demonstrate that nanorobots are highly promising for achieving efficient motion in tissues enabled by the nanoscale size and optimized design. The miniaturization advantages of smaller nanorobots have also been realized for overcoming cellular barriers and internalizing into cells [13].

Designing robots to perform tasks at the nanoscale is essentially a materials science or surface science problem because the operation and intelligence of tiny robots rely primarily on their materials and surface properties. Biomedical nanorobots are designed for environments involving unanticipated biological events, changing physiological conditions, and soft tissues. Therefore, diverse smart materials, such as biological materials, responsive materials, or soft materials, are highly desired to provide the necessary actuation and multifunctionality while avoiding irreversible robotic malfunctions in complex physiologically relevant body systems. Recent report has shown that the macrophage uptake of rotating magnetic microrobots could be avoided by adjusting the rotational trap stiffness [14]. Alternatively, coupling synthetic nanomachines with natural biological materials can minimize undesired immune evasion and biofouling effects experienced in complex biological fluids, leading to enhanced mobility and lifetime in these media [15]. Responsive materials are highly desired for designing configurable nanorobots for adaptive operation under rapidly changing conditions. Nanorobots are also desired to be soft and deformable to ensure maneuverability and mechanical compliance to human body and tissues [16,17]. Eventually, they should be made of transient biodegradable materials that disappear upon completing their tasks [18]. New fabrication and synthesis approaches, such as 3D nanoprinting, should be explored for large-scale, high-quality, and cost-efficient fabrication of biomedical nanorobots. Advancing nanorobots into the next level will thus be accomplished with new smart materials and cutting-edge fabrication techniques.

Biomedical nanorobots are expected to cooperate, with thousands of units moving independently and coordinately to target the disease site. The coordinated action of multiple nanorobots could be used for performing tasks (e.g., effective delivery of large therapeutic payloads or large-scale detoxification processes) that are not possible using a single robot. Although individual navigation and collective behavior of nanorobots have been explored, mimicking the natural intelligence group communication and synchronized coordination, from one to many, is a challenging issue. Advancing the swarm intelligence of nanorobots toward group motion planning and machine learning at the nanoscale is highly important for enhancing their precision treatment capability. Fundamental understanding of “active matter” and related quantitative control theory can guide the realization of such swarming behavior in dynamically changing environments. High-resolution simultaneous localization and mapping of nanorobots in the human body are experimentally difficult using conventional optical microscopy techniques. Future biomedical operation of nanorobots will require their coupling with modern imaging systems and feedback control systems for arbitrary 4D navigation of many-nanorobot systems.

Looking to the future, the development and application of micro/nanorobots in medicine is expected to become a vigorous research area. To realize the full potential of the micro/nanorobots in the medical field, nanorobotic scientists should work more closely with medical researchers for thorough investigations of the behavior and functionality of the robots, including studies on their biocompatibility, retention, toxicity, biodistribution, and therapeutic efficacy. Considering the promising results achieved recently in GI delivery and ophthalmic therapies, we strongly encourage nanorobotic scientists to look into the demands and needs of the medical community to design problem-oriented medical device for specific diagnostic or therapeutic functions. Addressing these specific needs will lead to accelerated translation of micro/nanorobots research into practical clinical use. We envision that with close collaboration between the nanorobotic and medical communities, these challenges can be gradually addressed, eventually expanding the horizon of micro/nanorobots in medicine.

Chapter 5 is based, in part, on the material as it appears in Science Robotics, 2017, by Jinxing Li, Berta Esteban-Fernández de Ávila, Wei Gao, Liangfang Zhang, Joseph Wang. The dissertation author was the primary investigator and author of these papers.

5.1 References

(1) Wang, J. *Nanomachines : Fundamentals and Applications*.

(2) Ma, X.; Jannasch, A.; Albrecht, U.-R.; Hahn, K.; Miguel-López, A.; Schäffer, E.; Sánchez, S. Enzyme-Powered Hollow Mesoporous Janus Nanomotors. *Nano Lett.* **2015**, *15*, 7043–7050.

(3) Dey, K.; Zhao, X.; Tansi, B.; Méndez-Ortiz, W. Micromotors Powered by Enzyme Catalysis. *Nano* **2015**.

(4) Gao, W.; Dong, R.; Thamphiwatana, S.; Li, J. Artificial Micromotors in the Mouse's Stomach: A Step toward in Vivo Use of Synthetic Motors. *ACS* **2015**.

(5) Li, J.; Thamphiwatana, S.; Liu, W.; Esteban-Fernández de Ávila, B.; Angsantikul, P.; Sandraz, E.; Wang, J. J. J. J. J.; Xu, T.; Soto, F.; Ramez, V. Enteric Micromotor Can Selectively Position and Spontaneously Propel in the Gastrointestinal Tract. *ACS Nano* **2016**, *10*, 9536–9542.

(6) Li, J.; Angsantikul, P.; Liu, W.; Esteban-Fernández de Ávila, B.; Thamphiwatana, S.; Xu, M.; Sandraz, E.; Wang, X.; Delezuk, J.; Gao, W. Micromotors Spontaneously Neutralize Gastric Acid for pH-Responsive Payload Release. *Angew. Chemie* **2017**, *129*, 2188–2193.

(7) Zhao, G.; Viehrig, M.; Pumera, M. Challenges of the Movement of Catalytic Micromotors in Blood. *Lab Chip* **2013**.

(8) Venugopalan, P.; Sai, R.; Chandorkar, Y.; Basu, B. Conformal Cytocompatible Ferrite Coatings Facilitate the Realization of a Nanovoyager in Human Blood. *Nano Lett.* **2014**.

(9) Servant, A.; Qiu, F.; Mazza, M.; Kostarelos, K. Controlled In Vivo Swimming of a Swarm of Bacteria-Like Microrobotic Flagella. *Advanced* **2015**.

(10) Felfoul, O.; Mohammadi, M.; Taherkhani, S.; de Lanauze, D.; Zhong Xu, Y.; Loghin, D.; Essa, S.; Jancik, S.; Houle, D.; Lafleur, M. Magneto-Aerotactic Bacteria Deliver Drug-Containing Nanoliposomes to Tumour Hypoxic Regions. *Nat. Nanotechnol.* **2016**, *11*, 941–947.

(11) Kagan, D.; Benchimol, M. J.; Claussen, J. C.; Chuluun-Erdene, E.; Esener, S.; Wang, J. Acoustic Droplet Vaporization and Propulsion of Perfluorocarbon-Loaded Microbullets for Targeted Tissue Penetration and Deformation. **2012**.

(12) Schamel, D.; Mark, A.; Gibbs, J.; Miksch, C.; Morozov, K. Nanopropellers and Their Actuation in Complex Viscoelastic Media. *ACS Nano* **2014**.

(13) Ávila, B. E.-F. de; Angell, C.; Soto, F.; Esteban-Fernández de Ávila, B.; Angell, C.; Soto, F.; Lopez-Ramirez, M. A.; Báez, D. F.; Xie, S.; Wang, J. Acoustically Propelled Nanomotors for Intracellular siRNA Delivery. *ACS Nano* **2016**, *10*, 4997–5005.

(14) Schuerle, S.; Vizcarra, I.; Moeller, J. Robotically Controlled Microprey to Resolve Initial Attack Modes Preceding Phagocytosis. *Science (80-.).* **2017**.

(15) Wu, Z.; Li, J.; de Ávila, B. E.-F.; Li, T.; Gao, W.; He, Q.; Zhang, L.; Wang, J. Water-Powered Cell-Mimicking Janus Micromotor. *Adv. Funct. Mater.* **2015**, *25*, 7497–7501.

(16) Huang, H.; Sakar, M.; Petruska, A.; Pané, S. Soft Micromachines with Programmable Motility and Morphology. *Nature* **2016**.

(17) Hines, L.; Petersen, K.; Lum, G.; Sitti, M. Soft Actuators for Small-Scale Robotics. *Adv. Mater.* **2016**.

(18) Chen, C.; Karshalev, E.; Li, J.; Soto, F.; Castillo, R.; Campos, I.; Mou, F.; Guan, J.; Wang, J. Transient Micromotors That Disappear When No Longer Needed. *ACS Nano* **2016**, *10*, 10389–10396.